



HAL
open science

Nouveaux Photosensibilisateurs Encapsulés dans des Complexes d'Arène-Ruthénium Actifs en Thérapie Photodynamique : signalisation Intracellulaire et Évaluation dans le Cancer Colorectal

Suzan Ghaddar

► **To cite this version:**

Suzan Ghaddar. Nouveaux Photosensibilisateurs Encapsulés dans des Complexes d'Arène-Ruthénium Actifs en Thérapie Photodynamique : signalisation Intracellulaire et Évaluation dans le Cancer Colorectal. Médecine humaine et pathologie. Université de Limoges; Université Libanaise, 2024. Français. NNT : 2024LIMO0122 . tel-04921284

HAL Id: tel-04921284

<https://theses.hal.science/tel-04921284v1>

Submitted on 30 Jan 2025

HAL is a multi-disciplinary open access archive for the deposit and dissemination of scientific research documents, whether they are published or not. The documents may come from teaching and research institutions in France or abroad, or from public or private research centers.

L'archive ouverte pluridisciplinaire **HAL**, est destinée au dépôt et à la diffusion de documents scientifiques de niveau recherche, publiés ou non, émanant des établissements d'enseignement et de recherche français ou étrangers, des laboratoires publics ou privés.

University of Limoges
ED 652 - Biologie, Chimie, Santé (BCS)
LABC/S, UR 22722, Faculty of Pharmacy

A thesis submitted to the University of Limoges
in partial fulfillment of the requirements of the degree of
Doctor of Philosophy
Cancer Biology

Presented and defended by
Suzan GHADDAR

On December 20, 2024

New Photosensitizers Encapsulated within Arene-Ruthenium Complexes Active in Photodynamic Therapy: Intracellular Signaling and Evaluation in Colorectal Cancer

Thesis supervisors:

Mr. **Bertrand LIAGRE**, University Professor, University of Limoges, France

Ms. **Mona DIAB-ASSAF**, University Professor, Lebanese University, Lebanon

JURY:

President of jury

M. **David LEGER**, University Professor, University of Limoges, France

Reporters

M. **Nadira DELHEM**, University Professor, University of Lille, France

M. **Mohamad MROUEH**, University Professor, Lebanese American University, Lebanon

Examiners

M. **Vincent SOL**, University Professor, University of Limoges, France

M. **Bruno THERRIEN**, University Professor, University of Neuchâtel, Switzerland

M. **Abdo JURJUS**, University Professor, American University of Beirut, Lebanon



To Jawdat SALAMI (*RIP*),
Honoring your strength in the cancer battle
and the enduring memory you left behind.

02/2024

“The only thing we have to fear is fear itself.”
Franklin D. Roosevelt, 1933

Acknowledgments

The completion of this work has been an ambitious pursuit driven by a passion for discovery. Not only does it represent the culmination of years of dedicated research and intellectual growth, but also the realization of a vision shaped by the invaluable support and inspiration of those who have walked this path with me.

Pr. Nadira DELHEM

University Professor

University of Lille, Inserm, CHU Lille, U1189-ONCOTHAÏ-Assisted Laser Therapy and Immunotherapy for Oncology, Lille F-59000, France

Pr. Mohamad MROUEH

University Professor

Lebanese American University, School of Pharmacy, Lebanon

Pr. David LEGER

University Professor

University of Limoges, Faculty of Pharmacy, Department of Biochemistry and Molecular Biology, Institute Ω Health, LABCiS UR22722, France

Pr. Abdo JURJUS

University Professor

American University of Beirut, Department of Anatomy, Cell Biology and Physiological Sciences, Faculty of Medicine, Lebanon

Pr. Vincent SOL

University Professor

University of Limoges, Faculty of Science and Technology, Department of Chemistry, Institute Ω Health, LABCiS UR22722, France

I sincerely appreciate all of you for contributing your expertise to this jury and for agreeing to evaluate my thesis work. I extend my deepest gratitude and highest respect to each of you.

Pr. Bertrand LIAGRE

University Professor

University of Limoges, Faculty of Pharmacy, Department of Biochemistry and Molecular Biology, Institute Ω Health, LABCiS UR22722, France

One of the greatest blessings in the journey of a PhD student is having an understanding and supportive director. I consider myself fortunate to have experienced this blessing and I am deeply grateful for the opportunities you provided me with. Despite your demanding schedule, you always kept your door open to offer guidance and support, for me, and for the entire laboratory team. I truly appreciate your unwavering dedication and will never forget the moments when you were there to help me navigate this challenging path.

Pr. Mona Diab-ASSAF

University Professor

Lebanese University, Faculty of Science, Lebanon

Thank you for giving me the chance to pursue my ambition and enter the field of science and research. I am sincerely thankful for your humanity, support, and compassion. During my Master's in Cancerology, I found the courses you taught us incredibly engaging and fueled my

motivation to delve deeper into cancer therapeutics research. Your constant care and encouragement have been a driving force continuing to inspire me throughout my PhD journey.

Pr. Bruno THERRIEN and Dr. Manuel GALLARDO-VILLAGRAN

University Professor and Doctor

University of Neuchâtel - Institute of Chemistry, Switzerland

Thank you for your collaboration and your consistent availability in synthesizing the key compounds essential to our research. Your efforts in providing these molecules were fundamental, as they formed the basis of our tests and enabled us to explore a highly significant and impactful topic in the field of science.

Pr. Guillaume Chemin

University Professor

University of Limoges, Faculty of Pharmacy, Department of Biochemistry and Molecular Biology, Institute Ω Health, LABCiS UR22722, France

Mrs. Aline PINON

Thank you for always being there to help us, from solving our smallest issues to tackling the biggest challenges. Your dedication and willingness to address every technical question have made you our go-to person for support. I am deeply grateful for your care, openness, and the constant reassurance you've provided. Your readiness to assist and your welcoming attitude have been invaluable.

Mrs. Frédérique MARTIN

Thank you for your constant help, kindness, and sense of humor that make the laboratory feel more like home.

Mrs. Catherine Ouk, Mrs. Claire CARRION and Mrs. Fabienne BARAIGE

I am grateful for the huge technical support you provided me to excel with various scientific devices, as well as your guidance and expertise. Your assistance with these analytical tools has been crucial in advancing my research, and I greatly appreciate your dedication and knowledge.

Laboratory colleagues

I would like to acknowledge **Hind, Cécile, Rayan, Léa, Soufyane, Valentin, Silvère,** and **Guillaume** for their kindness and readiness to assist whenever needed. Our teamwork was crucial in overcoming different challenges throughout this journey.

Family and friends

First, I want to extend my deep gratitude to my fiancé, **Ali**, for his unlimited support, encouragement, and assistance. Your motivation was crucial in helping me overcome many challenges, and you were always there to listen, whether it was about my smallest concerns or major issues. Even though we were often far apart, your presence was always felt in my heart.

Special thanks to all my family, especially my mother, father, and siblings for the motivation and joy they brought throughout the way.

Also, to my dear friends **Jacquie, Julia, Sana**, and everyone who positively impacted my journey by infusing happy moments and adventures that boosted my energy. To me, you are not only my friends but also a part of my family. Thank you for everything.

Last but not least, a special appreciation to my friend **Jean-Yves** for our scientific discussions which were the best I ever had. It is an honor to meet you and elaborate on our scientific discoveries together. Thank you for your invaluable support and dedicated time.

Rights

This creation is available under a Creative Commons contract:
« **Attribution-Non-Commercial-No Derivatives 4.0 International** »
online at <https://creativecommons.org/licenses/by-nc-nd/4.0/>



Table of Contents

Acknowledgments	4
Rights	7
Table of Contents	8
List of Figures.....	11
List of Tables	15
List of Abbreviations	16
Introduction	24
Chapter I. Colorectal cancer	25
I.1. The large intestine	25
I.1.1. Location and structure	25
I.1.2. Histology of the large intestine.....	27
I.1.3. Functions and state of the large intestine	28
I.1.4. Vascularization of the large intestine	29
I.1.5. Diseases of the colon	29
I.2. Cancer: general overview and prevalence	32
I.3. Colorectal cancer	33
I.3.1. Epidemiology.....	33
I.3.2. Risk factors and symptoms.....	34
I.3.3. Types	35
I.3.4. Pathways of CRC carcinogenesis.....	35
I.3.5. CRC development: genetics and histology	36
I.3.6. Classification of polyps	38
I.4. Screening and clinical diagnosis	39
I.4.1. Endoscopic diagnosis	40
I.4.2. Biochemical and histological diagnosis	40
I.5. Colorectal cancer therapies	41
I.5.1. Surgery.....	41
I.5.2. Radiotherapy	41
I.5.3. Chemotherapy	42
I.5.4. Targeted therapies and nanomedicine.....	42
I.5.5. Immunotherapy	43
I.5.6. Gene therapy.....	44
I.5.7. Laser therapy	44
I.5.8. Adoptive cell therapy (ACT).....	45
I.5.9. Anti-tumor vaccine therapies	45
I.6. Current targeted therapies for mCRC.....	46
I.7. New biomarkers of the clinical response	47
I.8. Staging classification	47
Chapter II. Photodynamic therapy	52
II.1. History of photodynamic therapy.....	52
II.2. Principles of photodynamic therapy.....	53
II.3. Mechanisms of action in photodynamic therapy	54
II.4. PDT-induced molecular damage and cell death	56
II.5. Characteristics and design of PSs.....	58
II.5.1. PS absorbance spectra	59
II.5.2. PS uptake and localization	60
II.5.3. Photobleaching of PS	61

II.6. Photo-physics and light sources.....	61
II.7. Principle structures of PSs	63
II.7.1. Non-tetrapyrrolic PSs	63
II.7.2. Tetrapyrrolic PSs.....	66
II.8. Pharmacokinetics of PS	70
II.9. Passive tumoral targeting.....	71
II.10. Current applications of PSs.....	71
II.11. PDT of CRC	73
II.12. Combination therapies with PDT in the treatment of CRC.....	75
Chapter III. Apoptosis	78
III.1. Apoptosis or programmed cell death.....	78
III.2. Physiological role of apoptosis	79
III.3. Caspases and cell death.....	80
III.4. Downstream activity of caspases	82
III.5. Other key factors of apoptosis.....	83
III.6. Apoptotic signaling pathways	84
III.6.1. Mitochondrial or Intrinsic Apoptotic Pathway.....	84
III.6.2. Extrinsic Apoptotic Pathway	85
III.7. Crosstalk between the intrinsic and extrinsic pathways	85
III.8. Apoptosis and cancer.....	87
III.9. PDT induced apoptosis	87
Chapter IV. Ruthenium Metal Assemblies	90
IV.1. Past and present states	90
IV.2. Platinum-based cancer therapy	90
IV.3. Ru applications in cancer therapy	92
IV.4. Ru coordinated PSs in PDT	95
IV.5. Arene implications within Ru complexes	96
IV.6. Arene-Ru metal assemblies as PS delivery systems	98
Chapter V. Objective of the Research Project	103
Chapter VI. Materials and Methods	105
VI.1. Materials.....	106
VI.2. Synthesis of the arene-Ru assemblies encapsulating a photosensitizer	106
VI.3. Cell lines and culture	106
VI.4. Treatment and illumination	106
VI.5. Cell viability assay	107
VI.6. Intracellular ROS generation.....	107
VI.7. Cellular internalization and localization	107
VI.8. Cell cycle analysis	108
VI.9. Apoptotic Assays	108
VI.9.1. Annexin V-FITC/PI dual staining	108
VI.9.2. Quantitative analysis of caspases-3/-7	109
VI.9.3. Protein extraction and western blot	109
VI.9.4. DNA fragmentation.....	110
VI.10. Statistical Analysis.....	110
Chapter VII. Results of <i>in vitro</i> experiments.....	111
VII.1. Cell viability assay	112
VII.2. ROS generation.....	115
VII.3. Cellular localization using confocal microscopy	118
VII.4. Cell cycle analysis	120
VII.5. Apoptotic assay	124

VII.5.1. Annexin V/PI	124
VII.5.2. Quantitative analysis of caspase-3/7 activity	129
VII.5.3. Western Blot	132
VII.5.4. DNA fragmentation.....	138
Chapter VIII. Discussion	141
Chapter IX. Conclusion and Perspectives.....	148
Bibliography	152
Publication.....	175
Abstract.....	195

List of Figures

Figure 1: Anatomy of the large intestine	26
Figure 2: (a) Histology of the large intestine optimized for its digestive function and (b) micrograph showing the simple columnar epithelium and tissue layers of the colon..	28
Figure 3: (a) Arterial supply, lymphatic drainage, and (b) venous drainage of the large intestine	29
Figure 4: Crohn’s disease-induced immune response. Complex interactions between various immune cells and cytokines determine the type of immune response and disease progression	31
Figure 5: Diverticulosis and diverticulitis of the colon	32
Figure 6: Hallmarks of cancer	33
Figure 7 : Worldwide (a) incidence and (b) mortality cases in 2022	34
Figure 8: The estimated number of CRC (a) incidents and (b) death cases in the top 10 countries with the highest incidence rates in 2020 and projections until 2040	34
Figure 9: Several genetic mutations contribute to the development of cancer	36
Figure 10: The somatic genetic mutations contributing to the development and progression of cancer	37
Figure 11: The molecular pathways contributing to the development and progression of CRC	38
Figure 12: Tubular adenoma with hematoxylin-eosin staining and visualization under (a) low and (b) high power microscopic magnifications with clear histological appearances of the branched tubular structures.....	39
Figure 13 : Villous adenoma with hematoxylin-eosin staining and visualization under (a) low and (b) high power microscopic magnifications with clear histological appearances of the long finger-like projections	39
Figure 14: Immune checkpoint inhibitors: (a) the interaction between PD-1 and PD-L1 prevents the T cell from killing the tumor cell (b) blocking this interaction with anti-PD-1 triggers the death of the tumor cell by the T cell	44
Figure 15: TNM classification system: the letter “T” refers to “Tumor” and is an indicator of the size and depth of the tumor. It ranges from Tx until T4.	48
Figure 16: TNM classification system: the letter “N” refers to “lymph nodes” and is an indicator of lymph nodes’ involvement. It ranges from Nx until N2.	48
Figure 17: TNM classification system: the letter “M” refers to “metastasis” and is an indicator of distant metastasis. It consists of M0 and M1.	49
Figure 18: The different stages of CRC representing its development and progression	49
Figure 19: The essential factors of PDT.....	53
Figure 20 : PS administration and selective tumor targeting of the patient.....	54
Figure 21: Jablonski diagram of PDT mechanism of action.....	55

Figure 22: (a) The variation in the ability of light of different wavelengths to penetrate along the depth of the tissue and (b) the phototherapeutic window where tissue absorption and light scattering are insignificant	60
Figure 23: Different laser light irradiation approaches corresponding to the various tumor locations	63
Figure 24: Chemical structure of hypericin	63
Figure 25: Chemical structure of curcumin	64
Figure 26: Chemical structure of methylene blue	64
Figure 27: Chemical structure of rose bengal	65
Figure 28: Third generation formulated through (a) chemical modification by linking the second-generation PS to a targeting moiety and (b) vectorization of PS through encapsulation in carriers	68
Figure 29: Features representing the apoptotic phenomenon	79
Figure 30: Physiological role of apoptosis in tissue and organ sculpting	80
Figure 31: Caspase structure and activation	81
Figure 32: Activation of initiator and effector caspases	82
Figure 33: Apoptosome assembly in the intrinsic (mitochondrial) apoptotic pathway	84
Figure 34: Biological factors involved in the extrinsic apoptotic pathways	85
Figure 35: Interaction between the intrinsic and extrinsic pathways	86
Figure 36: PDT induced cell apoptosis	88
Figure 37: Chemical structures of cisplatin, carboplatin, and oxaliplatin	91
Figure 38: Activation of cisplatin and DNA damage (a) through undergoing aquation reactions and (b) formation of intrastrand adducts and interstrand cross links	92
Figure 39: Structure of NAMI-A	93
Figure 40: Structure of KP1019	94
Figure 41: Structure of NKP1339	94
Figure 42: Structure of TLD1143	95
Figure 43: Examples of arene-Ru tetranuclear complexes conjugated to porphyrin to enhance PDT efficacy	96
Figure 44: Chemical structure of RAPTA-C	97
Figure 45: Biologically active arene-Ru metalla-assemblies with tetranuclear molecular structures	98
Figure 46: (a) Formation of arene-Ru metallaprisms from metallapanel and (b) dinuclear arene-Ru metallaclips	98
Figure 47: Synthesis of the metalla-prisms and the molecular structures of different guests that can be included into various host-guest systems	99
Figure 48: Examples of the different host-guest systems where the guest can be included in the cavities of (a) prismatic or (b) cubic metallacages	100
Figure 49: (a) Encapsulation or (b) functionalization of PS in arene-Ru metalla-assemblies	100

Figure 50: The host-guest systems investigated in our study with porphyrin PS acting as guests.	102
Figure 51: Evaluation of the photocytotoxicity of the arene-Ru assemblies, with or without porphyrin PS in their inner cavity, in the HCT116 cell line.	113
Figure 52 : Evaluation of the photocytotoxicity of the arene-Ru assemblies, with or without porphyrin PS in their inner cavity, in the HT-29 cell line.	114
Figure 53: Graphical representation of the IC₅₀ values (nM) determined by MTT assay in the HCT116 and HT-29 cell lines.	114
Figure 54 : Evaluation of ROS production by DCFDA staining in the HCT116 cell line.	116
Figure 55: Histogram representing the intracellular ROS production in the HCT116 cell line.	116
Figure 56: Evaluation of ROS production by DCFDA staining in the HT-29 cell line. ...	117
Figure 57: Histogram representing the intracellular ROS production in HT-29 cell line.	117
Figure 58: Detection of cytoplasmic localization in the HCT116 cell line after treatment with PS_CM1 or PS_CM2.	118
Figure 59: Detection of cytoplasmic localization in the HT-29 cell line after treatment with PS_CM1 or PS_CM2.	118
Figure 60: Investigation of possible co-localization with mitochondria, ER, and lysosomes in the HCT116 cell line.	119
Figure 61: Investigation of a possible co-localization with mitochondria, ER, and lysosomes in the HT-29 cell line.	120
Figure 62: PDT effect on the cell cycle progression of HCT116 cell line.	121
Figure 63: Histograms representing the PDT effect on cell cycle progression of HCT116 cell line.	122
Figure 64: PDT effect on the cell cycle progression of HT-29 cell line.	123
Figure 65 : Histograms representing the PDT effect on cell cycle progression of HT-29 cell line.	124
Figure 66: Histograms representing the percentages of apoptotic and viable cells after PDT in the HCT116 cell line	126
Figure 67 : Evaluation of the percentages of apoptotic cells after 24 h of PDT in HCT116 cell line.	126
Figure 68: Histograms representing the percentages of apoptotic and viable cells after PDT in the HT-29 cell line.	128
Figure 69: Evaluation of the percentages of apoptotic cells after 48h of PDT in the HT-29 cell line.	128
Figure 70: Caspase-3/7 activity revealed by green fluorescence in the HCT116 cell line.	130
Figure 71: Evaluation of the caspase-3/7 activity by fluorescence in the HCT116 cell line.	130

Figure 72: Caspase-3/7 activity revealed by green fluorescence in the HT-29 cell line.	131
Figure 73: Evaluation of the caspase-3/7 activity by fluorescence in the HT-29 cell line.	132
Figure 74: Effects of the assemblies with/without PDT on the protein expression of apoptotic markers in the HCT116 cell line.	134
Figure 75: Effects of the assemblies with/without PDT on the protein expression of apoptotic markers in the HT-29 cell line.	135
Figure 76: Effects of the assemblies with/without PDT on the expression of pro-apoptotic and anti-apoptotic proteins in the HCT116 cell line.	136
Figure 77: Effects of the assemblies with/without PDT on the expression of pro-apoptotic and anti-apoptotic proteins in the HT-29 cell line.	137
Figure 78: PDT-induced DNA fragmentation in the HCT116 cell line.	138
Figure 79: PDT-induced DNA fragmentation in the HT-29 cell line.	139

List of Tables

Table 1: Key pathological differences between Crohn’s disease and ulcerative colitis	30
Table 2 : Targeted therapies for mCRC approved by the FDA	46
Table 3: Classification of CRC based on their stages and the associated probability percentage of five–year survival	50
Table 4: Characteristics of hypericin, rose bengal, curcumin, and methylene blue	65
Table 5: Examples of first and second-generation PSs, their characteristics and uses	67
Table 6: Examples of targeted PSs of the third generation, their characteristics, and applications	68
Table 7: Examples of nano-vectorized PSs of the third generation, their characteristics, and applications	69
Table 8: PSs under clinical phase trials and approved for the treatment of different cancer types and diseases	72

List of Abbreviations

A

ACE	Angiotensin Converting Enzyme
AFPAA	Functionalized polyacrylamide
AIF	Apoptosis Inducing Factor
Akt	Protein Kinase B
ALA	Aminolevulinic acid
APC	Adenomatous Polyposis Coli
APC	Antigen Presenting Cell
APLS	Alkyl phospholipid analogs
ATCC	American Type Culture Collection
ATG16L1	Autophagy related 16 like 1
ATP	Adenosine triphosphate

B

BAK	Bcl-2 homologous Antagonist / Killer
BAX	Bcl-2 Associated X
BCL-2	B-cell lymphoma 2
BCL-XL	B-cell lymphoma-extra Large
BID	BH3 Interacting Domain
BIM	Bcl-2 Interacting Mediator of cell death
BMPR	Bone Morphogenetic Protein Receptor
BPD	Benzoporphyrin derivative
BRAF	B-subgroup Rapidly Accelerated Fibrosarcoma
BSA	Bovine Serum Albumin

C

C/EBPs	CCAAT/ Enhancer Binding Proteins
CA	Carbohydrate Antigen
CARD	Caspase Activation and Recruitment Domain
CAR	Chimeric Antigen Receptor

Cas 9	CRISPR associated protein 9
CDKN2A	Cyclin-dependent Kinase Inhibitor 2A
Ce6	Chlorin e6
CEA	Carcinoembryonic Antigen
CHOP	C/EBP Homologous Protein
CMP	CpG island Methylation Phenotype
COX-2	Cyclooxygenase-2
CRC	Colorectal Cancer
CRISPR	Clustered Regularly Interspaced Short Palindromic Repeats
CS NPs	Chitosan Nanoparticles
CT	Computed Tomography
CTNNB1	Catenin beta-1

D

DCF	2'-7'-Dichlorofluorescein
DCFDA	2'-7' Dichlorofluorescein diacetate
Dchq	2,5-dichloro-3,6-dihydroxy-1,4-benzoquinonato
DED	Death Effector Domain
DEVD	Asp-Glu-Val-Asp peptide sequence for cleavage by caspase 3
Dhbq	2,5-dihydroxy-1,4-benzoquinonato
DISC	Death Inducing Signaling Complex
DMSO	Dimethylsulfoxide
DNA	Deoxyribonucleic acid
Donq	5,8-dioxido-1,4-naphthoquinonato
Dotq	6,11-dioxido-5,12-naphthacenedionato

E

EBRT	External Beam Radiation Therapy
EGF	Epidermal Growth Factor
EGFR	Epidermal Growth Factor Receptor

EPO	Erythropoietin
EPR	Enhanced Permeability and Retention
ER	Endoplasmic Reticulum
ERK	Extracellular signal-regulated Kinase

F

FADD	Fas-associated Death Domain
FAP	Familial Adenomatous Polyposis
Fas	FS-7-associated Surface Antigen
FasL	FS-7-associated Surface Antigen Ligand
FBS	Fetal Bovine Serum
FGF	Fibroblast Growth factor
FIT	Fecal Immunochemical Test
FITC	Fluorescein isothiocyanate
FLICE	FADD-like IL-1 β -converting enzyme
FLIP	FLICE Inhibitory Proteins
FS	Flexible Sigmoidoscopy
FU	Fluorouracil

G

GCC	Guanylyl Cyclase C
G-CSF	Granulocyte Colony Stimulating Factor
gFOBT	guaiac-based Fecal Occult Blood Test
GIT	Gastrointestinal Tract
GSH	Glutathione

H

H ₂ O ₂	Hydrogen peroxide
HAL	Hexyl ALA ester
HBO ₂	Hyperbaric oxygen
HEPES	4-(2-hydroxyethyl)-1-piperazineethanesulfonic acid
HER	Human epidermal growth factor receptor

HGF	Hematopoietic Growth Factor
HIF	Hypoxia Induced Factor
HLA	Human Leukocyte Antigen
HNPCC	Hereditary Non-Polyposis Colorectal Cancer
HO ⁻	Hydroxide
HO ₂ [•]	Hydroperoxyl radical
HP	Haematoporphyrin
HPD	Haematoporphyrin Derivative
HRP	Horseradisch peroxidase
HSA	Human Serum Albumin

I

IARC	International Agency for Research on Cancer
IBD	Inflammatory Bowel Disease
IC ₅₀	Inhibitory Concentration 50
ICI	Immune Checkpoint Inhibitors
ICG	Indocyanine green
IFN γ	Interferon γ
Ig	Immunoglobulin
IL	Interleukin
IMRT	Intensity modulated radiotherapy
IV	Intravenously

J

JAK	Janus Kinase
-----	--------------

K

KRAS	Kristen Rat Sarcoma viral oncogene
------	------------------------------------

L

LED	Light Emitting Diodes
LDL	Low-Density Lipoprotein

M

mAb	Monoclonal Antibody
MAL	Methyl-Amino Leuvinat
MAPK	Mitogen-Activated Protein Kinase
mCRC	Metastatic Colorectal Cancer
MEK	Mitogen-Activated Protein Kinase Kinase
MMR	Mismatch repair
MOFs	Metal-organic Frameworks
MOMP	Mitochondrial Outer Membrane Permeabilization
MSI	Microsatellite instability
MSN	Mesoporous Silica Nanoparticles
Mst1	Mammalian Ste-20-like kinase 1
mTHPC	m-tetra hydroxyphenyl chlorin
mTOR	Mammalian target of rapamycin
MTT	3-(4,5-dimethylthiazol-2-yl)-2,5-diphenyltetrazolium bromide
MUTYH	MutY DNA glycosylase
MYC	Myelocytomatosis

N

NCP	Nanoscale Coordination Polymer
NF- κ B	Nuclear Factor kappa-light-chain-enhancer of activated B cells
NK	Natural Killer
NOD	Nucleotide-binding oligomerization domain-containing protein
NOXA	Phorbol-12-myristate-13-acetate-induced protein
NP	Nanoparticle
NPe6	Mono-L-aspartyl chlorin e6

O

O ₂	Oxygen
¹ O ₂	Singlet Oxygen
³ O ₂	Triplet oxygen

O ²⁻	Superoxide anion
OD	Optical Density
OS	Overall Survival

P

PAMAM	Poly amidoamine
PARP	Poly (ADP-ribose)-polymerase
PBS	Phosphate-Buffered Saline
Pc	Phthalocyanine
PDD	Photodynamic diagnosis
PDGFR	Platelet-Derived Growth Factor Receptor
PD-L1	Programmed Death-Ligand 1
PDT	Photodynamic therapy
PEG	Polyethylene Glycol
PEI	Polyethyleneimine
PG	Prostaglandin
PheoA-ss-GC	Pheophorbide A-Disulfide-Glycol Chitosan
PI	Propidium Iodide
PI3K	Phosphoinositide-3-Kinase
PI3KCA	Phosphoinositide-3-kinase Catalytic subunit alpha
Pp IX	Protoporphyrin IX
PS	Photosensitizer
PSM2	Proteasome subunit 2
Pt(II)	Platinum (II)
PTT	Photothermal therapy
PVA	Polyvinyl alcohol
PVDF	Polyvinylidene Fluoride

R

RAF	Rapidly Accelerated Fibrosarcoma
RAPTA	Ruthenium arene 1,3,5-triaza-7-phosphaadamantane

RAS	Rat Sarcoma
RIP	Receptor-Interacting Protein
RIPA	Radioimmunoprecipitation assay
RNA	Ribonucleic Acid
ROS	Reactive Oxygen Species
Rpm	Revolutions per minute
RPMI	Roswell Park Memorial Institute Medium
Ru	Ruthenium

S

SBRT	Stereotactic Body Radiotherapy
SCF	Stem cell Factor
SDS	Sodium Dodecyl Sulfate Polyacrylamide Gel electrophoresis
SEM	Standard Error of the Mean
SHP-1	Src Homology 2 domain-containing Phosphatase
SMANCS	Styrene-co-maleic acid anhydride non-covalent complex
SNPs	Silica Nanoparticles
SOD	Superoxide Dismutase
STAT	Signal Transducer and Activator of Transcription
STK1	Serine/Threonine Kinase 1

T

TAA	Tumor Associated Antigen
TAG	Tumor Associated Glycoprotein
tBid	Truncated Bid
TBS-Tween	Tris-Buffered Saline with Tween
TCR	T Cell Receptor
TGF	Tumor Growth Factor- Beta
Th2	T Helper lymphocytes 2
TiO ₂	Titanium Dioxide

TIL	Tumor Infiltrating Lymphocytes
TKI	Tyrosine Kinase Inhibitor
TNF	Tumor Necrosis Factor
TNFR	Tumor Necrosis Factor Receptor
TNM	Tumor-Nodes-Metastasis
TP53	Tumor protein p53
Tpp	tetra(4-pyridyl)porphyrin
TPPOH	5-(4-hydroxyphenyl)-10,15,20 triphenylporphyrin
TPS	Tissue Polypeptide Specific
Tpt	tris(pyridin-4-yl)-1,3,5-triazine
Tpvb	1,2,4,5-tetrakis {2-(4-pyridyl) vinylbenzene}
TRADD	TNFR1-associated protein with death domain
TRAF2	TNF Receptor-Associated Factor 2
Tris-HCl	Tris(hydroxymethyl)aminomethane hydrochloride

U

UV	Ultra-violet
----	--------------

V

VEGFR	Vascular Endothelial Growth Factor Receptor
-------	---

W

WB	Western Blot
WHO	World Health Organization
Wnt	Wingless/Int-1

X

X	Xylan
---	-------

Z

ZnO	Zinc Oxide
ZnPc	Zinc phthalocyanine
ZnPcS ₄	Zinc phthalocyanine tetrasulfide

I.1. The large intestine

I.1.1. Location and structure

The alimentary canal also called the “digestive tract” is the major digestive organ consisting of the stomach, small intestine, and large intestine. The large intestine is located at the terminal part of this canal and is around 150 cm in length and 8 cm in diameter. It is composed of the caecum, colon, and rectum. The colon follows a proximo-distal sequence subdivided into ascending, transverse, descending, and sigmoid colon. The rectum joins the sigmoid colon from the top and the anal canal from beneath (**Figure 1**) [1].

- **Caecum**

It represents the first segment of the large intestine, initiating from the junction with the small intestine known as the “ileocaecal junction” and extending inferiorly. It is about 5-7 cm in length and is fully enveloped with the peritoneum, supporting its mobility, and terminates by a small tail-like structure called the appendix, which is deprived of both taenia coli and appendices epiploicae. The appendix is located at the posteromedial position of the caecum and is mostly in its caudal position, yet in some cases, it can move behind the ascending colon or come in contact with the caecum posteriorly. The ileocaecal junction includes the ileocaecal valve or Bauhin’s valve which controls the flow of the content between the ileum of the small intestine and the colon. Its shape is like a large pouch, also named the caecal ampulla, where the rest of the food from the ileum is stored.

- **Ascending colon**

It represents the right lateral side of the colon, also known as the right colon, and extends vertically within 15 cm in length to reach up to the inferior surface of the liver. At this area, the colon curves transversally forming the “hepatic flexure” (right colic flexure) which is the immobile segment of the colon and is specifically located in front of the right kidney’s lower part. Only the anterior part of the colon is covered by the peritoneum, whereas the posterior part rests directly against the abdominal wall.

- **Transverse colon**

It is the longest segment of the colon, measuring about 40 cm, starting from the hepatic flexure and ending with the splenic flexure (left colic flexure). The hepatic flexure is noticeably lower than the splenic flexure because of the phrenicocolic ligament, which holds the splenic flexure up and connects it to the diaphragm. In this way, both the ligament and the left colic flexure are in superior adherence with the front side of the spleen. Being the most mobile segment of the intestine, the transverse colon is supported by a mesenteric sheet known as “mesenteric mesocolon” which is a layer of peritoneum joining this segment to the posterior abdominal wall.

- **Descending colon**

It represents the left lateral side of the colon, running vertically for 25 cm from the splenic flexure to the iliac fossa and connecting to the sigmoid colon which is located at the anterior side of the lower part of the left kidney. The abdominal wall directly joins its posterior surface, a ligament attaches its terminal side to the pelvic cavity wall, and the peritoneum shields the rest of the segment.

- **Sigmoid colon**

This segment is “S” shaped and situated at the inferior side of the descending colon, just before the rectum behind the bladder. It is about 35-40 cm in length. The mesocolon supports this

highly mobile segment, which extends from the left iliac fossa to the presacral area of the pelvic cavity.

- **Rectum**

The rectum is the terminal part of the large intestine joining the sigmoid colon from the top and the anal canal from beneath. It is localized in the pelvis, adjacent to the third sacral vertebra. Being around 15 cm in length, the rectum prolongs behind the sacrum and follows its curved structure. It is considered an extra-peritoneal or retroperitoneal organ, as it emerges from the peritoneum and lies posterior to the bladder. It contains three lateral bands that form the rectal valves, which are three internal transverse folds that help separate gas and feces. Moreover, the rectal ampulla, its terminal part, dilates and stores the already formed fecal matter. Like the appendix, both taenia coli and appendices epiploicae are absent on the rectum.

- **Anal canal**

After the whole process of food passage through the alimentary canal including the large intestine, the remaining food will reach the anal canal, which is positioned in the perineum, external to the abdominopelvic cavity. The anal canal is around 3.8-5 cm in length and ends with the opening of the anus. It is composed of internal and external anal sphincters. Both sphincters differ in the type of muscles that constitute them. The internal sphincter is composed of smooth muscles with involuntary contraction, whereas the external sphincter is made up of skeletal muscles with voluntary contractions [1], [2], [3], [4].

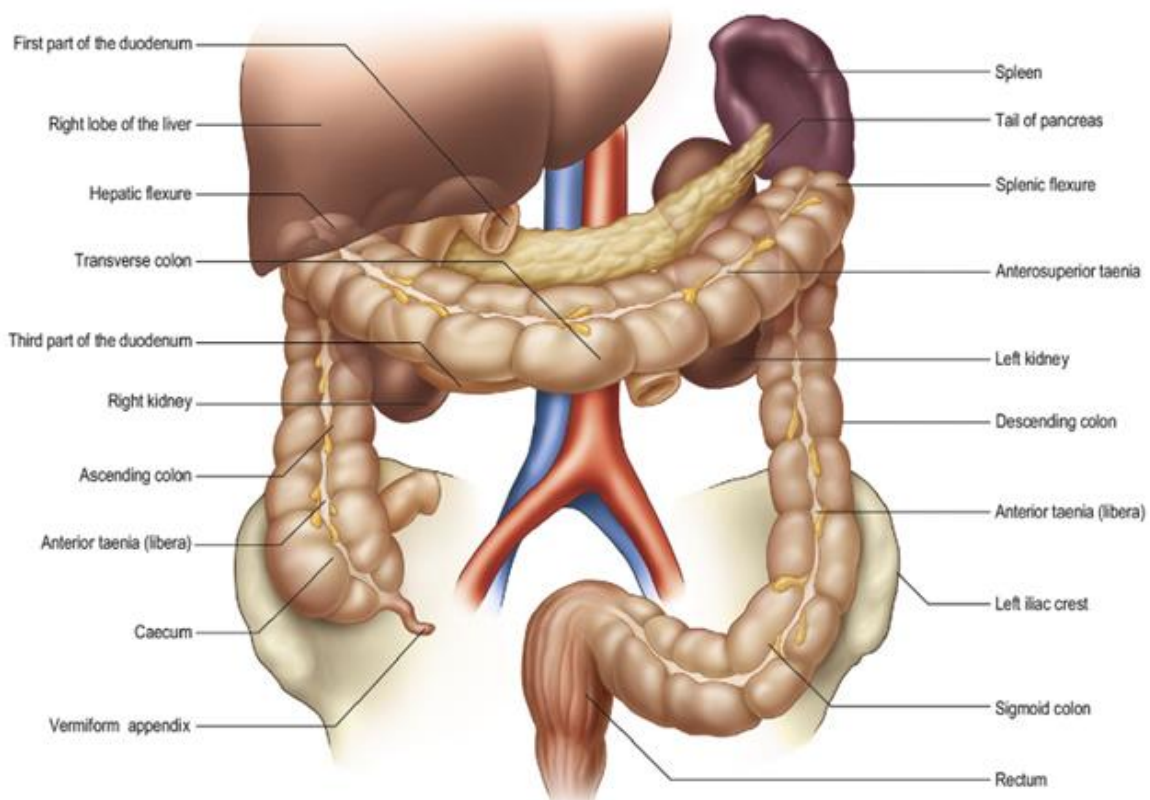


Figure 1: Anatomy of the large intestine [1]

I.1.2. Histology of the large intestine

Generally, the tissue layers of the large intestinal wall follow the same pattern as any other organ of the gastrointestinal tract (GIT). The outer layer is the tunica serosa, which is inferiorly followed by the tunica muscularis, tunica submucosa, and tunica mucosa, sequentially.

- **Tunica mucosa**

It represents the inner layer of the large intestine facing the lumen which is much smoother than the layer of the small intestine. It contains some cells that produce and secrete enzymes including colonocytes, involved in colonic absorption, and caliciform cells which form the caliciform glands of the large intestine secreting mucus into the intestinal lumen. These secretions aid in the production of fecal bolus and mucosal protection. In contrast to the anal canal, the colon's mucosa is made up of a simple columnar epithelium with brush borders where most cells are enterocytes involved in the absorption process. The enterocytes are highly present in the intestinal glands, along with goblet cells, which are associated with the production of the mucus that aids the fecal motility and provides overall protection to the intestine from the gases and acids produced by the enteric bacteria. The circular structures or villi are absent and are replaced with straight intestinal crypts called the "crypts of Lieberkühn", present in the sub-mucosa, acting as tubular glands secreting mucus. Between the crypts, many cell types forming the lamina propria are present including plasma cells, lymphocytes, and macrophages. The sub-mucosa consists of connective tissues and includes many blood vessels, lymphatic vessels, and nerves such as the Meissner plexus. The muscularis mucosae, a thin layer of smooth muscle, is located at the boundary between the mucosa and sub-mucosa.

- **Tunica muscularis**

The tunica muscularis represents the main muscular layer of the large intestinal wall and is composed of circular muscle fibers in its inner layer that undergo the rhythmic contractions that contribute to the large intestine's motility and enable the mixing and propelling of the colon contents. This layer is relatively thin, and the fibers' scattered contractions contribute to the colonic haustra's formation. The outer muscular layer does not provide an entire shielding of the colon and is composed of longitudinal muscle fibers arranged into groups of three distinct longitudinal bands called taenia coli that run along the length of the colon.

- **Tunica serosa**

It is the outermost layer, constituting a part of the peritoneum that covers the large intestine mainly through the connective tissue and mesothelium composing it. It doesn't provide entire coverage of the colon, instead, it partially covers the ascending colon, descending colon, and rectum (**Figure 2**) [2], [5], [6].

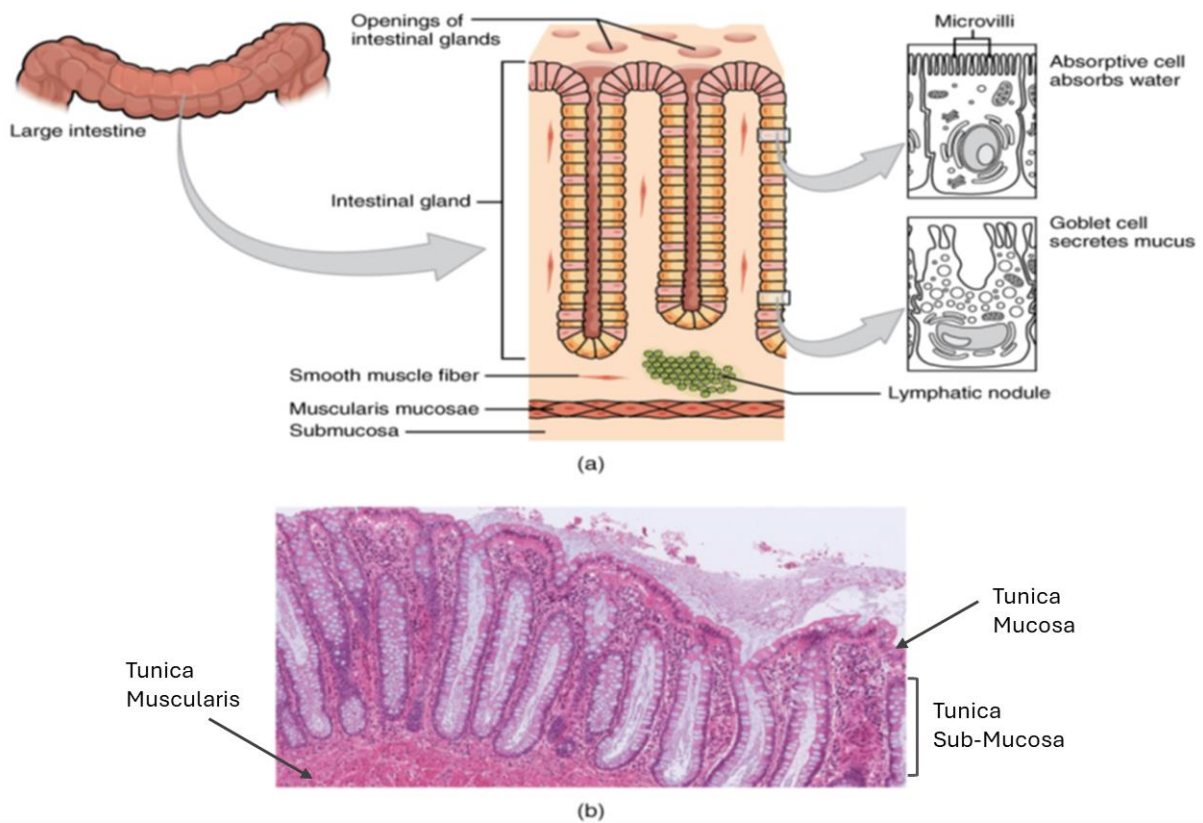


Figure 2: (a) Histology of the large intestine optimized for its digestive function and (b) micrograph showing the simple columnar epithelium and tissue layers of the colon [2]

I.1.3. Functions and state of the large intestine

The colon's main functions are to absorb water and electrolytes from the remaining ileal chyme and form feces for the excretion of the residuals from the body. Mainly, the mucous membrane removes water, electrolytes, and some metabolites by moving over luminal contents through muscular contractions of the intestine's wall. These movements enhance the absorption of fluids; therefore, reduced wall contractions can lead to diarrhea, whereas increased contractions can lead to constipation. Indeed, maintaining a regular pattern of muscular contractions is ultimately necessary for human well-being. In fact, each day the colon receives from the small intestine one to two liters of chyme, a liquid containing water, electrolytes, and unabsorbed nutrients. Moreover, the large intestine contains the enteric bacteria which produces vitamin K, an essential factor for the liver's synthesis of the clotting factors, and the mucus secretions are often associated with potassium that will be provided into the contents. Also, the bacteria in the colon's lumen undergo a process called "saccharolytic fermentation" causing the degradation of carbohydrate residues which yields the release of carbon dioxide, hydrogen, and methane gases forming the flatus gas within the colon. The bacteria of the large intestine forming populations of trillions in number create the "bacterial flora". While the colon lacks the interdigestive complexes regularly moving from the esophagus to the end of the ileum after passing through the stomach, in some cases the ascending colon can be affected by the contractile activities originating from the ileum. The intrinsic nerve plexus exerts its role in the colorectal contractions and when it's partially present or destroyed by trypanosomes, it can lead to the congenital Hirschsprung's disease and Chaga's disease, respectively. This explains the reason behind the colon's blockage or acute constipation after the uptake of psychoactive drugs for a long time. The muscular contractions are also highly affected by gut hormones such as cholecystinin, vasoactive intestinal peptide, motilin, and catecholamines as their

variable concentrations can control the intrinsic nerve plexus. For instance, after food intake, the movement increases significantly, most probably due to the cholecystikinin activity. Also, sleeping considerably diminishes the motility of the colon, whereas mental stress augments it. Consuming fiber-rich food aids in defecation because it increases water absorption and fecal bulk [2], [7], [8].

I.1.4. Vascularization of the large intestine

The large intestine is well vascularized with a complex of arteries and veins providing blood supply to the area of the large intestine. The ascending colon's blood supply up to the distal part of the transverse colon starts by the superior mesenteric artery from the aorta and is followed by the inferior mesenteric artery which slightly connects with the pudendal vessels in the anal region providing vascularization to the left colon and the sigmoid. Being situated between the superior and inferior mesenteric arteries, the transverse colon can benefit from both arterial supplies. The rectum is supplied by the superior rectal artery which is issued from the inferior mesenteric artery and by the middle and inferior rectal arteries originating from the internal iliac arteries. Conditions affecting the aorta can tighten or block the mesenteric arteries, especially the inferior mesenteric artery. In such cases, the marginal artery present near the intestinal wall will sustain the blood flow. Smaller arteries supplying the transverse colon are particularly susceptible to hardening. The veins generally follow the arteries with the superior and inferior mesenteric veins draining into the portal vein of the liver. The ascending colon's venous drainage flows to the right lobe of the liver, whereas the rectum and left colon drain to the left lobe due to the directional flow of blood in the portal vein. Concerning the lymphatic vessels, they travel alongside the arteries to the para-aortic lymph nodes, with smaller nodes situated on the colon wall and midway to the aorta. The lymphatic vessels of the rectum and anus drain into the lymph nodes of the iliac and inguinal regions. The extrinsic innervation of the large intestine is linked to the parasympathetic and sympathetic fibers, both efferent and afferent, which are connected to the central nervous system and mainly to the hypothalamus. The intrinsic innervation of the intestine represents a local innervation within the walls of the gastrointestinal tract through the myenteric and submucosal plexus (**Figure 3**) [4], [7].

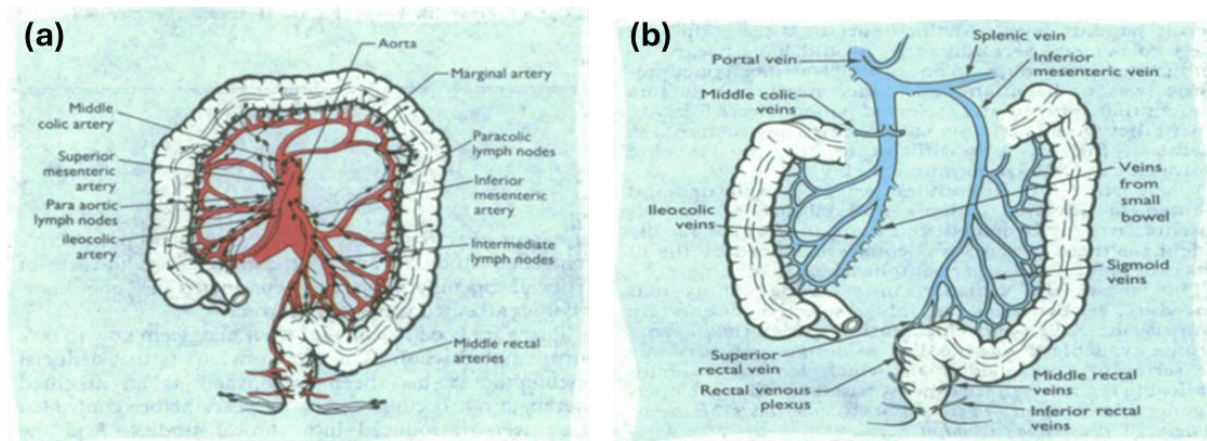


Figure 3: (a) Arterial supply, lymphatic drainage, and (b) venous drainage of the large intestine [7]

I.1.5. Diseases of the colon

The colon is susceptible to multiple different diseases that can be either benign or malignant. Benign diseases such as diverticulosis, Crohn's disease, and ulcerative colitis contrast with malignant diseases like colorectal tumors.

I.1.5.1. Inflammatory bowel disease

Inflammatory bowel disease (IBD) is a complex group of conditions characterized by permanent and recurrent chronic colon inflammation due to endoplasmic reticulum (ER) stress and cytokine dysregulation. It is triggered by individuals' genetic susceptibility alongside environmental and microbial factors. Imbalances and alterations of the gut microbiota can lead to an abnormal immune response and chronic inflammation in the gut. Interleukin-23 (IL-23) and IL-17A cytokines are particularly involved in promoting intestinal inflammation. Mainly, IL-17A was detected in the mucosa of Crohn's disease and ulcerative colitis [9]. The pathological differences are mainly in the specific location of the colon and the associated symptoms (**Table 1**).

Table 1: Key pathological differences between Crohn's disease and ulcerative colitis [10]

Key features	Crohn's disease	Ulcerative colitis
Location		
Upper parts of GIT	Rarely	Never
Distal Ileum	Very common	Never
Colon	Common	Always
Rectum	Rarely	Never
Signs and symptoms	Pain in the lower right abdomen, swelling, thickening of the bowel wall	Pain in the lower left abdomen, diarrhea, weight loss, rectal bleeding

Abbreviation: GIT, gastrointestinal tract.

- **Crohn's disease**

Crohn's disease is a chronic inflammatory disease of the GIT, with a growing incidence worldwide. This disease's onset is predominant in females and usually appears at young age, particularly, 30 years old or under. It is associated with transmural inflammation of all the layers of the intestinal wall with anal lesions in 81% of cases. This causes diarrhea, abdominal pain, anal lesions as well as the appearance of lifted inflamed mucosa resembling a "cobblestone" with imaging, and irregularities in the bowel structure including linear ulcerations and internal fistulae [11]. One key molecular basis of this disease lies in the dysregulation of the innate and adaptive immune responses in the gut. Immune response genes, including NOD2, ATG16L1, and IL23R, have been linked to a higher risk of Crohn's disease because their alterations can affect the mucosal immunity, the composition of the gut microbiota, and barrier functions, which can result in chronic inflammation. The key pathways involved in Crohn's disease pathogenesis include the nuclear factor kappa B (NF- κ B) signaling pathways, autophagy, and cytokine signaling pathways where their imbalances or dysregulation contribute to the development of chronic inflammation [12], [13], [14]. Additionally, Crohn's disease is known for its associated irregularities of the epithelial barrier of the colon which permits the movement of microbial antigens into this region. Thus, the mucosal immunity system will induce the differentiation of T-cells into T-helper type 1 (Th1) effector cells, leading to the generation and release of cytokines such as interferon-gamma (IFN- γ), tumor necrosis factor-alpha (TNF- α), and IL-2, which promote inflammation. On the other hand, T-helper type 2 (Th2) cells exert their role in reducing the inflammatory response through the generation of anti-inflammatory

cytokines such as IL-4, IL-5, IL-6, and IL-10. Natural killer (NK) cells and antigen-presenting cells (APCs) influence T cell differentiation, activation of T cells, and the overall complex interactions determining the course of the disease (**Figure 4**). Symptoms of Crohn's disease include abdominal pain, chronic diarrhea, fatigue, and weight loss. It is important to note that patients suffering from this condition are at risk of developing colorectal cancer (CRC) [10], [15].

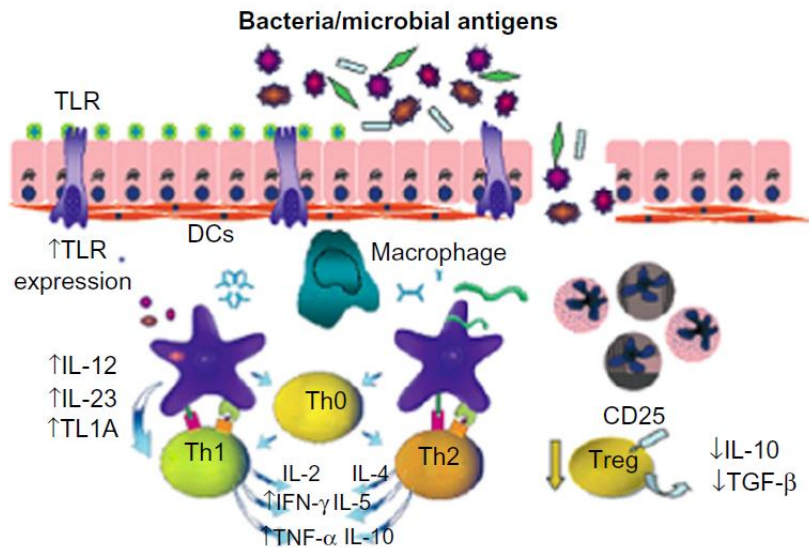


Figure 4: Crohn's disease-induced immune response. Complex interactions between various immune cells and cytokines determine the type of immune response and disease progression [10]

- **Ulcerative colitis**

It is mainly associated with the inflammation of the mucosal layer of the colon with rectal involvement in most cases. Its incidence is increasing worldwide and often affects adults aged between 30 and 40 years old. The recurrent inflammation causes bloody diarrhea and abdominal pain diagnosed by colonoscopy and histological findings. However, the anal lesions and deep intestinal fissures are less frequent [16]. Several genetic factors are involved in the development of this disease, mainly those implicated in the immune response, such as HLA genes, genes related to the mucosal barrier function, IL23R and IL10 genes. Like Crohn's disease, the NF-κB signaling pathway's alterations are highly implicated in this disease's pathology [10], [17]. Hence, this disease can be treated through the administration of immunosuppressants, 5-aminosalicylic acid-based drugs, and steroids [4], [18].

I.1.5.2. Diverticulosis and diverticulitis of the colon

Diverticulosis is a gastrointestinal condition characterized by the formation of the diverticula which are small pouches that form in the mucosa or sub-mucosa due to an increased pressure bulging the colon wall outward, especially in the sigmoid colon (**Figure 5**). Diverticula can be found on both the left and right sides of the colon. Left diverticula are pseudo-diverticula because they do not pass through all the layers of the colon, whereas diverticulosis of the right side of the colon is known as true diverticula as they can hit all the colonic layers. Diverticulosis prevalence increases with age and is mostly asymptomatic, yet symptoms such as bloating, abdominal pain, alterations in bowel habits and rectal bleeding might occur. Obesity, low fiber

diet, and physical inactivity can increase the risk of incidence of this disease. However, high-fiber diet intake may not necessarily provide against asymptomatic diverticulosis.

Colonic diverticulitis is another pathological condition characterized by inflammation or infection of the colon's diverticula and leading to chronic gastrointestinal symptoms. The pathogenesis of diverticulitis can be influenced by chronic inflammation and alterations in the gut microbiome. This can lead to a range of intestinal malformations including abscesses, perforations, strictures, obstructions, and fistulas forming complicated diverticulitis. However, uncomplicated diverticulitis is more common and can be limited to the thickening of the colon wall and pericolic inflammatory changes. It is also worth mentioning that there is a minor probability that patients with diverticulosis develop diverticulitis [19], [20], [21].

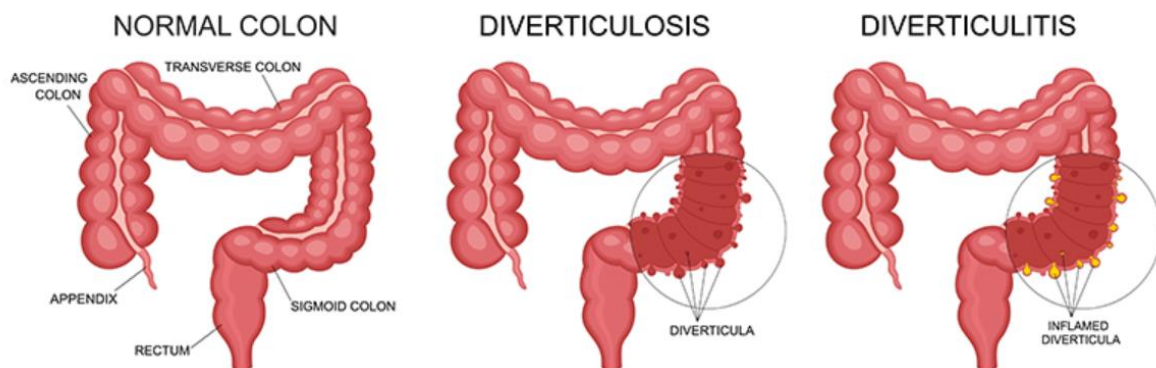


Figure 5: Diverticulosis and diverticulitis of the colon [22]

I.2. Cancer: general overview and prevalence

Cancer is a complex category of diseases distinguished by the unrestrained proliferation and growth of cells in any tissue within the body and their ability to spread into different body sites. It occurs because of a series of genetic mutations that transform healthy and normal tissue into malignant tissue by triggering the imbalance between cell growth and cell death. The transition from benign to malignant tumors is distinguished by the ability of the cells to penetrate the various histological layers of the affected organ. The most advanced form of cancer is in its metastatic stage where the tumor cells acquire their ability to detach from their surrounding environment and form secondary tumors in body sites distant from the original tumor site, via the blood or lymph. Therefore, certain hallmarks such as uncontrollable proliferation of cells, resistance to cell death, inducing angiogenesis, and metastasis, differentiate cancer from any other disease (**Figure 6**). Different factors can trigger the onset of these mutations such as exposure to environmental carcinogens, oncogenic viruses, and hereditary factors. The accumulation of mutations that can either activate the oncogenes or inhibit tumor suppressor genes such as KRAS and P53, respectively, triggers a cascade of events leading to the initiation and progression of cancer [23].

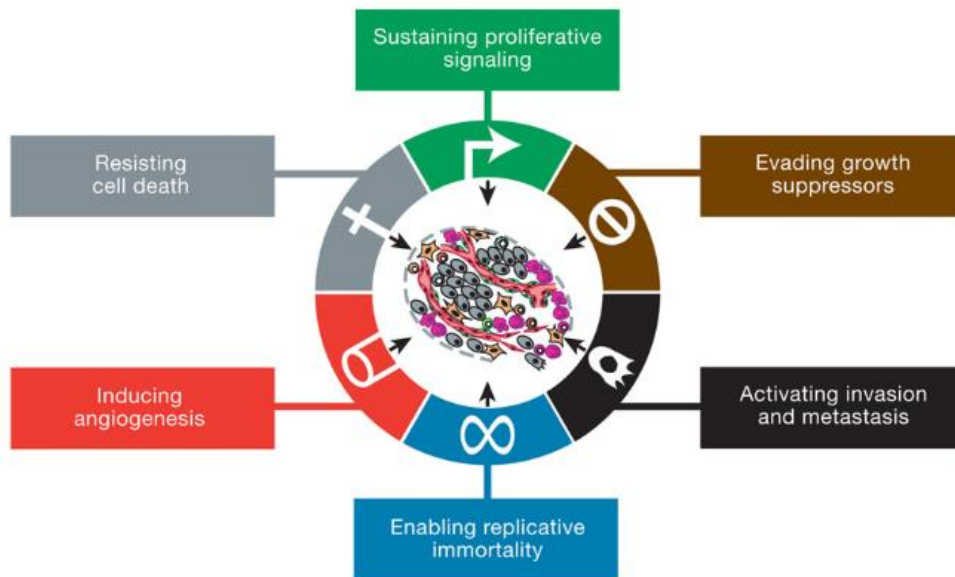


Figure 6: Hallmarks of cancer [23]

The global cancer incidence differs between transitioning and transitioned countries. Higher cancer incidence and mortality rates are estimated in transitioning countries due to aging, lifestyle, and limited access to healthcare facilities. On the other hand, transitioned countries have implemented effective measures for cancer control that lower the incidence and mortality rates. Therefore, integrating preventive and curative measures to help reduce the cancer burden and address the existing gaps between transitioning and transitioned countries is necessary. By 2040, there is an estimation of a significant increase in cancer incidence influenced by factors such as population growth, aging populations, changes in lifestyle behaviors, and environmental factors. Additionally, colorectal cancer prevalence can differ between sexes among different age groups and countries. For instance, Denmark, Iceland, and Sweden show higher rates of cancer incidence in females than in males of certain age groups. Also, there is an expected increase in cancer incidence in females as compared to males in the United States, Canada, Denmark, Germany, New Zealand, and the Netherlands. Whereas, globally, men experience a higher mortality rate of 43% from CRC compared to women.

Among the different types of cancer, CRC has been the focus of many research studies due to its potential for early detection and prevention through screening, high prevalence, and significant mortality [24]

I.3. Colorectal cancer

Currently, CRC is at a critical point where many changes are happening, but even with advancements in treatments, CRC remains the second leading cause of cancer-related deaths in France. Particularly, the treatment of metastatic CRC remains a major challenge, and finding innovative strategies for the treatment of CRC is essential to improving the patient's quality of life and limiting mortality rates [25].

I.3.1. Epidemiology

A study carried out in 2024 by the World Health Organization (WHO) and the International Agency for Research in Cancer (IARC) shows that in 2022, for both males and females, CRC is the third most common cancer and the second leading cause of mortality [24], [26] (**Figure 7**). Annually, it accounts for about 1.85 million diagnoses and 850,000 deaths [27]. In terms of frequency among both sexes, CRC ranks second in women after breast cancer and third in

men after prostate and lung cancers. Concerning the ages, the incidence rates increase with age and peak at the age of 92 and 87 in women and men, respectively [24], [28]. An epidemiological study performed by Yu Xi et al. demonstrated that the incident and death cases vary across different regions with China and the United States having the highest estimated new cases among the countries with a large number of diagnosed CRC cases. The number of new CRC cases in China is projected to increase significantly from 0.56 million in 2020 to 0.91 million in 2040, reflecting a 64% increase. In the United States, approximately 0.16 million new cases were estimated in 2020, with projections indicating an increase to 0.21 million by 2040. Other countries mentioned with high incidence rates include Japan, Russia, India, Germany, Brazil, the United Kingdom, Italy, and France. The mortality rates are expected to rise in line with the increasing incidence (**Figure 8**). The disparities in survival rates and the importance of early detection are highlighted, as CRC symptoms often appear at advanced stages, complicating treatment and increasing mortality. Notably, the increase in incidence is more pronounced among young adults and in economically transitioning countries [25].

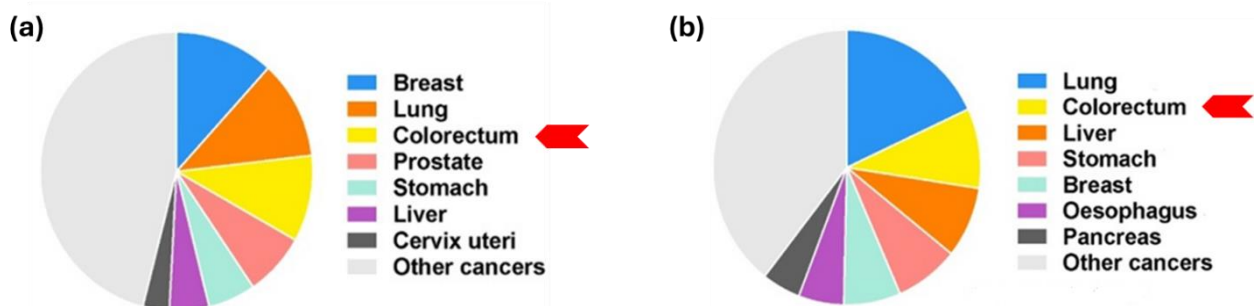


Figure 7 : Worldwide (a) incidence and (b) mortality cases in 2022 [25], [26]

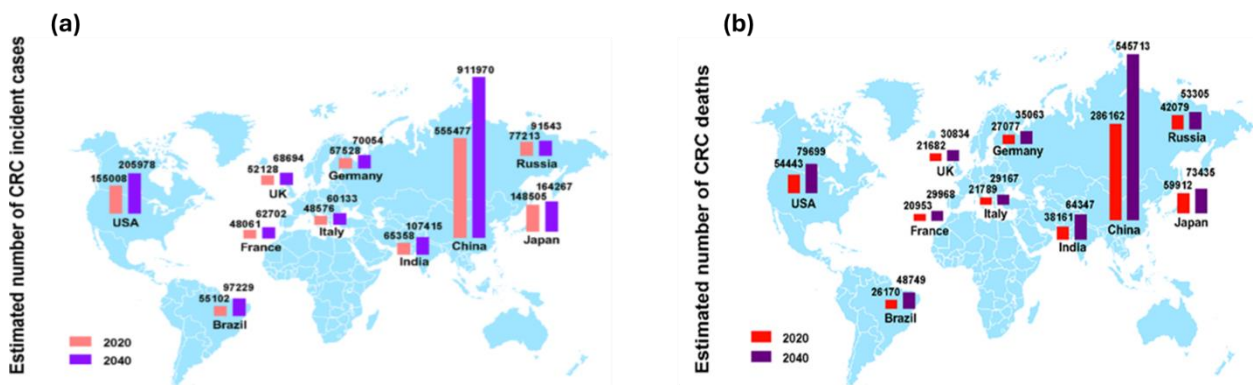


Figure 8: The estimated number of CRC (a) incidents and (b) death cases in the top 10 countries with the highest incidence rates in 2020 and projections until 2040 [25]

1.3.2. Risk factors and symptoms

A combination of environmental and genetic factors can trigger the development of CRC. Diets that are low in fiber, consumption of red and processed meats, as well as saturated fats increase the risk of CRC development. A sedentary lifestyle leads to obesity, with adipose tissue producing hormones that promote tumor growth. Smoking, particularly tobacco, introduces carcinogens that can damage DNA in the cells of the rectal and colon walls. Heavy alcohol consumption induces inflammation and oxidative stress promoting tumor development. Besides, the probability of developing CRC increases with age, with most cases diagnosed after the age of 50 years old. Also, the risk of CRC incidence varies across different racial and ethnic groups. Lastly, chronic inflammation associated with inflammatory bowel diseases increases the risk of tumor formation due to the cell damage of the colon lining. Early symptoms

include weight loss, alterations in bowel habits, abdominal pain, rectal bleeding, and iron deficiency. Genetic predisposition significantly increases the likelihood of the development of CRC. Hereditary diseases such as Lynch Syndrome (hereditary nonpolyposis colorectal cancer) and familial adenomatous polyposis (FAP) are linked with a high risk of CRC occurrence. Mutations in genes such as APC and CTNBB1 genes are associated with early-onset CRC and can influence its progression and development [29].

I.3.3. Types

I.3.3.1. Sporadic CRC

Sporadic CRC refers to the cancer that emerges in the colorectal area without known germline causes or family history. It is mainly a somatic genetic disease where biomarkers related to somatic genes such as tumor suppressor genes and oncogenes as well as epigenetics such as microsatellite instability (MSI), CpG island methylation phenotype (CMP) aid in the diagnosis, prognosis, and treatment of sporadic CRC [30].

I.3.3.2. Hereditary CRC

Hereditary CRC is linked to specific germline gene mutations that are inherited and predispose individuals to develop CRC at a younger age [31]. Additionally, there are hereditary syndromes such as Lynch syndrome and FAP that elevate the potential risk of developing CRC.

- **Lynch syndrome**

Lynch syndrome, also known as hereditary nonpolyposis colon cancer (HNPCC), is one of the most common genetic syndromes. It is caused by changes in the DNA mismatch repair (MMR) genes, which include MLH1, MSH2, MSH6, and PSM2. Patients with Lynch syndrome are prone to an increasing risk of CRC development.

- **Familial adenomatous polyposis**

FAP is a hereditary disease, mainly caused by mutations in the APC gene (tumor suppressor gene) with a significantly high predisposition to CRC development.

- **MUTYH-associated polyposis**

This disease is triggered by the mutation in the MUTYH (mutY DNA glycosylase) gene which is responsible for DNA repair.

- **Peutz-Jegher syndrome**

This syndrome is characterized by hamartomatous polyps' development in the GIT and is caused by mutations in the STK1 gene increasing the risk of CRC.

- **Juvenile polyposis syndrome**

The development of multiple juvenile polyps in the colon and rectum is induced by gene mutations in SMAD4 and BMPR1A genes and is associated with an increased risk of CRC [32].

I.3.4. Pathways of CRC carcinogenesis

Carcinogenesis is identified by a gradual transformation of a normal cell into a cancer cell after passing through a series of genetic mutations and epigenetic alterations that activate

oncogenes or inactivate tumor suppressor and mutator genes. Normally, tumor suppressor genes are recessive genes that inhibit cancer formation; however, when mutations or epigenetic changes trigger both alleles of the gene, this inhibition will be suppressed leading to tumor formation. On the other hand, mutations in oncogenes promote the hyperactivation of the translated protein. Additionally, acting as dominant genes, oncogenes' mutation of one allele is sufficient to induce cell growth and division. The sequence and type of genetic changes constituting the genetic pathways of carcinogenesis, result in the clonal evolution of premalignant lesions into malignant tissues and contribute to CRC development (**Figure 9**). CRCs most often develop from a polyp detected during a colonoscopy. Most sporadic CRC development follows the classical adenoma-carcinoma sequence. This process begins with the emergence of a unicryptal adenoma, which progresses through dysplasia and eventually develops into several crypts due to uncontrolled cell growth and proliferation, forming adenomas. These adenomas can further evolve into tubular to villous structures. Villous morphology becomes the dominant structure as the tumor progresses through this multi-step process, which can take between 10 to 40 years in sporadic CRC. Also, not all adenomas transform into malignant tumors. Although most polyps are benign, some can progress to cancer. CRC develops from a previously benign adenomatous polyp in 60-80% of cases. However, not all polyps advance to colon cancer. Out of a thousand polyps, approximately one hundred will reach a size of 1 cm, which increases the probability of progression to cancer, and about twenty-five may develop into CRC within ten years. Colon polyps are massive lesions that protrude from the intestinal mucosa into the intestinal lumen and usually arise due to defects in cell proliferation, differentiation, or apoptosis within the normal mucosa. While most polyps are benign, their diagnosis, frequent monitoring, and treatment are crucial, as some have the potential to progress into cancer [7].

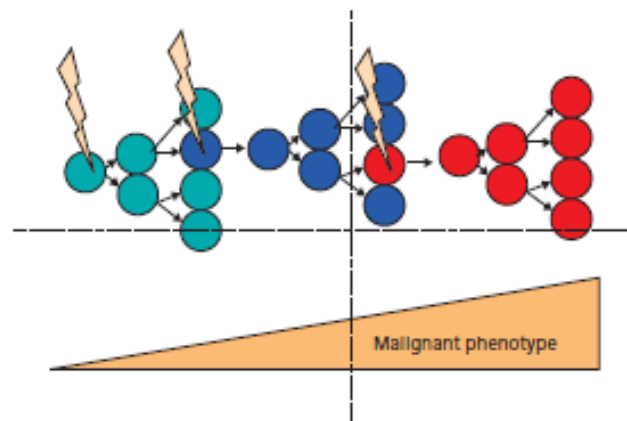


Figure 9: Several genetic mutations contribute to the development of cancer [7]

I.3.5. CRC development: genetics and histology

The molecular mechanisms behind the progression of CRC from normal epithelium to adenoma involve a complex of genetic and epigenetic modifications that influence various signaling pathways. Wnt signaling pathway is among the most influenced signaling pathways and is influenced by the accumulation of mutations in the adenomatous polyposis coli (APC) and CTNNB1 (β -catenin) genes. Such accumulation triggers the transcription of Wnt target genes such as MYC and cyclin D1 responsible for cell growth and proliferation and contributing to the formation of early adenomas. Further mutations triggering KRAS oncogenes and the deletion of chromosomes 17p and 18q holding SMAD (SMAD2 and SMAD4) and TP53 tumor

suppressor genes, respectively, induce the additional progression into intermediate, late adenomas and carcinomas. As the tumor progresses, the level of chromosomal instability increases, making them more susceptible to mutations (**Figure 10**). Hence, specific mutations or epigenetic changes in oncogenes and tumor suppressors with different frequencies and consequences accompany the progression of CRC. Such genetic and epigenetic mutations contribute to the activation of a variety of signaling pathways including Wnt, MAPK, and TGF- β pathways, and disrupt the DNA integrity [7]

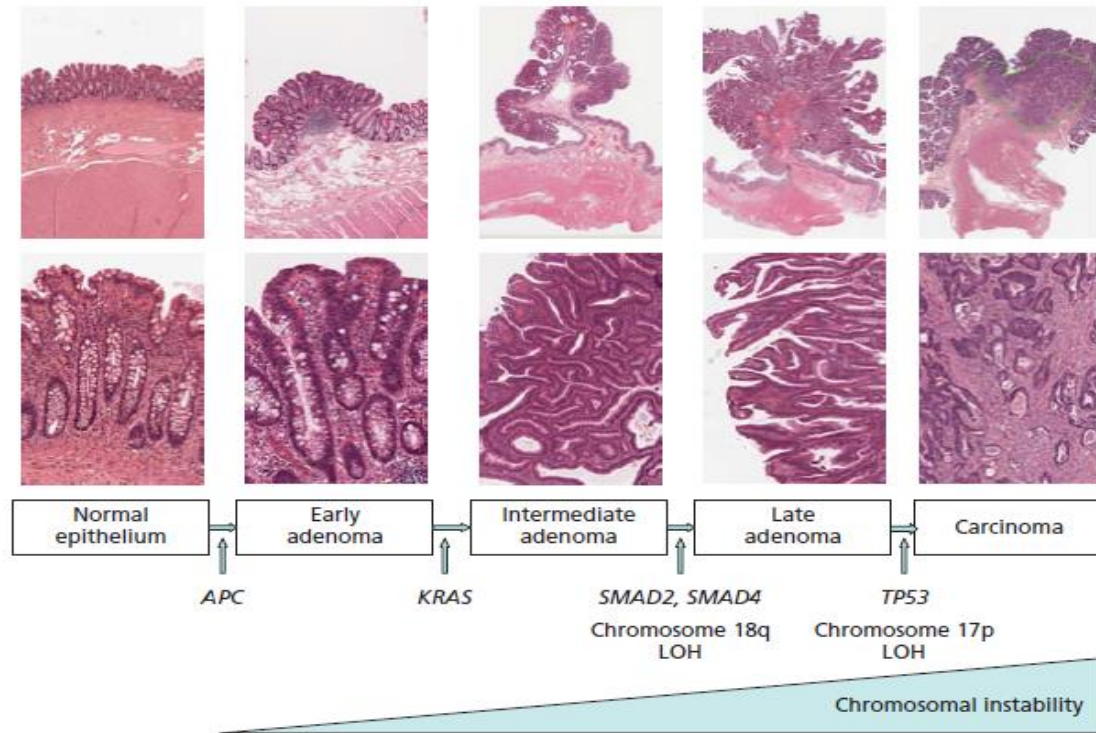


Figure 10: The somatic genetic mutations contributing to the development and progression of cancer [7]

Moreover, mutations in KRAS genes are highly observed with the formation of adenomas as they are involved in the activation of the MAPK/ERK signaling cascade which promotes oncogenesis and inhibits apoptosis. Furthermore, the loss of function of the PTEN (phosphatase and Tensin Homolog) gene and mutations in the PI3KCA (phosphatidy-4,5-biphosphate-3-Kinase catalytic subunit alpha) gene, encoding the p110 α catalytic subunit of the PIK3 gene, cause the activation of the AKT pathway which induces oncogenesis and malignant transformation. Also, the TGF- β /SMAD pathway can be disrupted due to mutations in the SMAD 4 gene, inhibiting its role in tumor-suppressing and favoring the growth, proliferation, and metastasis of cancer cells. The NF- κ B pathway can get constitutively active after mutation in the NF- κ B 1(subunit 1). Additionally, the NOTCH pathway also gets dysregulated either positively or negatively depending on the type of mutations affecting the NOTCH 1-4 gene. Mutations that lead to loss of function in these genes can result in pathway inactivation, while mutations that cause gain of function can lead to hyperactivation of the pathway. Finally, the JAK/STAT3 pathway is also involved in CRC development, particularly through its activation following mutations in the JAK1/2/3 (Janus Kinase 1/2/3) and STAT3 (Signal Transducer and Activator of Transcription 3) (**Figure 11**) [33]. Additionally, epigenetic changes such as DNA methylation and histone modifications also contribute to the initiation and progression of CRC. Hypermethylation of promoter regions in tumor suppressor genes, including MLH1 and CDKN2A, positively influences gene silencing and promotes oncogenesis by the disruption of DNA repair and cell cycle. Mismatch repair (MMR) systems, often leading

to microsatellite instability (MSI) are also linked to the neoplastic transformation that is particularly arising from the hereditary transformation seen in HNPCC or Lynch syndrome [34], [35].

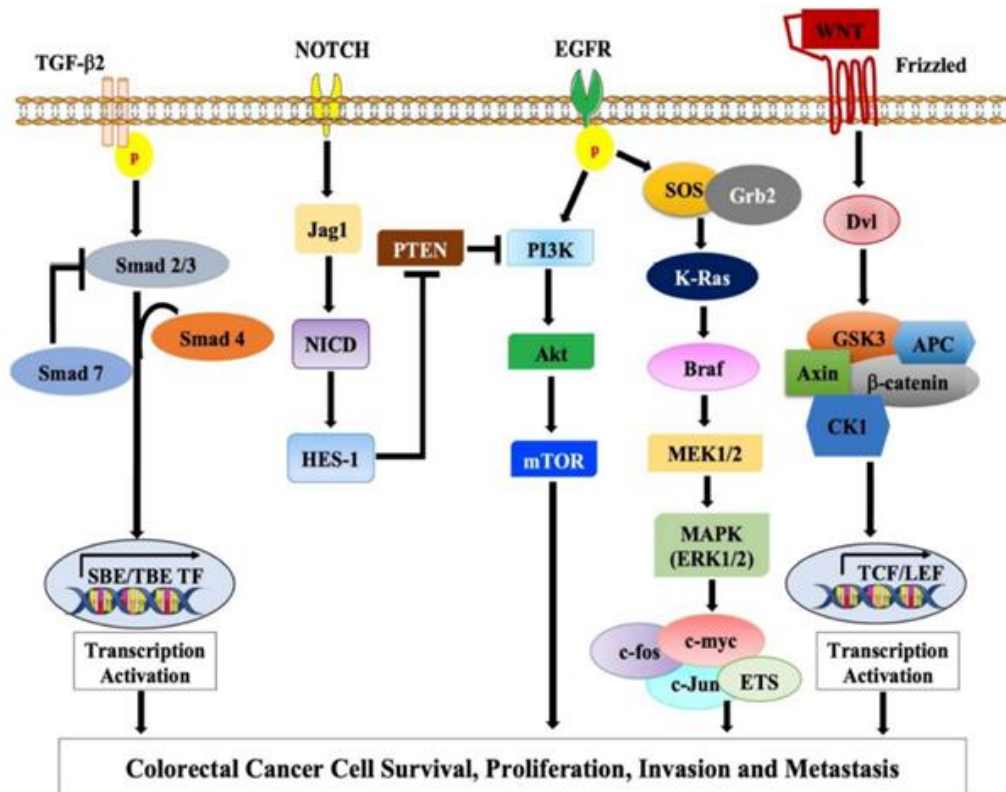


Figure 11: The molecular pathways contributing to the development and progression of CRC [33]

I.3.6. Classification of polyps

Polyps of the colon are histologically classified according to their size, morphology, and depth of invasion. Usually, small colonic polyps are asymptomatic and diagnosed incidentally during endoscopic and radiographic examinations carried out for other purposes. However, polyps can be painful as they ulcerate and bleed, and large polyps can cause intestinal obstruction. Colorectal polyps are classified by their macroscopic appearance as pedunculated (extending from the mucosa through a fibrovascular stalk) or sessile (flat, arising directly from the mucosa). The two major groups of polyps are the non-neoplastic (hyperplastic, hamartomatous, or inflammatory) and neoplastic (adenomas or dysplasia associated lesions). Only adenomatous polyps can develop into cancer. Hence, accurately identifying the type of polyps is crucial for determining the most effective treatment options and strategies to follow for a better patient outcome [3].

I.3.6.1. Non-neoplastic polyps

These polyps are usually benign and don't have the ability to develop into cancer. Hyperplastic polyps and hamartomatous polyps are the two main types of non-neoplastic polyps. The hyperplastic polyps, as their name implies, exhibit hyperplasia. They are the most common type of colorectal polyps with a diameter of less than 5 mm. However, larger polyps greater than 2 cm in size may pose a risk of developing dysplasia and malignancy. They're sessile and are most commonly found in the sigmoid colon and rectum. Hamartomatous polyps, also known as "juvenile polyps", are composed of connective tissue covered by hypertrophic

epithelium and form a pedunculated structure. They can also develop into dysplasia when they significantly outgrow their regular size [36]

I.3.6.2. Neoplastic polyps

Neoplastic polyps are a type of colorectal polyps that have the potential to develop into cancer. The adenomatous polyps are the most diagnosed neoplastic polyps in patients and are usually divided into three major subtypes according to their histology: tubular adenomas, villous adenomas, and tubulovillous adenomas. Tubular adenomas are characterized by the presence of tubular glands with a branching structure and are the most prevalent histological category, accounting for 65–80% of all excised polyps. Compared to villous adenomas, tubular adenomas are typically pedunculated and show less atypia. The risk of invasive carcinoma in tubular adenomas is generally low. Villous adenomas represent a smaller proportion (5-10%) of neoplastic polyps but are more likely to be sessile and exhibit severe atypia or dysplasia. Villous adenomas, especially when they are large, have a high risk of progressing into invasive carcinoma. Tubulovillous adenomas, which exhibit features of both tubular and villous structures, account for 10-25% of neoplastic polyps and have an intermediate risk of malignancy. The risk of carcinoma in tubulovillous adenomas falls between that of tubular and villous adenomas. (**Figures 12 and 13**) [36].

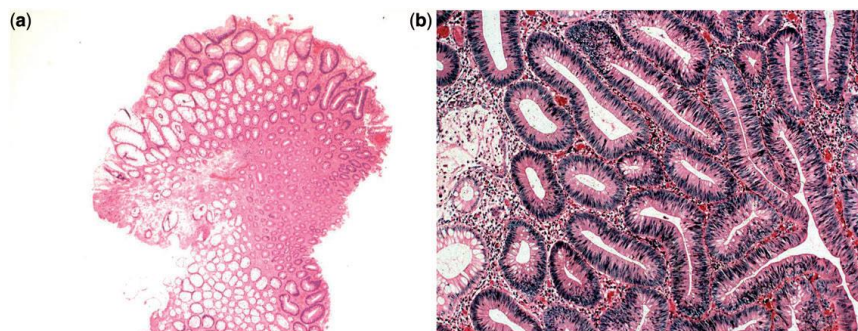


Figure 12: Tubular adenoma with hematoxylin-eosin staining and visualization under (a) low and (b) high power microscopic magnifications with clear histological appearances of the branched tubular structures [36]

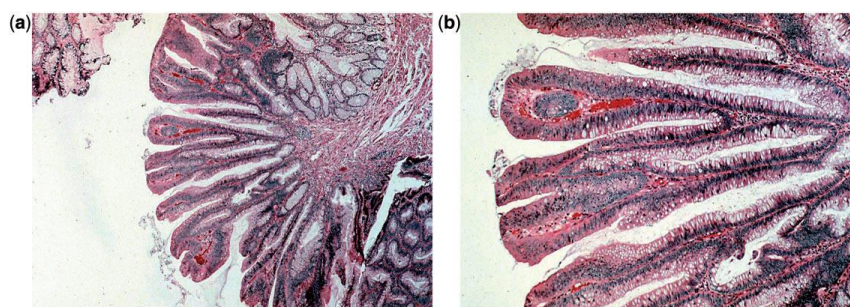


Figure 13 : Villous adenoma with hematoxylin-eosin staining and visualization under (a) low and (b) high power microscopic magnifications with clear histological appearances of the long finger-like projections [36]

I.4. Screening and clinical diagnosis

Screening for colorectal cancer is vital for the early detection and prevention of colorectal cancer, as well as the identification of other bowel diseases. Early screening and clinical diagnosis allow for the discovery of precancerous polyps or malignancies at a stage when they are more easily treatable and can significantly improve patient outcomes.

I.4.1. Endoscopic diagnosis

Colonoscopy is used not only as a diagnostic tool, but also a therapeutic one, as biopsies can be taken to assess the histology of the malignant lesion. Colonoscopy is the gold standard for CRC screening and diagnosis. It enables the removal of the dysplastic and/or premalignant lesions. The accuracy of colonoscopy in diagnosing CRCs varies between 88% and 98% for adenomas with a diameter of 10 mm. Surveys have demonstrated a 50% to 70% reduction in CRC occurrence, and a 30% reduction in CRC-associated deaths when early diagnosis is achieved with colonoscopy. Colonoscopy can also assess both the distal and proximal parts of the colon considering the complexity of the procedure, the requirement for bowel preparation with precise diet and time, and the need for sedation or anesthesia. It is worth emphasizing that when normal colonoscopy is not possible, virtual colonoscopy or computed tomography (CT) colonography can be used instead as they are accurate, non-invasive, and powerful diagnostic tools, with equivalent capabilities in detecting large lesions of 10 mm or more. Besides, CT colonography allows the examination of the colon using computed tomography (X-rays) to acquire images of the different sections of the colon, enabling the analysis and diagnosis of the colonic state. Flexible sigmoidoscopy (FS) provides inspection of the sigmoid colon and taking biopsies distally. Another non-invasive technique is the capsule endoscopy during which the patient ingests a capsule with a camera that captures the entire intestinal wall and then is naturally eliminated from the body [37].

I.4.2. Biochemical and histological diagnosis

When CRC is under investigation, it's essential to identify the family history of the patient, perform clinical diagnosis by digital rectal examination (DRE), and demonstrate the associated biomarkers such as the carcinoembryonic antigen (CEA), used for prognosis and examination. If clinically detectable, it is important to assess the extent to which the tumor is invasive, peripheral, large, and disseminated within the pelvis [38]. Biochemical analysis includes the examinations of the different antigens and biomarkers highlighting the onset of CRC. Upon the presence of a polyp, various tests should be performed to ensure the presence of the tumor and determine its stage. Biological and biochemical blood tests are carried out for the detection of certain biomarkers, in particular, CEA which is a protein usually found in normal physiologic conditions, yet it can be overproduced by tumor cells. There can still be cancerous tumors even if this antigen exhibited a normal level in blood; however, augmented levels is linked to the presence of cancer. Further blood tests to detect other antigens such as creatinine levels and complete blood counts (CBC) are necessary. Also, taking biopsies is a critical step for examining the tissue's morphological and histological features and determining the stage of the cancer. In addition, searching for certain gene mutations such as KRAS, BRAF, NRAS, BRAF and PIK3CA genes as well as epigenetic changes such as gene silencing or MSI. After diagnosis, the patient's treatment path can be directed toward the optimal treatment strategy aiming to enhance his/her life quality [39]. Although the carbohydrate antigen (CA 19.9) has a reduced diagnostic sensitivity and specificity by 34%-55% as compared to CEA, it is still used as a biomarker in the diagnosis of CRC. Additionally, the tissue polypeptide specific antigen (TPS) biomarker is also used with a high diagnostic sensitivity of 95% and moderate specificity of 83%. Other biomarkers include the hematopoietic growth factors (HGFs), tumor-associated glycoprotein-72 (TAG), stem cell factor (SCF), granulocyte-colony stimulating factor (G-CSF), and macrophage-colony-stimulating factors (M-CSF). G-CSF and M-CSF have a high specificity (95%) providing a reliable confirmation of the presence or absence of the disease. Another marker is the circulating tumor DNA (ctDNA) analysis which shows a growing area of research as a non-invasive method involved in the detection of tumor DNA fragments in the bloodstream [40]. An additional clinical analysis, the fecal immunochemical test (FIT), which

detects blood in stool, offers significant accuracy and higher compliance compared to the guaiac-based fecal occult blood test (gFOBT) [38].

I.5. Colorectal cancer therapies

Like any other type of cancer, conventional treatment methods such as surgery, radiotherapy, and chemotherapy, including both targeted therapy and immunotherapy, are used in CRC treatment.

I.5.1. Surgery

Surgery is the primary treatment option, especially at the early stages of CRC where the tumor is still small and localized into the colon and rectal areas without spreading into any other distant body sites. Additionally, upon metastasis, spreading cancer cells will reach the liver through the portal circulation as the first target site. One-third of patients are detected with liver metastasis three years after the first diagnosis which allows 15-20% of patients to undergo hepatectomy. Surgical resection combined with proper systemic chemotherapy can enhance the patient's quality of life and prognosis increasing their median survival rates. Surgery also reduces the recurrence and relapse of the patient especially when combined with adjuvant therapies, post-surgery, such as radiation or chemotherapy aiming at the residual cells that weren't removed by surgery. However, surgeries might also be accompanied by complications such as bowel dysfunction, infections, and bleeding that further require to be managed. Other factors that can impact the outcome and recovery process after surgery include age, comorbidities, and overall well-being [41]. Among the performed surgeries in the treatment of CRC, colostomy involves performing an incision in the anterior abdominal wall in which a part of the colon is brought to the surface of the skin. This aperture frequently forms an external colostomy bag along with a connected ostomy system. This gives the body an alternate route for excretion. Colostomies are also made to treat other medical conditions affecting the colon such as IBD and can also be temporary or permanent depending on the underlying condition. Hemicolectomy is a surgery involving the elimination of a part of the colon, either the right or the left side of the colon carrying the tumor. Polypectomy refers to the removal of polyps after early detection during colonoscopy to prevent the progression and development of colorectal cancer [42], [43].

I.5.2. Radiotherapy

Radiotherapy is a treatment modality based on the use of high-energy radiation such as external beam radiation (EBRT) and internal radiation therapy also called "brachytherapy" penetrating the body to trigger the death of the cancer cells. The specific brachytherapy model used in the treatment of rectal tumors is endorectal brachytherapy. Endorectal brachytherapy used in combination with EBRT can highly influence better control of rectal cancer and prevent recurrence. The radiations used can be photon radiations (X-rays and gamma rays), proton radiations, electron radiations, and radioactive isotopes. It started in the late 1980s and 1990s when it was detected that combining it with surgery as neo-adjuvant and adjuvant therapy improved the patient's outcome. Radiotherapy can also be used as a palliative treatment as it mitigates the symptoms associated with advanced cancer cases. Advances in the methods of radiotherapy used widely in clinics include intensity-modulated radiotherapy (IMRT) and stereotactic body radiotherapy (SBRT) is accompanied by reduced side effects and more accuracy. IMRT is based on the use of multiple beams with different intensities that can be adapted to best suit the tumor structure, giving it the advantage of being used for the treatment of complicated tumor structures and locations. This technique allows the radiation dose to be precisely modulated and delivered homogeneously to the tumor area while sparing healthy

tissues, thereby reducing toxicity. On the other hand, IMRT delivers high radiation doses in short periods into the tumor site and is often used for small and well-defined tumors. These augmented doses will cause significant DNA damage and cell death providing a local control of the tumor area [44], [45], [46].

I.5.3. Chemotherapy

The principal treatment strategy for all types of cancer is chemotherapy, which comprises the administration of a variety of chemical compounds that are administered orally or intravenously (IV) and cause toxicity to cancer cells. These compounds include enzymes, anti-metabolites, alkylating agents, plant-alkaloids, antitumor antibiotics, hormones, and enzymes. They can be administered as one drug type at a time or a combination of drugs, known as monotherapy and polytherapy, respectively. Chemotherapy can be neoadjuvant minimizing the tumor size before surgery, or adjuvant to kill the cancer cells remaining in the tumor and limit cancer recurrence and relapse. Chemotherapy acts by targeting the death of cancer cells through alkylating into DNA and deteriorating their integrity allowing the inhibition of DNA replication and the induction of cancer cell death. Also, drugs can act by building up a toxic microenvironment of the tumor which further weakens their aggressiveness and invasiveness. However, the major limitation of this type of therapy is not selective only towards the cancer cell, so it can affect surrounding normal healthy cells which contributes to adverse undesirable side effects. So far, none of the medications have spared the healthy cells while killing the cancer cells.

In CRC, 5-fluorouracil (5-FU), a pyrimidine analog acting as an inhibitor of the thymidine synthase enzyme, remains a first-line chemotherapeutic option. Nevertheless, it is accompanied by certain limitations such as low solubility and short half-life. Adjuvant chemotherapeutic drugs such as capecitabine, leucovorin, irinotecan, ramucirumab, cetuximab, and oxaliplatin are often used in combination with 5-FU to boost the therapeutic potency against CRC. However, some drugs are used as monotherapy without 5-FU, including regorafenib, a multi-kinase inhibitor affecting the vascular endothelial growth factor receptor (VEGFR) and platelet-derived growth factor receptors (PDGFR). Regorafenib also affects the SHP-1-STAT3 axis; SHP-1 (SH2 containing phosphatase-1 domain) by inhibiting the involved kinases leading to tumor growth and suppression of epithelial to mesenchymal transition. Chemotherapy, radiotherapy, and surgery can be combined to produce an optimal outcome in causing tumor eradication [47] [48] .

I.5.4. Targeted therapies and nanomedicine

To reduce the undesirable side effects associated with chemotherapy and radiotherapy, targeted therapy acted as a promising breakthrough in the field of cancer therapies. These therapies are based on the use of drugs well-designed to target cancer areas and be selective to the cancer cells. This includes the use of monoclonal antibodies that can directly bind to surface proteins, glycoproteins, and carbohydrates specific to the cancer cells or indirectly through interference with factors essential for the growth of the tumor. For example, bevacizumab is a monoclonal antibody targeting VEGFR present on the surface of endothelial cells. This receptor is activated after the binding of its VEGF ligand secreted by the tumor cells and the overall process is regulated by numerous factors that can either promote or inhibit angiogenesis, such as the vascular endothelial growth factor (VEGF) and fibroblast growth factors (FGF1 and FGF2). Consequently, the growth and formation of new blood vessels will be triggered to nourish the tumor and promote its development. Hence, the role of the bevacizumab drug will be highlighted through the suppression of this growth and inhibition of angiogenesis, thereby limiting blood supply and tumor progression. This targeted drug

category also includes cetuximab and panitumumab targeting the epidermal growth factor receptors (EGFRs). EGFR is a tyrosine kinase receptor and belongs to the erythroblastosis oncogene B ErbB and the human epidermal growth factor (HER) receptors. They become activated by the binding of their ligands EGF and TGF- α . Once activated, many signaling pathways such as JAK/STAT3, RAS, RAF, and MEK are induced causing cell growth and proliferation. EGFRs are overexpressed in cancers such as CRC, melanoma, glioma, and esophageal cancer [49], [50], [51].

Additionally, new approaches are being made to target cancer cells and enhance drug absorption and clearance. This involves the application of nanoparticles (NPs) ranging from 1 to 100 nm in size and holding the anticancer drug interiorly through encapsulation or on its surface. Different types of NPs can be mentioned. This includes polymers, micelles, nanocrystals, dendrimers, silica/gold nanoparticles, and liposomes. NPs are non-toxic and flexible as they can be modified and conjugated to functional groups with optimal compatibility with the body and selectivity towards cancer cells. Coupling of NPs with substrates, peptides, or antibodies can allow their binding to a receptor that is overexpressed on cancer cells. For instance, 5-FU can be coated by a pH-sensitive methacrylic-based copolymer to enhance its solubility and targeting capacity [52]. Similarly, folate-conjugated gold NPs are designed to actively target cancer cells as they express high levels of folate receptors. Moreover, magnetic NPs are also used in targeted cancer therapy through the application of external magnetic fields alone or in combination with hyperthermia or chemotherapy and can act as drug delivery systems [53].

1.5.5. Immunotherapy

Our immune system is often ready to respond to various pathogens, foreign structures, or even abnormal cells in our body. However, in some cases, this system fails to accomplish the desired outcomes or accidentally confers to undesired outcomes such as auto-immune disease. In the case of cancer occurrence, the immune system considers the abnormal cell as a foreign substance and tries to attack it, but when it is unable to differentiate between this cell and a normal cell or when the cancer cells secrete an immunosuppressive molecule, the immune system weakens, and cancer develops. Therefore, to boost the immune system against cancer cells, immunotherapy plays a significant role in modifying the immune response through certain ligands and drugs. This includes immune checkpoint inhibitors such as pembrolizumab, nivolumab, and atezolizumab that can interfere with the interaction between the immune cells such as T cells, and the cancer cells carrying immune checkpoints on their surface such as the programmed death-ligand 1 (PD-L1) which blocks the immune cells' activity. Therefore, these drugs inhibit these checkpoints and trigger the desired activity of the immune cells (**Figure 14**) [50], [51], [54], [55].

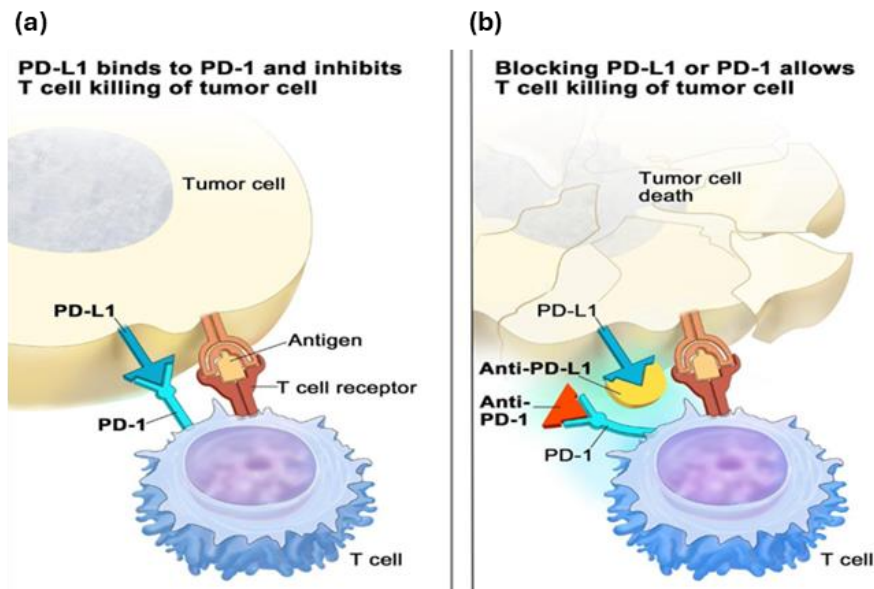


Figure 14: Immune checkpoint inhibitors: (a) the interaction between PD-1 and PD-L1 prevents the T cell from killing the tumor cell (b) blocking this interaction with anti-PD-1 triggers the death of the tumor cell by the T cell [56]

I.5.6. Gene therapy

With the development of science-based techniques, gene therapy is a method for inserting specific genes into the host genome, such as those associated with the expression of antibodies, cytokines, and specific receptors. The benefit of gene therapy is that, once the specific gene has been delivered successfully and inserted at the target site, it will stimulate sustained generation of the therapeutic molecule in the patient. Selecting the particular gene delivery system and targeting the appropriate cell for insertion are typical challenges in gene technology. The gene insertion system may employ viral or non-viral methods. In cancer, genes involved in the inhibition of angiogenesis and cell proliferation, as well as genes generating therapeutic antibodies, may be identified as suitable targets for gene therapy. Recent improvements are being made with the use of antisense genetic tools such as siRNA, miRNA, and CRISPR-Cas9 [57]. Gene therapies involve the adenovirus-mediated wild type p53 replacement therapy which is based on using adenoviruses to deliver the wild-type p53 gene to colorectal cancer cells with mutated p53 genes. Also, immunization and proper vaccination of patients with CRC to boost their immune system against specific antigens such as CEA leading to tumor regression [58].

I.5.7. Laser therapy

Laser therapy is a recent therapy based on the utilization of fundamental light energy sources. It is comprised of two major approaches which are photothermal therapy (PTT) and photodynamic therapy (PDT). PTT involves hyperthermia-mediated NPs. Once these particles are administered, they will reach the tumor site where they will accumulate and get exposed to light illumination of a specific wavelength. The electrons within the NPs will perform coordinated oscillations inducing the transformation of the near-infrared light into heat resulting in the death of the tumor cells. PDT in laser therapy permits the detection of tumor areas through photo-diagnosis and provides anti-cancer therapy, simultaneously. This therapy provides advantages as a focal and localized treatment modality diminishing the undesirable side effects [59], [60].

I.5.8. Adoptive cell therapy (ACT)

ACT is a personalized cancer therapeutic approach that enables the immune system to attack cancer cells. It is based on obtaining the immune cells from a patient's blood or tumor tissue through a process called 'leukapheresis', particularly T cells, which are then enhanced in the laboratory through exposing them to specific antigens or cytokines to improve their activity in the immune response. On the other hand, these cells can be modified through genetic engineering to induce the expression of chimeric antigen receptor (CARs) or T cell receptors (TCRs) which can recognize tumor associated antigens (TAA). Once a sufficient number of the modified or enhanced T cells is obtained, they are infused back into the patient. For metastatic colorectal cancer (mCRC), several metastatic lung lesions showed clear regression following the infusion of HLA-C*08:02-restricted tumor-infiltrating lymphocytes (TILs) specifically targeting the KRAS G12D mutation [61]. While this type of therapy holds a promising potential, different challenges are accompanied with its application in solid tumors like CRC. This includes the tumor microenvironment which is often an immunosuppressive environment due to certain cytokines, regulatory T cells and myeloid-derived suppressor cells that hinder the effectiveness of ACT. Other challenges include the heterogeneity in antigen expression exhibited by the tumor as well as the ACT associated side effects including cytokine release syndrome (CRS) and neurotoxicity. The first CAR T-cell therapy began in the early 2000s when it gained attention for its potential in treating hematological malignancies, particularly in patients with B-cell lymphoma. Nevertheless, the antigen targets used in CAR T-cell therapy for CRC are often also expressed in normal cells, making it challenging to accurately distinguish tumor-associated antigens (TAAs). As a result, this therapy lacks the high specificity and effectiveness in the treatment of CRC [62].

I.5.9. Anti-tumor vaccine therapies

Anti-tumor vaccine therapies are designed to enhance the potential of the immune system in recognizing and attacking cancer cells by targeting specific TAAs or tumor-specific antigens (TSAs). These vaccines aim to enhance the body's immune response against tumors, enabling regression and long-term immunity against cancer recurrence. This includes dendritic cell vaccines which employ dendritic cells that have been loaded with tumor antigens. Once administered, they activate T cells to recognize and attack cancer cells. Peptide vaccines consisting of peptides that correspond to specific tumor antigens which are also designed to elicit a targeted immune response. Viral or bacterial vector vaccines involving modified viruses or bacteria for the delivery of tumor antigens to the immune system to induce an immune response. Whole tumor vaccines which use whole tumor cells that are dead or modified to stimulate an immune response against a broad range of tumor antigens. Anti-tumor vaccines work by presenting tumor antigens to the immune system, particularly to T cells. This process activates T cells, which then proliferate and migrate to the tumor site to attack cancer cells. The vaccines can also promote the development of memory T cells, which provide long-lasting immunity against cancer recurrence. Anti-tumor vaccines are being actively investigated for their potential in treating CRC. Various clinical trials are underway to evaluate the safety and efficacy of different vaccine platforms in CRC patients. Some vaccines are designed to target specific antigens commonly expressed in CRC such as CEA and mucin 1 (MUC1). Several clinical trials have explored the use of peptide-based vaccines in CRC, aiming to elicit an amplified immune response against tumor cells. For example, vaccines targeting CEA have shown promise in early-phase trials. There is growing interest in combining anti-tumor vaccines with other immunotherapies, such as immune checkpoint inhibitors (e.g., anti-PD-1/PD-L1 therapies), to enhance the overall immune response against CRC. Anti-tumor vaccine

therapies represent a promising strategy against CRC, with ongoing research aimed at optimizing their efficacy and overcoming existing challenges. These vaccines harness the immune system's capability to identify and destroy cancer cells which offer the potential to enhance the patient outcomes and open new pathways for the treatment of CRC [62].

I.6. Current targeted therapies for mCRC

It is important to highlight and develop critical therapies for the treatment of mCRC as its corresponding 5-year survival rate is 15% after treating with the conventional cancer therapies including surgery, radiotherapy and chemotherapy. Whereas this rate is almost 65% for patients with early stages of CRC. Surgical excision of the tumor showed to enhance the overall survival (OS) of patients. However, almost 25% of patients are shown with tumor metastasis into different body sites at the time of diagnosis which limits their surgical effectiveness. In this case, to minimize the tumor size and enhance the survival of patients, chemotherapy alongside targeted therapy and/or radiotherapy is required. It is important to well explore the involved genetic mutations and resistance strategies to decide on the optimal therapeutic approach included in the first-line chemo- and targeted therapies. For instance, chemotherapy including FOLFOX (fluorouracil, leucovorin, and oxaliplatin), FOLFOXIRI (fluorouracil, leucovorin, oxaliplatin and irinotecan), FOLFIRI (fluorouracil, leucovorin, and irinotecan) can be combined to targeted drugs such as VEGF and EGFR inhibitors to be used as a primary option for the mCRC treatment. Fluorouracil-based chemotherapy showed to ameliorate the OS of patients suffering from mCRC up to 14 months. Subsequently, FOLFOX lengthened the OS of patients to reach 19.5 months. Cetuximab, an anti-EGFR, was approved by the FDA in 2004 and thereafter several targeted drugs gained approval for the treatment of mCRC (Table 2) [63], [64].

Table 2 : Targeted therapies for mCRC approved by the FDA [64]

Year Approved by the FDA	Drugs	Targets	Drug Details
2004	Cetuximab	EGFR	Chimeric mouse/human mAb (IgG ₁)
	Bevacizumab	VEGF-A	Humanized mAb (IgG ₁)
2006	Panitumumab	EGFR	Fully human mAb (IgG ₁)
2012	Aflibercept	VEGF-A, VEGF-B, PlGF	Fusion protein which consists of the binding portions of VEGF from VEGF-1 and 2 fused to the Fc portion of immunoglobulin G ₁ (IgG ₁)
	Regorafenib	VEGFR, FGFR, KIT, PDGFR, BRAF	Small molecule inhibitor of membrane-bound and intracellular receptor tyrosine kinases
2015	Ramucirumab	VEGFR-2	Fully human mAb (IgG ₁)
2017	Pembrolizumab	PD-1	Humanized mAb (IgG ₄)
	Nivolumab	PD-1	Fully human mAb (IgG ₄)
2018	Ipilimumab	CTLA-4	Fully human mAb (IgG ₁)
	Larotrectinib	TRK	Small molecule of tyrosine kinase inhibitor
2019	Entrectinib	TRK, ALK, ROS1	Small molecule of tyrosine kinase inhibitor
2020	Encorafenib	BRAF (V600E-mutant)	Small molecule kinase inhibitor

I.7. New biomarkers of the clinical response

Several biomarkers are correlated with the patient's response to the clinical treatments such as mutations in BRAF, KRAS, HER2 amplifications, the density of TILs and PD-L1 expression. Patients with BRAF mutations are associated with a poor prognosis and may indicate resistance to certain therapies. Also, KRAS mutations, particularly in codons 12 and 13, are associated with resistance to anti-EGFR therapies such as cetuximab and panitumumab. HER2-positive CRC may respond to targeted therapies such as trastuzumab. Additionally, high levels of PD-L1 expression in CRC may correlate with a better response to PD-1/PD-L1 inhibitors. Performing tests to reveal the PD-L1 expression can help identify patients who are more likely to benefit from ICIs. The presence and density of TILs, particularly CD8+ T cells, can be indicative of an active immune response against the tumor. High levels of TILs are often associated with better prognosis and may predict response to immunotherapy. Emerging biomarkers include tumor mutational burden (TMB) that are linked to mutations in DNA repair genes, such as POLE or POLD1 mutations, where tumors with high TMB are often more immunogenic and may respond better to ICIs due to the abundance of mutation-associated neoantigens. Mutations in POLE and POLD1 genes can lead to proofreading defects in DNA replication and are characterized by higher infiltration of CD8+ T cells as well as greater expression of cytotoxic markers, suggesting a similar immune response profile to dMMR/MSI-H tumors. The dMMR/MSI-H (mismatch repair deficiency/ microsatellite instability) in tumors contributed to a favorable response to ICIs in about 15% of CRC patients and in 5% of patients with metastasis. Also, the telomere length and telomerase activity are emerging as indicators of the immunity state, may serve as prognostic and predictive biomarkers in CRC therapy, and improving them could potentially improve the efficacy of immune-mediated therapies, including ACT and ICIs. The identification and validation of these emerging biomarkers are crucial for specifying treatment strategies in CRC according to the individual patient's biomarkers. By understanding the molecular characteristics of tumors, clinicians can better predict which patients are likely to benefit from specific therapies, ultimately improving treatment outcomes and minimizing adverse effects [62].

I.8. Staging classification

After tumor detection, it is crucial to detect the stage of the tumor, which can be divided into stages based on TNM classification systems. The TNM classification system of the American Joint Committee on Cancer (AJCC) is most used for CRC staging. The TNM classification is an international system for classifying cancers based on their anatomical spread. It allows stage assessment into three criteria: local, regional, and metastatic anatomical propagation. The three letters symbolize the spread of the cancerous disease at the site of the primary tumor (T), in the nearby lymph nodes (N), and at distant sites for potential metastases (M) [65], [66], [67].

The letter "T" symbolizes the initial tumor and is an indicator of the size and depth of the tumor. It is ordered from T0 in which no primary tumor is detected until T4 which refers to the most invasive form of the tumor. When cells become cancerous, they are localized to the inner surface of the colorectal wall, but in some cases, they can reach deeper layers. Investigating the tumor size, especially its histological extent, allows for the estimation of the degree of disease progression. The deeper the tumor has spread within the histological layers, the poorer the survival prognosis (**Figure 15**).

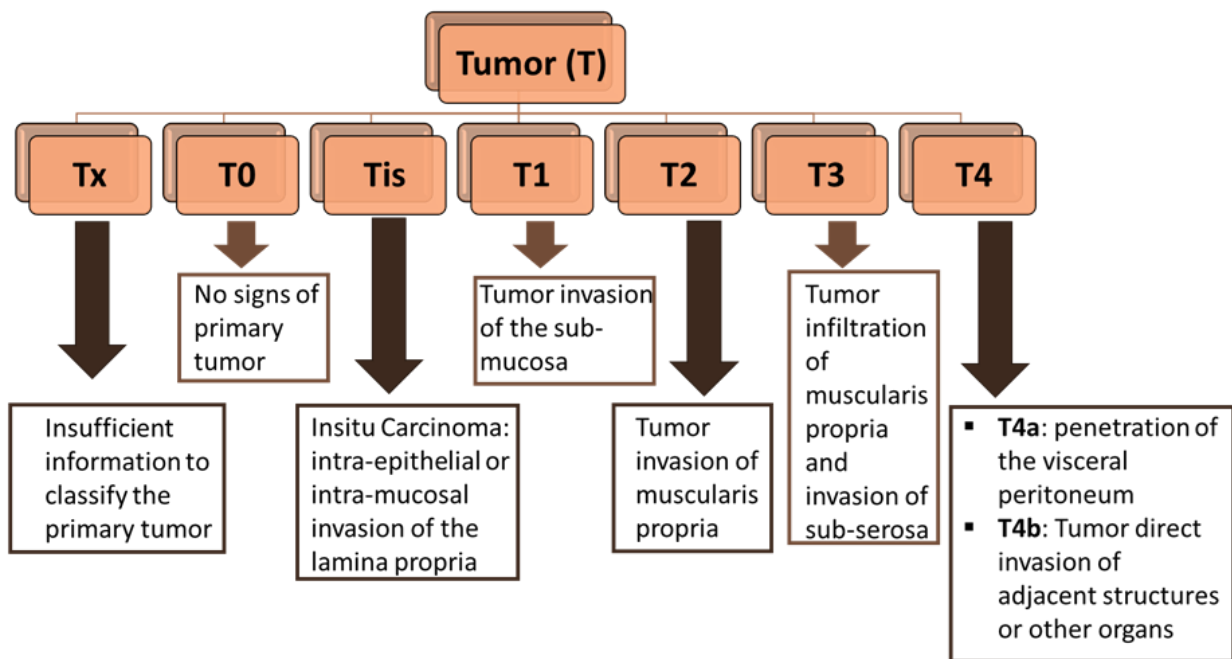


Figure 15: TNM classification system: the letter “T” refers to “Tumor” and is an indicator of the size and depth of the tumor. It ranges from Tx until T4. (Created using Microsoft office PowerPoint)

The letter “N” indicates lymph node involvement and the number of affected lymph nodes. It describes the cancer cells’ ability to spread to the organ’s surrounding lymph nodes. N0 means that the cancer has not spread to any nearby lymph nodes. N1, N2, or N3 means that the cancer has reached the lymph nodes and reveals the number, size, and location of affected lymph nodes. Indeed, the involvement of lymph nodes is a sign of poor prognosis, but the number of affected lymph nodes determines the chances of recovery (**Figure 16**).

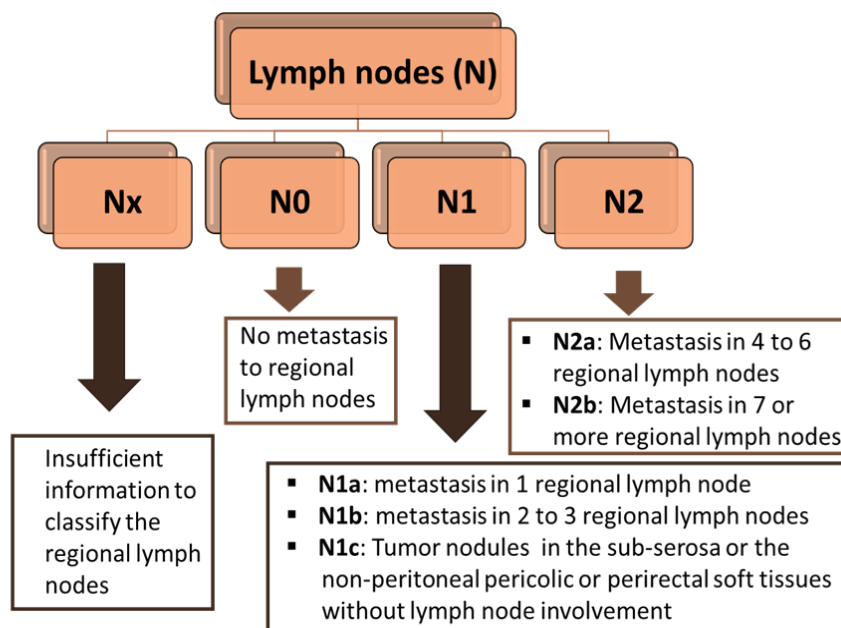


Figure 16: TNM classification system: the letter “N” refers to “lymph nodes” and is an indicator of lymph nodes’ involvement. It ranges from Nx until N2. (Created using Microsoft office PowerPoint)

The letter “M” indicates metastasis. After dissemination into the lymph nodes, the cancer cells will metastasize through the bloodstream to reach distinct body sites. Typically, the cells can now leave the large intestine and move to distant body organs forming a secondary tumor. A higher risk of metastasis is linked to a more advanced stage of cancer. M0 indicates the absence of known metastasis and M1 refers to the presence of metastasis regardless of the location or number of affected body sites (**Figure 17**).

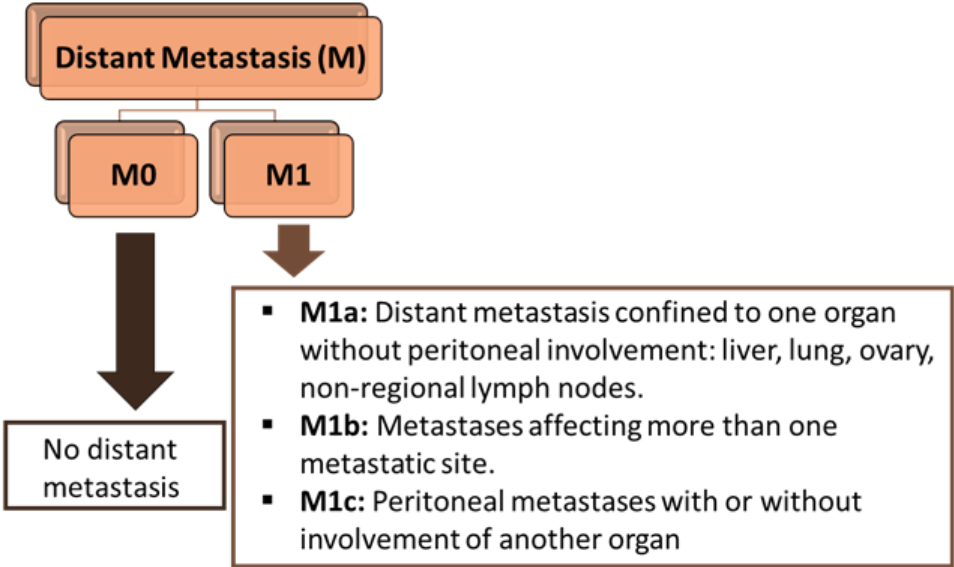


Figure 17: TNM classification system: the letter “M” refers to “metastasis” and is an indicator of distant metastasis. It consists of M0 and M1. (Created using Microsoft office PowerPoint)

The most common staging system used for CRC is the TNM classification. The grouping of TNM criteria enables the staging of CRC at the time of diagnosis. It progresses from stage 0 to stage IV and can generally establish the optimal therapeutic options for the patient. Higher stages often have elevated numbers and demonstrate a more advanced cancer progression (**Figure 18**).

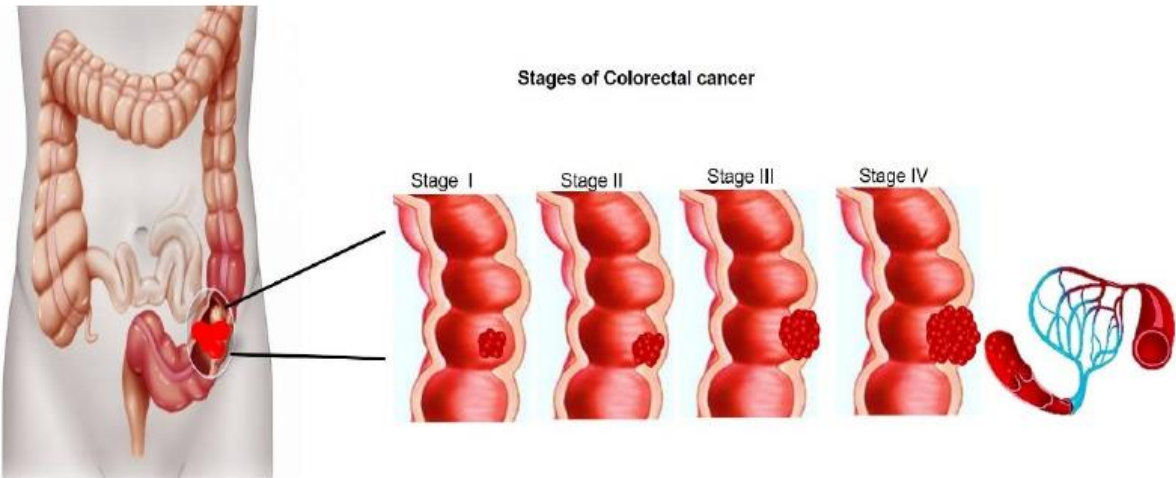


Figure 18: The different stages of CRC representing its development and progression [68]

- **Stage 0** (Carcinoma *in situ*)

It represents the earliest stage which is also referred to as carcinoma in situ or intramucosal carcinoma. Cancer cells are restricted to the mucosa (inner lining) of the colon or rectum. They can be detected in the epithelium, yet sometimes they may have invaded the connective tissue layer of the mucosa. However, cancer cells have not developed beyond the muscular layer of the mucosa.

- **Stage I**

The tumor has invaded the submucosa or even extended into the tunica muscularis of the colon or rectum but has not progressed to neighboring lymph nodes or distant sites.

- **Stage II**

This stage is further subdivided into II A, II B, and II C.

- Stage II A: the tumor has penetrated the layer of tissue between the muscularis and the serosa or has reached tissue beyond the muscularis where there is no serosa.
- Stage II B: the tumor has invaded the membrane that surrounds and supports the colon and rectum (serosa or visceral peritoneum).
- Stage II C: the tumor has progressed through the wall of the colon or rectum to other organs or regions of the body, such as the bladder, uterus, or prostate.

- **Stage III**

At this stage, cancer cells have infiltrated the lymph nodes near the colon or rectum. Stage III is also divided into stages III A, III B and III C based on the extent of the tumor and the number of affected lymph nodes.

- **Stage IV**

Stage IV is also known as metastatic CRC where the tumor has disseminated to other parts of the body (distant metastases), such as the liver or lungs. It is sub-divided into stage IV A, IV B, IV C.

- Stage IV A: the tumor has spread into one organ.
- Stage IV B: the tumor has extended to more than one organ.
- Stage IV C: it is the most aggressive stage of CRC where the tumor has invaded the peritoneum [65], [69] (**Table 3**).

Table 3: Classification of CRC based on their stages and the associated probability percentage of five-year survival [70]

Stage	TNM Classification	Five-Year Survival (%)
Stage 0	Tis-N0-M0	>90 %
Stage I	T1-2, N0, M0	
Stage II A	T3, N0, M0	60-85 %
Stage II B	T4a, N0, M0	

Stage II C	T4b, N0, M0	
Stage III A	T1-2, N1-2a, M0	25-65 %
Stage III B	T1-4a, N1-2b, M0	
Stage III C	T3-4b, N1-2b, M0	
Stage IV A	T (all)- N (all)- M1b	5-7 %
Stage IV B	T (all)- N (all)- M1a	
Stage IV C	T (all)- N (all)- M1c	

Considering a treatment that uses light, a source of energy and life to fight several diseases, including cancer, can be quite compelling. This is the potential of photodynamic therapy (PDT) as an innovative approach that combines light energy with modern medicine. Initially arising from a fusion of ancient wisdom and the forefront of research, PDT represents the intersection of science and innovation, offering a versatile and accurate procedure against cancer and other diseases.

II.1. History of photodynamic therapy

PDT has a rich history since ancient civilizations, yet not until the 20th century, it showed a significant development. Sunlight has been recognized to have a therapeutic potential in the ancient times when heliotherapy was practiced by the Greeks and individuals exposed themselves to sunlight for healing and health restoration. In the early 20th century, phototherapy was further discovered after the work of pioneers like Niels Finsen, Oscar Raab, and Herman von Tappeiner. Niels Finsen, a Danish physician, discovered the light's therapeutic potential for skin tuberculosis. He demonstrated certain wavelengths of light specifically in the ultraviolet range, exerting an anti-bactericidal effect against lupus vulgaris. Oscar Raab, a German scientist, conducted a study on acridine which is a coal tar, to see its effect when combining it with light. He observed an increased toxicity hypothesizing that it originated from the fluorescence and not light itself. Hence, he demonstrated the role of fluorescence in enhancing the biological effects of certain compounds which contribute to the understanding of light-induced reactions in living systems. This conclusion was also validated by an Austrian physician named Herman von Tappeiner. In the mid-20th century, the uptake and retention of haematoporphyrin (HP) was investigated by Auler and Benzer in the 1940s. They showed that HP was preferentially accumulated in tumor cells at higher levels than in normal and surrounding tissues. When tumors were then illuminated, necrosis occurred in the tumor demonstrating a PDT effect of HP. In the 1950s, post-war advances occurred in this field, Schwartz et al. manifested that the uptake of HP in tumors was inconsistent and its associated phototoxicity limited its use which recruited further research and investigations to overcome the associated challenges and optimize its potential in cancer treatment.

In the 1960s, a derivative of haematoporphyrin (HpD) was used as a candidate for phototherapy of tumors. Lipson et al. reported the first successful treatment of cancer using HpD on a patient with recurrent breast carcinoma. Further trials further validated the therapeutic effect of HpD which showed promising outcomes on various tumor types between the 1960s and 1970s. HpD is made up of monomers, dimers, and oligomers of porphyrins and was partially purified to remove the porphyrin monomers with low activity to yield Photofrin, a widely used photosensitizer (PS) in clinics. Finally, by the 1980s, PDT using porphyrins was applied to a wide range of tumors such as lung, esophagus, bladder, lung, and skin cancers. Hence, since the late 20th century until now, PDT has been the center of attention of a lot of researchers where a lot of studies are being conducted to optimize the potential of different photosensitive molecules and light dosimetry necessitating developments in photochemistry and photophysics to use in the PDT against cancer with minimal side effects and better outcomes. Ongoing research aims to enhance the development of novel photosensitizers (PSs), optimization of light systems, and imaging techniques for good monitoring of the response to treatments. Nowadays, PDT is being applied in clinics for the treatment of many cancer types. [71], [72], [73] .

II.2. Principles of photodynamic therapy

As its name implies, PDT is a therapy based on the use of photons referring to light. PDT is an innovative clinically approved and minimally invasive therapeutic procedure that can exert selective cytotoxic activity against tumor cells while preserving surrounding healthy tissues and thereby limiting side effects. It requires three essential factors to exert its potential, which are PS, light (photons), and oxygen (O_2) (**Figure 19**). The PSs are the molecules sensitive to light that cause their activation and trigger their biological effect. Upon the administration of this photoactive substance, it will accumulate in cancer cells and then will be exposed to light illumination at a particular dose (J/cm^2) and specific wavelength corresponding to its absorption band. The light-excited PS transfers energy to oxygen (O_2) creating singlet oxygen (1O_2) and ROS. These cytotoxic species produced initiate a cascade of biochemical events that cause cells' damage and death. This therapy overcomes one of the main challenges in cancer treatment which is targeting cancer cells and its selectivity stems from the localized nature of the illumination used to activate the PS, as well as the preferential accumulation of the PS into targeted tissues, thereby significantly limiting the systemic toxicity as compared to conventional chemotherapy treatments. Additionally, this therapy can be used alone or in combination with other therapies such as chemotherapy, radiotherapy, and surgery. PDT outcomes vary from a delay in the growth of the tumor with a better patient's quality of life to a total regression of the tumor [74].

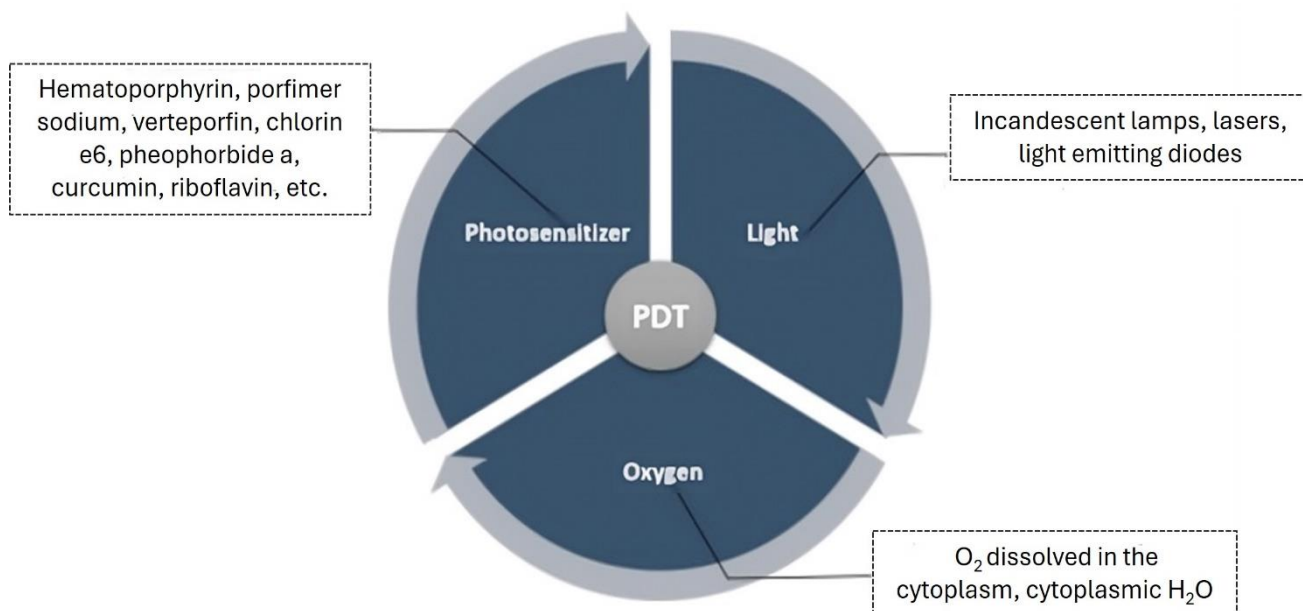


Figure 19: The essential factors of PDT [74]

The administration of PS can be either topically or systemically. Topical PDT is based on the use of PS applied locally (cream, solution, emulsion, subcutaneous injection); whereas systemic PDT is when PS is administered intravenously or orally. In both cases, the potential of these molecules will be confined to the tumor site as they can be designed to accumulate in cancer cells. Afterward, the area of the tumor will be exposed to light with a wavelength specific to its absorbance capacity causing the activation of the PSs, thereby triggering selective death of cancer cells (**Figure 20**). The drawback of systemic PDT is that the PS may not preferentially accumulate in the tumor site if not properly structured and designed. On the other hand, topical PDT ensures the local application of PS, and this paved the way for advancements in the field of dermato-oncological pharmacology. However, PDT offers a wide range of advantages over other anti-cancer therapies allowing it to be at the center of research and investigation for

improving the selectivity of PS and PDT applications in the treatment of deeper solid tumors [75], [76].

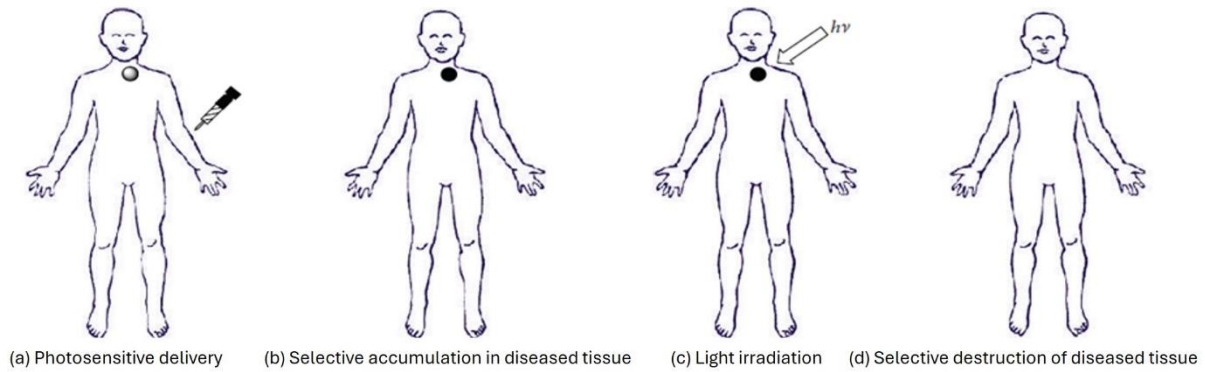


Figure 20 : PS administration and selective tumor targeting of the patient [75]

II.3. Mechanisms of action in photodynamic therapy

Over time, many cancer types were diagnosed and treated by photodynamic diagnosis (PDD) and PDT. Both approaches can occur simultaneously and share a common strategy based on the use of PS which can be excited by a specific wavelength of light in the visible or near-infrared regions. In PDD, the patient administers the PS that selectively accumulates in the tumor cells at relatively higher levels than normal tissues due to the enhanced permeability and retention (EPR) effect. This is a consequence of the poor lymphatic drainage and increased vessel permeability facilitating the way for the drugs and macromolecules to reach and accumulate in the tumor. Once the PS is absorbed and excited by light, it will emit fluorescence and become photoactivated. The produced fluorescence by the PS is used to identify and detect the tumor as it will illuminate it non-invasively and distinguish it from the surrounding tissues. These fluorescent properties are particularly beneficial during surgery permitting an accurate and effective fluorescence-guided resection of cancerous tissues. A study with fluorescein contributed to a total resection of the tumor in most of the patients. Also, indocyanine green fluorescence has revealed breast cancer lesions that were undetectable by clinical techniques such as palpations. In addition to indocyanine green, methylene blue offered many advantages in the detection of undetectable parathyroid adenomas and the treatment of breast, head, and neck cancers [77], [78], [79], [80], [81].

The PDT process starts when the PS is activated through the absorption of photons from light allowing its transformation from a singlet ground state (^1PS) to a short-lived, few nanoseconds or less, electronically excited singlet state ($^1\text{PS}^*$). At this stage, the PS is very unstable and can decay back to its ground state by losing excess energy through fluorescence emission or heat production by undergoing internal conversion. On the other hand, this excited singlet state can also undergo intersystem crossing to develop into a more stable long-lived electronically excited triplet state ($^3\text{PS}^*$) by electron spin conversion in the higher-energy orbital. $^3\text{PS}^*$ can also decay into the ground state through light emission (phosphorescence) or it can directly transfer energy into molecular oxygen (O_2) through type I and type II photochemical reactions. The long lifetime of tens of microseconds of $^3\text{PS}^*$ gives it an advantage in undergoing this interaction. In type I reaction, $^3\text{PS}^*$ reacts with biological substrates such as the cell membrane, lipids, proteins, and nucleic acids to give free radicals and radical ions through hydrogen atom abstraction, or electron transfer. These species can undergo a reaction with O_2 and stimulate the production of superoxide anion ($\text{O}_2^{\cdot-}$), hydroxyl radical (OH^{\cdot}), or hydrogen peroxide (H_2O_2). Type II reaction is predominant during PDT and occurs when the excited PS reacts directly with oxygen molecules to produce non-radical but highly reactive singlet oxygen $^1\text{O}_2$. The

kinetics of both reactions are highly dependent on the availability of oxygen, the nature of PS, and the substrate concentration, as well as they may occur simultaneously leading to the reversion of the excited state into its ground state. Indeed, the produced ROS are highly cytotoxic, have a short half-life, and can oxidize diverse biomolecules through the induction of redox reactions causing oxidative stress and subsequent cell death (**Figure 21**) [74], [82], [83], [84].

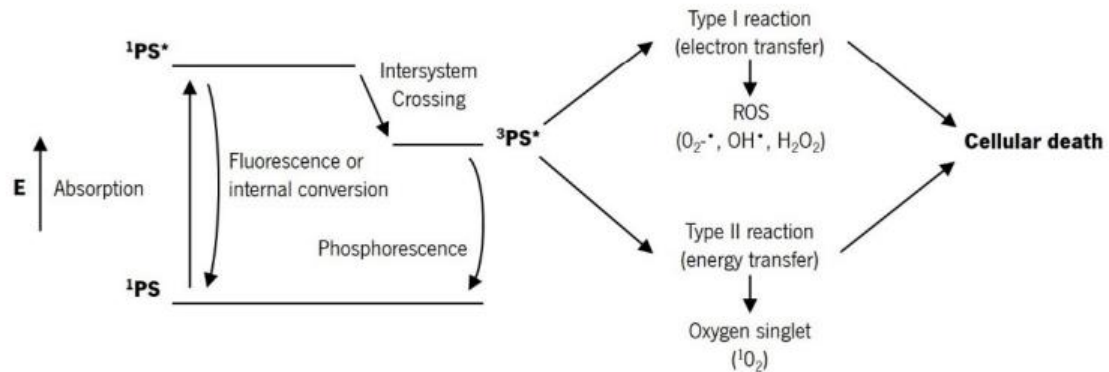


Figure 21: Jablonski diagram of PDT mechanism of action [85]

Type I photochemical reactions consist of the direct reaction of PS in an excited state with biological substrates by the transfer of electrons or hydrogen ions (H^+), resulting in the production of radical species. The oxidized forms of PS or substrate as well as their semi-reduced forms can react with the surrounding molecular oxygen to form peroxide radicals, leading to an auto-oxidation chain, and the superoxide anion ($O_2^{\cdot-}$). Although this species is not significantly reactive, it can interact with other substrates to form other ROS such as the hydroperoxyl radical (HO_2^{\cdot}), hydrogen peroxide (H_2O_2), and the hydroxyl radical ($\cdot OH$). ROS are strong oxidizing agents inducing cytotoxic reactions in many biomolecules. In type I photochemical reactions, oxygen is not implicated in the initial step of the reaction mechanism, but it has a powerful impact on the subsequent chemical reactions which allows the production of ROS [83].

Radical chain reactions cease only when two radical species react with each other through disproportionation or recombination. Disproportionation, a classic free radical reaction, can be catalyzed by enzymes of the superoxide dismutase (SOD) family. This process involves two molecules of the same radical (e.g., $O_2^{\cdot-}$) undergoing a redox reaction to produce oxidized products (1O_2 or 3O_2) and reduced H_2O_2 . In recombination reactions, two molecules of the same or different radicals react to form a covalently linked dimer. Lipid peroxidation is typical for cellular destruction regularly leading to necrosis. Hydroxyl radicals, being highly responsive to nonpolar species undergo hydrogen atom abstraction from saturated lipids yielding lipid radicals (L^{\cdot}). Subsequently, oxygen molecules, in their ground state, can combine with the lipid radicals resulting in the formation of peroxy radicals. Such radicals react with other lipids, inducing chain reactions across the membrane until disproportionation reactions occur. Given that the cell membrane is composed of a bilayer of phospholipids interacting with each other in close proximity and with membrane proteins, enabled free radical chain reactions to propagate across the membrane which triggers the rupture of the membrane and necrosis. Particular attention should be given to the damage inflicted on nucleic acids (DNA and RNA) by hydroxyl radicals (HO^{\cdot}) formed in type I reactions. Conversely, superoxide radicals ($O_2^{\cdot-}$) rarely interact with nucleic acids due to the repulsive forces between the negatively charged species. Although hydrogen peroxide (H_2O_2) is neutral, it reacts with most biomolecules at

negligible rates. The initial step in free radical reactions in this context typically involves the abstraction of hydrogen from sugar moieties or the addition of double bonds in nucleotides. Both pathways lead to the formation of radicals within nucleic acids, potentially initiating chain reactions that amplify damage either within the nucleic acid molecule itself or with neighboring molecules. Consequently, HO⁻ exhibits a versatile ability to damage nucleic acids, producing various damage patterns that can impair replication, transcription, and translation processes [86], [87].

When molecular oxygen is excited to its singlet state, the spin restriction that typically slows the rates of the reaction with non-radical molecules is removed. As a result, singlet oxygen possesses a low-energy empty valence orbital, making it a relatively powerful oxidizing agent compared to its ground-state triplet form. There are two main ways that singlet oxygen interacts with molecules: chemical reactions with biomolecules and scavengers, or physical interactions with quenchers. In the initial mechanism, a quenching molecule receives the excitation energy from singlet oxygen, which causes it to get excited and the oxygen to revert to its ground state. The excited quenching molecule can then undergo cleavage to form new products or react with biomolecules, causing potential damage. Singlet oxygen undergoes cycloaddition reactions with compounds containing conjugated double bonds, resulting in oxidized molecules that can further react to yield hydroperoxyl, hydroxyl, and carbonyl groups. Unsaturated lipids such as cholesterol and essential fatty acids can also react with singlet oxygen. These lipids are crucial for maintaining membrane integrity and producing various cytokines and hormones. Singlet oxygen interacts with the double bonds of unsaturated lipids, forming lipid peroxides, which can initiate free radical chain reactions and propagate oxidative damage across the membrane. This effect is particularly pronounced in mitochondrial membranes, potentially causing membrane rupture. Lipophilic PSs that preferentially undergo type II photodynamic reactions primarily produce singlet oxygen, effectively damaging the mitochondrial membrane and inducing apoptosis [88], [89], [90].

In type II photochemical reactions, oxygen enters the reaction directly at the first stage of the process. The excess energy of PS in the triplet state is transferred directly to molecular oxygen, thereby returning PS to its stable ground state and, above all, promoting the generation of singlet oxygen. Due to its high reactivity, singlet oxygen reacts with many biological substrates, causing cell death due to oxidative damage.

Type I and type II reactions can occur simultaneously. However, type II reactions predominate in antitumor PDT. Indeed, PDT-induced cytotoxicity is the result of oxidation phenomena involving the degradation of mitochondria (cholesterol, phospholipids), amino acids (histidine, tryptophan, methionine), and the lipids making up cell membranes [84].

II.4. PDT-induced molecular damage and cell death

Cell death is a fundamental mechanism promoted by certain biological events such as DNA damage and organelles' stress and dysregulation. The initiation and execution of cell death involve complex genetically encoded pathways that are extensively regulated and a slight change in these pathways such as mutations in any of its genes trigger malignancies. Thus, therapies, including PDT, have focused on triggering malignant cell death. PDT efficiently generates considerable quantities of ROS provoking the death of photosensitized cells. Excited photosensitizer (PS) molecules can transfer electrons or energy to the ground state of oxygen through type I or type II reactions producing either superoxide radicals (O²⁻) or singlet oxygen (¹O₂). Each of the ROS exhibits a specific chemical reactivity pattern towards the different biomolecules leading to distinct types of cellular damage.

In the context of PDT, achieving therapeutic success through targeting specificity has recently been enhanced by functionalizing PSs with specific targeting molecules, such as antibodies,

to recognize cells and improve the specificity of the therapy. However, ROS produced within the cell will damage all susceptible molecules within their diffusion radius. Excessive or prolonged oxidative stress can lead to significant detrimental effects, including inflammation, cell death, and tissue damage. The extent of these harmful effects depends on the site of ROS production, its rate, duration, and total yield. Moreover, the balance between apoptotic and necrotic cell death pathways induced by ROS injury is directly influenced by the level of oxidative stress and other factors, such as the localization of the PS. Consequently, ROS primarily react with biomolecules close to their production site, specifically in the PS accumulation region. The extent of damage distributed to each cellular structure largely depends on the PS accumulation site, the concentration of targets in that area, and the cell's capacity to repair oxidative damage.

PDT can induce apoptosis, necrosis, and autophagy, representing three distinct forms of cell death that frequently occur with PDT. However, other forms of cell death including ferroptosis, necroptosis and pyroptosis can also be triggered after PDT. Mainly, the cellular response to PDT is influenced by several factors, including the type of the cell, its metabolic and genetic characteristics, and experimental conditions such as the total irradiance applied, the specific types of PSs used, and their intracellular localization. The initial site of PDT-induced damage may influence the subsequent activation of specific cell death pathways. The extent of PDT-induced injury can modulate the cellular response, potentially initiating autophagy as an initial rescue mechanism. In this scenario, PDT-damaged cells may attempt to contain and eliminate damaged proteins through autophagic processes. However, when PDT-induced damage exceeds the repair capacity of the cells, apoptosis is triggered. At higher PDT doses, necrosis can also occur, as the proteins involved in autophagy and apoptosis may be rapidly degraded, leading to the disruption of cellular integrity. Additionally, PDT-induced closure of tumor vasculature may result in localized nutrient and oxygen deprivation, further contributing to secondary necrosis. Understanding the sequence of events critical to PDT-mediated apoptosis remains incomplete. Defining these processes will be crucial for optimizing PDT protocols and enhancing its efficacy as an anti-cancer therapeutic approach.

PDT can induce irreversible photodamage to various cellular organelles, including the mitochondrial outer membrane, ER, Golgi apparatus, and lysosomes. The specific site of damage is influenced by the subcellular distribution of the PS. Given that most PSs are localized outside the nucleus, DNA damage, mutations, and carcinogenesis typically occur indirectly during PDT. Generally, apoptosis arises from PS activation within mitochondria or the ER, leading to substantial oxidative stress. In contrast, necrosis is commonly associated with PS localization in the plasma membrane. Cell death is crucial for maintaining and regulating homeostasis in multicellular organisms. It serves as a primary mechanism for the immune system to eliminate cells that are infected with pathogens or harbor potentially carcinogenic mutations. The pathways responsible for initiating and executing cell death are complex, genetically encoded, and subject to extensive regulation. Mutations in genes that govern cell death are common and can lead to either the loss of tumor-suppressing proteins or the overexpression of proteins that drive uncontrolled cell proliferation, both of which are significant in cancer progression. Consequently, PDT aims to induce two principal cell death pathways, necrosis and apoptosis, representing their therapeutic targets [91], [92].

During PDT, lesions occur at the level of cellular organelles such as:

- **Ribosomes**

Ribosomes are large complexes composed of proteins and RNA, crucial for synthesizing all cellular proteins. They contain multiple oxidatively labile sites that can result in functional inactivation when damaged. Such impairment of ribosomes is lethal to the cell, as it disrupts

protein synthesis, including the translation of antioxidant defense and repair systems necessary for maintaining cellular redox balance [93].

- **Mitochondria**

Mitochondria are critical in apoptosis signaling cascades. Numerous PSs, especially cationic lipophiles, can selectively accumulate in mitochondria, leading to rapid permeabilization and destruction upon photoactivation. Elevated levels of lipid peroxides in the outer mitochondrial membrane can open membrane permeability pores, facilitating the release of caspase activators such as cytochrome c and apoptosis-inducing factor (AIF), which contribute to apoptotic cell death [94].

- **Lysosomes**

Lysosomes are organelles responsible for degrading damaged or unwanted intracellular and extracellular biomolecules. They maintain an acidic internal environment (pH 4.5-5) and contain over 50 enzymes that degrade various biological substrates. When PDT is targeted to lysosomes, it can cause membrane rupture, releasing the lysosomal contents into the cytoplasm. This release includes cathepsins, which can promote mitochondrial membrane permeabilization by cleaving BH3-only family proteins or directly activating caspases to initiate the intrinsic apoptosis pathway [95].

- **Endoplasmic reticulum**

The pathway that ultimately determines the cell's fate is governed by the level of oxidative stress to which the organelle has been exposed. Low to moderate ROS levels can activate survival pathways through autophagy induction and antioxidant production. Conversely, high levels of oxidative stress can increase ER membrane permeability, leading to the release of calcium ions and triggering intrinsic apoptosis mediated by mitochondria. Furthermore, ER stress induced by PDT has been linked to the activation of CCAAT-enhancer binding proteins (C/EBPs) and its homolog, CHOP, which is also inducible by DNA damage. The CHOP transcripts promote the expression of apoptosis-related genes that determine the cell's fate [96].

II.5. Characteristics and design of PSs

Special characteristics should be taken into consideration when designing an ideal photosensitizer [97]:

1. PSs must be chemically pure with known composition and good stability.
2. PSs should be able to accumulate in the tumor tissues.
3. PSs must have cytotoxicity only in the presence of light so that the likelihood of developing undesirable pharmacological side effects such as hypotension or allergic reactions is reduced.
4. PSs are supposed to have a high quantum yield of $^1\text{O}_2$, a high molar extinction coefficient, and high absorbance in red or far-red regions. The capability of the PS to absorb in such regions is of great importance as it is linked to the light's penetration into deep layers of tissues, making it effective for treatment. This way, the PS and light doses can be reduced while still achieving their intended effect. The absorbance of PS falling between 500 and 600 nm has a penetration of 4 mm and the absorbance between 600 nm and 800 nm has a penetration capacity of around 8 mm.
5. It's also important that the PS has a high clearance rate to reduce the side effects in the body.

6. PS synthesis should be almost uncomplicated, and the materials required for synthesis should be accessible to enable large-scale production.
7. PS should not aggregate in biological environments because this reduces their photochemical efficiency.
8. To possess short drug-to-light intervals (time between PS administration and light exposure), allowing for an effective treatment outcome.

The first PSs applied in PDT trials were HP and HpD. As mentioned earlier, HpD localization in tumors was detected by fluorescence, and its effect on cancer cells was validated to be successful after light exposure. The use of the porfimer sodium also called “Photofrin®” grabbed the first approval for its clinical use in PDT in 1994 in Canada for the treatment of bladder cancer. Nevertheless, porfimer sodium wasn’t characterized as an ideal PS since it contains many oligomers of HP making it chemically unpure, has weak absorption capacity in the red region, low selectivity, and is associated with side effects mainly skin phototoxicity. This recruited the development of a new generation of PSs with enhanced characteristics. Basically, different synthetic and natural PSs have been investigated *in vitro* and *in vivo* such as synthetic porphyrins, benzoporphyrins, chlorins, bacteriochlorophylls, naphthalocyanines, and natural hydroxiquinone including porphycenes and hypericins. Moreover, a pro-photosensitizing metabolite 5-aminolevulinic acid (ALA) was subjected to PDT studies [74], [98]. 5-aminolevulinic acid (ALA) is a natural metabolite acting as a precursor of endogenous porphyrin PS. The heme synthesis from glycine and succinyl CoA is controlled by negative feedback by the free heme to ALA synthase. To overcome this feedback, exogenous ALA can be administered allowing the assembly of the downstream targets. In this case, ferrochelatase, an enzyme catalyzing the addition of iron into protoporphyrin IX (PpIX) will become a rate-limiting enzyme and PpIX will be overproduced in tumor cells contributing to the photosensitization [74], [98]. The fact that PpIX has a rapid clearance from the tissues permits the administration of ALA as a treatment for early tumors. ALA esters also are less hydrophilic than ALA and are used as alternatives for their enhanced penetration and selectivity toward the tumor. These esters include ALA hexyl ester (HAL) and ALA methyl ester (MAL). Most of the PSs used nowadays for PDT are cyclic tetrapyrrolic structures including porphyrins and their derivatives, phthalocyanines, chlorins, bacteriochlorins [99].

II.5.1. PS absorbance spectra

As mentioned earlier, an ideal PS has a high quantum yield with a capacity of absorbance in high wavelengths especially in the red and far-red regions of the spectrum (650-850 nm), as this region provides a potent ability of light penetration into deep tissue layers. As illumination is a major and crucial step in PDT, well-investigating the optical characteristics of the PS is highly essential. Physiologically, innate chromophores such as melanin and hemoglobin present in blood can absorb light at wavelengths less than 650 nm restricting light penetration. On the other hand, wavelengths greater than 1,300 nm are absorbed by water molecules. Thus, the optimal light penetration wavelengths falling between 650 nm and 1,300 nm constitute the “therapeutic window” (**Figure 22**). However, light energy at wavelengths greater than 850 nm is insufficient to permit the generation of singlet and triplet oxygen species contributing to the need for the PS to absorb two photons instead of one photon of a short wavelength to yield the same outcome [97], [99].

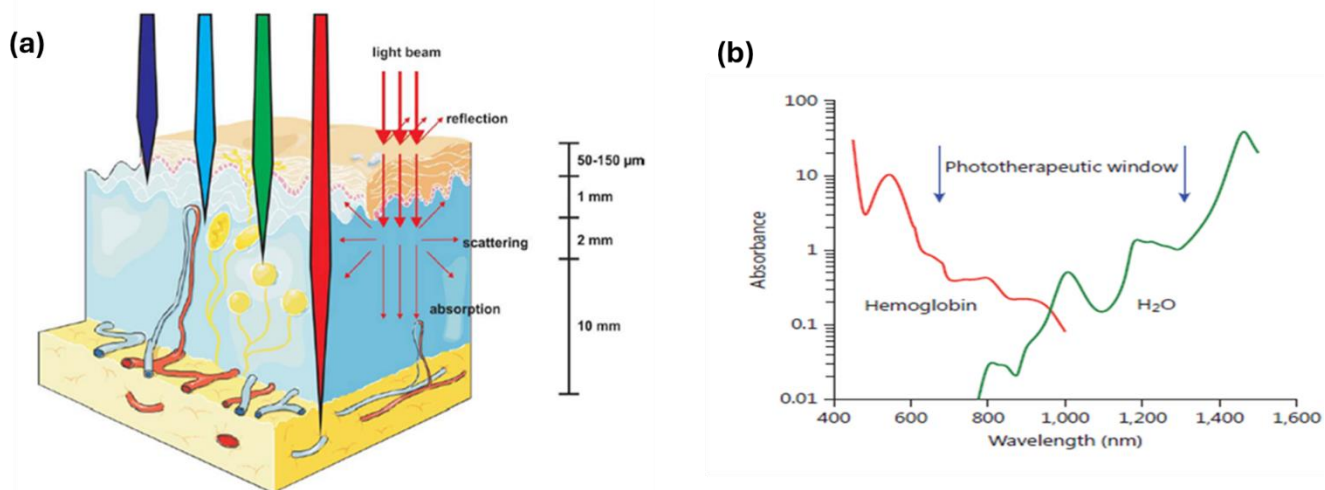


Figure 22: (a) The variation in the ability of light of different wavelengths to penetrate along the depth of the tissue and (b) the phototherapeutic window where tissue absorption and light scattering are insignificant [97], [99]

II.5.2. PS uptake and localization

To enhance the design of PS drugs, it is important to well investigate the general uptake of PS into the cells and their involved mechanisms. Among the established targets, mitochondria, lysosomes, plasma membrane, nuclei, and cytoskeletal localizations were revealed in studies of various PS and the vessels supplying the tumor. This was facilitated since most of the PS are auto-fluorescent allowing their detection by fluorescence microscopy. The fluorescence emission is not the same with all PS binding sites which will make it difficult to acquire precise information about the main sites affected by photodamage. Since the generated $^1\text{O}_2$ can travel only a very short distance of $0.02\ \mu\text{m}$ within the cell after its generation, this permits the detection of the initial PS localization within the cell before photo-activation after finding the sites of photodamage. This allows many scientists to focus on the affected cellular targets rather than the PS binding sites. For example, studies show that for the “photofrin” PS, the mitochondria were highly affected after photoactivation through mitochondrial changes, and ALA-yielding proto-porphyrin IX in the mitochondria induces apoptosis; whereas, PS that localizes in the plasma membrane usually triggers cell necrosis. Hydrophilic PS that form aggregates are likely to be internalized into the cells by pinocytosis or endocytosis mechanisms and be hosted in cell lysosomes and endosomes, then liberated with hydrolytic enzymes following the exposure to light illumination. Additionally, most of the PSs accumulate in the cell cytoplasm rather than the nucleus, so DNA mutations and oncogenesis are not associated with PS administration [71]. Most PSs are not site-specific and can localize in different subcellular compartments. Changes after PDT can be early detected through microscopic observations and biochemical alterations of the cell and organelles’ membranes. This involves lipid peroxidation, protein cross-linking, de-polarization, and inhibition of membrane-linked enzymes such as Ca^{2+} , Na^+ , K^+ and Mg^{2+} ATPases [98].

Charge, hydrophobicity, and the three-dimensional structures of the PS are the main factors influencing the mode of internalization and the localization of the PS into the cells. First, research demonstrated that negatively charged PS does not facilitate transport across plasma membranes. However, if a PS possesses at most two negative charges and exhibits high hydrophobicity, it compensates for this limitation, enabling it to pass through the plasma membrane and enter the cell. On the other hand, positively charged PS can easily diffuse through the plasma membrane due to the electrostatic attraction between these positive charges and the negative charges of the plasma membrane which offers a facilitated uptake and accumulation into the target cells. These positively charged PSs can also be found in the

mitochondria because of the negative charges on the mitochondrial membranes. Additionally, these positively charged PSs can interact with negatively charged protein subunits, which also contribute to their uptake into the target cells. Second, hydrophobicity strengthens the uptake, and the longer the alkyl side chains, the easier it is to internalize the PS. However, the length should not exceed a certain limit, as this could lead to an opposite outcome. The right length of the side chain can allow molecules to pass through deeper layers of lipid membranes and change their locations within the cells. For instance, positively charged metalloporphyrin with an additional 2 to 6 carbons in the aliphatic tails alters the cytosolic localization into mitochondrial localization. Third, the shape, bulkiness, and three-dimensional structure of the PS can also influence its uptake and localization. Isomers of the same compound can contribute to different outcomes because the alkyl chains are positioned differently. The orientations of the different chains interfere with the electrostatic attractions, disrupting the accessibility to the molecular charges.

The cellular distribution determines the PDT efficacy as the different targets regulate different signaling pathways. PS targeting the mitochondria triggers an apoptotic response rapidly through the disruption of the electron transport chain, mitochondrial membrane potential, and mitochondrial swelling representing mitochondrial damage. Concerning the PSs that localize in the biological membranes such as the cell plasma membrane allow the generation of high levels of singlet oxygen and lead to the peroxidation of the membrane, inhibition of the protein complexes, and disruption of the signaling pathways leading to cell death. The PSs with cytoskeletal targeting are also interestingly involved in cell death as these PS can act as microtubule inhibitors by binding to the tubulin and preventing its polymerization, which contributes to arresting the cells in the mitotic phase of the cell cycle [99].

II.5.3. Photobleaching of PS

As already explained, the singlet oxygen 1O_2 has a very short lifetime but a very high reactivity, so it is likely to react with cellular substrates located in its immediate environment triggering the production of ROS and thereby cell death. Similarly, oxygen molecules can react with PSs, causing their degradation. This phenomenon is known as photobleaching, and it consists of photo-degradation and photo-transformation mechanisms. Photo-degradation consists of the fragmentation of the PS structure that results in the formation of several photoproducts with little or no ability to absorb light. In the case of photo-transformation, the PS structure remains intact, but its ability to absorb light is modulated as its capacity of absorbance in certain spectral bands is reduced, the emitted fluorescence intensity is diminished, or by the formation of new absorption and emission bands. The formation of new bands has the benefit of inducing the formation of new photoproducts, which can themselves be used as PSs. Photobleaching is a fundamental problem in PDT since it deteriorates the accuracy of the concentration of delivered PS in the tumor zone [100], [101]. Photobleaching of PS occurs when it absorbs light and performs a cascade of photochemical reactions that contribute to its degradation. Consequently, the PS therapeutic efficiency will be reduced due to lower levels of ROS generation. The extent of photobleaching depends on the type of PS, the light dose, and the duration of exposure. Understanding photobleaching is crucial as it influences PS drug designs and treatment strategies that can be modulated accordingly to better control tumor growth and improve patient survival rates [71]

II.6. Photo-physics and light sources

The efficiency of PDT is highly dependent on the interaction between the PS and the light source through PS's ability to get excited into a higher and more stable excited triplet state. PS

must meet specific criteria such as strong absorbance and high quantum yield for generating ROS. Various light sources are used in PDT including lasers, light-emitting diodes (LED), and conventional lamps. Initially, conventional lamps were used to emit light in a broad spectrum of wavelengths making it difficult to target the tumor site and achieve optimal activation of the PS in these regions due to the lack of targeted or uniform light delivery. Conventional lamps also have several disadvantages including thermal effects, low light intensity, and unmanageable light doses. The combination of lasers and single-stranded optical fibers has added flexibility to PDT allowing light delivery into deep tumors either interstitially or endoscopically. Lasers are the most used in PDT due to their ability to generate high-energy monochromatic light specific to the absorbance wavelength of each PS. This allows the laser light to be focused, delivered through optical fibers, and directed to the target site using specially designed illuminator tips. Various laser types such as diode lasers are involved in clinical PDT worldwide, providing multichannel units for complicated procedures. LEDs also show a promising modality of light source as they have different shapes and sizes with the capability of generating high-energy light of a specific desired wavelength. Hence, the field of studying and evaluating the optimal PDT applications is referred to as “dosimetry”. It allows the determination of the optimal drug and light doses, drug-to-light intervals, and the associated side effects. Dosimetry ensures the desired homogeneity over the area of treatment requiring accurate dosimetry tools to realize the optimal conditions for a full PDT potential. Different techniques can be used to irradiate the tumor and subsequently activate the PS. They can be customized for special applications such as intraoperative PDT of brain tumors where the LED probe is designed with a cylindrical tip to fit inside a balloon catheter, interstitial PDT with a reduced invasiveness in which a small and flexible LED catheter can be percutaneously implanted into the tumor, and PDT of wide-surface lesions through a large LED array. PDT of superficial and thin tumors is the least difficult as they are accessible and present only at the surface of the mucosa, so they do not require deep light penetration. In this case, the light delivery occurs through a fiber coupled to a microlens on its tip to irradiate the tumor and its nearby tissues of 0.5-1 cm (**Figure 23 A**). To irradiate tumors exceeding 1 cm in thickness, laser fibers coupled to a light diffuser at its end are implanted in tumor tissues with the potential of accurate interstitial positioning using image guidance techniques such as CT, magnetic resonance imaging, or ultrasound. For large tumors, multiple fibers are positioned near each other to irradiate the whole tumor area (**Figure 23 B**). It is mostly used when a substantial tumor resection is required or when the patient is not a good candidate for surgery. Intraoperative PDT can occur if the patient administers the PS before the surgical resection of the tumor in several days which is specified based on the drug-light interval of the PS used in the treatment. Hence, the tumor will be removed surgically, and an intra-operative PDT will take place after the operation. Lights used through the operation procedure should be well-filtered to eliminate the wavelengths that can activate the PS before the end of the surgical tumor resection (**Figure 23 C**). Intracavity PDT is performed for tumors located in tubular body structures such as the esophagus, bronchus, and uterus using intracavity light diffuser systems [102].

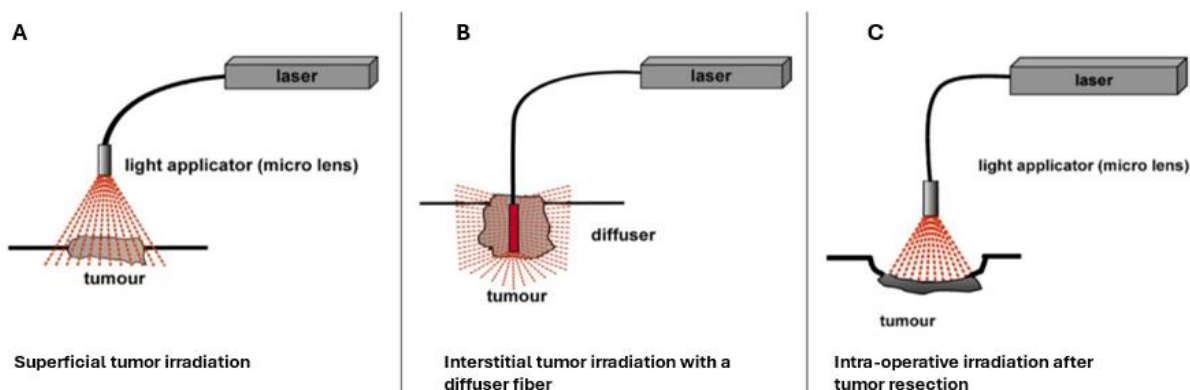


Figure 23: Different laser light irradiation approaches corresponding to the various tumor locations [102]

II.7. Principle structures of PSs

II.7.1. Non-tetrapyrrolic PSs

II.7.1.1. Hypericin

Hypericin (**Figure 24**) is biosynthesized from acetyl coenzyme A and malonyl coenzyme A in plants belonging to the *Hypericum* genus, particularly *Hypericum Perforatum*. It is characterized by a unique polycyclic structure consisting of three benzene rings joined to a central pyran ring and a phenanthrenequinone core. It contains a conjugated system of double bonds that gives it a deep red color contributing to its photodynamic properties. Also, hypericin is strongly lipophilic which limits its solubility and bioavailability in aqueous environments. Thus, it forms aggregations in biological fluids, which can affect its stability and distribution in the body. Environmental factors such as temperature, light, and pH can affect the stability and efficacy of hypericin.

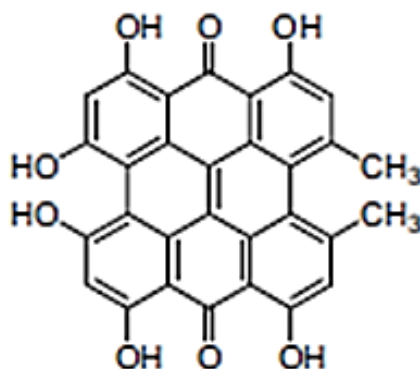


Figure 24: Chemical structure of hypericin [103]

It has also been reported to interact with biological macromolecules, including human serum albumin and low-density lipoprotein, which can influence its pharmacokinetics and pharmacodynamics [103]. Additionally, it can interact with cellular lipid membranes. Hypericin is reported for its ability to generate superoxide radicals and singlet oxygen after PDT with maximal absorption at 595nm (**Table 4**), as well as for its antiviral activity against a range of viruses [104], [105].

II.7.1.2. Curcumin

Curcumin (**Figure 25**) is a natural polyphenolic compound belonging to the curcuminoid family and consists of two methoxy groups and one hydroxyl group attached to two aromatic rings in addition to the presence of an active ketone functional group. The ketone, methoxy, and phenol groups contribute to its apoptotic and antioxidative properties. They are hydrophobic compounds which limit their solubility and bioavailability. They can interact with metallic and non-metallic compounds through hydrogen bonding to exert their biochemical reactions. Once they are activated by light with a maximal excitation wavelength of 547 nm (**Table 4**), they can induce ROS production leading to cell damage and death. It exerted photo-cytotoxic effects on different cancer cell lines including prostate, fibroblasts, and HeLa cells as well as in antimicrobial PDT. Its use as a treatment modality is considered non-invasive for cancer patients [106].

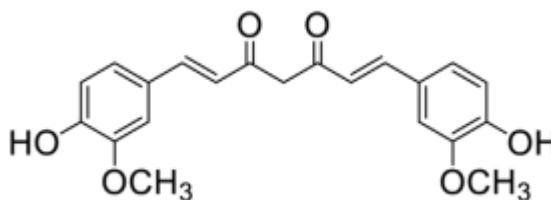


Figure 25: Chemical structure of curcumin [107]

II.7.1.3. Methylene blue

Methylene blue (**Figure 26**) is a tricyclic phenothiazine, positively charged PS. It is amphiphilic, a characteristic that offers methylene blue a lot of advantages such as its ability to be transported throughout the body and cross the plasma membrane of the cells. It also has a high extinction coefficient and absorption capacity in a wavelength range between 600 and 900 nm (**Table 4**). When excited, it undergoes a type II reaction predominantly and generates high levels of singlet oxygen. Pre-clinical studies of methylene blue for their effect on tumors were successfully performed on various cancer types such as squamous cell carcinoma and breast cancer and has been used in clinics for the treatment of Malaria, methemoglobinemia, poisoning from cyanide or carbon monoxide, and neurodegenerative diseases because it has a history of safe application on human. As it is protonated, it displays a preferable accumulation in the mitochondria of the cells as well as it can accumulate in lysosomes and interact with proteins, nucleic acids, and lipids after crossing the plasma membrane. Nevertheless, methylene blue is unstable as it can get easily degraded by enzymes which limits its use in healthcare modalities [108], [109].

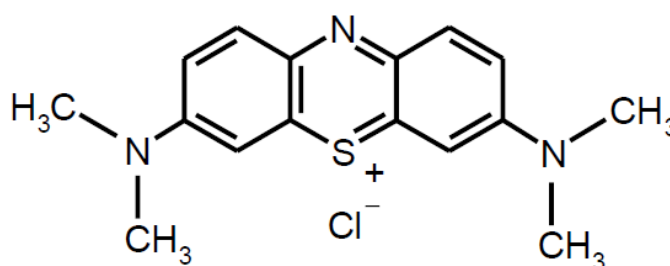


Figure 26: Chemical structure of methylene blue [110]

II.7.1.4. Rose bengal

Rose bengal (**Figure 27**) belongs to the xanthene class of dyes having a rose-to-red color. It has an absorption capacity in the range between 500 and 800 nm (**Table 4**). When excited by light it exerts anti-cancer and anti-microbial properties through the generation of singlet oxygen. However, its limitations are that it has reduced penetration capacity into tissues due to its low solubility which restricts its application to surface tumors and can stimulate photosensitivity reactions such as redness [111].

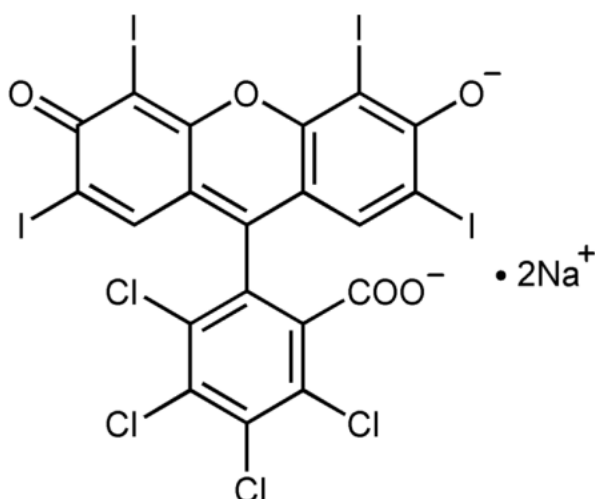


Figure 27: Chemical structure of rose bengal [112]

Table 4: Characteristics of hypericin, rose bengal, curcumin, and methylene blue [105], [113]

Photosensitizer	Charge	Excitation Maximum (nm)
Hypericin	Neutral	595
Rose bengal	Anionic	559
Curcumin	Neutral	547
Methylene blue	Cationic	632

II.7.1.5. Inorganic PS structures

Photocatalytic metal-based PSs include transition metal complexes, semiconductors, and metal-organic frameworks (MOFs). Generally, these structures well possess electronic characteristics that enable light absorption and energy transfer processes. For example, new organometallic systems containing transition metals such as ruthenium or iridium are designed with complexes that have the highest molar absorbance capacity in the visible spectral region and high stability in their lowest excited states, which contributes to their high efficiency in energy conversion. Other examples include semiconductor materials like titanium dioxide (TiO₂) and zinc oxide (ZnO), valued for their stability and ability to generate charge carriers when exposed to light. These inorganic structures have essential roles in the development and

stabilization of PSs in artificial photosynthesis and PDT. Additionally, the application of ruthenium bipyridyl complexes especially $[\text{Ru}(\text{bpy})_3]^{2+}$ where bpy is 2,2'-bipyridine, makes them one of the most studied inorganic PSs allowing for their unique photophysical properties. These complexes displayed high photoabsorption in the visible region and has a long-lived metal-to-ligand charge transfer excited state which improves the light absorption capacity and the catalysis of photoredox reactions [114], [115].

II.7.2. Tetrapyrrolic PSs

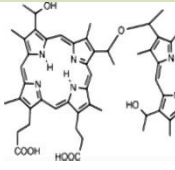
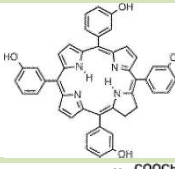
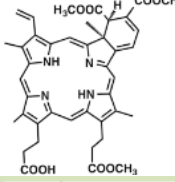
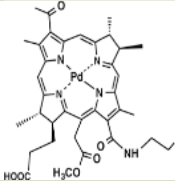
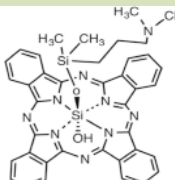
II.7.2.1. First generation PSs

The tetrapyrrolic class of PSs contains the largest number of compounds explored as PSs for PDT, approved and tested clinically. As mentioned earlier, the first tetrapyrrolic PS used in PDT was obtained from hemoglobin. The hematoporphyrin derivative later known by the trade names Photofrin® and Photogem® was approved in 1990 and remains today the most widely used PS in clinical PDT. Photofrin®, also known as porfimer sodium, has demonstrated effective photocytotoxicity in the treatment of many solid cancers, including skin, lung, esophageal, and bladder cancers. However, this PS was withdrawn from the market in 2012, as it has several drawbacks. Firstly, the compound is not pure and is composed of a complex mixture of porphyrins that is not well-defined and difficult to reproduce. It also has a low absorbance in the red, which limits its use to superficial tumors. In addition, its lack of selectivity for cancer cells, combined with low clearance, leads to cutaneous photosensitization in patients after treatment. To overcome the disadvantages of first-generation PS, and to come as close as possible to the characteristics of the ideal PS, new so-called second-generation PSs have been developed (**Table 5**) [116], [117].

II.7.2.2. Second generation PSs

The second-generation PSs have been developed through various chemical modifications to the structure of tetrapyrrolic compounds. Unlike first-generation PSs, these are pure compounds. The majority of these compounds are of synthetic origin, but they can also be synthesized from natural molecules. Second-generation PSs have an optimized light absorption spectrum in the red to enable treatment of larger or deeper tumors. In addition, these compounds have a high singlet oxygen quantum yield, enhancing the anti-cancer effect of PDT, and a much higher clearance than first-generation PSs. Consequently, the phototoxicity associated with the previous generation would become limited. In addition, these molecules are more rapidly eliminated from the body, limiting the period of cutaneous photosensitization. The four most explored structures are porphyrins, chlorins, bacteriochlorins, phthalocyanines and their derivatives. This includes compounds like Verteporfin, also known as Visudyne. Verteporfin is a benzoporphyrin derivative that was developed and undergone Phase III clinical trials for the treatment of cutaneous non-melanoma skin cancer and macular degeneration. Also, Foscan is another second-generation PS, a chlorin-derivative with a red-shifted and increased long wavelength absorption capacity permitting better tissue penetration and overall PDT efficacy and safety profiles (**Table 5**) [118], [119], [120].

Table 5: Examples of first and second-generation PSs, their characteristics and uses

Generation	Class	Name	Structure	λ max (nm)	Use	References
First	Porphyrin	Photofrin hematoporphyrin derivative (HpD)		630	Bladder and lung, Esophagus and brain cancers	[121], [122]
Second	Chlorin	Foscan m-tetrahydrophnylchlorin (mTHPC)		652	Head and neck cancers	[117], [123]
	Chlorin	Visudyne or verteporfin / Benzoporphyrin derivative (BPD)		690	Age-related macular degeneration	[117], [124]
	Bacteriochlorin	TOOKAD® (WST-11)		753	Prostate Cancer	[117], [125]
	Phthalocyanine (Pc)	Silicon phthalocyanine (Pc4)		675	Stomach, skin, breast cancers	[117], [126]

II.7.2.3. Third generation PSs

Third-generation PSs are still under development to improve the tumor selectivity of second-generation PSs, these new PSs have undergone chemical modifications by substituting them with chemical motifs that can be specifically recognized by tumor cells. This relies on the covalent conjugation of PS to various targeting ligands (macromolecules or small molecules) that exhibit specific molecular recognition ability with a cognate receptor that is overexpressed on the tumor or other cells of interest. These motifs are generally biomolecules: steroids, sugar, amines, vitamins, or antibodies. Tumor cells have specific antigens on their surface that are not found in healthy cells, making it possible to use antibodies directed against these specific antigens as vectors to increase PS targeting efficiency. In addition to conjugated PS, the third generation includes vectorized and encapsulated PSs. The use of nanotechnology in PDT can be divided into two different approaches. When the nanoparticle (NP) is itself the PS, such as gold and silver NPs, the NP can absorb light improving the efficacy of PDT. Also, the NP can serve as a delivery system of PS which is the active element, to improve solubility and ensure better targeting of tumor sites. This includes dendrimers, liposomes, and mesoporous silica NPs (**Figure 28**) (**Table 6**) [127], [128], [129].



Figure 28: Third generation formulated through (a) chemical modification by linking the second-generation PS to a targeting moiety and (b) vectorization of PS through encapsulation in carriers [130]

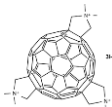
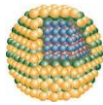
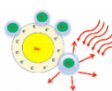
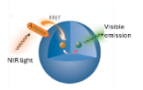
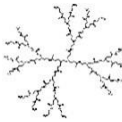

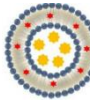
Table 6: Examples of targeted PSs of the third generation, their characteristics, and applications

Class	Ligand	PS	Target	Application	References
Monoclonal Antibodies	Herceptin (Trastuzumab)	Porphyrin	HER2	Breast Cancer	[131]
Lipoproteins	Low-Density Lipoprotein (LDL)	Chlorin e6 (Ce6)	LDL Receptors	Cancer	[132]
Serum Proteins	Human Serum Albumin (HSA)	Chlorin e6 (Ce6)	HSA Receptors	Cancer	[133]
Peptides	RGD peptide (Arg-Gly-Asp)	Phthalocyanine	Integrin Receptors	Breast Cancer	[134]
Carbohydrates	Mannose	Meso-tetraphenylporphyrin	Mannose Receptors	Cancer	[135]
Steroids	Estradiol	Pheophorbide a	Steroid Receptors	Breast Cancer	[136]
Vitamins	Folic Acid	Chlorin e6 (Ce6)	Folate Receptors	Cancer	[137]

Most PSs used in clinical or preclinical development are hydrophobic and tend to aggregate in an aqueous environment, whereas their monomeric state is necessary to maintain their photophysical, chemical, and biological properties for effective PDT. In addition, the inadequate affinity of most PSs for tumor sites also results in damage to healthy tissue after PDT. To circumvent these problems, it is necessary to develop delivery systems for PS to ensure more selective delivery to tumor sites. In the ongoing quest to improve the efficacy and safety of PDT, NPs with high loading capacity and flexibility to accommodate PSs with varying physico-chemical properties have been introduced. Designing an effective delivery system for PS requires knowledge of the physicochemistry of the PS, its specific therapeutic application,

and the characteristics of the delivery system's interaction with biological structures. The integration of PS into its delivery system requires consideration of several highly important properties besides its charge, this includes its stability, solubility, size and molecular weight. Indeed, the vectorization of PSs generally leads to changes in its biodistribution which usually reinforces the passive and active EPR effect. One or other of these mechanisms aims to increase the concentration of the PS at the desired site of action and reduce its toxicity. PS vectorization could then be one of the solutions for improving efficacy and circumventing the resistance and limitation phenomena of PDT (**Table 7**) [138], [139].

Table 7: Examples of nano-vectorized PSs of the third generation, their characteristics, and applications

Class	PS	Structure	Objective	Application	Reference
Functionalized Fullerenes	BB6		Photostability	Antimicrobial	[140]
Quantum Dots	Tetraphenyl porphyrin quantum dots		Solubilize the PS	Anti-cancer Anti-microbial	[141], [142]
Gold or Silver NPs	Conventional PS		Plasmonic Enhancement	Anti-cancer	[143], [144]
Upconversion NPs	Hypocrelline A		Excitation near infrared and emission in blue	Anti-cancer	[145], [146]
Dendrimers	PAMAM-zinc Phthalocyanine (ZnPc)		Prevention of aggregation	Anti-cancer and atherosclerosis	[147], [148]
Mesoporous Silica NPs	PEI-PEG-MSN/ ZnPc		Solubilization and Protection	Anti-cancer	[149]
Liposomes	Foslip® (meta-tetra(hydroxyphenyl) chlorin) (m THPC), Fospeg® (Foslip polyethylene glycolyl)		Solubilize and protect PS, reduce the secondary side effects	Anti-cancer	[150], [151]

To further improve the properties and performance of PSs, a new generation, referred to as the fourth generation PSs, has emerged few years ago. These PSs involve the employment of mesoporous silica and MOFs which are identified as porous carriers. Such carriers can hold more than one PS molecule and are designed to enable a spatiotemporal release of the PSs. An example of this generation is the porous Au@Rh (gold@rhodium) nanostructures holding ICG PSs within their pores and allowing their controlled release through their diffusion out of the pores in response to specific stimuli such as changes in the tumor microenvironment. Also, these nanostructures hold cell membrane coating on their surface which facilitate their homologous binding and selective accumulation at the tumor site. Additionally, the catalytic properties of their structure allow the decomposition of endogeneous H₂O₂ to O₂, which

alleviates tumor hypoxia. Both the third and fourth generation of PSs are classified as advanced pharmaceutical formulations due to their promising potential in PDT. However, fourth generation PSs are still under development and require further research [152], [153].

II.8. Pharmacokinetics of PS

As previously demonstrated, PDT includes the injection of a PS either systematically or topically, and then the targeted tissue is exposed to the light wavelength corresponding to the PS absorption spectrum. Once a PS is in the bloodstream, a set of reactions occurs, the timing of which depends on the PS's composition. The PS must be equivalent to the components of the blood depending on the solvent or vehicle used for the injections. The PS may undergo degradation, release from its delivery vehicle, or interact with various serum proteins and cells present in the blood during this process.

Systemic PSs have the ability to bind to blood vessel walls. It is postulated that tumor vasculature and those of the surrounding normal tissue are morphologically and physiologically different, which may influence the localization and accumulation of PSs. Once adhered to the blood vessels, PSs penetrate the vessel walls at rates determined by their binding affinity to the endothelial lining. Thus, PSs with stronger binding exhibit slower diffusion rates across the vessel wall, whereas those with fragile binding diffuse across the vessel wall more rapidly. After crossing the blood vessels, the PS is released to enter the parenchyma in the target organ/tumor. If the organ is the liver or another metabolically active organ, the PS might be subjected to chemical transformations under catalysis of metabolic enzymes. However, this is uncommon for most of the tetrapyrrole-based PSs, including porphyrins, chlorins, and phthalocyanines which are the PSs widely applied in clinical practice. It has been revealed that the localization of the PS in the intracellular space depends on its characteristics such as its hydrophobic or hydrophilic tendency and the charge and asymmetry of its structure. Certain PSs, either charged or possessing a polar region, are too hydrophilic to cross biological membranes, leading to their internalization through endocytosis. On the other hand, some PSs are mostly hydrophobic, with few or no polar groups, allowing them to freely diffuse through the plasma and into other cellular organelles. The PSs are eventually cleared from the tissue, though the exact mechanism remains unclear. It can be assumed that if the PS accumulates in a tumor or a non-metabolic organ, it is returned to the circulation through the lymphatic system. Finally, the PS is eliminated from the body. In most clinically used PSs, the process begins with metabolism by hepatic cells which is transported into the bile, passes through the intestines, and is ultimately excreted through the feces [117], [154].

It is crucial to differentiate between selective accumulation and retention of PS in tumors. PS with faster pharmacokinetics mostly localize in tumors due to selective accumulation, whereas those with slower pharmacokinetics localize commonly due to selective retention. The selective accumulation model suggests that the increased vascular permeability, which is prominent with tumor neovascularization, allows for the preferential extravasation of PS. These rapidly acting PS often bind to albumin with a relative size that enables passage through the "pores" of the tumor endothelium. In contrast, in the selective retention model, the PSs are retained in tumors while being eliminated from surrounding healthy tissues and organs. Tumor selectivity and retention of PSs are promoted by two key features of tumor tissues. Firstly, tumor cells overexpress low-density lipoprotein (LDL) receptors due to the increased cholesterol catabolism in proliferating tissues, leading to higher LDL receptor expression. The hydrophobicity of LDL molecules enables their role as effective carriers of hydrophobic molecules to deliver the cholesterol molecules that are crucial for membrane formation during cell division. Hence, LDL can transport hydrophobic PS to neoplastic tissues. Secondly, the acidic pH in the tumor microenvironment enhances the retention of PS. As the tumor develops and its periphery extensively receives oxygen molecules, an intra-tumoral hypoxic condition

arises. This acidic environment can change the physico-chemical properties of PS, particularly their charge, making it easier for them to enter cancer cells. For example, protonation of the carboxylic acid groups in hematoporphyrin increases its lipophilicity, enabling its entry into tumor cells via simple diffusion through the plasma membrane. Moreover, the PS distribution between albumin and LDL is pH dependent. Studies have shown that the acidic tumor environment favors the binding of PS to LDL enhancing the selectivity and accumulation of PS in tumors [155], [156].

II.9. Passive tumoral targeting

Passive targeting of the tumor occurs due to the EPR effect. The latter phenomenon occurs when the endothelial cells' junctions lining the blood vessels become highly permeable due to the pathology of a disease. Especially, upon the existence of a tumor, the lymphatic drainage becomes poor allowing macromolecules and NPs used in therapies to accumulate in the interstitial space following their passive diffusion into the tumor areas. These molecules consist of poly (styrene-co-maleic acid anhydride) conjugated to peptides and proteins, as well as hydroxypropyl methacrylate-based macromolecular drugs. The EPR effect augments the accumulation of drugs in tumors due to their extended circulation time in blood and the ligand-mediated target of drugs in regions with reduced blood supply, through passive diffusion, improving the drug efficacy and delivery to the target areas. Additionally, the tumor can secrete vascular permeability factors that increase the vascular permeability facilitating the tumor development. Hence, in this case, a key element is to inhibit tumoral angiogenesis by inhibiting VEGF, a factor responsible for the vascularization, limiting the tumoral supply of nutrients and others [157]. On the other hand, to enhance the EPR effect, some drugs including nitric acid oxide releasing agents (nitroglycerin), ACE inhibitors, and angiotensin II-induced hypertension allow the drug transport to elevate by 2 to 3 folds, thereby boosting the overall therapeutic efficacy. Other vascular mediators such as heme-oxygenase-1, carbon monoxide, TGF- β inhibitors, and TNF- α can also favor better efficiency of therapies. Indeed, the physiological factors enhancing the tumoral EPR effect endogenously include abnormalities and dysfunctions in the tumor vasculature, the presence of large pore sizes, and the absence of smooth-muscle layers which is responsible for the regulation of the blood volume in response to the blood pressure. Additionally, there are some methods used in clinics such as using polymeric drugs with extended retention and plasma half-life permitting a less-frequent administration. Innovative drugs, such as SMANCS-Lipiodol, have also been developed, enabling the delivery of macromolecular drugs under a hypertensive state of the patient, which results in improved accumulation within the solid tumors [158].

II.10. Current applications of PSs

As previously mentioned, PDT has been employed in the treatment of various diseases and cancer types. Just like any other drug, PSs must successfully navigate phases I, II, and III of clinical trials and receive approval prior to their official application and use in therapies. Clinical phase trials are currently underway for various PSs, while others have received approval for cancer treatment (**Table 8**).

Table 8: PSs under clinical phase trials and approved for the treatment of different cancer types and diseases [159], [160]

PS	λ Absorption Range	Approval Status	Applications
Indocyanine green (ICG)	Near-infrared (>800 nm)	FDA approved for diagnostic in ophthalmology, hepatology, cardiology, and fluorescence-tracked cancer surgery	Chronic periodontitis and topical melanoma PDT
Methylene blue	600-665 nm	Approved in Canada for nasal decolonization of <i>Staphylococcus aureus</i> , and periodontal diseases	Antimicrobial potential against filamentous fungi and yeasts, dental caries, basal cell carcinoma
5-Aminolevulinic acid (ALA)	410-630 nm	FDA approved for dermatological conditions	Hypertrophic actinic keratoses on the face and scalp, vulvar lichen sclerosis, glioblastoma
Methyl-aminoleuvinat (MAL)	630 nm	FDA approved for dermatological conditions	Actinic keratoses, basal cell carcinoma, Bowen disease, viral warts
Hervix/Cysview	380-450 nm	EU and FDA approved for intravesical administration and diagnosis of bladder cancer	Bladder cancer, prostate cancer, colon cancer
Meta-tetrahydroxy-phenylchlorin (m-THPC)	652 nm	Approved in EU for advanced head and neck cancer as a palliative treatment	Pancreatic cancer, biliary cancer, breast cancer metastases
Verteporfin	689 nm	Approved in Japan for macular	Choroidal hemangioma, gastric cancer

		degeneration related to age	
Talaporphin sodium	664 nm	Approved in Japan for early endobronchial carcinoma	Esophageal cancer, gastric cancer, bile duct carcinoma
Lutetium texaphyrin	732 nm	Phase I trial	Skin metastases, breast cancer, prostate cancer
Porfimer sodium	630 nm	Phase I / II / III	Palliative advanced rectal cancer and advanced CRC
Npe6	664 nm	Phase I	Different malignant tumors

II.11. PDT of CRC

Among the challenges of conventional chemotherapy for CRC, the lack of specificity in targeting the cancer cells is prominent and recruits the intervention of selective treatment approaches that maintain the patient's healthy tissues. The application of PDT in the treatment of CRC is quite promising and minimally invasive, especially for early-stage tumors and is also considered as a palliative option for advanced stages of cancer. PDT for CRC aids in overcoming the challenge of multi-drug resistance and stimulates the immune system. By inducing tumor cell damage, PDT exposes tumor-associated antigens, which activate immune cells to perform their anti-tumor function and promote cancer cell death. Many preclinical and clinical studies have been conducted on PDT for CRC, as well as the effects of combining PDT with other treatments such as radiotherapy and surgery. Given CRC's resistance to conventional therapies, PDT may be an innovative and promising treatment. Moreover, as CRC is a well-localized solid tumor, it represents a good candidate in terms of accessibility for PDT treatment as it can be performed relatively simply by colonoscopy. Recently, PDT using PSs such as porphyrin or chlorin derivatives has received increasing attention in the treatment of CRC. PDT's chemical mechanism entails the simultaneous interaction of molecular oxygen, the PS, and a suitable wavelength of light source. When PS absorbs visible light during PDT, it converts that energy into the surrounding molecular oxygen which causes several ROS to be produced. According to early studies carried out in the 1980s and 1990s, PDT produced positive response rates and recovery in CRC patients. Indeed, the first clinical use of PDT for CRC was in 1986 when Mexican surgeon Lemuel Herrera-Ornelas used Photofrin HpD (hematoporphyrin derivative-HPD) illuminated with a 630 nm wavelength on 14 CRC patients. This study was elaborated by analyzing biopsies derived from the CRC patients and showed a significant eradication of cancer cells [127]. The study went on to prove the efficacy of PDT against CRC, especially in reducing side effects compared with conventional treatments. After the success of this first CRC study, numerous clinical trials have been carried out with the aim of demonstrating the efficacy of PDT in CRC treatment. A study by Gavrina et al. explored the efficacy of PDT using chlorin (Ce6) conjugated to polyvinyl alcohol (PVA) NPs in mouse models xenografted with the murine CRC line CT26. Using *in vivo* fluorescence imaging, Ce6-

PVA NPs were found to have a higher accumulation in the tumor and greater photobleaching compared to the use of Ce6 alone. On histological examination, CT26 tumors showed faster regression with much more advanced necrosis after PDT with the Ce6-PVA NPs complex compared with PDT-Ce6 alone. This study revealed that vectorization of Ce6 into PVA is an effective approach to improve PDT's photoactivity efficacy and selectivity for the treatment of colorectal cancer [161]. Another study carried out in our laboratory by Bretin et al. demonstrated the efficiency of vectorizing third-generation PS in NPs for tumor targeting by PDT in CRC. This study is based on the use of 5-(4-hydroxyphenyl)-10,15,20-triphenylporphyrin (TPPOH) attached to xylan (X)-coated silica nanoparticles (SNPs). The results showed greater phototoxicity with TPPOH-X SNPs-PDT than with free TPPOH-PDT *in vitro* on HT-29, HCT116 and SW620 human CRC cell lines and *in vivo* on xenograft mouse models [162].

More recently, a study by Simelane et al. successfully demonstrated the creation of a bioactive nanoconjugate delivery system, ZnPcS₄-AuNP-S-PEG5000-NH₂-Anti-GCC mAb (BNC), based on PEGylated AuNPs. These systems were functionalized with metallized ZnPcS₄ PDT fluorescent PS, and anti-GCC mAbs specific for PDT treatment. In addition, they were functionalized with specific mAbs targeting GCC to overcome the challenges of PDD and PDT of CRC *in vitro*. The final BNC was photostable with selectively enhanced subcellular accumulation in the targeted CRC compared to healthy cells *in vitro* for successful PDD. Furthermore, final-PDT BNC exhibited significantly higher cell death rates (34%), compared to PS-PDT treatment alone (15%). The above results suggest that the improved PDD and PDT outcomes are due to the specific accumulation of nano-vectorized PS in CRC cells cultured *in vitro* with enhanced targeting of bioactive anti-GCC. Consequently, this final synthesized BNC platform could enhance PDT against CRC due to its targeting capabilities and serve as a simultaneous early diagnostic measure in further studies [163].

At present, preclinical research is being carried out to improve the anticancer performance of existing PS through better tumor targeting which paves the way for the creation of new and more effective PS and optimizes light illumination in terms of power, time, or illumination systems. Unlike chemotherapy or other conventional treatments, the promising results of previous clinical trials, whether for early-stage tumors or palliative treatment of high-stage lesions without involving serious side effects allowed PDT to remain a great aspiration for many patients. Different PSs have been investigated through *in vitro* culturing of human colorectal tumor cells as *in vitro* studies are the first preliminary step in building the base for further complex studies and investigations of PDT whether on animal models or clinically on patients. The evaluation of various parameters such as the selection of PS, light wavelength, ideal concentration, and drug-light time intervals offers profound and reliable insights. Such research allows the detection of the mode of action of the PS and the PDT-induced cell death mechanisms such as apoptosis, necrosis, and autophagy as well as monitoring ROS production in these cells. Aside from the studies performed on the cell monolayers, it is important to consider the investigations on more complex structures such as 3D tumor models that are closer to the real tumors and to determine the cellular interactions and the extracellular matrix components as compared to the monolayer cultures. Among the *in vitro* preclinical studies performed on CRC we can mention porfimer sodium (2.5-10 µg/mL) on HT-29, temoporfin (0.125-1 µg/mL) on Colo 201, phthalocyanine Pc 4 (0-300 nM) on HCT116, and 5-ALA (3 mM) on SW-620. Animal studies are also fundamental requirements before initiating clinical trials. It's crucial to perform such studies on nude animals to eliminate the possibility of an immune attack on the tumor cells. Many human CRC cell lines are grown as xenograft tumors subcutaneously in nude mice exposed to PDT. Thus, phthalocyanine Pc4 (1 mg/kg) was administered intravenously into female nude mice xenografted with SW-480 tumor CRC cells, and porfimer sodium or liposomal pheophorbide (30 mg/kg) with intraperitoneal

administration to male athymic nude mice with HT-29 tumor cells xenografts. Clinical procedures performing PDT of CRC rely on light exposure through an endoscope using optical fibers that target tumor tissue while sparing the normal cells. The majority of clinical trials investigating PDT of CRC are at the pilot, phase I, and phase II stages. Phase I trials typically involve a small number of terminal patients and focus primarily on safety and toxicity. Phase II trials expand on these studies with a larger patient group. Limited data from phase III trials are available, and no phase IV trials have been conducted, as PDT is not yet authorized for CRC management. Nevertheless, current trials demonstrate that PDT is an effective treatment option for CRC. Various PSs are clinically used in CRC treatment including photofrin, 5-ALA, and temoporfin. These PSs can be photoactivated through light sources that can be through endoscopic laser and/or interstitial laser [160].

Even though PDT is considered a promising targeted approach in the treatment of CRC, it is associated with drawbacks limiting its efficacy. This includes the poor solubility of the PS, low selective uptake, tumor hypoxia, and cancer stem cell resistance to PDT. Nevertheless, the PS hydrophobicity was managed, as previously mentioned, by the development of third-generation PSs involved in the treatment of CRC. The latest studies demonstrated the effectiveness of PDT against CRC using various PSs and delivery systems through focusing on the design of PSs with enhanced solubility and capacity to absorb in red and infrared light regions with enhanced tissue penetration. This includes chitosan nanoparticles (CS NPs), lipid NPs, PheoA-ss-GC NPs, functionalized polyacrylamides (AFPAA) and chlorin-core star-shaped blocked copolymer which showed selectivity and efficacy towards CRC models *in vitro* and *in vivo* [68]. All these studies hold promising potential and advancements in the future of PDT in CRC.

II.12. Combination therapies with PDT in the treatment of CRC

PDT can be combined with different therapeutic approaches to enhance its efficiency. Combining PDT with immunotherapy including immune checkpoint inhibitors enhances the anti-cancer immunity. Interestingly, NPs are being designed to encapsulate both a PS and an immune checkpoint inhibitor within the same nanocarrier. For example, a study by Xu et al. involved up conversion NPs chlorin e6-imiquimod (UCNP-Ce6-R837) which incorporate R837, a Toll-like receptor 7 agonist, enhancing the anti-tumor immunity with chlorin e6 PS [164]. Another study by He et al. was based on the synthesis of nanoscale coordination polymer (NCP) core-shell nanoparticles (NCP@pyrolipid) where the PS is pyrolipid and is positioned in the shell which harbors oxaliplatin in its core. Combining PDT, oxaliplatin chemotherapy, and the checkpoint blocking therapy anti-PDL1 enhanced CRC antitumor immunity and therapeutic efficacy even with metastatic CRC. Additional combinations of chemotherapeutic drugs with PSs such as brigatinib with Ce6 PS and cetuximab-conjugated Ag₂S quantum dots integrate chemotherapy and PDT to target CRC. PDT can also be combined to photothermal therapy (PTT) for the treatment of CRC in which the effects of generated ROS can be enhanced with hyperthermia. For instance, gold nanorod@SiO₂ NPs and SN-38-encapsulated photonic micelles showed to significantly improve the antitumor efficacy [160], [165].

Chemotherapeutic anti-cancer drugs such as doxorubicin, belonging to anthracycline group, showed an ability to control the tumor growth in mice models. Cisplatin augments the PDT anti-tumor potential and methotrexate, an anti-metabolite, stimulate the synthesis of protoporphyrin IX contributing to a better *in vitro* cytotoxicity of PDT with ALA. Other drugs such as vincristine, 5-azadeoxycytidine and bortezomib which are inhibitors of microtubules, DNA methyltransferases and proteasomes, respectively, caused a better effectiveness in the anti-tumor potential of PDT. Other combination therapies include combining radiotherapy with PDT which showed a two-way enhancement strategy. PDT confers the sensitization of cells to

radiotherapy, and in turn, radiotherapy synergizes with PDT to augment its anticancer efficacy. COX-2 inhibitors which modulate the arachidonic acid cascade and suppress the cell survival also enhance PDT. Additionally, various agents involved in increasing the accumulation of PS in cancer cells such as vitamin D, imatinib, lipid-lowering and salicylate drugs can also be considered. Vitamin D and imatinib usually elevate the accumulation of ALA-induced protoporphyrin IX and the second-generation PSs, respectively. Lovastatin enhances the *in vitro* LDL binding and the internalization of porfimer sodium into cancer cell and salicylate drugs exert similar impact on the uptake of PSs by tumor cells. Another strategy used for a better PDT efficacy is increasing the levels of oxygen within the tumor. This can be achieved through the administration of hyperbaric oxygen and erythropoietin (EPO) which improves chemotherapy induced anemia and hyperthermia. Hyperthermia positively influences the membrane permeability of cells through enhancing the PS uptake, improving the blood flow to the tumor microenvironment, and elevating the oxygen concentration. Moreover, targeting key mechanisms involved in cell protection and survival can enhance PDT outcomes. Inhibiting the SOD enzyme by 2-methoxyestradiol and blocking heme degradation pathways with specific inhibitors or siRNAs that disrupt iron chelation are effective strategies. Buthionine sulfoximine reduces cellular GSH levels, while certain vitamin E derivatives promote the production of ROS leading to a boosted PDT efficacy. Also, agents that promote cell apoptosis, such as Bcl-2 antagonist, and those that affect cell cycle progression, like ceramide analogs, can enhance the effect of PDT. Rapamycin, an mTOR inhibitor, and ursodeoxycholic acid, which sensitizes mitochondrial membranes in tumor cells are also involved in improved PDT results. Finally, combining two PSs, 5-ALA and low-dose porfimer sodium, showed PDT-induced cytotoxicity *in vitro* with reduced skin photosensitivity [97].

Using anti-angiogenic agents such as anti-VEGF or anti-VEGFR, TNP-470, and matrix metalloprotease inhibitors as well as elevating IL-12 expression by adenoviruses are all beneficial for PDT. Hypoxia or low oxygen supply is usually associated with PDT, which triggers the expression of many angiogenic growth factors such as hypoxia-induced factor (HIF)-1 α , cyclooxygenase (COX-2), basic fibroblast growth factor, VEGF, prostaglandin (PG) E₂, and matrix metalloproteinase. The link between PDT and elevated HIF-1 α and VEGF expression levels was first reported by the study of Ferrario et al. with photofrin PS-mediated PDT in tumors of mammary carcinomas. This contributed to the development of the approach of combining anti-angiogenic agents with PDT which resulted in a decrease in the VEGF expression levels as demonstrated by the study of Zhou et al., highlighting a better anti-tumoral outcome as compared to PDT alone. Also, the receptor tyrosine kinase inhibitors (TKI) with its anti-angiogenic potentials enhanced the efficacy of PDT. Additionally, combining COX-2 inhibitors with PDT highly diminished the production of PGE₂ and VEGF that is stimulated by PDT [166]. For PDT/PTT tumor targeting therapy, Wang et al. created polydopamine NPs coated with hyaluronic acid and conjugated Ce6. The compound's combined actions showed enhanced accumulation inside tumors, greater suppression of tumor development, and enhanced phototoxic impact in mice harboring HCT116 tumors [167]. Yang et al. generated sub-100 photonic micelles encapsulated in SN-38 for efficient trimodal (photothermal, chemotherapy, and PDT) cancer treatments, showing a noticeably higher *in vivo* anticancer effectiveness compared to a single treatment in mice with an HT-29 colon in the nude xenograft for cancer [168].

PDT can be associated with acute inflammation primarily due to the phototoxic damage of tumor cells activating various immune cells at the tumor site. In contrast to radiotherapy and chemotherapy which may not induce systemic immunity, the PDT induced immune cell activation is beneficial because it generates a robust immune response targeting residual tumor cells. Various immunotherapy agents were evaluated in combination with PDT to further potentiate this immune response. This includes non-specific immunotherapy agents such as

the *Corynebacterium parvum* vaccine, *glucan Schizophyllan*, and *Bacillus Calmette-Guérin*, as well as specific immune agents like granulocyte-macrophage colony-stimulating factor, TNF- α and IL-7. The observed synergistic effect of this combination is due to the enhanced recruitment of the activated macrophages to the treatment area which can amplify the immune response against the tumor site. Not only does this approach enhance the overall PDT effectiveness but also it reduces the therapy associated side effects including the collateral damage in surrounding healthy tissues formed due to the induced inflammatory response. Eventually, combining immunotherapy with PDT enhances tumor destruction and improves the patient's prognosis while potentially mitigating the risk of tumor recurrence [166].

III.1. Apoptosis or programmed cell death

Apoptosis is one of the most extensively studied and well-characterized forms of cell death, often referred to as programmed cell death. Apoptosis was first discovered in the 1970s and was thought to occur in conjunction with mitosis. Many years later, the definition of apoptosis was established as the ATP-dependent, genetically programmed and enzyme-mediated death of unwanted or harmful cells. Apoptosis occurs when the cytoskeleton and DNA degrade by proteases and endonucleases, respectively, through various homeostatic or pathological routes. However, when the process is uncontrolled, apoptosis does not happen in the appropriate order or at the right rate. During development, apoptosis, in conjunction with cell proliferation, shapes tissues and organs. For example, the apoptosis of cells between the toes facilitates their separation [169]. In the immune system, apoptosis selectively eliminates self-reactive or ineffective T-cells which are responsible for destroying damaged or infected cells in the body. At the molecular level, apoptosis plays a crucial role in various biological functions and its dysregulation is associated with numerous diseases including cancer. The evasion of apoptosis is considered a hallmark of cancer. In normal cells, growth and proliferation are tightly regulated by a balance of growth-promoting and growth-inhibitory mechanisms. However, cancer cells often harbor mutations that bypass antiproliferative signals promoting uncontrolled growth. Under stress, normal cells undergo apoptosis, but cancer cells lack this mechanism which leads to their uncontrolled proliferation and tumor growth [170].

Apoptosis is a key mechanism by which chemotherapeutic agents kill cancer cells and mutations in the apoptotic pathways often lead to resistance to such treatments. It is mediated by caspases which are enzymes that regulate the downstream intrinsic and extrinsic signaling pathways. Numerous studies, conducted over the last several decades, have shed light on the function of apoptosis in the regulation of cell death and its implications in several diseases. It involves the systematic fragmentation of cells into apoptotic bodies, which are then efficiently phagocytosed and removed by immune cells, thereby preserving the integrity of surrounding tissues. The apoptotic process is primarily mediated by cysteine-aspartic proteases known as caspases. It is characterized by distinct morphological changes and typically does not provoke an inflammatory immune response. The process of apoptosis is characterized by a cascade of events leading to a programmed cell death. Apoptotic cells shrink due to the dysregulation of the lamins and actin filaments of the cytoskeleton, primarily driven by caspases. These cells become highly eosinophilic, retract from neighboring cells, and lose cell-to-cell contact. The nucleus of the apoptotic cell becomes intensely basophilic. A key feature of apoptosis is pyknosis, where nuclear chromatin condenses into one or more dark-staining masses against the nuclear envelope. This is followed by the dissolution of the nuclear membrane and the action of endonucleases which cleave the DNA into regularly sized short fragments. Subsequently, the condensed cytoplasm and nucleus fragment into apoptotic bodies, which detach from the cell and get eliminated by the macrophages through a process called efferocytosis. In contrast to pyroptosis, necrosis or ferroptosis in which cell swelling and inflammation are typical, apoptosis maintains an intact cell membrane without provoking inflammation. Macrophages efficiently clear apoptotic cells with minimal to no inflammation in the surrounding tissues rendering the process immunologically silent. Additionally, the apoptotic process entails a series of biochemical events that result in specific cellular alterations including the loss of membrane asymmetry and adhesion, cell shrinkage, nuclear fragmentation, chromatin condensation, and the fragmentation of chromosomal DNA which are considered as key features of apoptosis (**Figure 29**) [171].

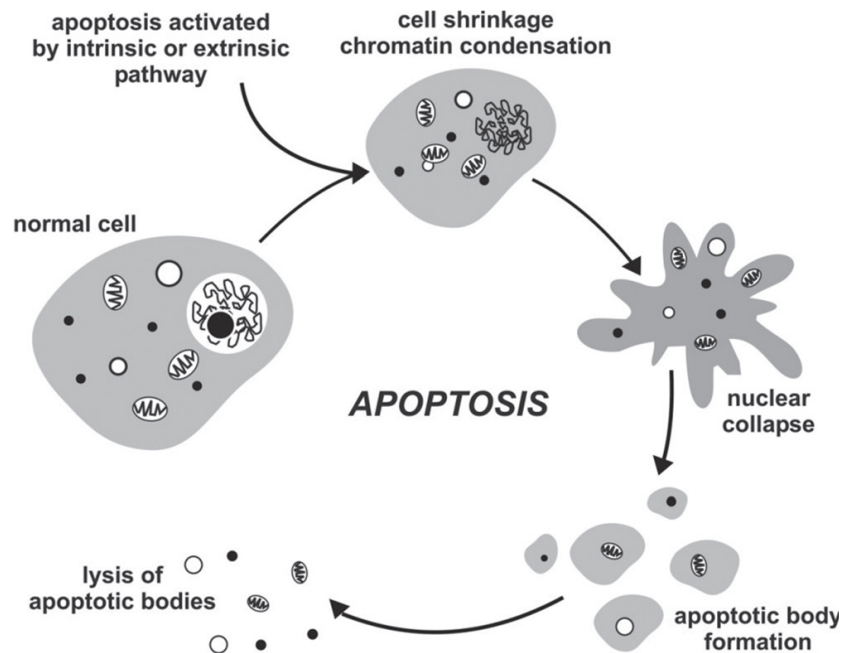


Figure 29: Features representing the apoptotic phenomenon [170]

III.2. Physiological role of apoptosis

Apoptosis exerts a crucial role throughout the development of the organism's physiology and maintaining tissue homeostasis in adulthood. During embryogenesis, apoptosis intervenes and enables the destruction of structures initially formed, particularly during sexual differentiation. When the embryo is genetically male, the anti-müllerian hormone (AMH) is secreted by the Sertoli cells in the testes. This induces the degeneration of the Müllerian ducts through apoptosis. Simultaneously, testosterone secreted by Leydig cells maintains Wolff's ducts. In contrast, when the embryo is genetically female, AMH and testosterone are not secreted due to the absence of a testes which allows the persistence of the Müllerian ducts and the relapse of the Wolffian ducts [172].

Given its capacity to eliminate cells with minimal disturbance to surrounding tissue, apoptosis is a particularly well-suited 'clean and silent' form of cell death for tissue morphogenesis. It is widely established that apoptosis is the primary mechanism for the elimination of organs and tissues that are only necessary in the periods of embryonic or larval stages or that are phylogenetic remnants. This includes the resorption of the tadpole tail, the regression of the umbilical arteries after birth, and the degeneration of the pronephros in mammals and amphibians (**Figure 30 A**). Additionally, apoptosis plays a significant role in tissue sculpting, as the removal of many cells can result in the formation of new structures. A classic example is the role of apoptosis in finger morphogenesis where it leads to the death of cells forming the interdigital space early in embryogenesis and a lack of apoptosis activity leads to a lack of finger differentiation. (**Figure 30 B**) [173].

Apoptosis is also involved in the development of the immune system, where autoimmune B and T lymphocytes are eliminated. As previously noted, apoptosis is involved in maintaining tissue homeostasis especially in highly renewable tissues such as skin, eliminating aging cells and excess T cells after an immune response [174].

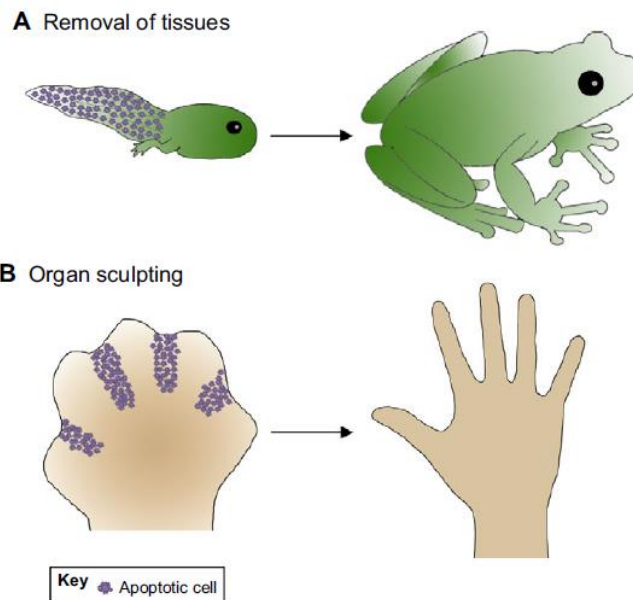


Figure 30: Physiological role of apoptosis in tissue and organ sculpting [173]

III.3. Caspases and cell death

Caspases are a family of proteases also known as “Cysteiny Aspartate-Specific Proteases” as they contain a cysteine residue at their catalytic site. They are the major key contributors to apoptosis and are regulated by various upstream factors. Caspases are categorized into several distinct subsets based on their specialized functions. Among these, the effector (executer) and initiator caspases are critical regulators of apoptosis. Effector caspases, including caspase-3, -6, and -7, are responsible for executing cell death by proteolytically cleaving a wide array of cellular substrates. The activation of these caspases involves the cleavage of their inactive monomeric forms into active dimers, which then propagate apoptotic signaling cascades. Once activated, they will cleave several cellular substrates promoting cell death and the phagocytic removal of cellular debris. Caspase-3, the most activated effector caspase, plays a pivotal role by catalyzing the cleavage of key cellular proteins and inducing chromatin condensation. Additionally, caspase-3 activates DNase enzymes leading to DNA fragmentation and internucleosomal cleavage.

Initiator caspases, such as caspase-2, -8, -9, and -10 in various vertebrates, play a role in the upstream activation of effector caspases. Unlike effector caspases, initiator caspases are activated through conformational changes rather than direct cleavage. Multiple upstream signals recruit initiator caspases to large macromolecular signaling complexes via their extended pro-domain where they undergo dimerization and activation. The activation of each initiator caspase is regulated by distinct signals and platforms, allowing for specialization in different cellular contexts.

Additionally, a third subset of caspases includes those involved in non-apoptotic processes, particularly inflammation. These inflammatory caspases, such as caspase-1, -4, -5, -11, and -12, are integral to the inflammatory response [175], [176], [177].

III.3.1.1. Structure of caspases

Caspases are initially synthesized as enzymatically inactive precursors. The active form of caspases is a tetramer composed of two large and two small subunits. Pro-caspase zymogens contain a catalytic C-terminal domain and an N-terminal prodomain. The active site is located in the catalytic domains of caspases and consists of both a small and a large subunit which together form the enzymatically active conformation. The large subunit carries the catalytic cysteine residue which is crucial for the enzyme's activity. The small subunit includes residues essential for shaping the substrate-binding pockets and facilitating substrate recognition. The structure and function of caspase prodomains vary significantly. Apoptotic effector caspases (such as caspase-3, -6, and -7) and caspase-14 possess very short prodomains typically consisting of 20-30 amino acids. In contrast, initiator caspases and inflammatory caspases have large prodomains that can extend up to 220 amino acids. These larger prodomains contain homotypic protein-protein interaction motifs such as the caspase activation and recruitment domain (CARD) found in caspases-1, -2, -4, -5, and -9, as well as the death effector domain (DED) present in caspases-8 and -10. These interaction motifs are crucial for the dimerization and recruitment of initiator caspases into caspase activation complexes. Activation of procaspases requires enzymatic cleavage to achieve a mature, fully active tetrameric conformation. This stringent activation requirement is crucial for the tight regulation of caspase activity preventing inappropriate activation of caspase cascade. Depending on the specific protein-protein interaction motifs present in their prodomains, different caspases are activated through distinct biochemical mechanisms (**Figure 31**) [178], [179].

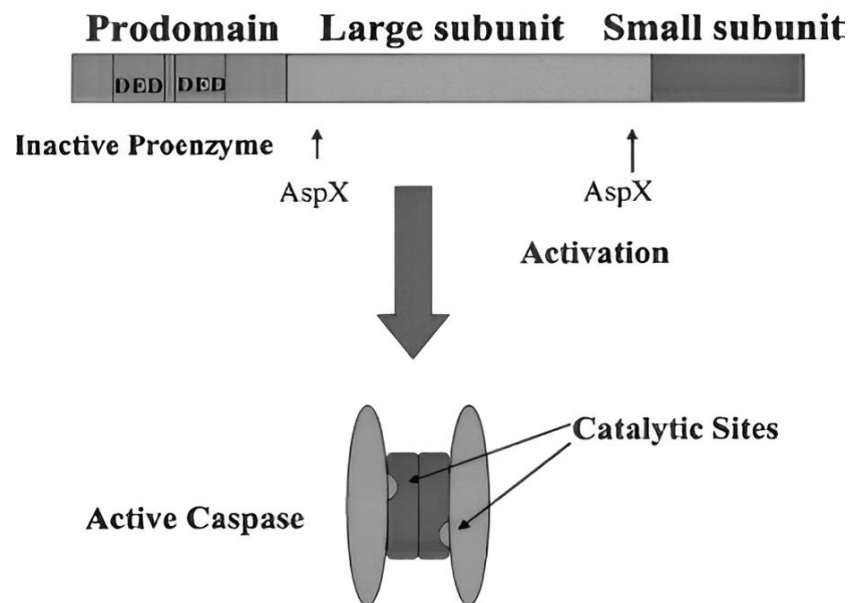


Figure 31: Caspase structure and activation [180]

III.3.1.2. Activation of initiator caspases

Initiator caspases containing a long prodomain exist as inactive zymogenic monomers in normal cells. After auto-proteolytic processing, the prodomains of the initiator caspases are removed by proteolysis to promote a mature enzyme conformation with full catalytic activity. Initiator caspases exist as inactive monomers, each comprising a large subunit, a small subunit, and a prodomain. Upon receiving apoptotic signals, these monomers undergo proximity-induced dimerization which is facilitated by adaptor proteins bringing two monomers

together. This dimerization is considered as the “classical model” that is crucial for the activation of the initiator caspases through the stimulation of the catalytic activity and self-proteolytic cleavage between the small and large subunits of the catalytic domains. The researchers believe that homo-dimerization is the initial event that triggers the activation of initiator caspases mediating downstream signaling to effector molecules (**Figure 32**) [181].

III.3.1.3. Activation of effector caspases

Effector pro-caspases exist as inactive dimers in normal cells and lack the prodomain that is usually present in the initiator procaspases, yet they are composed of large and small subunits. They lack protein-protein interaction motifs, so their activation relies on proteolytic cleavage at specific sites by upstream active initiator caspases. Like initiator caspases, cleavage of the effector caspases within the catalytic domain triggers conformational changes in the active site resulting in the formation of an active tetramer with a substantial increase in the catalytic activity. This inter-chain cleavage facilitates the transition of effector caspases from their inactive dimeric form to an active enzymatically competent state. Once activated, effector caspases execute the apoptotic program by cleaving various cellular substrates. Thus, while initiator caspases require dimerization followed by proteolytic processing for activation, effector caspases are directly activated through proteolytic cleavage by the initiator caspases, highlighting a key distinction in their activation mechanisms (**Figure 32**) [182].

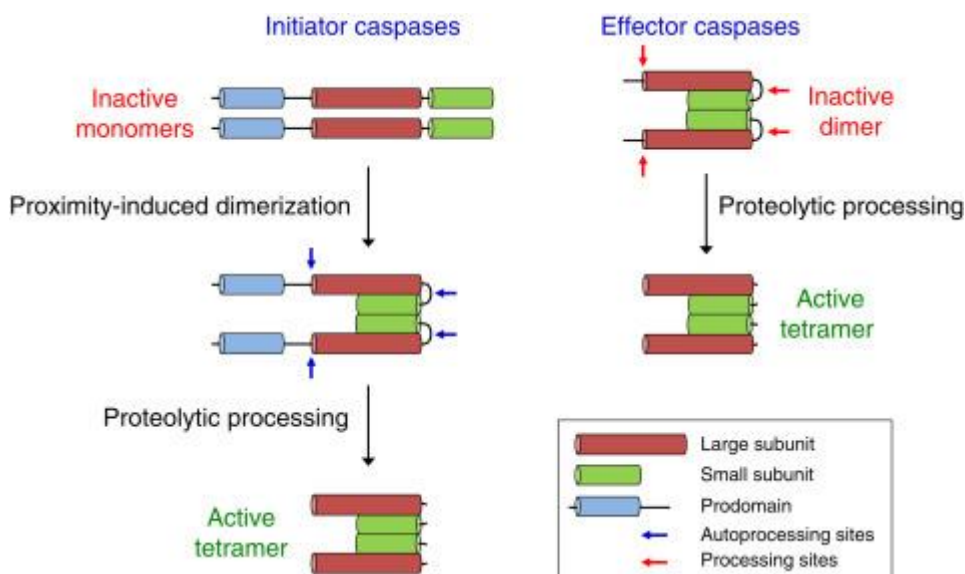


Figure 32: Activation of initiator and effector caspases [183]

III.4. Downstream activity of caspases

Initiator caspases target effector caspases which subsequently cleave numerous substrates leading to cell death [184]:

- **Caspases and apoptosis-regulating proteins:** This includes caspases themselves, as well as other proteins that regulate apoptotic processes.
- **Mediator and regulator proteins in apoptotic signal transduction:** These proteins facilitate the transmission of apoptotic signals within the cell.

- **Proteins maintaining intermediate filament integrity:**
 - **Lamins A/C and B:** Cleavage of these proteins results in nuclear envelop disruption and nuclear lamina disassembly, respectively.
 - **Stk4 and Mst1 kinases:** Cleaved forms of these kinases become constitutively active, promoting apoptotic morphology.
- **Proteins involved in transcription and DNA repair:**
 - **Poly (ADP-ribose)-polymerase (PARP):** Once cleaved, PARP loses its ability to repair DNA damage which compromises the genomic integrity.
- **Cell-cycle regulatory proteins:**
 - **Akt:** Cleavage of Akt leads to the inactivation of cell-cycle inhibitors, ultimately resulting in the loss of survival signaling.

III.5. Other key factors of apoptosis

- **TNF- α :** It is a cytokine produced and released by macrophages and serves as a key extrinsic mediator of apoptosis. It binds to the tumor necrosis factor receptor (TNFR1) initiating the activation of caspases.
- **Fas:** T cells express the Fas receptor, which is upregulated during infection. Subsequently, activated T lymphocytes generate Fas ligands. When Fas on the same or adjacent cells binds to these ligands, they trigger apoptosis by activating caspases. The Fas receptor, a transmembrane protein within the TNF family, interacts with Fas ligand (FasL) to start the activation of caspases.
- **Bcl-2 genes:** Located on chromosome 18, these anti-apoptotic genes encode the Bcl-2 protein, which inhibits Apaf-1 and cytochrome c release from the mitochondria. Cytochrome c, situated between the inner and outer mitochondrial membranes, binds to Apaf-1 upon release to activate procaspase-9.
- **TP53 suppressor gene:** This gene is transcribed and translated to a protein that controls the cell cycle and suppresses tumors. In response to DNA damage from chemotherapeutic agents, hypoxia, or ionizing radiation, TP53 inhibits the cell cycle in the G1 phase, thereby preventing the proliferation of damaged cells and facilitating DNA repair. Severe DNA damage induces the activation of TP53 gene (p53) which promotes the expression of the BAX gene leading to apoptosis. The products of the BAX genes are pro-apoptotic proteins that antagonize the effects of the anti-apoptotic Bcl-2 gene. The optimal equilibrium between anti-apoptotic and pro-apoptotic genes governs this process in which an increase in the pro-apoptotic signals from BAX can lead to cell death when they surpass the protective effects of Bcl-2.
- **Cytotoxic CD8+ T-cell pathway:** These cells release perforins which form pores in the target cell membrane. Then, granzymes are secreted into the target cells through these pores leading to caspase activation and apoptosis [171].

III.6. Apoptotic signaling pathways

Like any other physiological phenomenon, apoptosis requires stimuli such as ultraviolet radiation, cellular stress and cytokines to be triggered. Based on the nature of the stimulus and its location whether intracellular or extracellular, two main induction pathways can be involved in apoptosis: the intrinsic or mitochondrial pathway and the extrinsic or death receptor pathway. Generally, both apoptotic pathways follow the same pattern which is associated with three different phases [185]:

1. Initiation or induction phase: This phase is reversible where the stimulus triggers initiating caspase through several adaptor molecules.
2. Execution phase: This phase is non-reversible in which executing caspases are involved and maintain the apoptotic process.
3. Cell degradation phase: In this phase, the apoptotic cell features, previously mentioned, are induced to destroy the cells.

III.6.1. Mitochondrial or Intrinsic Apoptotic Pathway

This pathway is activated when intracellular stress arises from factors such as DNA damage caused by X-ray or UV light exposure, chemotherapeutic agents, hypoxia, or the accumulation of misfolded proteins. Under stress conditions, cytochrome c leaks from the mitochondrial intermembrane space into the cytosol, leading to the activation of caspase-9. The regulation of this pathway is controlled by the BCL-2 and TP53 genes. This pathway is primarily characterized by mitochondrial outer membrane permeabilization (MOMP), which leads to the activation of caspase-9. MOMP is facilitated by the proteins Bax and Bak which belong to the Bcl-2 family. These proteins form pores in the mitochondrial membrane compromising membrane integrity and causing the release of cytochrome c from the mitochondrial intermembrane space. Upon release, cytochrome c binds to the adaptor protein Apaf-1 (apoptotic protease activating factor 1) leading to the assembly of a large multiprotein complex known as the apoptosome. The apoptosome subsequently activates caspase-9 which plays a crucial role in the apoptotic cascade (**Figure 33**).

The activation of Bax and Bak, and consequently MOMP, is regulated by the interplay between pro-apoptotic and anti-apoptotic proteins of the Bcl-2 family. "BH3-only" pro-apoptotic proteins, such as Bid, Bim, Puma, and Noxa, possess one of the four Bcl-2 homology domains and can directly activate Bax and Bak. Conversely, anti-apoptotic proteins, including Bcl-2, Bcl-XL, A1, and Mcl-1, inhibit apoptosis by binding to and sequestering BH3-only proteins and directly inhibiting the activity of Bax and Bak [186].

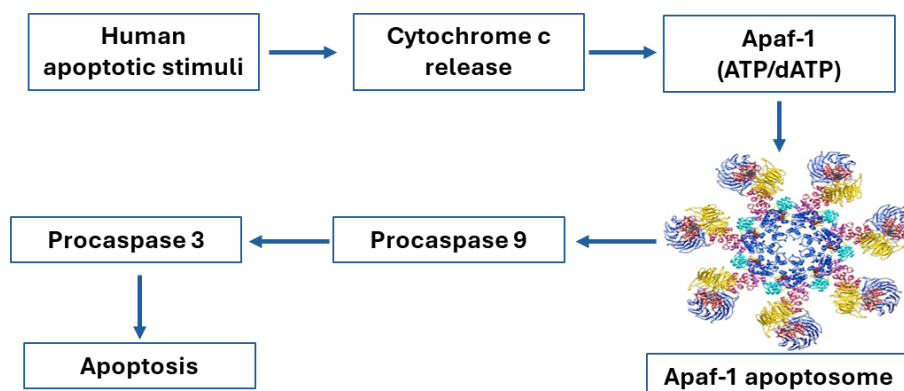


Figure 33: Apoptosome assembly in the intrinsic (mitochondrial) apoptotic pathway [187]

III.6.2. Extrinsic Apoptotic Pathway

The extrinsic apoptotic pathway is initiated when a cell acquires death signals from various cells. This receptor-mediated pathway begins when ligands from neighboring cells bind to death receptors found on the surface of the cell, thereby triggering apoptosis. The primary receptors involved include Fas, TNFR, CD95/FAS, and TRAIL receptors (DR4 and DR5). These receptors interact with their respective ligands including FasL and TNF- α . These receptors and ligands are members of the tumor necrosis factor superfamily. Upon ligand binding, these death receptors recruit the adapter protein Fas-associated protein with Death Domain (FADD) which binds to the receptors and facilitates the recruitment and dimerization of inactive caspase-8 monomers into active caspase-8 homodimers. This process leads to the formation of the death-inducing signaling complex (DISC) which consists of FADD, procaspases-8 and -10, and cellular FLICE (FADD-like IL-1 β -converting enzyme) inhibitory proteins (cFLIP). Once caspase-8 is activated within the DISC, it is released and subsequently cleaves and activates effector caspases such as caspase-3 and caspase-7 leading to the execution of apoptosis.

Additionally, the binding of TNF- α to its receptor TNFR1 results in the formation of another complex (complex I) that includes TNFR1-associated protein with death domain (TRADD), TNFR1, TNF receptor-associated factor 2 (TRAF2), and TNF- α -related receptor-interacting protein (RIP). Complex I can either activate the nuclear factor kappa light chain enhancer of activated B cells (NF- κ B) pathway or transition into complex II which comprises TRADD, TNFR1, TRAF2, RIP, FADD, procaspase-8, and procaspase-10 (**Figure 34**) [188].

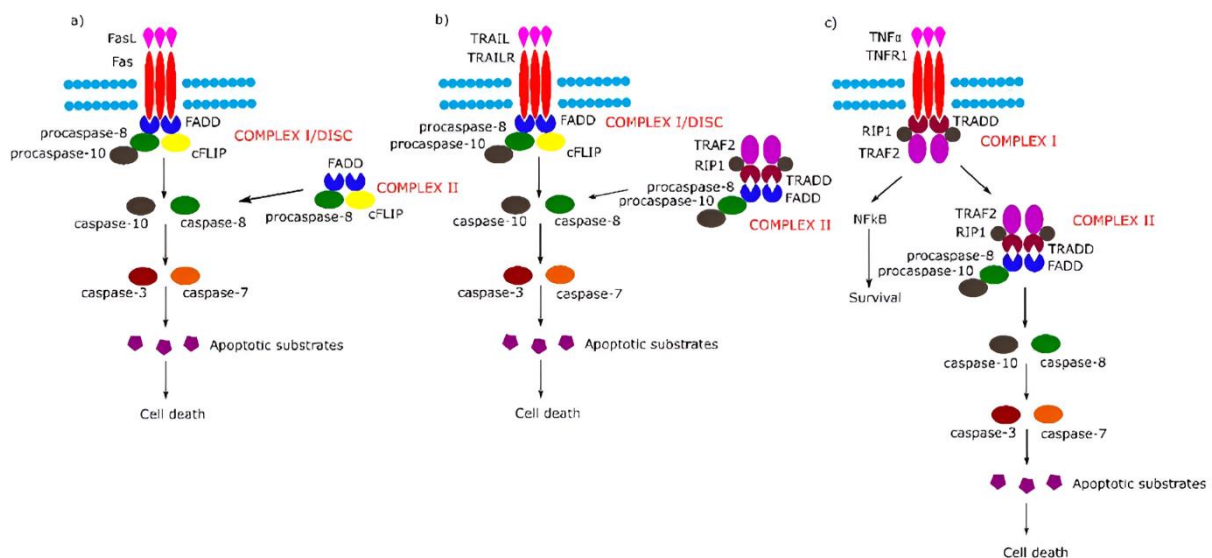


Figure 34: Biological factors involved in the extrinsic apoptotic pathways [188]

III.7. Crosstalk between the intrinsic and extrinsic pathways

The interaction between the intrinsic and extrinsic apoptotic pathways is one of the key processes that govern apoptosis since it allows the realization of various apoptotic signals if necessary. This complex interconnection becomes vital in regulating the intracellular environment and is involved in homeostasis, defense, and the removal of unhealthy or undesirable cells.

The pro-apoptotic protein known as Bid serves as the primary connector between the two pathways. When the extrinsic pathway is initiated, for instance, through the activation of death

receptors such as CD95 (Fas) by their ligands' binding, caspase-8 is brought to the DISC. On activation, caspase-8 cleaves Bid into its active form, which is named tBid. After that, this truncated form of Bid moves into the mitochondria, where it activates cytochrome c and other apoptotic proteins that move from the mitochondria's intermembrane gap into the cytosol. It's important to note that cells are divided into type I and type II cells based on the apoptotic pathway that is more prominent. Type I cells are mostly subjected to the extrinsic apoptotic pathway while type II cells' apoptosis is mainly induced by the intrinsic apoptotic pathways. For example, when the intracellular levels of growth factors or cytokines increase, type II cells become more resistant to apoptosis as the intrinsic apoptotic pathway becomes downregulated. This underscores the influence of the cellular environment on the apoptotic outcome. On the other hand, type I cells respond significantly to external stimuli and are endowed with a very effective DISC mechanism that activates the extrinsic pathway apart of the intrinsic pathway. Thus, even when type I cells receive inhibitory signals that block apoptosis, they can still undergo cell death if their death receptors are activated. This independence, in a way, also contributes to the understanding of apoptotic signaling as it shows that different forms of cells may respond differently to apoptotic triggers because of the specific signaling mechanism within each cell type and the stimuli perceived by the cell. The intrinsic and extrinsic pathways of apoptosis are not simply demonstrated since it is a rather complex and flexible process that cells can use to adapt their responses to apoptotic signals. This intercommunication is employed in sustaining life processes through the dialog between survival and death proteins in development, tissue homeostasis, and cancer. In certain pathophysiologic conditions such as in cancer cells, the crosstalk can go where anti-apoptotic Bcl-2 proteins are upregulated hence enhancing tumor survival and growth. In cancer cells, the dysregulation in these pathways contributes to apoptotic resistance and promotes tumor growth and development. Hence, it is crucial to understand the dynamism of this crosstalk for designing therapeutic approaches that can efficiently promote apoptosis in cancer cells to enhance the efficacy rates and the survival of the patients (**Figure 35**) [189].

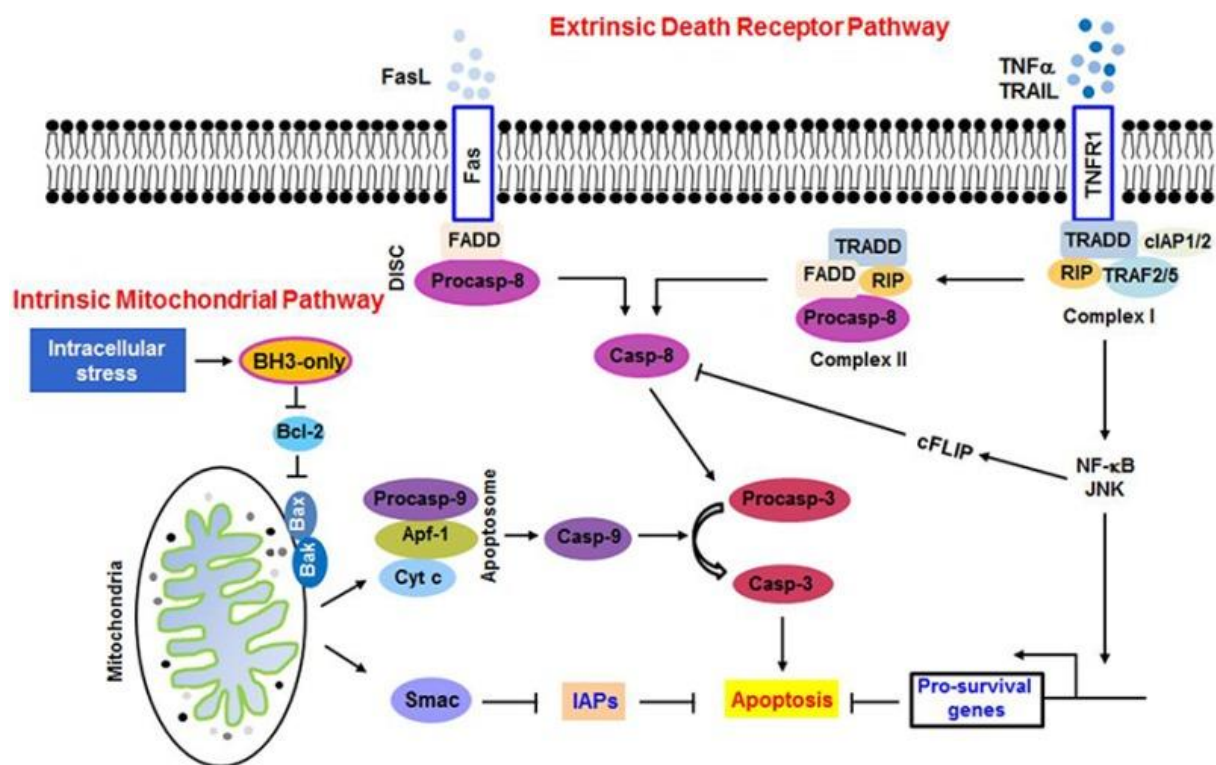


Figure 35: Interaction between the intrinsic and extrinsic pathways [190]

III.8. Apoptosis and cancer

As previously mentioned, the hallmarks of cancer include self-sufficiency of growth signals, the ability to induce the formation of new blood vessels and resistance to cell death. Apoptosis is among the vital processes that prevent the formation of cancer and tumor growth; however, several mechanisms of apoptosis suppression can be found in malignancies. These prognostic changes of apoptotic regulation allow the survival of cancer cells through the emergence of certain mutations that could lead to the increased invasiveness of cells, angiogenesis, aberrant cell proliferation, and termination of differentiation. Cancer cells evade apoptosis through several mechanisms including the inhibition of caspases' activity. The major mechanisms of evasion include increased expression of anti-apoptotic Bcl-2 proteins and/or decreased expression of the proapoptotic proteins Bax and/or Bak. Although Bcl-2 is not recognized as an oncogene, any mutations that involve this protein will enhance the rate of carcinogenesis. Bcl-2 is overexpressed in more than 50% of cancers regardless of the tissue origin, as tumor cells become resistant to intrinsic apoptosis and various apoptotic anticancer treatment modalities. Additionally, cancer cells often exhibit augmented sensitivity to apoptosis in response to microenvironmental stress factors such as nutrient deprivation and hypoxia. Generally, tumor cells are more responsive to the extrinsic apoptotic pathway compared to the intrinsic pathway suggesting that targeting the extrinsic pathway may be more effective in cancer therapies. Besides, mutations in oncogenes and tumor suppressor genes influence apoptotic processes contributing to apoptotic evasion. For instance, tumor suppressor p53 promotes the transcription of pro-apoptotic proteins within the Bcl-2 family. Mutations in p53 lead to apoptotic evasion which recruits anti-cancer drugs that induce apoptosis in another mechanism. Anti-cancer therapies aim to regulate or even eliminate the abnormal growth of cancer cells through strategies involving the use of the cell's proapoptotic pathways. Many anticancer agents are formulated to interfere with different mechanisms of both the intrinsic and extrinsic apoptotic pathways by stimulating the apoptotic signals and blocking the anti-apoptotic signals. Targets of anti-cancer therapies include death-receptor ligands, inhibitors of Bcl-2 and X-linked inhibitor of apoptosis protein (XIAP), as well as analogs of alkyl phospholipids (APLs) which normally induce apoptotic signals. While it is efficient to target various stages within the apoptotic pathways, determining the optimal target remains a significant challenge. Further research and development of the apoptosis-inducing anticancer therapies will be essential to identify the most effective targets that can yield the best therapeutic outcome in cancer patients [191].

III.9. PDT induced apoptosis

PDT of cancer cells trigger apoptosis through multiple complex pathways that include plasma membrane death receptors, mitochondria, lysosomes, ER, caspases, Bcl-2 proteins, ROS generation and specific signaling pathways. PSs, such as porphyrin, Photoditaz Porfimerate Sodium, and Metvix, preferentially accumulate in mitochondria, lysosomes and ER. After their photo-activation, PSs generate ROS that induce oxidative stress to lipids, proteins, and DNA of cells leading to activation of apoptotic signal transduction pathways. PSs targeted to the mitochondria release cytochrome c upon photoactivation to form the apoptosome complex that activates caspase-9 and caspase-3 which cleaves nuclear lamins, PARP, DNA-protein kinase (DNA-PK), inhibitor of caspase-activated DNase (ICAD), and many other effectors. Using Fas and TNFR, caspase-8 induces the activation of caspase-3 which activates Bid. As previously mentioned, the latter is cleaved into tBid to trigger the release of mitochondrial cytochrome c. Lysosomal PSs cause the release of cathepsin that cleaves Bid and caspase-3 influencing

apoptosis. Also, PDT-induced ER damage releases calcium (Ca^{2+}) which in turn enhances apoptosis. Members of the Bcl-2 family are involved in the regulation of apoptosis after PDT, but the role of every protein might be ambiguous. influencing apoptosis. Also, PDT-induced ER damage releases calcium (Ca^{2+}) which in turn enhances apoptosis. Members of the Bcl-2 family are involved in the regulation of apoptosis after PDT, but the role of every protein might be ambiguous. As noted earlier, the anti-apoptotic proteins including Bcl-2, Bcl-xL prevent cytochrome c liberation and caspase activation while proteins of pro-apoptotic group, such as Bax, promote a contrary effect represented by the release of cytochrome c and caspase activation. Due to its pro-apoptotic effects, PDT can activate Bax proteins and disturb the progression of the cell cycle in which an arrest in the G1 phase can be induced by increasing the levels of p21/WAF1/CIP1 expression and decreasing the expression of cyclins and cyclin-dependent kinases. Moreover, since PDT is widely known to activate stress kinases such as p38 MAPK, multiple signaling pathways are stimulated and may converge with mitochondria-mediated apoptotic pathways. Indeed, PDT triggers apoptosis through the production of ROS, stimulation of death receptors, activation of caspases, disruption of the cell cycle, and dysregulation of signaling pathways. All these mechanisms give a general view of the PDT mechanisms involved in identifying and destroying cancer cells (Figure 36) [94].

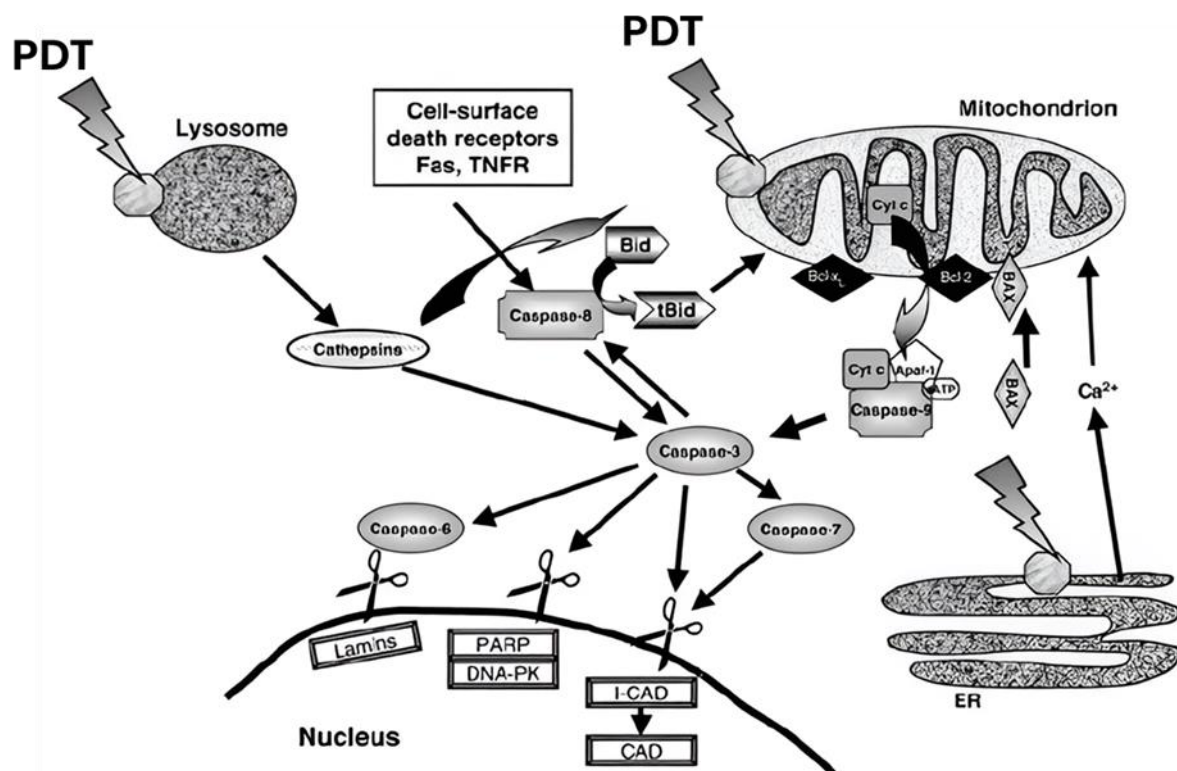


Figure 36: PDT induced cell apoptosis [94]

Different research studies demonstrated that PDT induces cell death by triggering apoptosis. For instance, a study by Baron et al. using silicon phthalocyanine (Pc 4) as PS showed that it induced the activation of caspases including caspase-3 which appeared as a key feature of apoptosis since their activation levels were higher in the photosensitized as compared to the control cells. Additionally, the evaluation of tissue sections taken at 24h post-illumination showed a positive staining of caspase-3. Parallel findings showed the disruption of the anti-apoptotic proteins such as Bcl-2 and Bcl-xL leading to the loss of mitochondrial membrane potential and the release of cytochrome c into the cytosol. It was also suggested that the type II photochemical reaction took place due to the elevated levels of protein-derived peroxides

revealed in A375 skin cancer cells post-illumination. Thus, it is found that measuring caspase-3 levels is a potent biomarker of the apoptotic clinical responses to Pc-4-PDT in cutaneous neoplasms [192].

Another study by Bissonnette et al. was based on the evaluation of the ability of ALA to induce apoptosis in T lymphocytic lesions in patients with psoriasis. The results showed that the activated T lymphocytes which are prevalent in psoriatic skin are more sensitive to photosensitization and undergo apoptosis as compared to dormant T cells and that the illumination with high fluence rates is correlated to higher levels of apoptosis. The induction of apoptosis in lesional T lymphocytes indicates that ALA-PDT could be an effective therapeutic modality for psoriasis and potentially other conditions characterized by T lymphocyte activation, such as atopic dermatitis and alopecia areata [193].

IV.1. Past and present states

PDT has arisen as a promising approach for treating various diseases including cancer. It was approved as an anticancer treatment nearly two decades ago; however, its clinical use remains limited, and only a few porphyrin-, chlorin-, and bacteriochlorophyll-based- PSs have received approval. Ongoing research tends to focus on determining the optimal PS to enhance the efficacy of PDT. This has led to the emergence and development of metal-based PSs, particularly platinum (Pt(II))- based compounds such as oxaliplatin, carboplatin, and cisplatin. Such advancements have paved the way to understanding the interactions between biomolecules (DNA, proteins, etc.) and metal complexes [194]. The therapeutic application of metals has a rich historical background originating from around four thousand years ago in ancient China where gold was used in the treatment of skin ulcers and mercury sulfide was employed, for various medical conditions. Subsequently, in ancient Rome the act of placing silver coins in drinking water reservoirs aided in the prevention of water poisoning due to prolonged storage. During the 9th and 11th centuries BCE, scientists such as Rhazes and Avicenna identified the toxicological effects of mercury in animals and its use as an ointment for dermatological problems. Also, another metallic compound is arsenic trioxide which was utilized in Chinese medicine as an antiseptic for the treatment of rheumatoid disorders and psoriasis. Additionally, this metallic compound was among the compounds suggested for the treatment of leukemia in the 18th and 19th centuries but was later replaced by radiotherapy and chemotherapy in the early 20th century due to their association with considerable side effects [195]. The involvement of different metal ions in normal physiological processes has prompted their investigation as anti-cancer therapeutic agents. The advancements were mainly driven by the discovery of diamminedichloroplatinum (II) which was the base for further metal studies in this field. Its mechanism involves forming DNA cross-links, disrupting replication and transcription, and inducing cell death. The clinical success of cisplatin prompted the research into the role of other metal ions such as gallium, zinc, cobalt, and silver for cancer therapy. This research established the potential of metal-based drugs and extended investigations into the roles and therapeutic potential of various metal complexes. Indeed, it became the foundation for the development of the field of metal-based cancer drugs [196].

IV.2. Platinum-based cancer therapy

The development of platinum-based compounds with reduced toxicity and enhanced selectivity recruited a lot of investigations in the field of metal-based cancer therapies. Cisplatin, carboplatin, and oxaliplatin (**Figure 37**) are among the major platinum-based chemotherapeutic agent used in clinics due to their well-defined mechanism of action. Cisplatin is an effective first-generation anticancer drug against numerous malignant tumors such as breast, ovarian, and CRC. However, it is a non-specific chemotherapeutic agent contributing to systemic toxicity by affecting both cancerous and healthy tissues. Several side effects are associated with cisplatin including neurotoxicity, nephrotoxicity, ototoxicity, and myelosuppression and its prolonged use can result in severe damage to healthy tissues. Various strategies have been developed to overcome the associated toxicity, such as liposome encapsulation, drug delivery through nanoparticles, and bio-conjugation to target proteins overexpressed in cancer cells. Then, carboplatin, a second-generation platinum-based chemotherapeutic drug, was developed as a less toxic alternative to cisplatin. It has a higher stability due to the presence of cyclobutane dicarboxylate ligand which replaces the more reactive chloride ligands found in cisplatin resulting in a slower activation and lower overall toxicity. The low systemic toxicity of carboplatin permits its use in high doses to treat highly

aggressive tumors. It was FDA approved in 1989; nevertheless, the development of tumor resistance to cisplatin and carboplatin remained a major challenge limiting the efficacy of such therapies. To address this issue, third-generation platinum-based drugs such as oxaliplatin have emerged. Oxaliplatin use was approved for clinical use in 2002, and its mechanism of action is similar to that of cisplatin but does not produce cross-resistance with either cisplatin or carboplatin. Consequently, oxaliplatin can be used simultaneously with cisplatin in cancer therapy. Cisplatin was approved for its clinical use in 1978 alongside second-generation drugs such as carboplatin and oxaliplatin. Pt (II) based drugs act by slowly hydrolyzing the anionic ligands in the cell to form aqueous cationic complexes that will bind to DNA and create stable cross-links. These cross-links diminish the potential of the DNA to replicate and undergo transcription, ultimately leading to cell death [197], [198], [199].

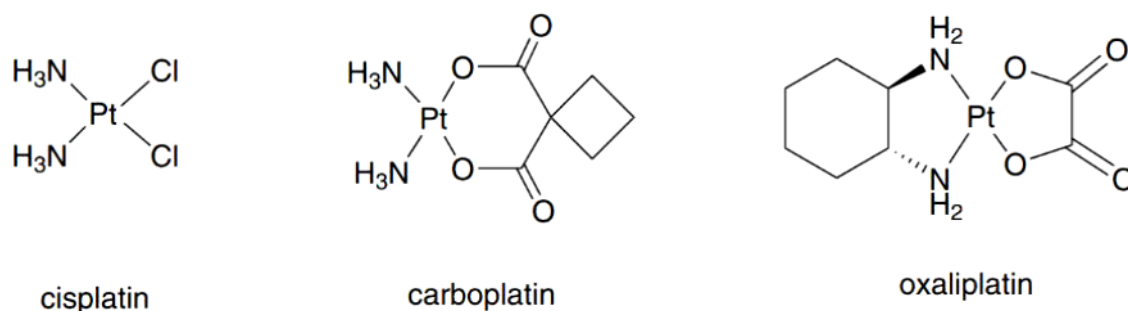


Figure 37: Chemical structures of cisplatin, carboplatin, and oxaliplatin [200]

For instance, cisplatin is a small simple molecule consisting of one platinum atom bonded to two amine groups and two chlorides. Despite its simplicity, it is an extremely potent drug. Under conditions of low chloride concentration that can be found in the cytosol, cisplatin undergoes aquation representing a process in which one or both chloride ligands are replaced by water molecules (**Figure 38 a**). This transformation renders cisplatin highly reactive and allows it to readily bind to various biomolecules within the cell. In its reactive form, cisplatin covalently attaches to DNA bases, forming DNA adducts. Specifically, cisplatin reacts with the nucleophilic N7-sites of purine bases and can covalently link purines through a double reaction. When purines are on the same strand, intrastrand adducts are formed, whereas, if the purines are on opposite strands, an interstrand crosslink is produced (**Figure 38 b**). Cisplatin-induced DNA adducts inhibit transcription and DNA synthesis, triggering a complex intracellular signal transduction cascade as the cell attempts to resolve the lesions. This response involves cell cycle arrest for DNA repair mechanisms to take place. If the repair mechanisms are insufficient or the damage is too extensive, the cells ultimately undergo apoptosis [201]. Even though current Pt(II)-based drugs are effective, the associated side effects and resistance limit their use. Therefore, it is necessary to identify alternative transition metal complexes that could potentially offer better efficacy and safety profiles in cancer therapy [201], [202].

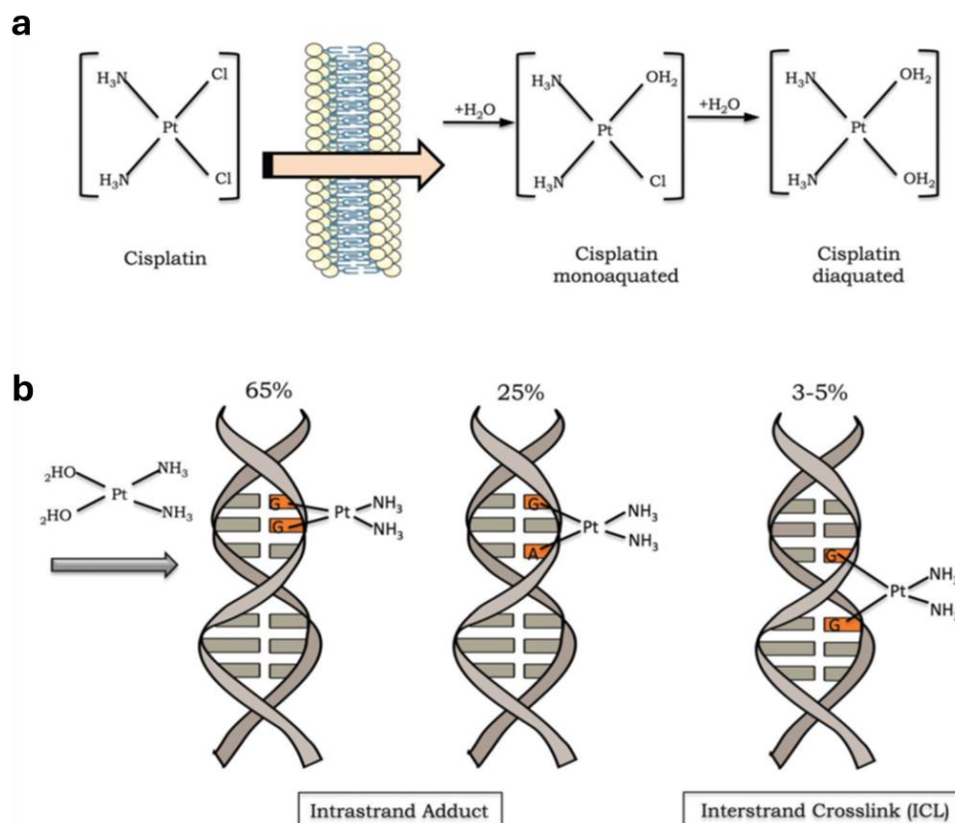


Figure 38: Activation of cisplatin and DNA damage (a) through undergoing aquation reactions and (b) formation of intrastrand adducts and interstrand cross links [201]

IV.3. Ru applications in cancer therapy

Transition metal complexes made up of organic ligands bonded to a central metal showed to be crucial in several applications throughout human history. Ruthenium (Ru), a second-row transition metal exhibits distinctive characteristics that make it remarkable among its metal series as well as a potent alternative to Pt(II)-based drugs due to its lower toxicity and selective targeting. Ru has Lewis acid nature combined with moderate oxophilicity which enables the transmission of a range of useful properties to various industrial and scientific fields. Ru has grabbed the awareness of scientists in the field of medicinal organic chemistry that witnessed advancements in recent years. One of the most studied Ru complexes is the tris(2,2'-bipyridine) ruthenium (II) $[\text{Ru}(\text{bpy})_3]^{2+}$ and its derivatives. Under visible light illumination, it enters a long-lived triplet photoexcited state that facilitates electron transfer process and lead to the generation of ROS and cytotoxicity of cancer cells. In this context, a new field of research was produced and the Ru chemical effects continued to be elaborated by new discoveries and potential applications especially due to Ru potential in exhibiting multiple oxidation states and different electron transfer mechanisms. This also encompasses the study of Ru coordination and organometallic chemistry as well as their application in the fields of biology, nanoscience, redox reactions and photoactive materials which became a major focus and showed rapid advancements in recent years. Ru is characterized by a wide spectrum of oxidation states making it highly active in redox reactions with a typically reversible nature. This attracted the performance of detailed studies revolving around Ru unique photophysical and photochemical properties. The discovery and exploration of Ru complexes as anticancer therapies gained attraction in the late 1970s after the success of cisplatin and the search for alternative metal-based drugs. Earlier research is marked by the study of Dwyer et al. in the 1950s which focused on the development of bioactive Ru polypyridyl complexes, but mainly for their antimicrobial properties. Since then, research has significantly expanded and focused on the synthesis of

novel Ru(II) and Ru(III) complexes as potential anticancer agents and elucidating their mechanisms of action. Most of these compounds, regardless of the ligands attached to the Ru ion, exhibit minimal cytotoxicity and toxicity compared to cisplatin, necessitating higher therapeutic doses. Ruthenium complexes have garnered attention as alternatives to platinum-based drugs due to their lower toxicity and selective targeting of cancer cells. Ru(III) complexes typically remain in their Ru(III) oxidation state which is relatively inactive until they reach the tumor site. The tumor microenvironment is distinguished by its low oxygen content and pH compared to healthy tissue facilitating Ru(III) reduction to the more reactive Ru(II) oxidative state. This process, known as “reduction activation,” enables Ru(III) compounds to be selectively toxic. Another mechanism potentially contributing to the anticancer effect is the high affinity of Ru(III) for the iron-binding sites of transferrin. This binding capability allows for the targeted delivery of Ru(III) complexes to tumors with a high density of transferrin receptors. Many Ru complexes in both oxidative states have been synthesized and demonstrated to possess antitumor activity *in vitro*. Despite the promising attributes of the Ru complex, none of them have received approval for clinical use as anticancer drugs. Nevertheless, several compounds, such as NAMI-A, KP1019, NKP1339, and TLD1443 have progressed to clinical trials demonstrating the potential of Ru-based chemotherapeutics in cancer treatment. Current research aims to develop new metal-based anticancer drugs that enhance efficacy and selectivity while reducing toxicity compared to existing therapies [203], [204], [205], [206], [207], [208].

- **NAMI-A**

NAMI-A or imidazolium trans-imidazole dimethylsulfoxide tetrachlororuthenate (III) is an innovative ruthenium-based anticancer agent (**Figure 39**). Stability studies conducted by Sava et al. using a reversed-phase-high-performance liquid chromatographic assay demonstrated that NAMI-A is unstable in aqueous solutions which necessitates the development of a lyophilized formulation for long-term storage and use in clinical settings. Moreover, it was found that it has the highest stability within the pH range of 3-4 and is photostable. Additionally, preclinical studies determined the anti-metastatic efficacy of NAMI-A in the treatment of lung metastasis in murine tumor models with low exhibited toxicity and its mechanism of action appeared to be independent of the primary tumor type and metastatic stage, yet further investigations are needed. Additionally, cytotoxicity of NAMI-A is also attributed to its ability to bind to DNA and form cross-links. However, when phase II clinical studies were conducted, they showed that it led to acute side effects in patients which ceased its further investigations [209], [210].

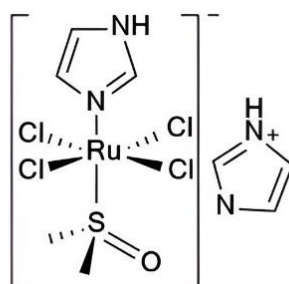


Figure 39: Structure of NAMI-A [211]

- **KP1019**

KP1019 or indazole trans- [tetrachlorobis(1H-indazole)ruthenate(III)] is the second Ru-derived antitumor compound to undergo clinical trials (**Figure 40**). It showed promising activity against a range of tumor types including CRC [212]. KP1019 induces apoptosis in CRC cell lines

(SW680 and HT-29) through the mitochondrial pathway highlighted by a reduction in the mitochondrial membrane potential [213], [214]. Caspase-3 activation was detected four hours post-treatment with KP1019 followed by the formation of apoptotic bodies within 6-8 hours. The apoptotic effect of KP1019 was independent of the p53 status of the tumor cells indicating that DNA strand breaks were not the direct cause of cell death [215]. In phase I clinical trials, KP1019 did not show any side effects revealing its potential as a promising therapeutic agent. Nevertheless, KP1019 was not further investigated due to its poor water solubility, significant side effects in phase II trials, and inadequate efficacy for clinical studies [216].

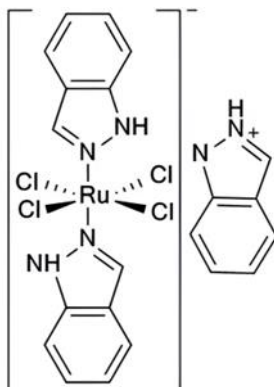


Figure 40: Structure of KP1019 [211]

- **NKP1339**

To overcome the low solubility trait of KP1019, sodium salt derivatives were added to yield NKP1339 also known as sodium trans-[tetrachloridobis(1H-indazole) ruthenate(III)] (**Figure 41**). NKP1339 ruthenium-based compound exhibits a rapid cellular uptake typically 1 hour after drug exposure. It exerts its anti-cancer effect through inducing ER stress and interfering with the integrity of the unfolded protein response which is usually triggered as a defense mechanism to the ER stress to maintain cell survival and proliferation. Hence, NKP1339 ultimately promotes cell death through increasing cellular stress. Additionally, NKP1339 showed a better overall safety profile compared to traditional chemotherapeutic agents. Its design promotes a selective targeting towards cancer cells reducing the associated toxicity and side effects. Phase I clinical trials showed promising results after the use of NKP1339 for the treatment of solid tumors which promoted it as a viable candidate for further clinical development particularly due to its unique mechanism of action and its ability to synergize with other treatments such as sorafenib [217].

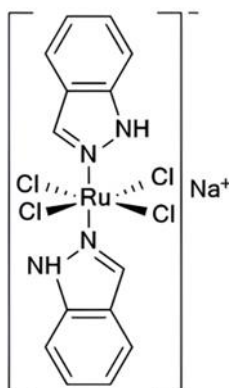


Figure 41: Structure of NKP1339 [211]

- **TLD1443**

TLD1443 (**Figure 42**) also known as trans-tetrachloridobis (dimethylsulfoxide) ruthenium (III) has been shown to have photosensitive characteristics as it was designed with considering the photophysical and chemical characteristics of Ru(II) complex. It showed a highly enhanced effectiveness of phototherapy with prominent significance on bladder cancer and with reduced toxicity *in vitro* and *in vivo* and is undergoing phase II clinical trials [218], [219].

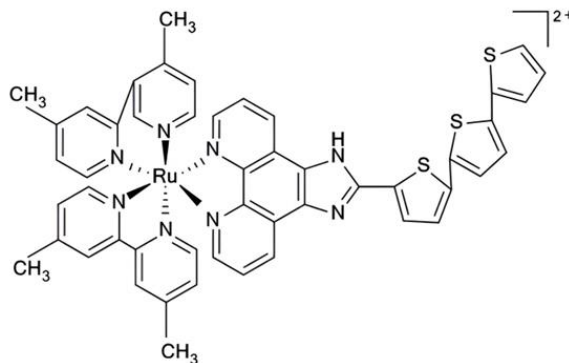


Figure 42: Structure of TLD1443 [211]

IV.4. Ru coordinated PSs in PDT

The selectivity of PDT as an anticancer treatment is based on the local generation of cytotoxic ROS in tumor tissue due to both the preferential uptake of PS by malignant tissue and the subsequently localized light illumination. In fact, PS, at the concentrations used for PDT, is non-toxic in the dark and only turns photocytotoxic upon exposure to light at its appropriate wavelength. To improve tumor cell selectivity, the PS can be coupled to a tumor-targeting moiety, such as a peptide, folic acid, or sugar [220], [221], [222].

The coupling of PS to a vector is advantageous either through passive or active targeting:

- Passive targeting occurs by regulating the amphiphilicity and improving the solubility of these compounds in biological media to avoid self-aggregation.
- Active targeting is promoted using vectors to enhance specific cell recognition which augments the therapeutic efficacy.

Many of these targeting strategies offer the benefit of transporting the PS molecules across the cell membrane which highly impacts the intracellular accumulation of the photoactive compounds and enables the targeting of photosensitive intracellular sites to elevate the photodynamic efficacy.

Various PS conjugated to Ru complexes have been designed and tested *in vitro* [223]. These complexes have several objectives:

- Elevate the PS solubility through specific Ru ligands and coordination
- Combine the cytotoxicity of Ru with the photodynamic activity of PS
- Enhance the PS's tumor selectivity and cellular uptake by improving its specificity to transferrin receptors expressed on cancer cells.
- Following tumor illumination, join the PS activity and Ru-induced DNA photocleavage.

Porphyrin and its Ru-conjugated derivatives have been well-investigated as PSs (**Figure 43**). In particular, to benefit from cumulative tumor suppressive effects, the synthesis of compounds where porphyrin chromophores are conjugated to peripheral metal moieties is an intriguing strategy combining porphyrin's phototoxicity and the metal moiety's cytotoxicity [223], [224]

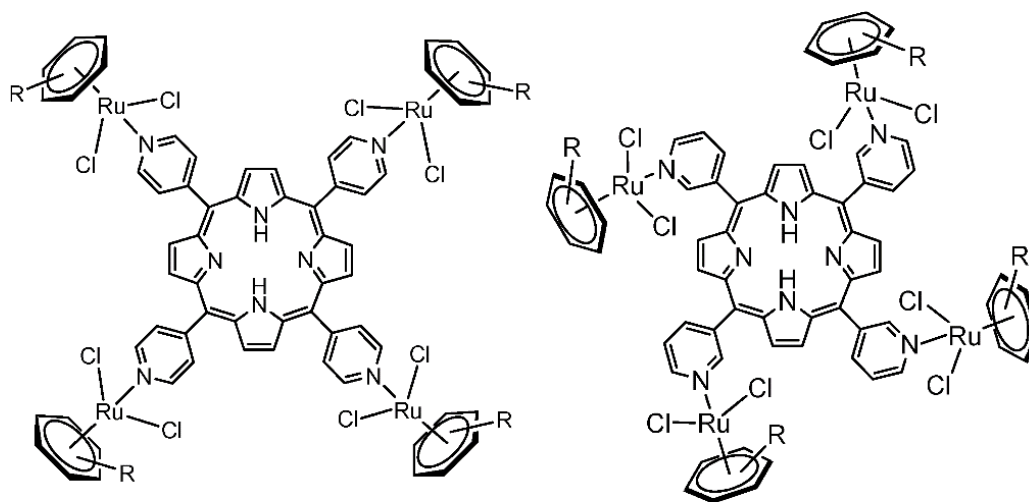


Figure 43: Examples of arene-Ru tetranuclear complexes conjugated to porphyrin to enhance PDT efficacy [223]

Research has demonstrated that metal-porphyrin conjugates not only exert the basic PDT functions but also offer additional benefits such as enhanced tumor selectivity. Porphyrins tend to be preferentially absorbed and retained by tumor tissues mainly through low-density lipoprotein receptor-mediated endocytosis [223]. Collaborative studies with Swiss researchers have revealed that neutral meso-pyridylporphyrin conjugates with organometallic Ru(η^6 -arene)Cl₂ moieties exhibit a cytotoxic effect on ME300 human melanoma cells upon activation with visible light. Similar findings were reported by Swavey et al. Furthermore, which focused on a mixed-metal supramolecular complex, especially $[(\text{bpy})_2\text{Ru}(\text{dpp})]_2\text{RhCl}_2^{5+}$ which has been shown to effectively photocleave DNA when exposed to visible light. This complex combines two ruthenium light absorbers with a central rhodium atom which form a unique excited state known as metal-to-metal charge transfer (MMCT). This is different from other systems that rely on metal to ligand charge transfer (MLCT) states that do not exhibit DNA photocleavage. The findings suggest potential for developing new DNA-cleaving agents based on this structural motif, with implications for both research and therapeutic applications in molecular biology. Gianferrara et al. reported on the synthesis and characterization of various new Ru-porphyrin conjugates, which included both Ru(II) fragments and Ru (II) coordination compounds. Among these, water-soluble tetracationic Ru-TedabpyPP compounds displayed phototoxic effects with cell proliferation inhibition after exposure to visible light within the range 590-700 nm in MDA-MB-231 breast cancer cell line [224], [225].

IV.5. Arene implications within Ru complexes

As evidenced by previous studies, investigations for alternative metal-based anticancer agents are recurring with Ru compounds showing high potency and promising results. Despite developing numerous Ru-based anticancer agents, none have achieved clinical application. Even though NAMI-A and KP1019 have progressed to clinical trials and demonstrated prospective efficacy, extensive research continues to investigate Ru-based drugs as novel anticancer therapies [226], [227]. Unfortunately, organometallic compounds are unstable and prone to decomposition when exposed to water and air. However, numerous organometallic complexes have been identified to exhibit aqueous solubility and stability. Jaouen introduced the term “bioorganometallic chemistry” in 1985, growing the interest in organometallic anticancer drug discoveries [228]. Anti-tumoral and anti-metastatic arene-Ru complexes idea started with the pioneering work of Tocher et al. in 1992 who conducted the first study that exhibited augmented toxicity after conjugating metronidazole [1- β -(hydroxyethyl)-2-methyl-5-

nitro-imidazole] anti-cancer agent coordinated to a benzene ruthenium dichloride fragment [229], [230]. Subsequently, it was extensively investigated through the work of Sadler and Dyson. The work of Sadler's team has focused on a series of arene-Ru compounds studied on A2780 ovarian cancer models *in vitro* and *in vivo*. They demonstrated that the treatment didn't exert cross-resistance in cisplatin-resistant models or even high toxicity which is quite promising. Concerning Dyson's work, a series of arene-Ru complexes named RAPTA (Ru arene PTA) were synthesized using 1,3,5-triaza-7-phosphaadamantane (PTA) as ligand. These complexes were examined biologically and RAPTA-C (η^6 -*p*-MeC₆H₄Prⁱ)Ru(pta)Cl₂ showed great efficacy through several pathways including p53/JNK pathway (**Figure 44**) [231], [232]. The fundamental structure of RAPTA is defined by its coordination complexes where Ru metal center is coordinated to arene and various ligands such as phosphine ligands that augment its biological efficacy. These compounds exhibit anticancer properties through several mechanisms such as inducing apoptosis in cancer cells, suppressing tumor growth, and disrupting angiogenesis. This is supported by studies showing a reduction in mature blood vessels in tumors treated with RAPTA-C in athymic mice bearing LS174T colorectal adenocarcinoma [233]. Another study conducted by Dyson's team in 2008, where they fabricated another series of RAPTA adduct complexes and characterized them. Upon their study on cancer cell lines, they showed a high cytotoxicity on breast cancer (T-47D) and colon cancer (WiDr) cell lines [234]. It also demonstrated the importance of ligand choices on the biological activity of these complexes. Additionally, RAPTA-C stability profile was well-characterized and showed a promising stability in aqueous environments. Some factors can influence its stability such as ligand modifications, pH changes and interactions with biomolecules (proteins and nucleic acids) [235].

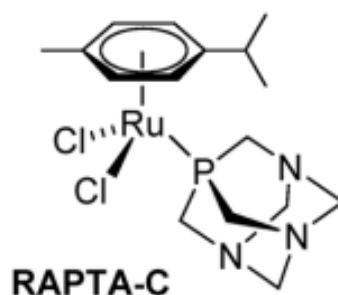


Figure 44: Chemical structure of RAPTA-C [233]

In 2009, two different tetranuclear arene-Ru metallacycles have demonstrated a biological advantage. The complexes $[(\eta^6$ -*p*-cymene)₄Ru₄(μ -oxanato)₂(bpy)₂]⁴⁺ (**Figure 45 a**) and $[(\eta^6$ -*p*-cymene)₄Ru₄(μ -dihydroxybenzoquinonato)₂(bpy)₂]⁴⁺ (**Figure 45 b**) interact with DNA due to the oxanato derivatives, and exert anti-proliferative effects against various cancer cell lines including Colo320, MCF-7 and A549 corresponding to colorectal cancer, breast cancer, and lung cancer cell lines, respectively [236], [237].

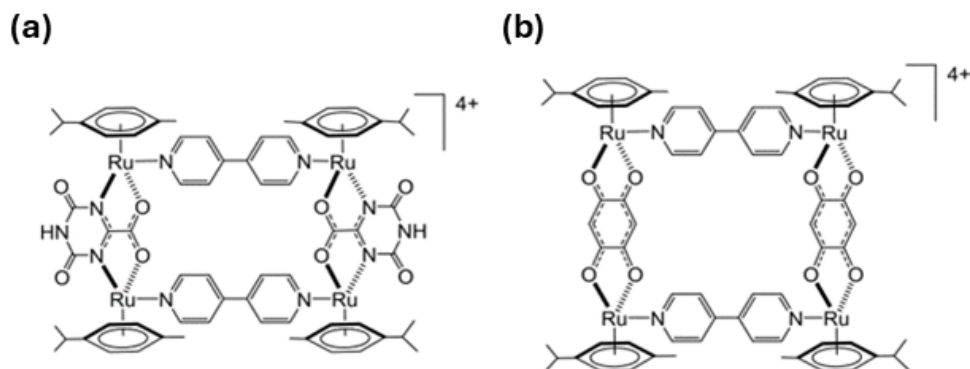


Figure 45: Biologically active arene-Ru metalla-assemblies with tetranuclear molecular structures [236]

Our chemist collaborators focused on a step-controlled strategy for synthesizing the arene-Ru assemblies in which the metal based elements such as the metallaclips also called “spacers” and metallapanel are well-subjected to prior organization. These elements can be confined and characterized or can be synthesized and react without being purified. In both ways, the formed product is the same and the synthesis of the arene-Ru assemblies requires this methodology. They have used dinuclear arene-Ru complexes with tetradentate bridging ligands which form highly stable dinuclear complexes in which some of them can be subjected to further functionalization (**Figure 46 a**). The dinuclear complexes represented, in **Figure 46 b**, are all *cis* isomers which represents the only coordination responsible for the formation of a discrete assembly. Nevertheless, *cis-trans* interconversion might occur rapidly depending on the nature of the ligands [236].

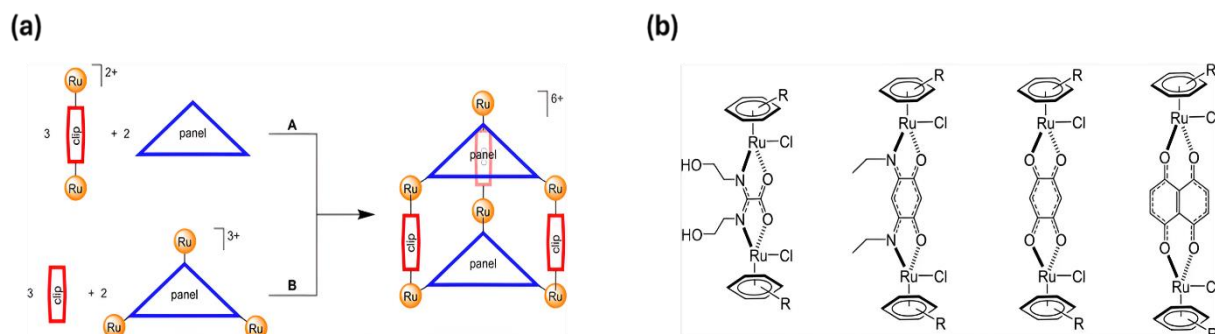


Figure 46: (a) Formation of arene-Ru metallaprisms from metallapanel and (b) dinuclear arene-Ru metallaclips [236]

IV.6. Arene-Ru metal assemblies as PS delivery systems

In a further attempt to address the solubility and stability challenges of Ru-based PS, metal assemblies have been receiving substantial attention, but these systems have remained relatively unexplored as vectors for drug encapsulation. Numerous groups have looked at the building of transition metal complexes with polydentate ligands to create supramolecular structures that are spatially different. There has been much research done on the precise arrangement of coordination blocks and linear ligands to create square assemblies, with four metal centers bridged by four equivalent bidentate ligands, and rectangular assemblies, with four metal centers bridged by ligands of varying lengths. A few years later, discrete geometries in three dimensions were produced using the same technique. Up to now, a wide range of two- and three-dimensional structures with square planar geometries made of transition metals have been created. These molecular assemblies have been used to create isolation

environments that allow PS to enclose and protect its visitors, who may include molecules that are unstable or sensitive. These assemblies have been referred to as “host-guest” systems [236], [238], [239], [240]. This term was first invented by the pioneering work of Jean-Marie Lehn, Charles J. Pedersen, and Donald J. Cram as they won the first Nobel Prize in Chemistry in 1987 for the development of molecules with highly selective structure-specific interactions [241].

In 2008, our Swiss collaborator proved the potential of ruthenium-metallaprisms $[\text{Ru}_6(p\text{-cymene})_6(\text{tpt})_2(\text{dhbq})_3]^{6+}$, $[\text{Ru}_6(p\text{-cymene})_6(\text{tpt})_2(\text{dchq})_3]^{6+}$, $[\text{Ru}_6(\text{C}_6\text{Me}_6)_6(\text{tpt})_2(\text{dhbq})_3]^{6+}$, and $[\text{Ru}_6(\text{C}_6\text{Me}_6)_6(\text{tpt})_2(\text{dchq})_3]^{6+}$ to encapsulate square planar complexes and aromatic molecules. The inclusion systems can be formed when large aromatic molecules including pyrene, fluoranthene, benzo[e]pyrene, triphenylene, or coronene are present to give the assembly of interest. Fortunately, the incorporation of pyrene is flexible as it can be included even if it carries a functionalized aliphatic substituent. This dynamism paved the way for a synthesis of arene-Ru metallaprismatic cages that have the potential to encapsulate aromatic and functionalized aromatic groups so that they can be used as delivery vectors. The host-guest systems were further elaborated to include compounds of interests including PSs (**Figure 47**) [242].

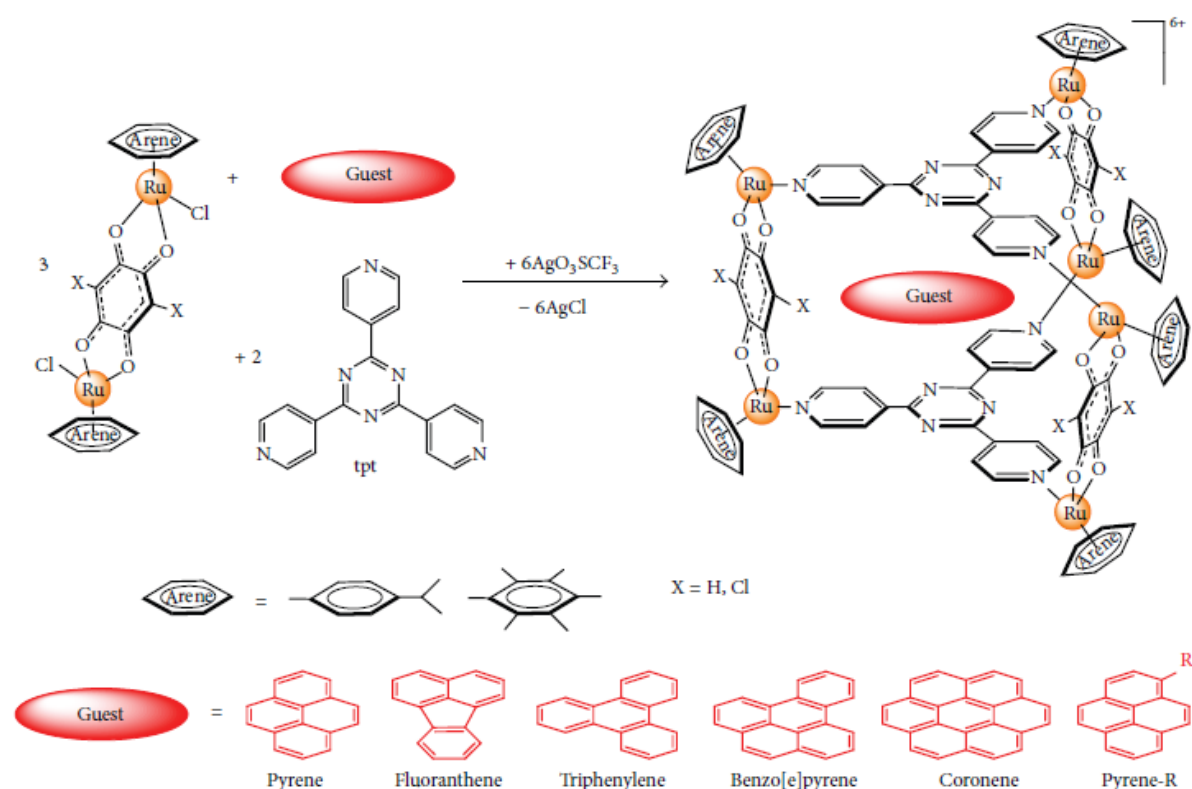


Figure 47: Synthesis of the metalla-prisms and the molecular structures of different guests that can be included into various host-guest systems [242]

Different forms of arene-Ru metal cages can be obtained such as prismatic and cubic cages. The metallaprism $[\text{Ru}_6(p\text{-cymene})_6(\text{tpt})_2(\text{dhbq})_3]^{6+}$ and the large octanuclear metalla-cube $[\text{Ru}_8(p\text{-cymene})_8(\text{dhbq})_4(\text{tbpv})_2]^{8+}$ (tbpv: 1,2,4,5-tetrakis {2-(4-pyridyl) vinylbenzene}) are both hydrophilic allowing the encapsulation and delivery of porphyrin intracellularly (**Figure 48**). The release of porphyrin showed to be higher from the cubic than from the prismatic cages due to its larger dimensions and its phototoxicity was absent when it was still present inside the cage [242]

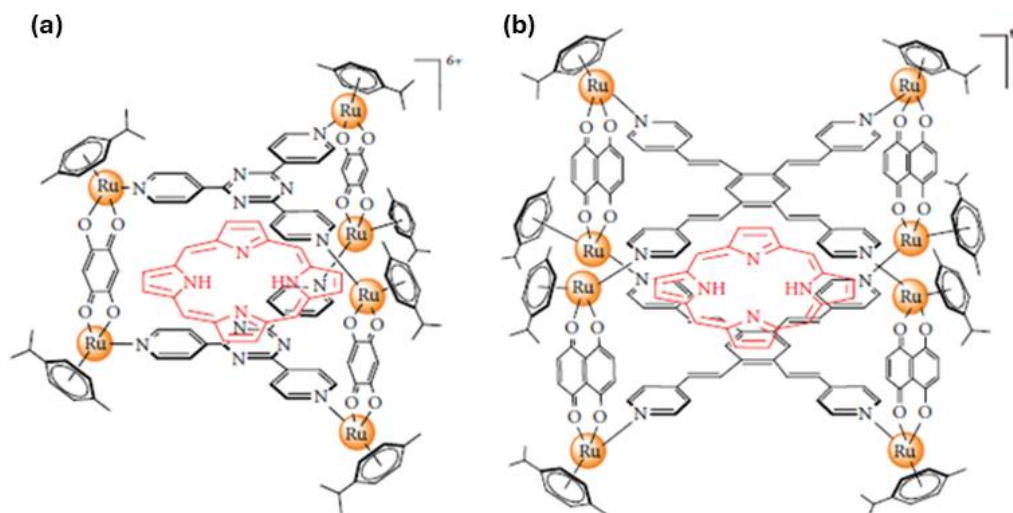


Figure 48: Examples of the different host-guest systems where the guest can be included in the cavities of (a) prismatic or (b) cubic metallacages [242]

Numerous metal assemblies have performed an essential role as host systems, but arene-Ru has gained special consideration because of its advantageous characteristics. The initial compound, the arene-Ru dimers are uncomplicated to synthesize, inert, and stable at room temperature. Additionally, they are generally highly soluble in traditional organic solvents, giving them great interest in biological applications [243], [244].

Several studies have shown that employing arene-Ru-based metal cages as vehicles can address the poor solubility of PSs in two different ways:

- The first type of cage enhances the solubility of these organometallic complexes in biological fluids and can transport and release PS into target cells by hosting them as guests in their internal cavities (**Figure 49 a**).
- The second type of cage depends on the PS being integrated into the metal cage's original structure, which guarantees the PS's optimal physiological solubility and continuous availability for illumination (**Figure 49 b**).

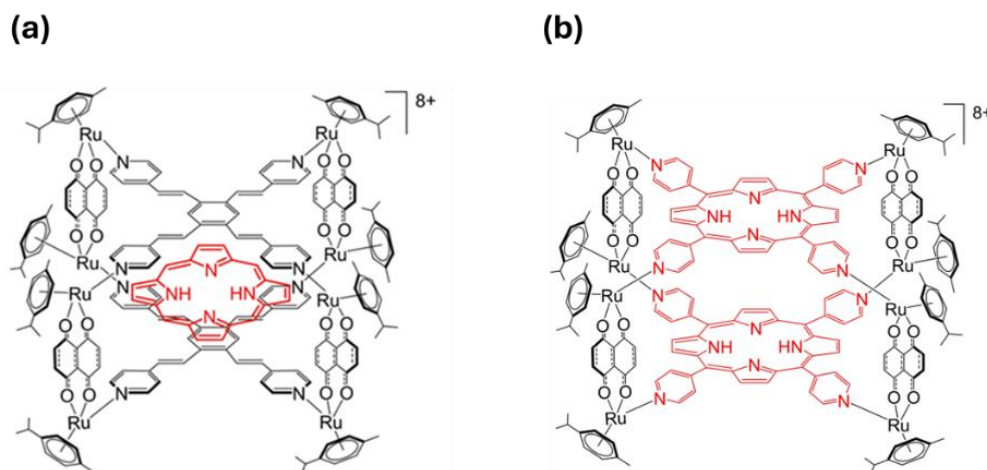


Figure 49: (a) Encapsulation or (b) functionalization of PS in arene-Ru metalla-assemblies [236]

Metal cages are constructed from two main blocks:

- The bimetallic arene-Ru complex (spacer) acts as the edges of the cage. A tetradentate spacer ligand separates the two Ru atoms, determines the distance between them, and defines the size of the cage.
- The panel ligand determines the shape of the metal cage such as prismatic and cubic metal cages.

The internal cavity of the cage is hydrophobic which permits the internalization of planar compounds containing hydrophobic groups that are added to the reaction mixture alongside the panel ligands. If the structure and size of these compounds permit their internalization, these compounds will end up in the cavity through hydrophobic affinity. This is the approach used to introduce poorly water-soluble PS into metal cages for effective delivery into cells [243].

Whereas the second type of metal cage is constructed so that the PS is an integral component of the cage structure and used as a panel ligand. The PS containing pyridine substituents can be conjugated to Ru atoms in a way similar to that of triangular panels. This new encapsulation strategy in which the PS is a part of the cage's structure rather than a guest in the internal cavity of the cage has provided a major advantage in improving PDT efficiency. Indeed, once the cage has been integrated into the cell, it is no longer necessary to release the PS to ensure its activity [245], [246].

Several porphyrin derivatives have been previously investigated in PDT to treat various diseases with promising results. For this, in collaboration with chemists, we decided to study porphin, the simplest form of porphyrin PS, for its initial photosensitizing characteristics from which different complex PSs can be derived known as "porphyrin derivatives". Porphin possesses advantageous photophysical and photochemical characteristics that distinguish it from other PSs. This includes its high rigidity and good coplanarity of its large cyclic structure composed of four conjugated pyrrole rings interconnected by methine bridges. It has a versatile structure that can be easily chemically modified and functionalized for optimal photo efficiency in various applications. It exhibits strong UV-visible absorption with a maximum absorption around the therapeutic window of 630 nm which is lower than that of chlorins (644 nm) and bacteriochlorins (736 nm) with fluorescence at room temperature. Additionally, they are derived from naturally occurring compounds like heme which makes them more biocompatible and less toxic than other systemic PSs. They almost have a facilitated physiological metabolism and clearance providing safer profiles and reducing long-term toxicity. They also exhibit strong photostability permitting their long-term effectiveness, high photodynamic activity through efficient electron transfer, and almost negligible dark toxicity [247], [248], [249].

The distinctiveness of PDT as an anticancer therapy depends fundamentally on the local generation of cytotoxic ROS in tumor tissues, inducing cell death. Indeed, the rapid proliferation of cancer cells causes a reduction in O₂ concentrations in the target tissue which may result in less efficient ROS production.

To overcome this obstacle, some research groups have proposed oxygenating tumor tissue with hyperbaric oxygen therapy (HBO₂) before PDT. Additionally, some of these Ru complexes have hydroxide groups or other substituents in the arene ligands that may help to increase the presence of oxygen species, which in turn might produce more ¹O₂ and boost the generation of ROS [250].

Following the synthesis of these proprietary metal assemblies by our Swiss collaborators, Gallardo-Villagrán was the first to test this type of vectorized molecules on an *in vitro* model of rheumatoid arthritis. Indeed, this study demonstrated the cytotoxic effects of several types of prismatic and cubic arene-Ru-based metal cages for the functionalization of different types of PS for PDT. The results obtained were very encouraging, with IC₅₀ values in the nanomolar range and no cytotoxicity in the dark [251].

In our investigation, the porphin PS is lodged within the internal cavity of prismatic arene-Ru metallocages. Two different cages were implemented which are **M1** [(η⁶-*p*-cymene)₆Ru₆(donq)₃(tpt)₂] [CF₃SO₃]⁶⁺ and **M2** [(η⁶-*p*-cymene)Ru]₆(dotq)₃(tpt)₂][CF₃SO₃]⁶⁺ containing arene-Ru vertices, panels (tpt = 2,4,6-tris(pyridin-4-yl)-1,3,5-triazine) and spacers

(donq = 5,8-dioxido-1,4-naphthoquinonato; dotq = 6,11-dioxido-5,12-naphthacenedionato) that act as edges [251] (**Figure 50**).

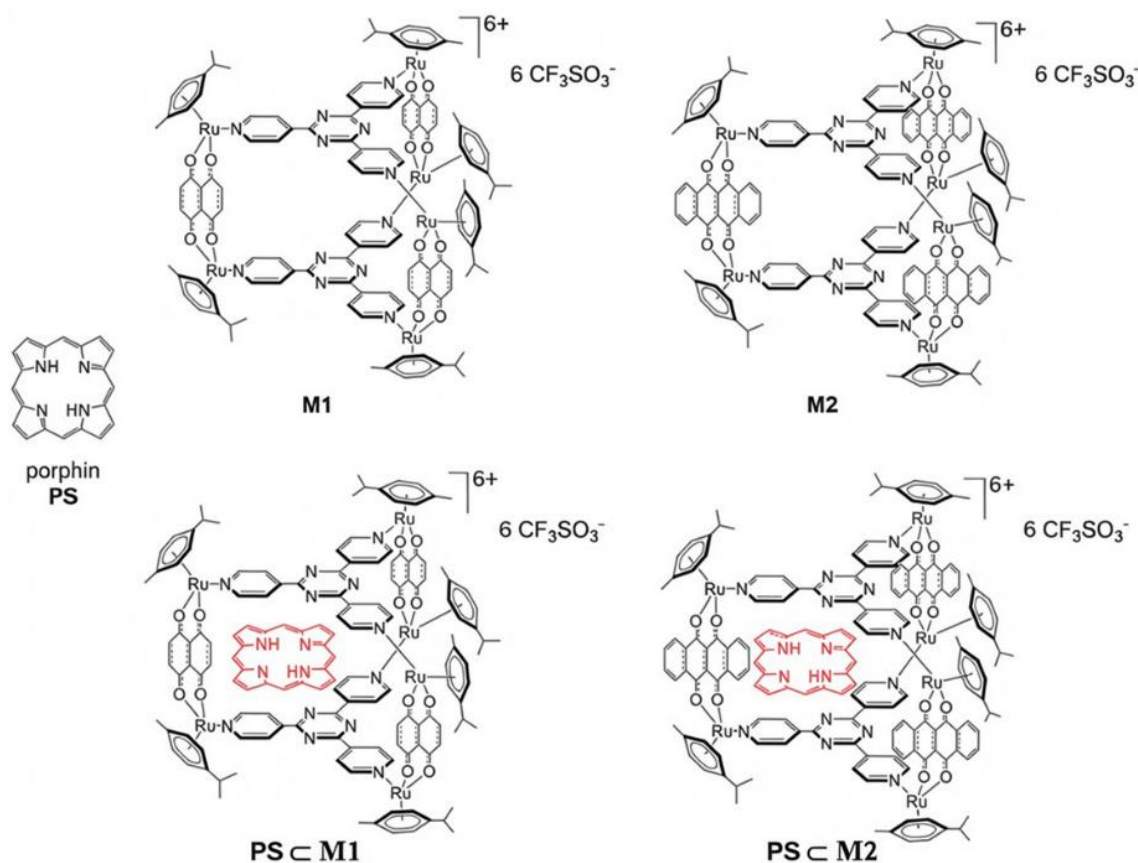


Figure 50: The host-guest systems investigated in our study with porphin PS acting as guests.

In this project, we focused on investigating the effect of porphin PS encapsulated within the prismatic Ru assemblies on human colorectal cancer cell lines. This interest is based on the exceptional properties of this metal assembly. In fact, this encapsulation structure offers our treatment several advantages [243], [244]:

- a- Combining the cytotoxic effect of porphin with that of Ru to enhance the effect of PDT.
- b- Porphin has poor solubility in biological media due to its planar structure and lack of polar groups, so its encapsulation ensures cellular internalization.
- c- This prismatic metal assembly contains ligand substituents, such as hydroxide groups, that could potentially promote ROS generation.
- d- Once formed, the Ru-based assembly is stable in its environment.

All these features make our system one of the best PS encapsulation systems for improving PDT efficacy.

The emergence of therapeutic approaches for the focal treatment of cancerous lesions in the colon is indicative of an evolution in the field of cancer research. In particular, CRC remains a formidable challenge as it ranks among the primary cancer types in terms of incidence and mortality. Standard treatment options including surgery, radiotherapy, and chemotherapy do not often show success, especially in typical cases of cancer metastasis and recurrence with high resistance to treatments. Hence, focusing on developing innovative CRC therapies is necessary for providing a selective targeting of the tumor and limit the drawbacks accompanied by conventional cancer therapies. Among these approaches, PDT emerged to act on tumor cell destruction while preserving the surrounding healthy tissues. It is based on the administration of a PS which is taken up by cancer cells and activated by light to induce oxidative chemical reactions leading to tumor destruction. Among the PSs used currently, tetrapyrrole derivatives including porphyrins, chlorins, bacteriochlorins, and phthalocyanines show a constrained application due to their photophysical properties such as their low solubility and ability to form molecular aggregations in biological media which diminish the efficacy of their intravenous administration and tumor selectivity. Consequently, there is an ongoing effort in the research community to discover and develop better PS with enhanced therapeutic potential in PDT. In this manner, Ru conjugation to PS has appeared as a promising approach, and especially the coupling of Ru with polypyridyl ligands to porphyrins has garnered significant interest for their photoactive DNA cleavage properties. Ru has been recently integrated into organometallic assemblies that can act as delivery vectors of PS to the tumor cells promoting optimal efficacy and selectivity.

This research project aims to further advance this field by investigating the anticancer potential and the underlying mechanisms of action of innovative prismatic arene-Ru metallacages encapsulating porphin PS in their inner cavity as an advanced drug delivery system. Our objective was obtained through *in vitro* assays testing to evaluate these compounds as PS against human CRC cell lines HCT116 and HT-29 which are classified into stage I and stage II, respectively. The assays are performed to attain the following purposes:

- Investigation of whether the presence of two additional aromatic rings in the structure of the spacer of the arene-Ru cage can significantly enhance the overall anti-cancer efficacy
- Detection of the presence of phototoxicity and/or dark toxicity
- Evaluation of the PS internalization into the cell lines and their co-localization in cellular organelles
- Detection of the difference in the antiproliferative activity of the Ru metal cage with and without porphin PS in the inner cavity
- Evaluation of the oxidative stress induction by the PS and its consequences on the cell cycle progression, specifically by evaluating each of sub-G1, G1, S, and G2 phases
- Identifying the induced cell death mechanism through molecular analysis of key cell death biomarkers
- Evaluation of the expression and activity of proteins involved in apoptosis to provide a deeper insight into the involved anti-cancer mechanism

VI.1. Materials

RPMI 1640 media with or without phenol red as well as fetal bovine serum (FBS), L-glutamine, penicillin/streptomycin solution, and type I collagen were supplied by Gibco BRL (Cergy-Pontoise, France). 3-(4,5-dimethylthiazol-2-yl)-2,5-diphenyltetrazolium bromide (MTT), anti- β -human-actin antibody, acetic acid and the "Cell death detection enzyme-linked immunosorbent assay^{PLUS} (ELISA)" kit were purchased from Sigma-Aldrich (Saint-Quentin-Fallavier, France). Anti-human caspase-3, anti-cleaved caspase-3, anti-PARP, anti-Bax, anti-Bcl-2 antibodies and anti-rabbit IgG H&L secondary antibody coupled to horseradish peroxidase (HRP) were supplied by Cell Signaling Technology - Ozyme (Saint-Quentin-en-Yvelines, France). The cellular ROS detection kit containing 2',7'-dichlorofluorescein diacetate (DCFDA) was purchased from Abcam (Paris, France). LysoTracker, MitoTracker, ER-Tracker, HRP-coupled mouse anti-IgG-IgM H&L secondary antibody, Alexa Fluor® 488 annexin V/Dead Cell Apoptosis kit and propidium iodide (PI), 5X sample buffer (Pierce™ Lane Marker Reducing Sample Buffer), polyvinylidene fluoride (PVDF) membrane, and molecular weight marker (Page Ruler Plus Prestained Protein Ladder) are from Thermo Fisher Scientific (Villebon-sur-Yvette, France). Immobilon Western chemiluminescent HRP substrate, RNase A, and protease inhibitor (Complete™ Mini Protease Inhibitor Cocktail) was obtained from Merck (Lyon, France), and caspase-3/7 reagent from Sartorius (Göttingen, Germany).

VI.2. Synthesis of the arene-Ru assemblies encapsulating a photosensitizer

The **PS<M1** and **PS<M2** assemblies were synthesized and purified by our collaborator at the University of Neuchâtel (Switzerland) according to the literature [244]. He synthesized the arene-Ru dinuclear dimers $\text{Ru}_2(\rho\text{-cymene})_2(5,8\text{-dioxido-1,4-naphthoquinonato})\text{Cl}_2$ and $(\text{Ru}_2(\rho\text{-cymene})_2(6,11\text{-dioxido-5,12-naphthacenedionato})\text{Cl}_2$ [252] and the panel ligands 2,4,6-tris(pyridin-4-yl)-1,3,5-triazine [253] following reported methods. The PS, 21H,23H-porphin (PS), was synthesized as reported in the literature [254] and the corresponding lodging into arene-Ru assemblies was attained by host-guest interactions. Stock solutions were prepared at 1 mM concentration in DMSO and stored at -20 °C.

VI.3. Cell lines and culture

Human CRC cell lines HCT116 and HT-29 were purchased from the American Type Culture Collection (ATCC) (LGC Standards, Molsheim, France). The HCT116 cell line was isolated from stage I colorectal carcinoma in an adult male. The HT-29 cell line originates from a stage II colorectal carcinoma of a 44-year-old female. Cells were grown in RPMI 1640 medium for culturing and were supplemented with 10% FBS, 1% L-glutamine, 100 U/mL penicillin, and 100 $\mu\text{g}/\text{mL}$ streptomycin. Cultures were in a humidified atmosphere containing 5% CO_2 in an incubator thermostatically regulated at 37°C. For all *in vitro* experiments, the cells were seeded at 1.2×10^4 and 2.1×10^4 cells/ cm^2 for HCT116 and HT-29 cells, respectively.

VI.4. Treatment and illumination

The stock solutions of **PS<M1** and **PS<M2** assemblies were diluted in a culture medium to obtain the final concentration required, and the medium was replaced by a red phenol-free culture medium before illumination. The maximal concentration of DMSO in the culture medium was less than 0.1% in all cases which is non-toxic.

Illumination of cells was done using a Lumidox® II device (Analytical Sales and Services, Flanders, New Jersey, USA) under red visible light at 630 nm, at 75 J/cm^2 , and fluence rate of 70 mW/LED , for 6 min.

VI.5. Cell viability assay

This assay relies on the reduction of the tetrazolium salt MTT to formazan crystals by the mitochondrial enzyme succinate dehydrogenase. This reaction represents the metabolic activity of the cells and results in the formation of violet precipitates within the mitochondria, with the amount of precipitate being directly proportional to the number of viable cells. The formazan crystals are dissolved in DMSO, and the optical density at 550 nm is measured using a spectrophotometer. This measurement allows for the quantification of living cells and the comparison of cell viability between treated and control groups, whether or not they were exposed to illumination. HCT116 and HT-29 cells were seeded into 96-well plates at a pre-determined density and cultured for 24 h in 100 μ L of culture medium. After 24 h of cell adhesion and growth, cells were treated with **PS<M1** and **PS<M2** which were diluted in RPMI 1640 medium to obtain an appropriate range of concentration, or left untreated, for 24 h. The medium was then replaced with 100 μ L of red phenol-free culture medium, and the cells were either illuminated or not using a Lumidox lamp (630 nm). At 12 h, 24 h and 48 h post-illumination, 10 μ L of MTT solution (5 mg/mL in phosphate-buffered saline (PBS)) was added to each well. After 3 h of incubation at 37°C, the medium was removed and 100 μ L of DMSO was added per well to solubilize the formed formazan crystals. The absorbance of each well was then measured at 550 nm using a spectrophotometer (Thermo Scientific, Multiskan FC). Wells containing only 100 μ L of DMSO served as blanks. Cell viability is expressed as a percentage relative to the control cells: (mean OD of treated cells / mean OD of control cells) \times 100 \pm SEM. IC₅₀ values for each cell line and compound represent the concentration at which only 50% of cells remain viable compared to control cells. It was expressed as a percentage of cell viability for each treatment condition relative to the untreated cells.

VI.6. Intracellular ROS generation

Cellular ROS generated after the illumination of cells was quantified using 2',7'-dichlorofluorescein diacetate DCFDA substrate which diffuses into the cell and is deacetylated by cellular esterases into a non-fluorescent compound. This compound is then oxidized in the presence of cellular ROS to produce 2',7'-dichlorofluorescein (DCF) which is a fluorescent molecule detectable by flow cytometry (excitation: 485 nm; emission: 535 nm). Cells were seeded in 75 cm² culture flasks for 24 h, then they were treated or not with **PS<M1** and **PS<M2** assemblies at their determined IC₅₀ values. After 24 h, the cells with different treatment conditions were collected and incubated with DCFDA for 30 min before illumination. The quantification of cellular ROS production was determined directly after illumination through CytoFLEX LX (Beckman Coulter). H₂O₂ was used as a positive control at 800 μ M concentration.

VI.7. Cellular internalization and localization

The localization of the compounds within HCT116 and HT-29 cells was determined by confocal microscopy. Cells were seeded into incubation chambers (ibidi μ -Slide 8 wells; Clinisciences, Martinsreid, Germany) coated with a gel prepared by mixing collagen type I (3 mg/mL) and acetic acid (20 mM) and incubated for 24 h before their treatment or not with **PS<M1** and **PS<M2** at their IC₅₀ values. After 24 h of treatment, the cells were labeled with MitoTracker (50 nM), ER-tracker (500 nM), or LysoTracker (50 nM) and then image acquisitions were taken by a Carl Zeiss LSM 510 Meta — \times 1000 confocal laser microscope. The natural fluorescence of the assemblies permitted their observation within the cells with emission (excitation: 405/561 nm; emission: 650/673 nm). Additionally, the excitation/emission wavelengths of the

fluorescent compound allowed proper determination of the localization of the compounds of interest. LysoTracker fluorescence (excitation/emission: 504/511 nm), MitoTracker fluorescence (490/516 nm), and ER-Tracker fluorescence (504/511 nm).

VI.8. Cell cycle analysis

The distinct phases of the cell cycle progression were assessed for both HCT116 and HT-29 cell lines by flow cytometry using PI staining. Cells were seeded into 75 cm² flasks and incubated for 24 h. The treatment or not with **PS<M1** and **PS<M2** assemblies at their determined IC₅₀ values was done after 24 h of incubation. The media was replaced by phenol red phenol-free media. Illumination of cells was carried out after 24 h and then pellets of 1×10⁶ cells were collected at 12 h, 24 h, and 48 h post-illumination. The cells were washed with PBS and fixed with the addition of 1 mL of chilled 70% ethanol in PBS and stored at -20°C. Before flow cytometry analysis, the cell pellets were washed with cold PBS and centrifuged, then they were resuspended with 500 µL of cold 1X PBS along with 30 µL of RNase A (10 mg/mL) and incubated for 30 min at room temperature. After incubation, the cells were stained with 25 µL of PI (1 mg/mL) allowing the determination of the percentage of cells present in each phase of the cell cycle using the FACs system (BD Biosciences, San Jose, CA, USA). The results were displayed as cytograms, showing peak fluorescence (FL3, PI fluorescence) with respect to the number of cells analyzed. Pellets of 1×10⁶ cells were analyzed at a rate of 300 cells per second. The cell distribution according to DNA content representing different phases of the cell cycle was determined from these cytograms using ModFit LT software (Verity Software, USA).

VI.9. Apoptotic Assays

VI.9.1. Annexin V-FITC/PI dual staining

The application of annexin V, a protein with a strong affinity to phosphatidylserines, is the principle of this method of apoptotic analysis. Cells in the early stages of apoptosis can be identified by combining annexin V with the fluorochrome FITC. This staining along with the PI staining permits the differentiation between the viable cells, early apoptotic cells, and late apoptotic cells. Phosphatidylserines are normally exposed to the intracellular compartment. However, the ATP-dependent flip-flop phenomenon, mediated by the enzyme flippase, is one of the first steps in cell death. It results in the translocation of phosphatidylserines to the exterior side of the plasma membrane. Consequently, cells in the early stage of apoptosis will be stained with annexin V. PI is a DNA-intercalating agent that only penetrates cells when the plasma membrane is disrupted which is the case during necrosis or in the late stages of apoptosis. Annexin V negative/PI negative cells indicate viable cells; annexin V positive/PI negative indicates early apoptotic cells; and annexin V positive/PI positive indicates late apoptotic cells. The condition corresponding to annexin V-negative and PI-positive indicates nuclear debris and possible necrosis. Cells were seeded into 75 cm² flasks and were treated or not by the determined IC₅₀ values of **PS<M1** and **PS<M2** assemblies after 24 h of incubation. Then, cells were illuminated or not and were harvested by trypsin at 12 h, 24 h, and 48 h post-illumination. Cell pellets of 2.5 × 10⁵ for each condition were prepared, washed in PBS, centrifuged, and resuspended in 300 µL of Annexin V lysis buffer (1X). The cells were labeled with 5 µL Annexin V-FITC and 1 µL of PI (0.1 mg/mL) and then were kept in the dark and at room temperature for 15 min. The percentage of cells undergoing apoptosis was then determined by CytoFLEX LX (Beckman Coulter).

VI.9.2. Quantitative analysis of caspases-3/-7

Activated caspases-3/-7 were quantitatively analyzed using the IncuCyte® S3 live cell analysis system (Sartorius) with a green caspase-3/-7 reagent. This method involves tracking the green fluorescence emitted by the reagent through the acquisition of image and video scans of the cells over time. The reagent, NucView™488, combines the caspase-3/-7 recognition sequence (DEVD) to allow the measurement of apoptosis as it occurs. Initially non-fluorescent, the reagent is added to the culture medium and accumulates inside cells. In living cells, the DEVD sequence is not cleaved by caspases-3/-7, so no fluorescence emission is detected. However, in apoptotic cells, activated caspases-3/-7 cleave the DEVD sequence triggering the release of the dye and the production of green fluorescence in the nuclei, as the dye can bind to the DNA, enabling the real-time monitoring of caspase-3 enzymatic activity. HCT116 and HT-29 cells were seeded in 96-well plates, cultured for 24 h, and then treated with **PS-M1** and **PS-M2** at their respective IC₅₀ values. After 24 h, the culture medium was replaced with red phenol-free medium, and cells were either illuminated or left untreated. They were then exposed to the caspase-3/-7 green reagent (5 μM) and placed in the IncuCyte® S3 system. Images were captured every 2 h, with four images per well at 10x magnification in both phase contrast and green fluorescence. At each time up to 48 h, the apoptotic cells were quantified using IncuCyte® software (Sartorius) by determining the ratio of fluorescent cells to the total number of cells in each well.

VI.9.3. Protein extraction and western blot

HCT116 and HT-29 cells were seeded in 75 cm² culture flasks at the specified density and incubated for 24 h. They were then treated with either **PS-M1** and **PS-M2** at their respective IC₅₀ values or left untreated. After 24 h, the medium was replaced with red phenol-free medium, and the cells were subjected to illumination or not. Cells of different conditions were collected 12 h, 24 h, and 48 h post-illumination, washed with PBS, and pelleted by centrifugation at 1,500 rpm and 4°C for 5 min to extract and identify specific proteins of interest. For total protein extraction, cells were lysed with RIPA lysis buffer (containing 50 mM HEPES, pH 7.5; 1% Deoxycholate; 1% Nonidet P-40; 0.1% SDS; 150 mM NaCl; and 20 μg/mL Aprotinin) with a protease inhibitor solution. After centrifugation at 12,000 rpm for 20 min at 4°C, the lysates were collected. The protein levels were quantified using the Bradford colorimetric method after acquiring the measurements on the spectrophotometer at 595 nm and compared to a standard curve of bovine serum albumin (BSA) ranging from 0 to 2 mg/mL. The exact calculated quantity of protein extracts was mixed with 5X sample buffer and denatured at 95°C for 5 min. Then they were separated on 12.5% SDS-PAGE gels for approximately 2 h at 90 V in migration buffer (25 mM Tris-HCl, pH 8.3; 192 mM Glycine; and 0.1% SDS) using the XCell SureLock Mini-Cell Electrophoresis System (Thermo Fisher Scientific). Post-electrophoresis, proteins were transferred to PVDF membranes (Amersham Pharmacia Biotech, Saclay, France) that were priorly activated by methanol, rinsed, and equilibrated with the gel in transfer buffer (50 mM Tris; 380 mM Glycine; 0.1% SDS; and 20% Methanol). Transfer was conducted at 100 mA for 90 min. The primary antibody was applied in blocking buffer overnight at 4°C with agitation. After several rinses with TBS-Tween 0.1%, the membrane was incubated with the appropriate secondary antibody for 1 h at room temperature with agitation. Rabbit secondary antibodies (1:2000) and mouse secondary antibodies (1:5000) were used. Excess secondary antibody was removed by rinsing in washing buffer. Apoptosis-related human proteins were studied by membrane probing with primary anti-PARP-1 (1:1000), primary anti-cleaved caspase 3 (1:1000), and primary anti-pro-caspase 3 (1:1000), primary anti-Bax (1:1000) and primary anti-Bcl-2 (1:1000). For loading control, primary human anti-β-actin (1:5000) was used. After

incubation with the primary antibodies overnight at 4°C, appropriate secondary antibodies were used to incubate the membranes for at least 1 h. The blots were revealed using Immobilon Western Chemiluminescent HRP substrate which is based on a chemiluminescence reaction in a G:BOX system (Syngene, Cambridge, UK).

VI.9.4. DNA fragmentation

The “Cell Death Detection Enzyme-Linked Immunosorbent assay^{PLUS}” kit was used to assess the level of DNA fragmentation in the different cell conditions. After the cells were seeded in 75 cm² flasks for 24 h, the cells were treated or not using the IC₅₀ values of **PS_CM1** and **PS_CM2** assemblies. After 24 h, the cells were illuminated or not and cell pellets of 2 × 10⁵ cells were collected for each condition after 12 h, 24 h, and 48 h post-illumination. These pellets were then resuspended in 400 µL of lysis buffer and incubated at room temperature for 30 min. After centrifuging at 200 g for 10 min, 20 µL of the supernatant from the lysed cells was transferred into wells coated with streptavidin. Then, 80 µL of a solution containing biotinylated anti-histone antibodies and peroxidase-conjugated anti-DNA antibodies was added to each well. This is followed by a 2 h incubation period with shaking at 300 rpm in the dark. The mono- and oligo-nucleosomes generated by DNA fragmentation were bound by the peroxidase-conjugated anti-DNA antibodies and anti-histone antibodies which themselves were bound to the streptavidin at the bottom of the wells. Following three washes, 100 µL of the peroxidase substrate solution (2,2'-azino-bis (3-ethylbenzothiazoline-6-sulfonic acid “ABTS”) was added to each well. The incubation with the substrate was for 15 min and a color change was observed during and after this period due to the peroxidase enzyme linked to the anti-DNA antibodies. The amount of oxidized ABTS was directly proportional to the level of DNA fragmentation. The reaction was then stopped using a stop solution and the optical density of each condition was measured at 405 nm. A blank reading was obtained using the ABTS solution with a reference wavelength of 492 nm. The average absorbance values (405 nm – 492 nm) were calculated for each condition and compared to those of the control samples. The DNA fragmentation levels were expressed as a fold change compared to the control cells.

VI.10. Statistical Analysis

All data are expressed as the mean ± standard error of the mean (SEM) of at least three independent experiments. The statistical significance of the results was evaluated by a two-tailed unpaired Student's *t*-test and expressed as **p* < 0.05, ***p* < 0.01, and ****p* < 0.001.

VII.1. Cell viability assay

To investigate the effects of our arene-Ru assemblies *in vitro*, we conducted a comprehensive series of experiments using two human CRC cell lines, HCT116 and HT-29. These cell lines serve as well-established models for studying the efficacy of potential chemotherapeutic agents on different stages of CRC. The experiment is based on treating the cells with two compounds, **PS<M1** and **PS<M2**, which are porphyrin-based systems encapsulated within arene-Ru assemblies. Also, the empty assemblies, **M1** and **M2**, which lack the porphyrin component in their inner cavity were tested. This setup allowed us to differentiate between the effects of the porphyrin component and the arene-Ru assembly itself. Following the treatment, the cells were divided into two groups: one exposed to red light illumination (630 nm wavelength and a fluence of 75 J/cm²) and the other kept in the dark. This dual approach enabled us to evaluate the photoactivation-dependent cytotoxicity or “photocytotoxicity” of the compounds. The impact on cell viability was measured at three time points, which are 12 h, 24 h, and 48 h post-illumination, using the MTT assay. This assay is widely recognized for its ability to evaluate cellular metabolic activity and offers a reliable indicator of cell viability and proliferation.

The results of the MTT assay provided critical insights into the cytotoxic potential of these compounds. In the absence of light, no significant cytotoxic effect was observed on either the HCT116 or HT-29 cell lines after treatment with **PS<M1**, **PS<M2**, **M1**, or **M2**, even at 1000 nM concentration. This finding indicates that these compounds are inherently non-toxic to cells under dark conditions (**Figures 51** and **52**). Additionally, the lack of cytotoxicity in the dark strongly suggests that any reduction in cell viability observed under illuminated conditions can be attributed to the photoactivation of the porphyrin component, rather than intrinsic toxicity of the assemblies themselves.

Upon exposure to red light, however, a marked decrease in cell viability was observed in cells treated with **PS<M1** and **PS<M2**, indicating a strong phototoxic effect. This phototoxicity was both dose- and time-dependent, with significant reductions in cell viability detected at 12 h, 24 h, and 48 h post-illumination for both the HCT116 and HT-29 cell lines (**Figures 51** and **52**). The IC₅₀ values, which represent the concentration of the compound required to inhibit 50% of the cells, were determined to be in the nanomolar range for both **PS<M1** and **PS<M2** host-guest systems. These low IC₅₀ values highlight the high potency of these compounds when activated by light.

For the HCT116 cell line, the IC₅₀ values for **PS<M1** were calculated as 666 nM, 602 nM, and 588 nM at 12, 24, and 48 h post-illumination, respectively. Similarly, the IC₅₀ values for **PS<M2** were determined to be 647 nM, 541 nM, and 518 nM at the same time points. In the HT-29 cell line, the IC₅₀ values for **PS<M1** were slightly higher, at 892 nM, 672 nM, and 536 nM, while those for **PS<M2** were 884 nM, 593 nM, and 539 nM at 12, 24, and 48 h post-illumination, respectively (**Figure 53**). The relatively lower IC₅₀ values for **PS<M2** compared to **PS<M1** in both cell lines suggest a slightly higher phototoxic efficacy of **PS<M2**, although both assemblies are highly effective.

Notably, under illuminated conditions, the phototoxicity was significantly pronounced, while in the dark, no IC₅₀ values could be determined, further underscoring the essential role of light activation in the cytotoxic effects observed. Interestingly, the individual components **M1** and **M2**, which do not contain the porphyrin, did not show any significant changes in cell viability under either illuminated or non-illuminated conditions (**Figures 51** and **52**). This finding strongly suggests that the complete **PS<M1** and **PS<M2** assemblies are crucial for the

observed photodynamic activity due to the presence of the porphin PS, with **M1** and **M2** which are mainly used as delivery vehicles of the porphin into the cancer cells, in the studied concentrations.

In summary, these results demonstrate that the **PS◊M1** and **PS◊M2** assemblies possess significant phototoxic activity, leading to substantial reductions in cell viability upon light exposure. The specificity of this phototoxic effect, combined with the lack of intrinsic toxicity under dark conditions, highlights the potential of these compounds as targeted photodynamic PDT agents. Subsequently, the IC_{50} values determined post-illumination will serve as a basis for further exploration of the therapeutic potential and mechanistic aspects of these compounds, including their interactions with cellular components and the pathways involved in cell death.

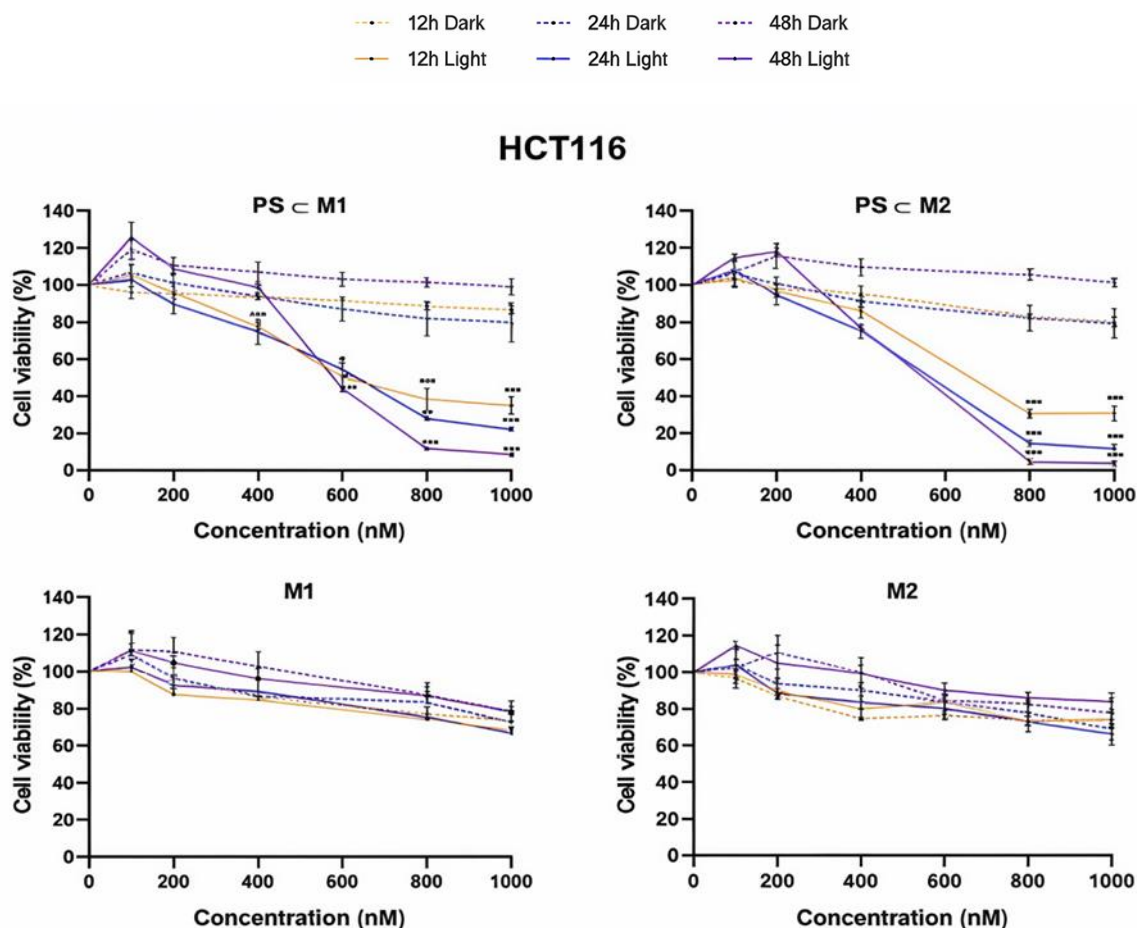


Figure 51: Evaluation of the photocytotoxicity of the arene-Ru assemblies, with or without porphin PS in their inner cavity, in the HCT116 cell line.

HCT116 cell line was cultured in RPMI medium for 24 h. After 24 h, cells were treated or not with **PS◊M1**, **PS◊M2**, **M1** or **M2**. Illumination (630 nm, 75 J/cm²) or not of the cells occurred 24 h after treatment and the cell viability for all the conditions was determined 12 h, 24 h, and 48 h post-illumination. Data are represented as a mean \pm SEM of three independent experiments. * $p < 0.05$, ** $p < 0.01$ and *** $p < 0.001$.

HT-29

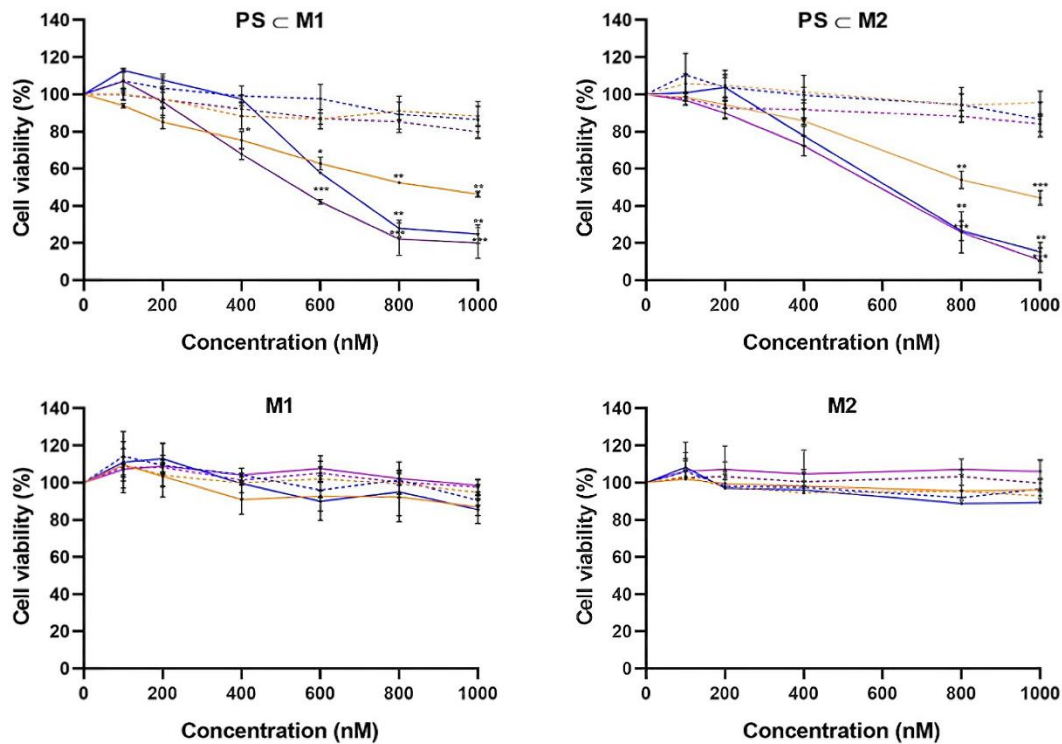


Figure 52 : Evaluation of the photocytotoxicity of the arene-Ru assemblies, with or without porphyrin PS in their inner cavity, in the HT-29 cell line.

HT-29 cell lines was cultured in RPMI medium for 24 h. After 24 h, cells were treated or not with **PS \subset M1**, **PS \subset M2**, **M1** or **M2**. Illumination (630 nm, 75 J/cm²) or not of the cells occurred 24 h after treatment and the cell viability for all the conditions was determined 12 h, 24 h, and 48 h post-illumination. Data are represented as a mean \pm SEM of three independent experiments. *p < 0.05, **p < 0.01 and ***p < 0.001.

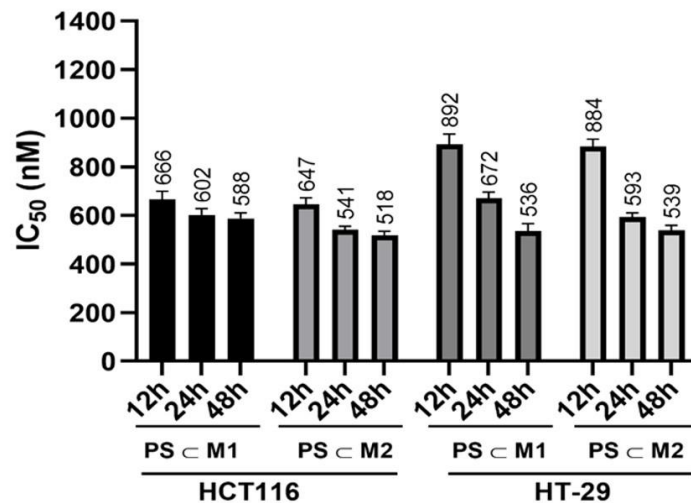


Figure 53: Graphical representation of the IC₅₀ values (nM) determined by MTT assay in the HCT116 and HT-29 cell lines.

HCT116 and HT-29 cell lines were seeded and cultured in RPMI medium for 24 h. After 24 h of incubation, cells were treated or not with **PS \subset M1** or **PS \subset M2**. Illumination (630 nm, 75 J/cm²) or not of the cells occurred 24 h after treatment and the cell viability for all the conditions was determined 12 h, 24 h, and 48 h post-illumination. Data are represented as a mean \pm SEM of three independent experiments.

VII.2. ROS generation

The efficacy of PDT is intrinsically linked to the production of ROS, which plays a pivotal role in the mechanism of cell damage and death induced by PDT. To quantitatively assess the levels of ROS generated by our porphyrin loaded arene-Ru assemblies, we conducted experiments using the DCFDA, a widely useful fluorogenic dye measuring ROS activity in live cell samples. Cells were treated with DCFDA and subsequently analyzed using flow cytometry immediately after illumination. H₂O₂ was used as a positive control to ensure the reliability of ROS detection and to establish a baseline for comparison. The results of these experiments revealed a substantial increase in ROS production in the treated cells following light exposure, compared to both the treated non-illuminated cells and the control cells. This significant increase in ROS levels underscores the effectiveness of light-induced activation of the **PS<M1** and **PS<M2** assemblies in generating cytotoxic ROS species. Specifically, in the HCT116 cell line, treatment with the **PS<M1** assembly under light exposure led to a remarkably high level of ROS production, with a measured value of 88.46%. This level was significantly greater than the 12.79% observed in the absence of light, indicating that ROS production is primarily driven by the photoactivation process (**Figures 54 and 55**). Similarly, the **PS<M2** assembly induced a notable ROS level of 89.20% under light exposure, in contrast to the 16.79% measured in dark conditions. These findings demonstrate that both **PS<M1** and **PS<M2** are highly effective in producing ROS when exposed to light, with ROS levels under illuminated conditions exceeding those in the dark by more than 5 folds.

Parallel results were found with the HT-29 cell line, where ROS levels reached 83.02% and 87.68% for **PS<M1** and **PS<M2**, respectively, under light exposure. These values were significantly higher than the 6.03% and 7.40% observed in the absence of light for **PS<M1** and **PS<M2**, respectively (**Figures 56 and 57**). These data highlight the critical role of photoactivation in the function of the **PS<M1** and **PS<M2** assemblies. The substantial increase in ROS levels following illumination provides compelling evidence of the effectiveness of these assemblies in generating cytotoxic ROS species. This ROS production is a key mechanism through which the **PS<M** assemblies exert their PDT effects, leading to the targeted destruction of cancer cells.

The clear distinction in ROS levels between illuminated and non-illuminated conditions further affirms the effectiveness of these **PS<M** assemblies as promising candidates for PDT applications. The potential of these assemblies to produce ROS offers a controllable and targeted approach to cancer treatment, minimizing damage to surrounding healthy tissues and enhancing therapeutic outcomes.

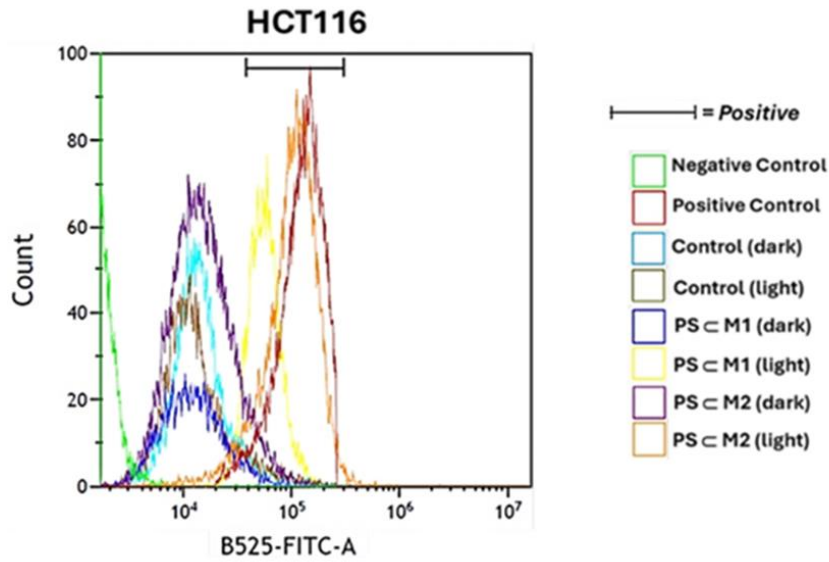


Figure 54 : Evaluation of ROS production by DCFDA staining in the HCT116 cell line.

HCT116 cells were seeded and incubated for 24 h followed by their treatment with **PS<M1** or **PS<M2**. After 24 h, cells were stained with DCFDA and illuminated (630 nm, 75 J/cm²). Immediately after illumination, cells were analyzed using flow cytometry. Quantification of the intensity of fluorescence emitted due to DCF formation is correlated to the level of ROS generation. A shift to the right can be observed with data of flow cytometry in the presence of a high fluorescence intensity which is linked to high DCF formation.

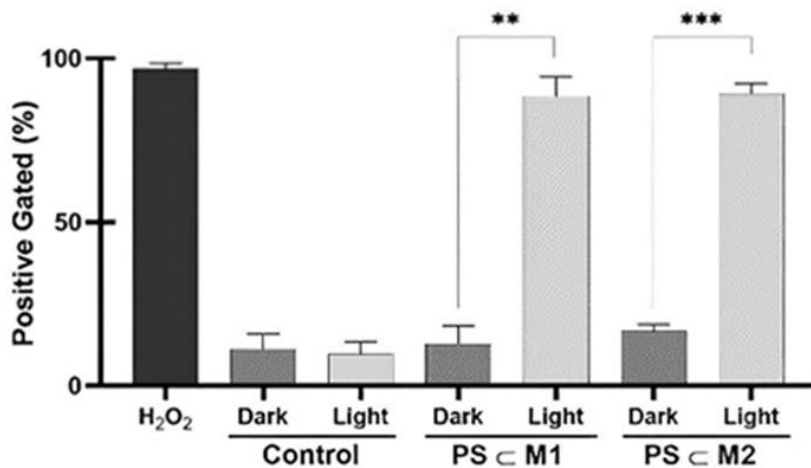


Figure 55: Histogram representing the intracellular ROS production in the HCT116 cell line.

HCT116 cells were seeded and incubated for 24 h followed by their treatment with **PS<M1** or **PS<M2**. After 24 h, cells were stained with DCFDA and illuminated (630 nm, 75 J/cm²). Immediately after illumination, cells were analyzed using flow cytometry. Quantification of the intensity of fluorescence emitted due to DCF formation is correlated to the level of ROS generation. Data are represented by histograms as a mean ± SEM of three independent experiments. **p < 0.01 and ***p < 0.001.

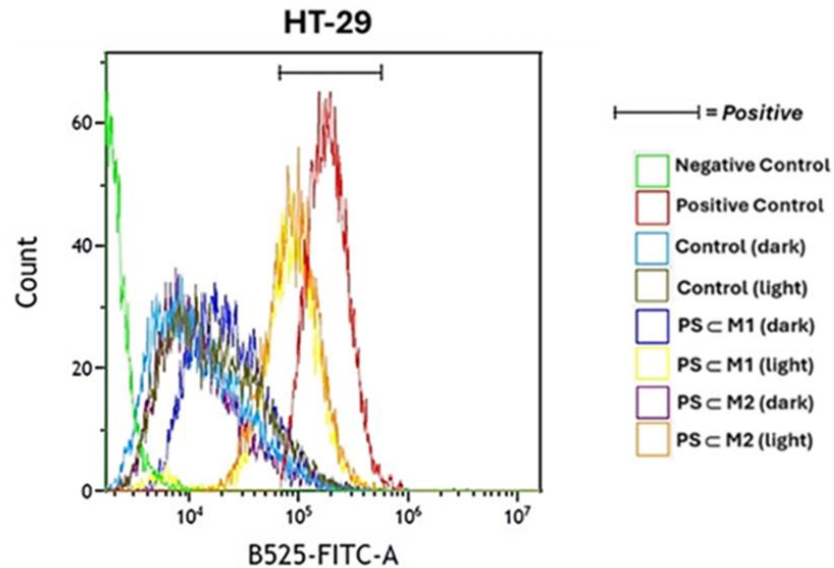


Figure 56: Evaluation of ROS production by DCFDA staining in the HT-29 cell line.

HT-29 cells were seeded and incubated for 24 h followed by their treatment with **PS<M1** or **PS<M2**. After 24 h, cells were stained with DCFDA and illuminated (630 nm, 75 J/cm²). Immediately after illumination, cells were analyzed using flow cytometry. Quantification of the intensity of fluorescence emitted due to DCF formation is correlated to the level of ROS generation. A shift to the right can be observed with data of flow cytometry in the presence of a high fluorescence intensity which is linked to high DCF formation.

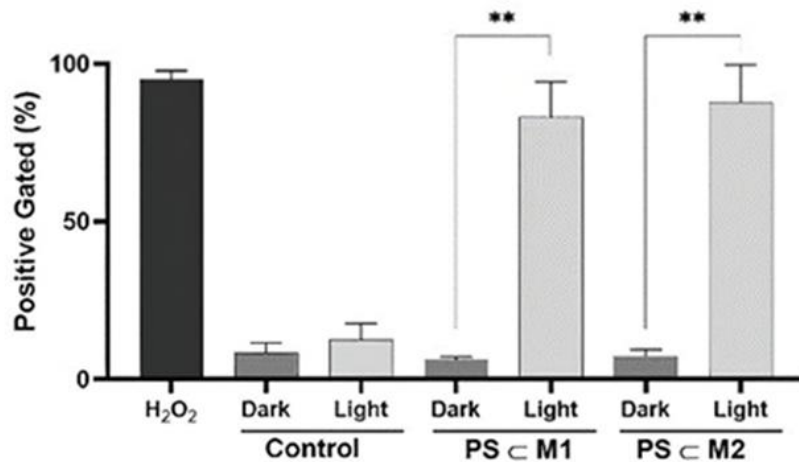


Figure 57: Histogram representing the intracellular ROS production in HT-29 cell line.

HT-29 cells were seeded and incubated for 24 h followed by their treatment with **PS<M1** or **PS<M2**. After 24 h, cells were stained with DCFDA and illuminated (630 nm, 75 J/cm²). Immediately after illumination, cells were analyzed using flow cytometry. Quantification of the intensity of fluorescence emitted due to DCF formation is correlated to the level of ROS generation. A shift to the right can be observed with data of flow cytometry in the presence of a high fluorescence intensity which is linked to high DCF formation. Data are represented as a mean \pm SEM of three independent experiments. ** $p < 0.01$.

VII.3. Cellular localization using confocal microscopy

The intracellular localization of the **PS◁M** assemblies within cells was determined using confocal microscopy, a powerful tool for visualizing and analyzing the spatial distribution of molecules within cellular compartments. Upon internalization of the metallacages into the cells, the guest molecule, porphyrin, is released from the assemblies, enabling it to be excited by light and undergo photoactivation [255]. Porphyrin, which possesses inherent autofluorescent properties in the red or infrared regions, can be efficiently tracked within the cells, providing valuable insights into its intracellular dynamics and localization [256], [257]. Following treatment with **PS◁M1** and **PS◁M2** assemblies, the fluorescence was predominantly observed in the cytoplasm of the HCT116 and HT-29 cells. This cytoplasmic accumulation is a crucial observation as it confirms the successful cellular uptake of these assemblies which primarily interact with cytosolic targets (**Figures 58** and **59**). The cytoplasmic localization of porphyrin PS is significant for understanding the intracellular distribution and potential mechanisms of action of these assemblies, particularly in relation to their ability to exert therapeutic effects through interactions with specific cellular structures.

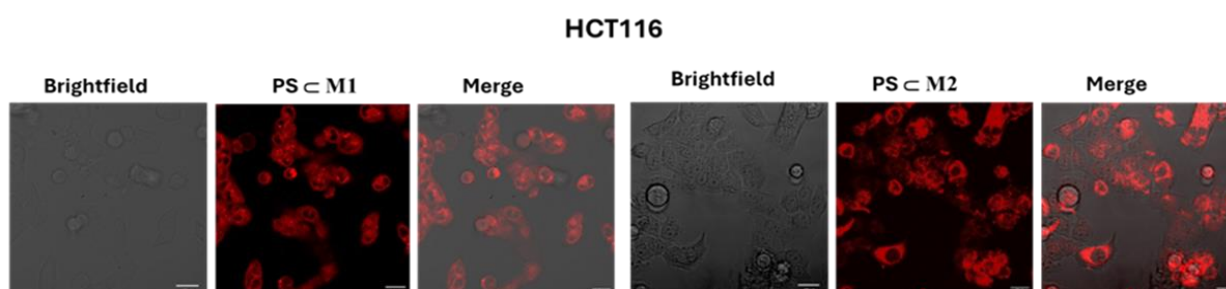


Figure 58: Detection of cytoplasmic localization in the HCT116 cell line after treatment with PS◁M1 or PS◁M2.

Detection of cellular internalization of **PS◁M1** and **PS◁M2** in the HCT116 cell line by confocal microscopy. Cells were seeded into incubation chambers and cultured for 24 h. Cells were then treated with the compounds, and the fluorescence was measured by confocal microscopy (laser Zeiss LSM 510 Meta—x 1000). The internalization was processed using the Image J image-processing software (version 1.54f).

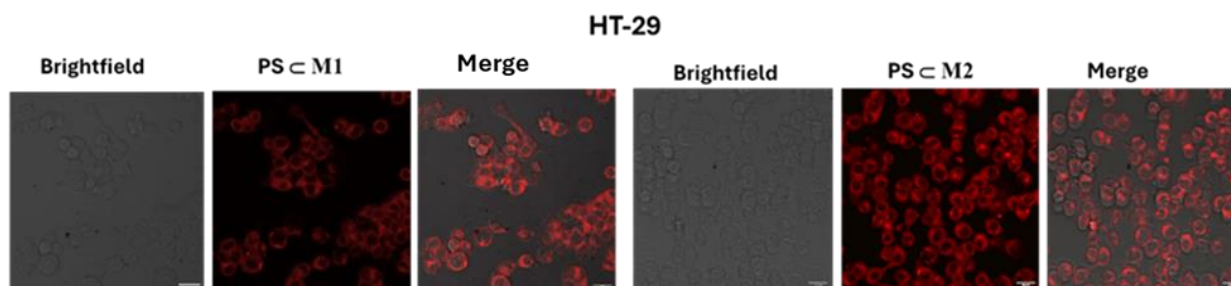


Figure 59: Detection of cytoplasmic localization in the HT-29 cell line after treatment with PS◁M1 or PS◁M2.

Detection of cellular internalization of **PS◁M1** and **PS◁M2** in the HT-29 cell line by confocal microscopy. Cells were seeded into incubation chambers and cultured for 24 h. Cells were then treated with the compounds, and the fluorescence was measured by confocal microscopy (laser Zeiss LSM 510 Meta—x 1000). The internalization was processed using the Image J image-processing software (version 1.54f).

To further investigate the intracellular targeting of our **PS◁M** assemblies and assess their potential co-localization with various cytoplasmic organelles, specific markers were used to stain and track mitochondria, lysosomes and ER. The results from these co-localization studies

revealed that, following treatment with both **PS◁M1** and **PS◁M2** complexes, there was a clear co-localization with mitochondria which was evident in both HCT116, and HT-29 cell lines after the image acquisitions obtained from mitochondrial staining were overlaid with those corresponding to the **PS◁M** assemblies (**Figures 60** and **61**). The co-localization with mitochondria suggests that the porphyrin, upon release from the metallacages, preferentially localizes within the mitochondria, which reveals a potential interaction with mitochondrial components by exerting a critical role as typical target for PDT and in regulating cell death pathways. However, no significant co-localization with lysosomes or ER was observed, which provides important insights into the internalization and trafficking pathways of the assemblies. Indeed, these findings underscore the specificity of the **PS◁M** assemblies in targeting key organelles but also highlights their potential for inducing mitochondrial-mediated apoptosis in cancer cells through the generation of ROS near the mitochondria, potentially leading to the disruption of mitochondrial function and the initiation of cell death pathways. The understanding of this intracellular distribution is vital for optimizing the design and application of these assemblies in future PDT protocols.

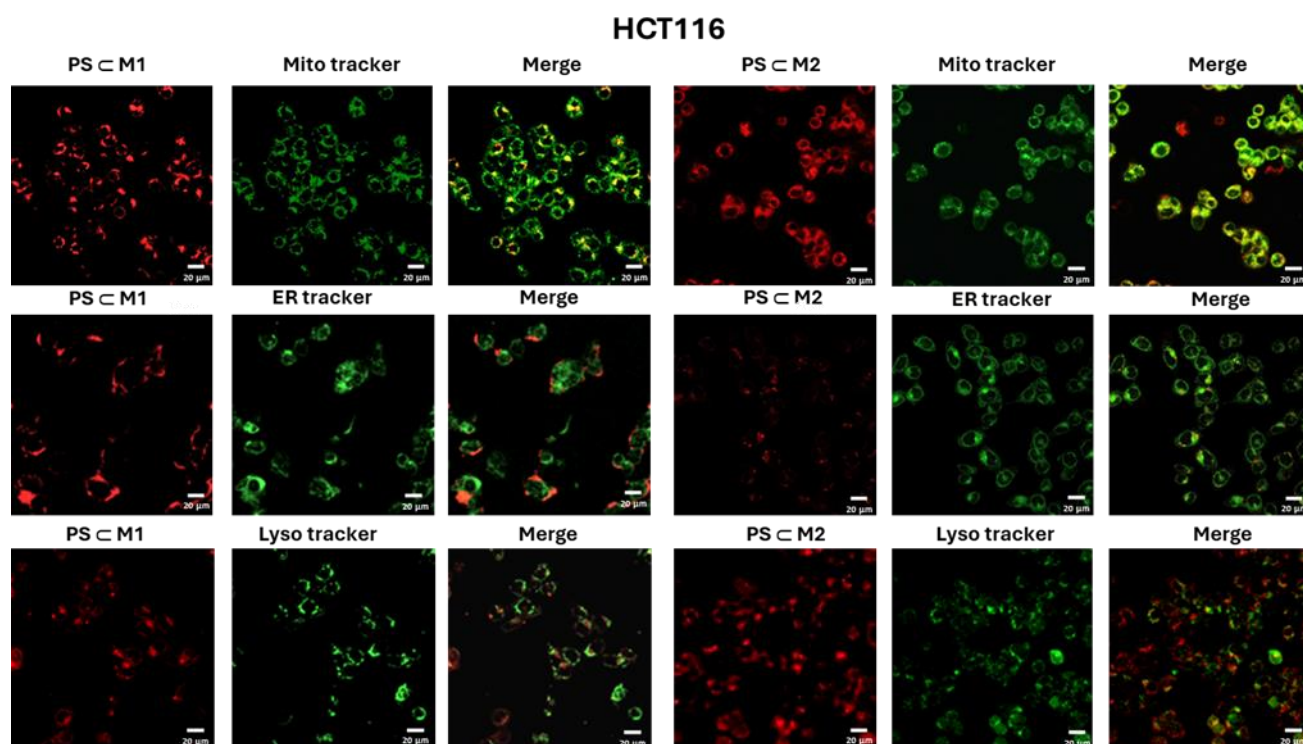


Figure 60: Investigation of possible co-localization with mitochondria, ER, and lysosomes in the HCT116 cell line.

Detection of a possible co-localization with mitochondria, ER and lysosomes in the HCT116 cell line by confocal microscopy after treatment with **PS◁M1** and **PS◁M2**. Cells were seeded into incubation chambers and cultured for 24 h. Cells were then treated with the compounds and incubated with the mitotracker, lysotracker and ER tracker before the fluorescence was detected by confocal microscopy (laser Zeiss LSM 510 Meta—x 1000). The internalization was processed using the Image J image-processing software (version 1.54f).

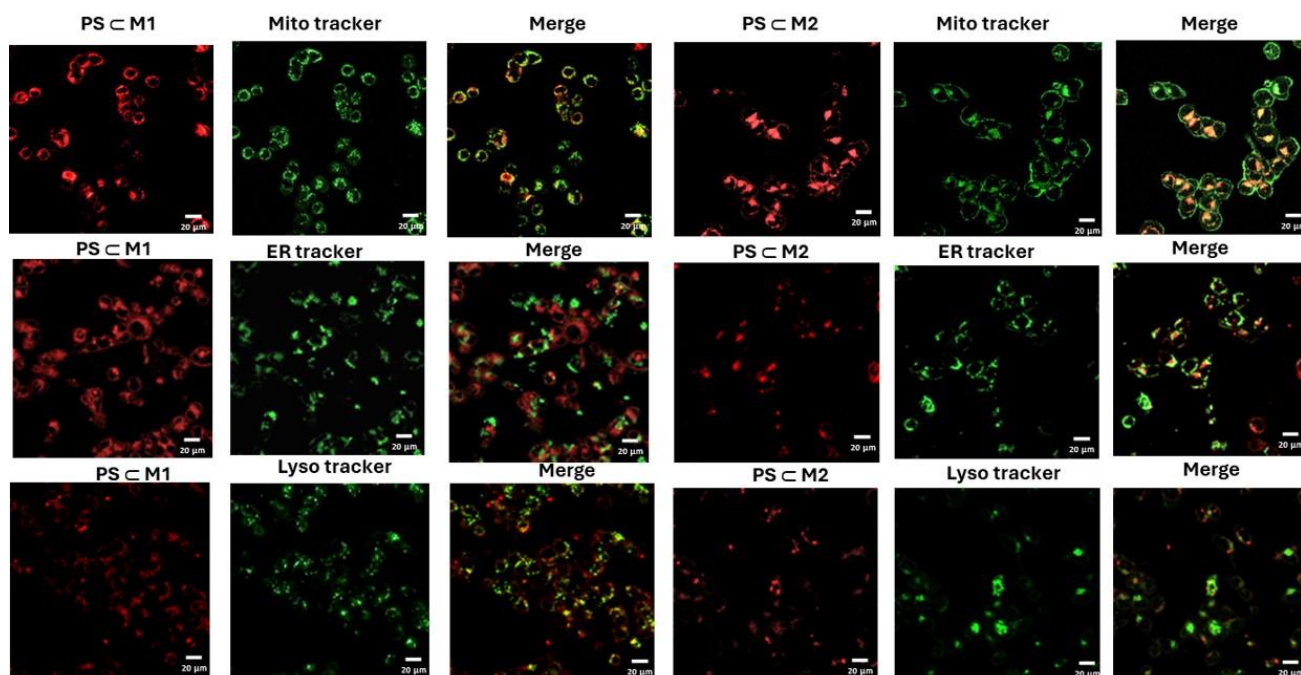


Figure 61: Investigation of a possible co-localization with mitochondria, ER, and lysosomes in the HT-29 cell line.

Detection of a possible co-localization with mitochondria, ER and lysosomes in the HT-29 cell line by confocal microscopy after treatment with **PS \subset M1** and **PS \subset M2**. Cells were seeded into incubation chambers and cultured for 24 h. Cells were then treated with the compounds and incubated with the mitotracker, lysotracker and ER tracker before the fluorescence was detected by confocal microscopy (laser Zeiss LSM 510 Meta— \times 1000). The internalization was processed using the Image J image-processing software (version 1.54f).

VII.4. Cell cycle analysis

Given the rapid proliferation rate of cancer cells, it is crucial to investigate the impact of the **PS \subset M** assemblies on cell cycle progression. Thus, the number of cells at each phase were monitored using DNA labeling with PI. This method allowed the analysis of the distribution of cells across the different phases of the cell cycle in the HCT116 and HT-29 cell lines using flow cytometry (**Figures 62, 63, 64 and 65**).

In the HCT116 cell line, treatment with **PS \subset M1** and **PS \subset M2** assemblies under light exposure led to notable changes in the cell cycle distribution. At 12 h post-illumination, the proportion of cells in the sub-G1 phase which is an indicative of apoptosis was 8.43% for **PS \subset M1** and 8.23% for **PS \subset M2**. These values were significantly higher compared to the control cells with 1.48% of cells in the sub-G1 phase. This increase suggests that the **PS \subset M** assemblies induce early apoptosis within 12 h of light exposure. At 24 h post-illumination, the sub-G1 phase percentage increased significantly to 21.42% for **PS \subset M1** and 34.34% for **PS \subset M2** as compared to 0.60% in the control cells. This indicates a pronounced apoptotic response driven by the **PS \subset M** assemblies. By 48 h post-illumination, the sub-G1 phase cells continued to increase, reaching 24.14% for **PS \subset M1** and 36.67% for **PS \subset M2** as compared to 3.66% in the control group. The data suggests that while the proportion of apoptotic cells peaks at 24 h, it remains elevated at 48 h indicating a sustained apoptotic activity. Additionally, we observed a noticeable accumulation of cells in the G1 phase, with a significant decrease in the number of cells moving

to the S phase. This effect was particularly prominent at 12 h and 24 h post-illumination. The accumulation in the G1 phase, combined with a reduction in the number of cells in the S phase indicates that the **PS_CM** assemblies induce G1 phase arrest. This observation is consistent with the hypothesis that the maximum phototoxic effect occurs at 24 h post-illumination, with induced apoptosis and G1 phase arrest contributing to the overall therapeutic efficacy (**Figures 62 and 63**).

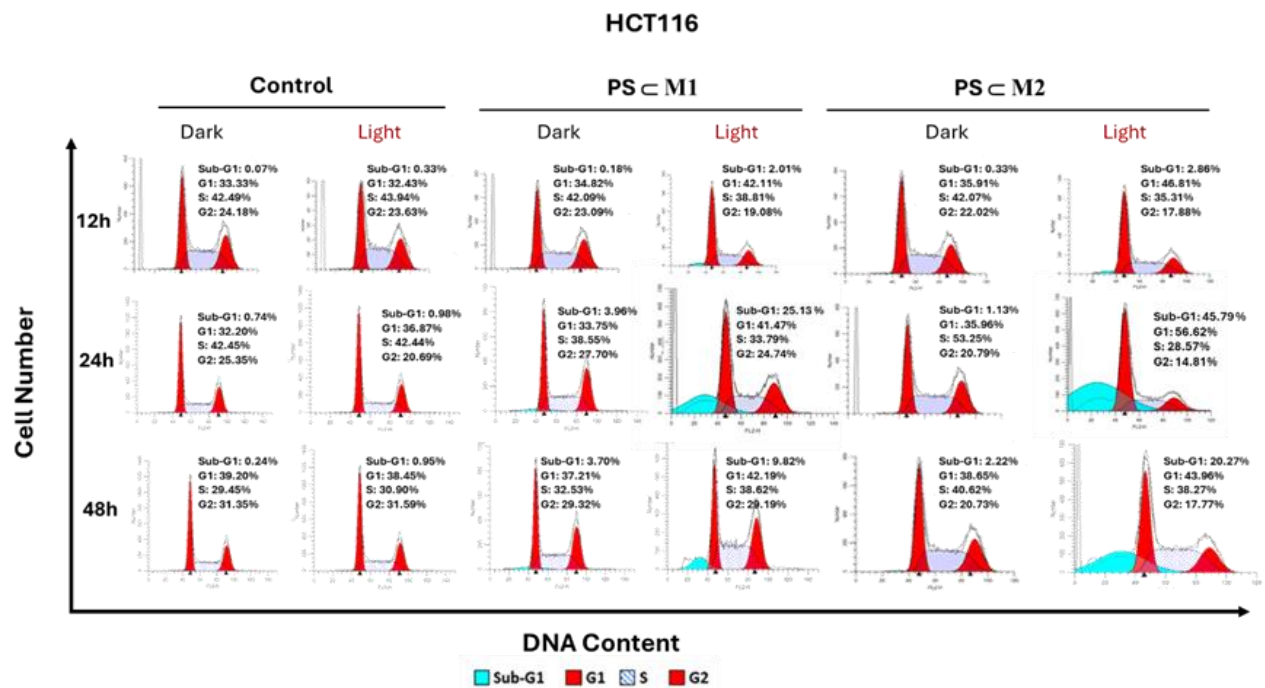


Figure 62: PDT effect on the cell cycle progression of HCT116 cell line.

Cell cycle distribution analysis on HCT116 cell line after the photoactivation of **PS_CM1** and **PS_CM2**. Cells were seeded for 24 h in a culture medium before the treatment or not with the assemblies at their determined IC₅₀ concentrations. After 24 h of treatment, cells were illuminated or not with red light at 630 nm and 75 J/cm². Cells were collected at 12 h, 24 h, and 48 h post-illumination for analysis by flow cytometry using PI staining. Images of cell cycle distribution on HCT116 cells at the three time points post-illumination are represented of one experiment.

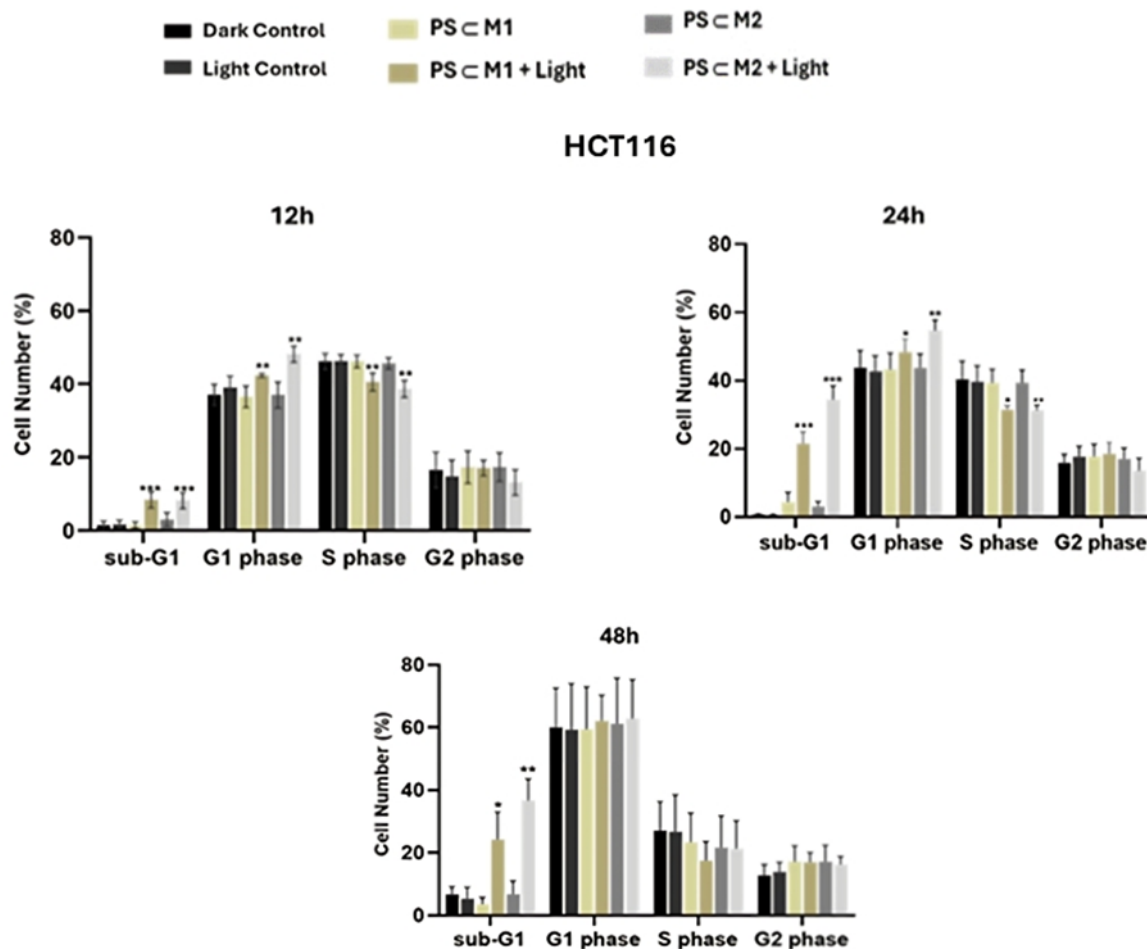


Figure 63: Histograms representing the PDT effect on cell cycle progression of HCT116 cell line.

Cell cycle distribution analysis on the HCT116 cell line after the photoactivation of **PS \subset M1** and **PS \subset M2**. Cells were seeded for 24 h in a culture medium before the treatment or not with the assemblies at their determined IC₅₀ concentrations. After 24 h of treatment, cells were illuminated or not with red light at 630 nm and 75 J/cm². Cells were collected at 12 h, 24 h, and 48 h post-illumination for analysis by flow cytometry using PI staining. Histograms representing the percentage cell number at each phase of the cell cycle on the HCT116 cell line are displayed as a mean \pm SEM of three independent experiments. *p < 0.05; **p < 0.01 and ***p < 0.001.

In the HT-29 cell line, the sub-G1 phase was not observed at 12 h post-illumination; however, it became evident at 24 h, with 3.96% of cells in the sub-G1 phase for **PS \subset M1** and 2.49% for **PS \subset M2**, compared to 0.03% in the control cells. The proportion of cells in the sub-G1 phase continued to increase at 48 h post-illumination to reach 11.02% for **PS \subset M1** and 12.28% for **PS \subset M2**. This delayed onset of the sub-G1 phase in HT-29 cells highlights a time-dependent apoptotic response, indicating a progressive accumulation of apoptotic cells over time. Moreover, in HT-29 cells, there was a persistent accumulation of cells in the G2 phase at 12 h, 24 h, and 48 h post-illumination, accompanied by a significant reduction in cells entering the G1 phase. This suggests that the **PS \subset M** assemblies induce a cell cycle arrest in the G2 phase, thereby blocking the cells' ability to proceed to mitosis (**Figures 64 and 65**). It is important to mention that in both cell lines, the assemblies did not affect overall cell cycle progression in the absence of light (**Figures 62, 63, 64 and 65**). However, the observed differences in apoptotic responses between the HCT116 and HT-29 cell lines indicate that HT-29 cells exhibit a slower apoptotic response compared to HCT116 cells. This difference may be attributed to variations in cellular machinery and differential sensitivity to the treatments.

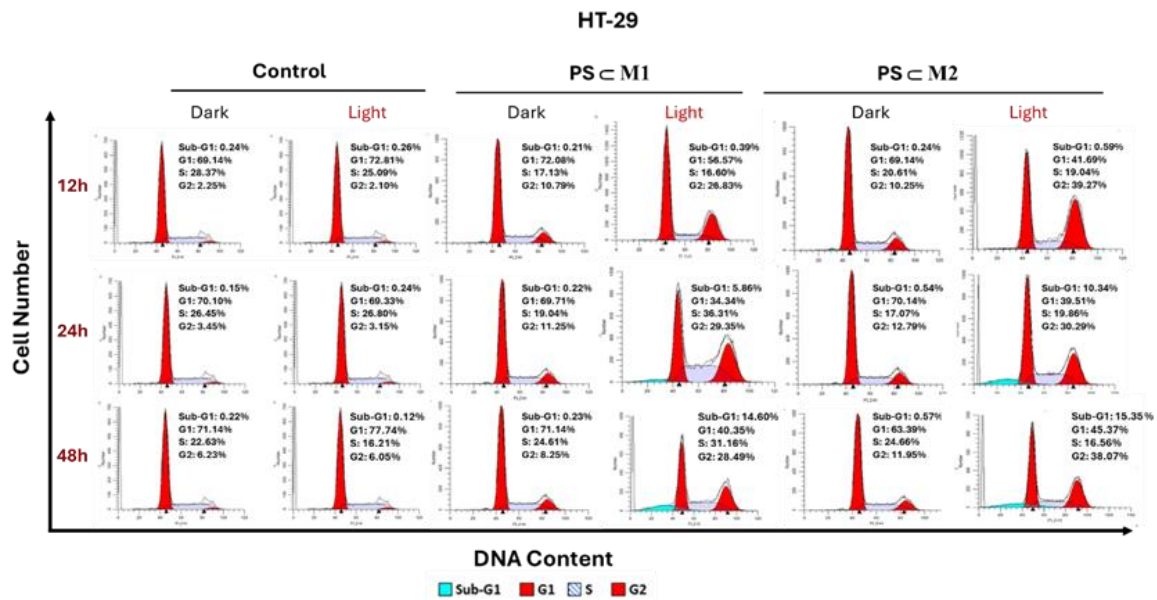


Figure 64: PDT effect on the cell cycle progression of HT-29 cell line.

Cell cycle distribution analysis on HT-29 cell line after the photoactivation of **PS<M1** and **PS<M2**. Cells were seeded for 24 h in a culture medium before the treatment or not with the assemblies at their determined IC₅₀ concentrations. After 24 h of treatment, cells were illuminated or not with red light at 630 nm and 75 J/cm². Cells were collected at 12 h, 24 h, and 48 h post-illumination for analysis by flow cytometry using PI staining. Images of cell cycle distribution on HT-29 cell line are represented at the three time points post-illumination of one experiment.

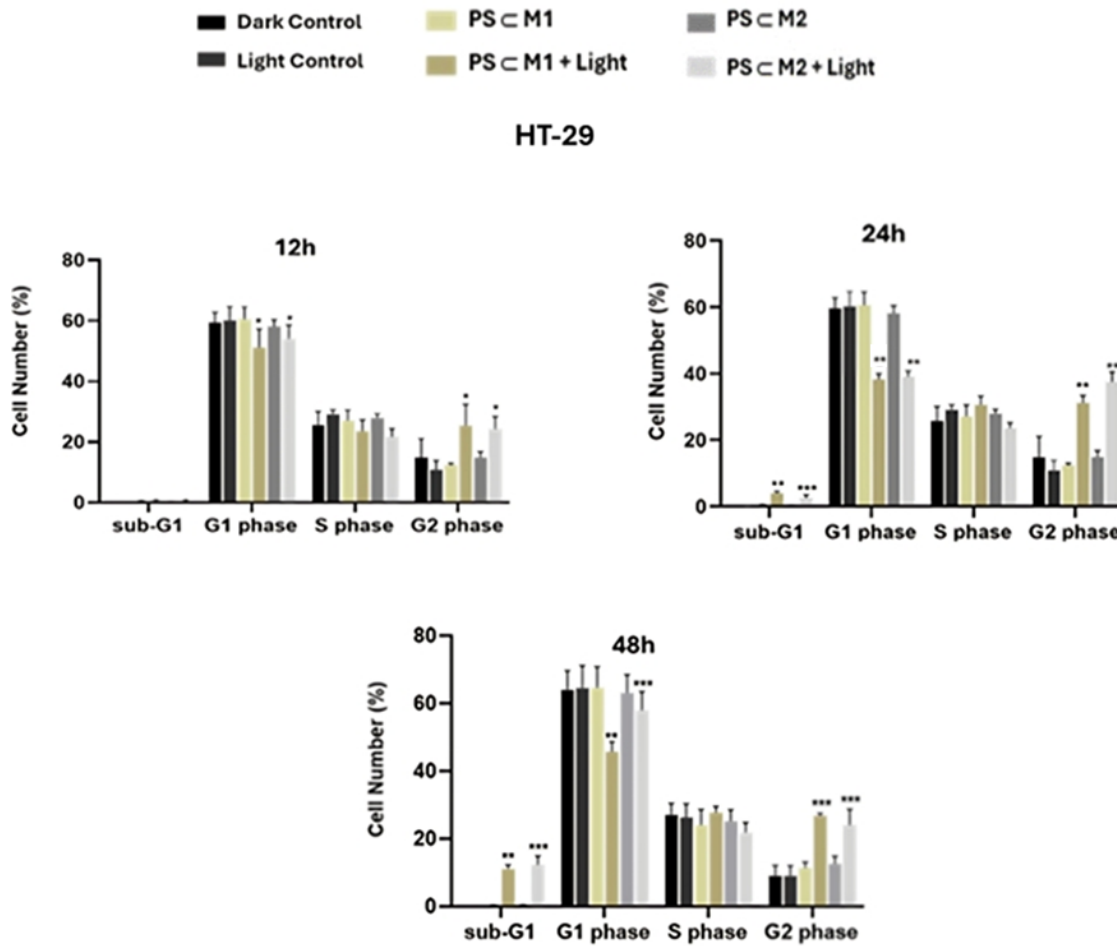


Figure 65 : Histograms representing the PDT effect on cell cycle progression of HT-29 cell line.

Cell cycle distribution analysis on the HT-29 cell line after the photoactivation of **PS \subset M1** and **PS \subset M2**. Cells were seeded for 24 h in a culture medium before the treatment or not with the assemblies at their determined IC₅₀ concentrations. After 24 h of treatment, cells were illuminated or not with red light at 630 nm and 75 J/cm². Cells were collected at 12 h, 24 h, and 48 h post-illumination for analysis by flow cytometry using PI staining. Histograms representing the percentage cell number at each phase of the cell cycle on the HT-29 cell line are displayed as a mean \pm SEM of three independent experiments. *p < 0.05; **p < 0.01 and ***p < 0.001.

In summary, these findings demonstrate that the **PS \subset M** assemblies induce significant changes in cell cycle progression with an arrest in the G1 phase of the HCT116 cell line and the G2 phase of the HT-29 cell line.

VII.5. Apoptotic assay

VII.5.1. Annexin V/PI

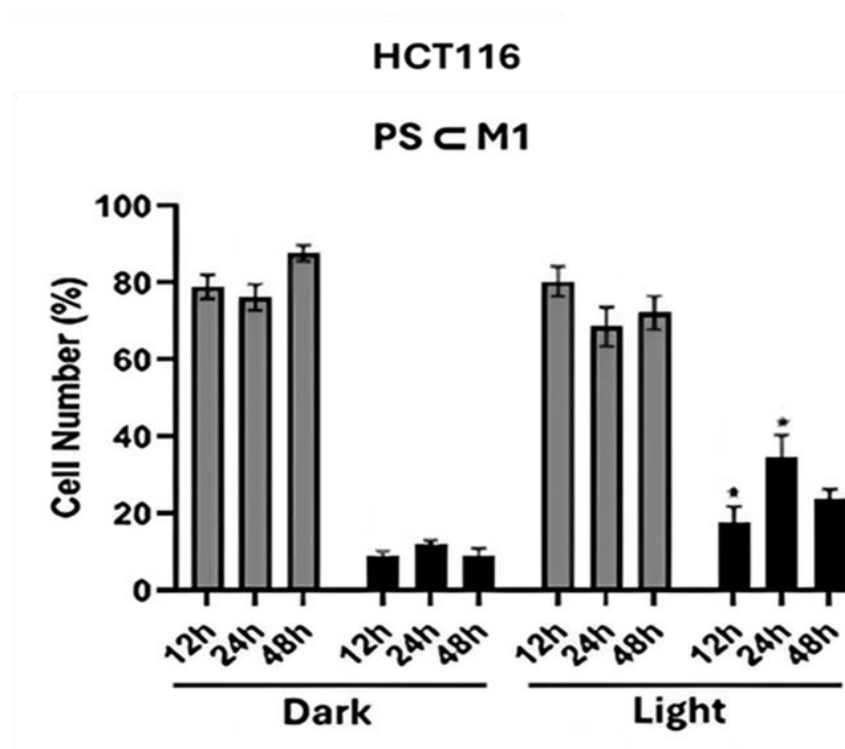
To gain a deeper understanding of the apoptotic mechanisms suggested by the sub-G1 phase of the cell cycle, a comprehensive investigation using an Annexin V-FITC/PI dual staining assay was performed and analyzed through flow cytometry. This assay allows for the distinguishing between the different stages of apoptosis within a population of cells. Early apoptotic cells are characterized by the binding of Annexin V, which occurs due to the translocation of phosphatidylserine from the inner to the outer leaflet of the plasma membrane through a process often referred to as membrane flip-flop. This change in membrane asymmetry serves as an early marker of apoptosis. On the other hand, the late apoptotic cells are not only identified by the annexin V staining but also by PI uptake which can only occur in

the cells with compromised membrane integrity. By using this dual staining approach, we were able to accurately quantify and differentiate between cells in early and late stages of apoptosis, providing critical insights into the effectiveness of the **PS<M1** and **PS<M2** assemblies as inducers of cell death.

The results of flow cytometry were quantified and represented by histograms showing the variations in the percentages of viable and apoptotic cells (a combination of early and late apoptotic cells for each condition) after treatment with **PS<M1** or **PS<M2** at 12 h, 24 h and 48 h post-illumination and in the dark (**Figures 66, 67, 68 and 69**). In our experiments on the HCT116 and HT-29 cell lines, a significant increase in the number of cells stained positively with only annexin V (annexin V+/ PI-) and with both annexin V and PI (annexin V+/ PI+), was observed following treatment with **PS<M1** and **PS<M2** assemblies and illumination. However, the control groups and the treated non-illuminated groups displayed minimal staining.

In the HCT116 cell line, the percentage of apoptotic cells at 12 h post-illumination was 17.64% for the cells treated with **PS<M1** and 19.81% for those treated with **PS<M2**. After 24 h of illumination, the apoptotic activity significantly increased, reaching 34.38% for **PS<M1** treated cells and 49.05% for **PS<M2** treated cells. These numbers represent a nearly threefold increase compared to the apoptotic rates of the treated cells that were kept in the dark, which showed 11.96% and 14.50% of apoptotic cells, for **PS<M1** and **PS<M2** treated cells, respectively. This increase indicates induction of cell death, likely driven by the accumulation of ROS and subsequent damage to cellular components. By 48 h post-illumination, while the percentage of apoptotic cells decreased slightly to 23.90% for **PS<M1** and 36.37% for **PS<M2**, these levels remained significantly elevated compared to controls (**Figures 66 and 67**).

■ Viable cells ■ Apoptotic cells



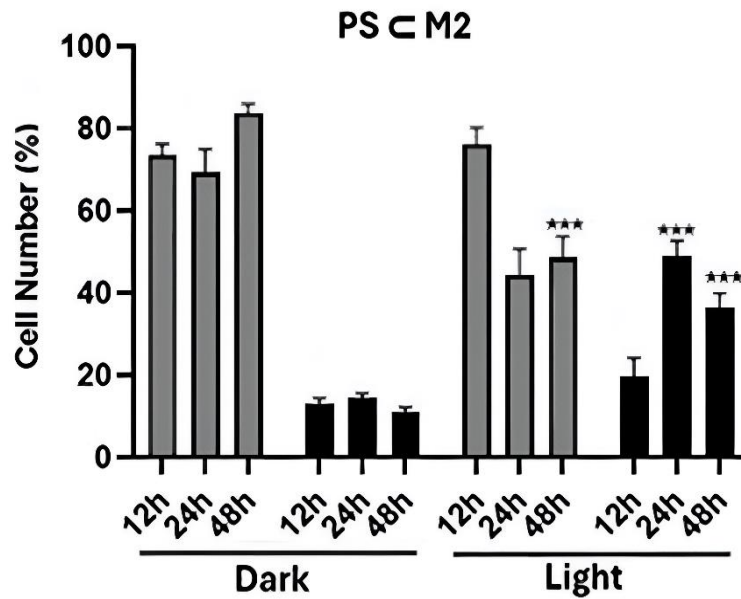


Figure 66: Histograms representing the percentages of apoptotic and viable cells after PDT in the HCT116 cell line

Apoptosis due to photoactivation was assessed on the HCT116 cell line. Cells were seeded and incubated for 24 h then treated or not with **PS<M1** and **PS<M2** assemblies at IC₅₀ concentrations. Cells were either illuminated (630 nm, 75 J/cm²) or not after 24 h of treatment and then they were collected at 12 h, 24 h, and 48 h post-illumination. The collected cells were stained with Annexin V- FITC and PI and their state was revealed by flow cytometry. Histograms represent the viable and apoptotic (early + late) cell percentages of the treated HCT116 cells whether subjected or not to a prior illumination. Data is represented as a mean ± SEM of three independent experiments. *p < 0.05; **p < 0.01 and ***p < 0.001.

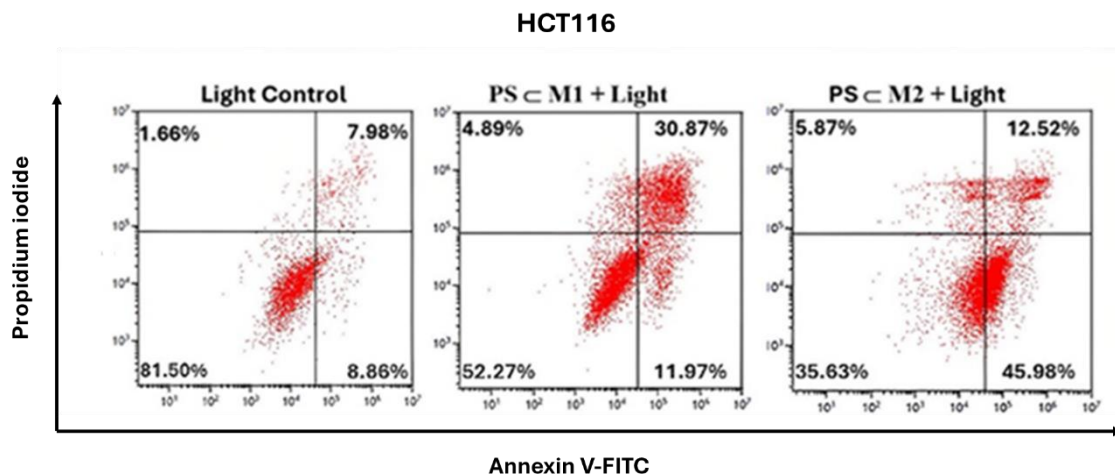
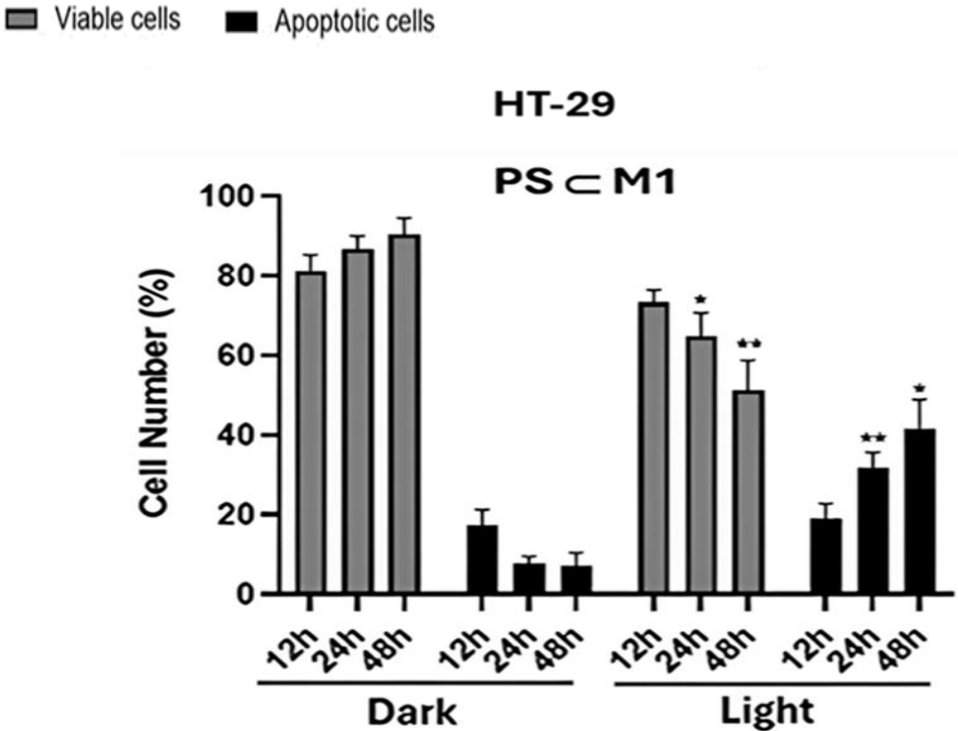


Figure 67 : Evaluation of the percentages of apoptotic cells after 24 h of PDT in HCT116 cell line.

Apoptosis due to photoactivation was assessed on the HCT116 cell line. Cells were seeded and incubated for 24 h then treated or not with **PS<M1** and **PS<M2** assemblies at IC₅₀ concentrations. Cells were either illuminated (630 nm, 75 J/cm²) or not after 24 h of treatment and then they were collected at 12 h, 24 h, and 48 h post-illumination. The collected cells were stained with Annexin V- FITC and PI and their state was revealed by flow cytometry. Representative data from flow cytometry for the HCT116 cell line at 24 h post-illumination is shown.

In contrast, the HT-29 cell line exhibited a different temporal pattern of apoptosis. At 12 h post-illumination, apoptosis rates in these cells were 19.04% for **PS<M1** and 21.59% for **PS<M2**. However, the progression of apoptosis in HT-29 cells was more gradual. By 24 h post-illumination, apoptosis had increased to 31.68% for **PS<M1** and 34.13% for **PS<M2**, showing a steady, but not a rapid escalation as that observed with the HCT116 cell line. The non-illuminated cells, in contrast, exhibited relatively low levels of apoptosis, with rates at 7.81% and 11.86%, respectively confirming that the PS assemblies' effect is predominantly light-dependent. By 48 h post-illumination, the apoptotic response in HT-29 cells further augmented, with 40.12% of cells in the **PS<M1** treated group and 41.56% in the **PS<M2** treated group. Similarly, the non-illuminated treated groups remained unaffected, with apoptosis rates of 6.11% and 6.95%, for **PS<M1** and **PS<M2** treated groups, respectively. This gradual yet sustained increase in apoptotic cells suggests that HT-29 cells may require more time to fully engage their apoptotic pathways in response to the treatment (**Figures 68 and 69**).



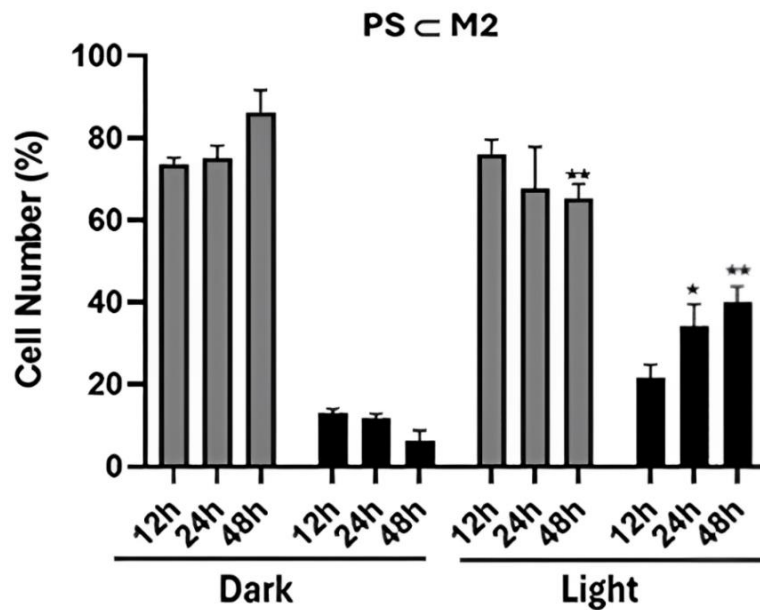


Figure 68: Histograms representing the percentages of apoptotic and viable cells after PDT in the HT-29 cell line.

Apoptosis due to photoactivation was assessed on the HT-29 cell line. Cells were seeded and incubated for 24 h then treated or not with **PS \subset M1** and **PS \subset M2** assemblies at IC_{50} concentrations. Cells were either illuminated (630 nm, 75 J/cm²) or not after 24 h of treatment and then they were collected at 12 h, 24 h, and 48 h post-illumination. The collected cells were stained with Annexin V- FITC and PI and their state was revealed by flow cytometry. Histograms represent the viable and apoptotic (early + late) cell percentages of the treated HCT116 cells whether subjected or not to a prior illumination. Data are represented as a mean \pm SEM of three independent experiments. * $p < 0.05$; ** $p < 0.01$ and *** $p < 0.001$.

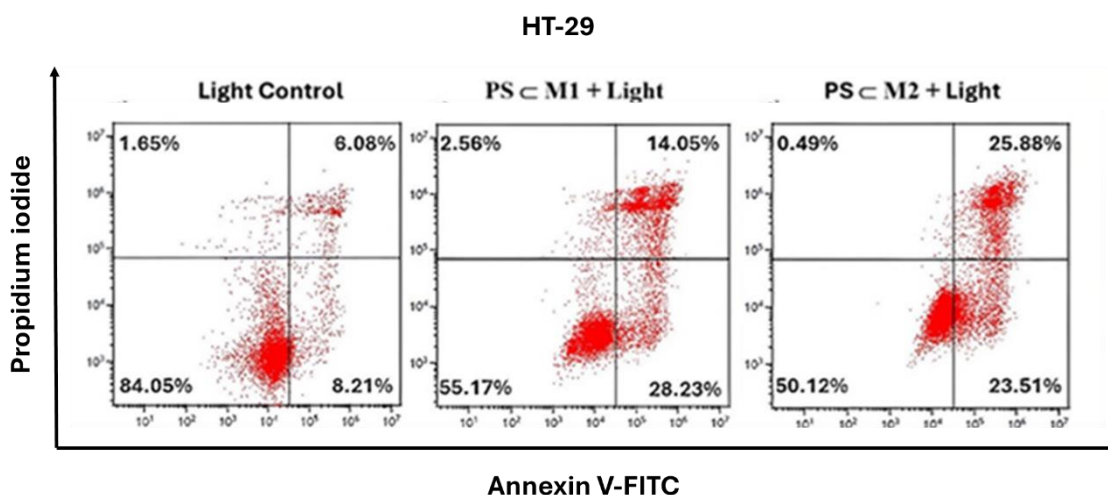


Figure 69: Evaluation of the percentages of apoptotic cells after 48h of PDT in the HT-29 cell line.

Apoptosis due to photoactivation was assessed on the HCT116 and HT-29 cell line. Cells were seeded and incubated for 24 h then treated or not with **PS \subset M1** and **PS \subset M2** assemblies at IC_{50} concentrations. Cells were either illuminated (630 nm, 75 J/cm²) or not after 24 h of treatment and then they were collected at 12 h, 24 h, and 48 h post-illumination. The collected cells were stained with Annexin V- FITC and PI and their state was revealed by flow cytometry. Representative data from flow cytometry for the HT-29 cell line at 48 h post-illumination is shown.

These findings highlight the effectiveness of **PS<M1** and **PS<M2** assemblies in inducing significant apoptotic cell death mechanism in both HCT116 and HT-29 cell lines following illumination. The distinct patterns of apoptosis between these two cell lines underscore the importance of understanding the cellular responses to treatment, which can lead to the development of better designed and effective therapeutic strategies.

VII.5.2. Quantitative analysis of caspase-3/7 activity

Caspase-3/7 is a crucial effector enzyme that plays a key role in the execution phase of apoptosis. Its activity is characterized by its own cleavage, triggering a cascade of proteolytic events that lead to the breakdown of various downstream proteins vital for cell survival. This process ultimately results in the disruption of the cellular state, triggering its subsequent death. To better understand the role of caspase-3/7 in apoptosis, its activity was monitored in real-time using the advanced live-cell imaging technology provided by the Incucyte® S3 system, which allowed continuous observation over a period of 48 h.

After treating HCT116 and HT-29 cell lines with **PS<M1** and **PS<M2** complexes, cells were either illuminated or not and placed in the Incucyte® S3 system which enables the capturing of images of the cells every 2 h. The observed green fluorescence indicates active caspase-3/7 enzymes. This fluorescence is generated when caspase 3/7 cleaves a specific substrate linked to a fluorescent marker permitting the observation of the conditions with active caspase-3/7 enzymes and the quantitative assessment of the enzyme's activity. The continuous monitoring provided a detailed temporal profile of caspase-3/7 activation which offers significant insights into the apoptotic process triggered by **PS<M1** and **PS<M2** assemblies.

Quantification of the fluorescence intensity showed a marked increase in caspase-3/7 activity after illumination of HCT116 cells treated with **PS<M1** and **PS<M2**. This increase was evident at multiple time points compared to both non-illuminated treated cells and untreated control cells (**Figures 70** and **71**). After 12 h of illumination, the fluorescence intensity was 51.47% in the **PS<M1** treated cells and 79.40% in the **PS<M2** treated cells. The fluorescence intensity further increased at 24 h post-illumination to reach 73.98% for **PS<M1** and 95.46% for **PS<M2**. At 48h, the fluorescence intensity reached 91.39% and 99.55% in the **PS<M1** and **PS<M2** treated groups, respectively. However, the fluorescence intensity for the non-illuminated groups remained minimal over time and didn't exceed 14% in the **PS<M1** treated group and 33% in the **PS<M2** treated group. Similarly, the fluorescence intensity of the control cells remained very low at around 5-6%. The data indicated that caspase-3/7 activation was significantly higher in illuminated cells, occurring in a time-dependent manner with activity progressively increasing with time.

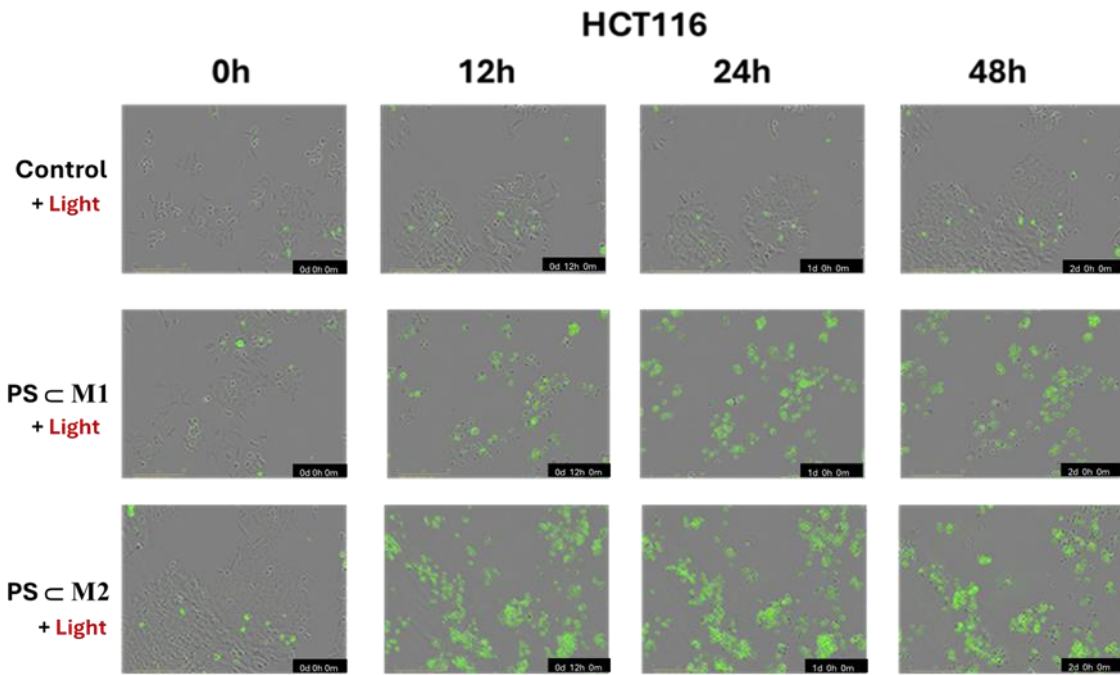


Figure 70: Caspase-3/7 activity revealed by green fluorescence in the HCT116 cell line.

HCT116 cells were seeded in 96-well plates, cultured for 24 h, and then treated with **PS_CM1** and **PS_CM2**. After 24 h, the culture medium was replaced with phenol red-free medium, and cells were either illuminated or not. They were then exposed to the caspase-3/7 green reagent (5 μ M) and placed in the IncuCyte® S3 system. Images were captured every 2 h, with four images per well at 10x magnification in both phase contrast and green fluorescence. Representative images are shown.

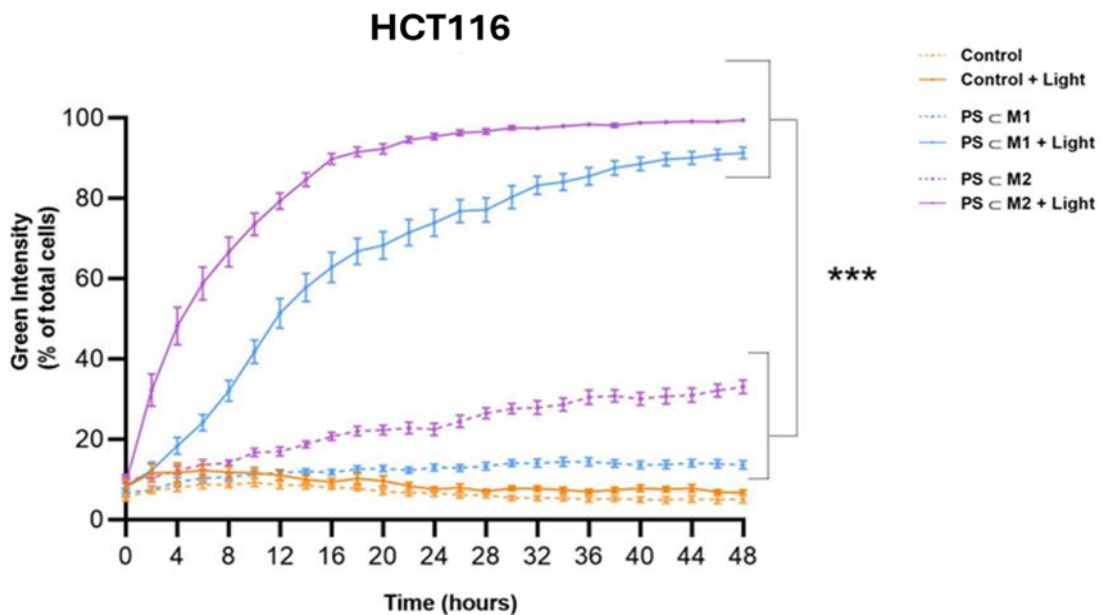


Figure 71: Evaluation of the caspase-3/7 activity by fluorescence in the HCT116 cell line.

HCT116 cells were seeded in 96-well plates, cultured for 24 h, and then treated with **PS_CM1** and **PS_CM2**. After 24 h, the culture medium was replaced with phenol red-free medium, and cells were either illuminated or not. They were then exposed to the caspase-3/7 green reagent (5 μ M) and placed in the IncuCyte® S3 system. Images were captured every 2 h, with four images per well at 10x magnification in both phase contrast and green fluorescence. At each time point up to 48 h, the apoptotic cells were quantified using IncuCyte® software (Sartorius) by

determining the ratio of fluorescent cells to the total number of cells in each well. Data are represented as a mean \pm SEM of three independent experiments. *** $p < 0.001$.

In the HT-29 cell line, the illumination of the cells treated with **PS<M1** or **PS<M2** showed a significant increase in caspase-3/7 activity as compared to the control and treated non-illuminated cells (**Figures 72 and 73**). After 12 h of illumination, the fluorescence intensity was 25.71% in the **PS<M1** treated cells and 41.79% in the **PS<M2** treated cells. The fluorescence intensity further increased at 24 h post-illumination to reach 50.47% for **PS<M1** and 65.47% for **PS<M2**. The fluorescence intensity continued to rise steadily over time 48h, to reach 89.86% and 93.54% in the **PS<M1** and **PS<M2** treated groups, respectively. However, the fluorescence intensity for the non-illuminated treated groups remained minimal over time and didn't exceed 13% for **PS<M1** and 12% for **PS<M2**. Additionally, the fluorescence intensity of the control cells, whether exposed to illumination or not, relatively remained at 4% over the time period of 48h.

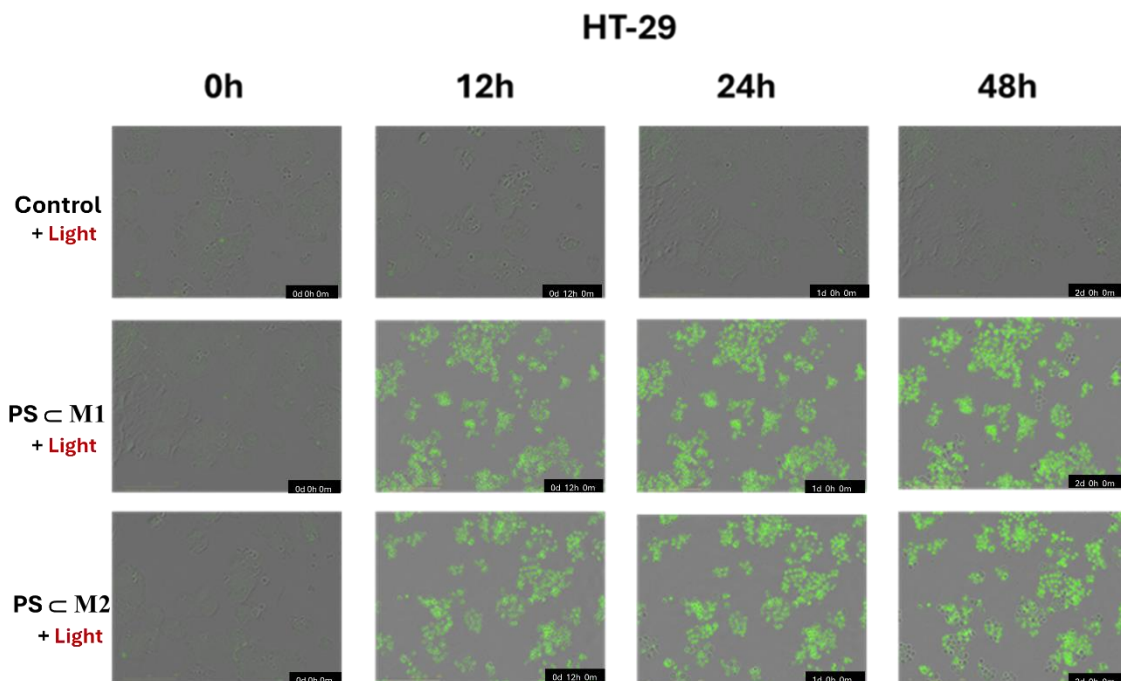


Figure 72: Caspase-3/7 activity revealed by green fluorescence in the HT-29 cell line.

HT-29 cells were seeded in 96-well plates, cultured for 24 h, and then treated with **PS<M1** and **PS<M2**. After 24 h, the culture medium was replaced with red phenol-free medium, and cells were either illuminated or left untreated. They were then exposed to the caspase-3/7 green reagent (5 μ M) and placed in the IncuCyte® S3 system. Images were captured every 2 h, with four images per well at 10x magnification in both phase contrast and green fluorescence. Representative images are shown

HT-29

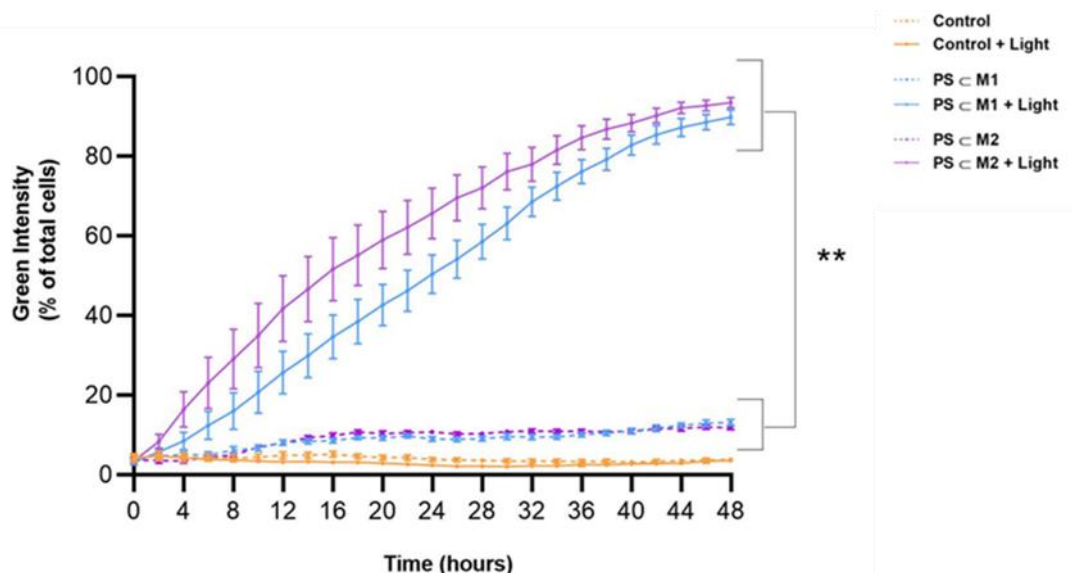


Figure 73: Evaluation of the caspase-3/7 activity by fluorescence in the HT-29 cell line.

HT-29 cells were seeded in 96-well plates, cultured for 24 h, and then treated with **PS_CM1** and **PS_CM2**. After 24 h, the culture medium was replaced with red phenol-free medium, and cells were either illuminated or left untreated. They were then exposed to the caspase-3/7 green reagent (5 μ M) and placed in the IncuCyte® S3 system. Images were captured every 2 h, with four images per well at 10x magnification in both phase contrast and green fluorescence. At each time up to 48 h, the apoptotic cells were quantified using IncuCyte® software (Sartorius) by determining the ratio of fluorescent cells to the total number of cells in each well. Data are represented as a mean \pm SEM of three independent experiments. **p < 0.01.

As previously mentioned, control and non-illuminated treated cells in both HCT116 and HT-29 lines showed minimal to null increase in caspase-3/7 activity over different time points. Fluorescence intensity in these groups remained constant and low, indicating that apoptotic pathways remained inactive in the absence of illumination. This lack of activation further confirms the specificity of **PS_CM1** and **PS_CM2** treatments in inducing apoptosis through a light-dependent mechanism.

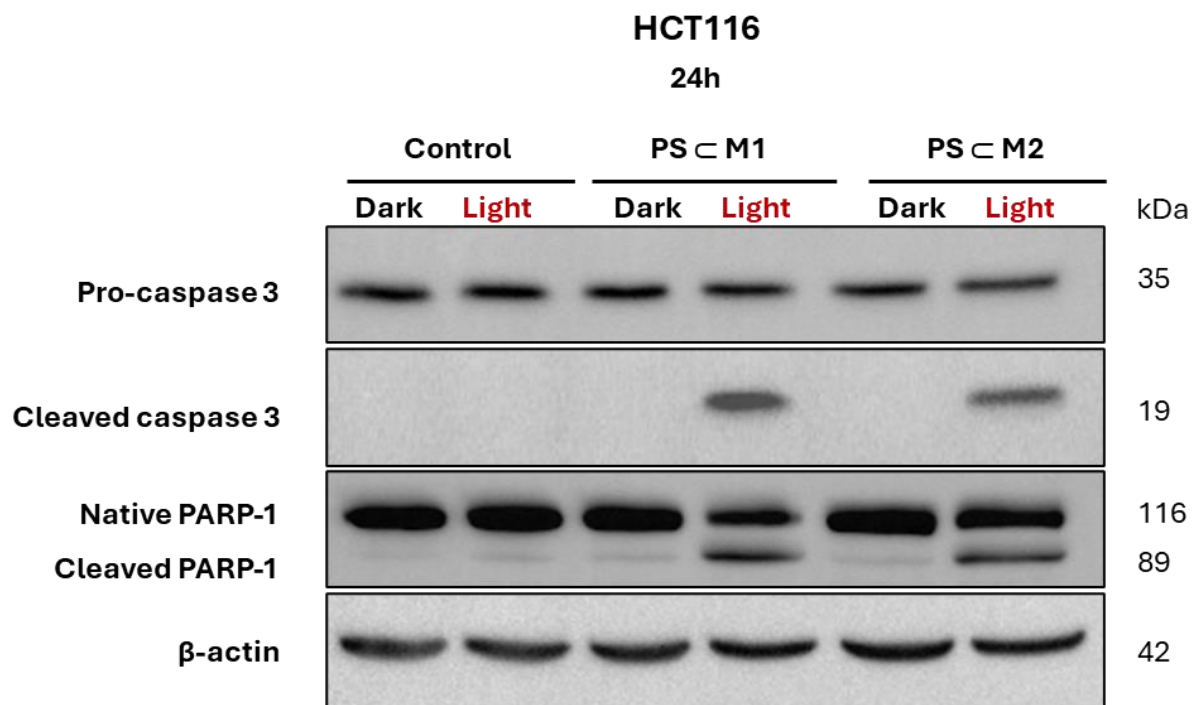
These findings validate the activation of caspase-3/7 enzyme in inducing potent apoptotic effects after treatment with **PS_CM1** and **PS_CM2** assemblies and illumination, in both HCT116 and HT-29 cell lines.

VII.5.3. Western Blot

To evaluate the onset of apoptosis, we conducted a comprehensive analysis of the expression of apoptosis-related proteins by Western blot (WB). Apoptosis involves a complex cascade of events conducted within the cells ultimately leading to the activation of several apoptotic proteins, including caspase-3. Caspase-3 is initially produced as an inactive precursor, known as “pro-caspase-3”. This enzyme is activated following proteolytic cleavage. Once cleaved, caspase-3 performs crucial functions in the apoptotic process by targeting and cleaving several key cellular proteins. One of its critical substrates is poly (ADP-ribose) polymerase-1 (PARP-1). The cleavage of PARP-1 by active caspase-3 impairs the enzyme's ability to repair DNA, which effectively signals the cell to commit to the apoptosis pathway. Therefore, analyzing the levels of caspase-3 and PARP-1 expression in HCT116 and HT-29 cell lines provided insights into the initiation and progression of apoptosis in response to our treatments.

WB analysis aimed to evaluate the impact of photoactivation on the expression of apoptotic markers. Cells treated with **PS<M1** and **PS<M2** assemblies were exposed to illumination, and their protein expression was compared to those of treated non-illuminated and control cells. For both cell lines, the results revealed a distinct activation pattern of caspase-3, evidenced by the presence of its cleaved form, exclusively in cells subjected to illumination following treatment with **PS<M1** or **PS<M2**. This cleavage was not observed in cells kept in the dark or in control cells, indicating that the activation of caspase-3 was specifically triggered by the light-dependent activation of the PSs. This pattern was consistently observed at both 24 and 48 h post-illumination, reinforcing the role of our treatments in inducing apoptosis through light activation (**Figures 74 and 75**).

In addition to caspase-3 activation, we assessed PARP-1 cleavage, which was only evident in cells that were treated and illuminated, further supporting the conclusion that our treatments effectively induced apoptosis. This cleavage was observed at both 24 and 48 h in HCT116 and HT-29 cells, correlating with the observed activation of caspase-3 and confirming the induction of the apoptotic pathway (**Figures 74 and 75**).



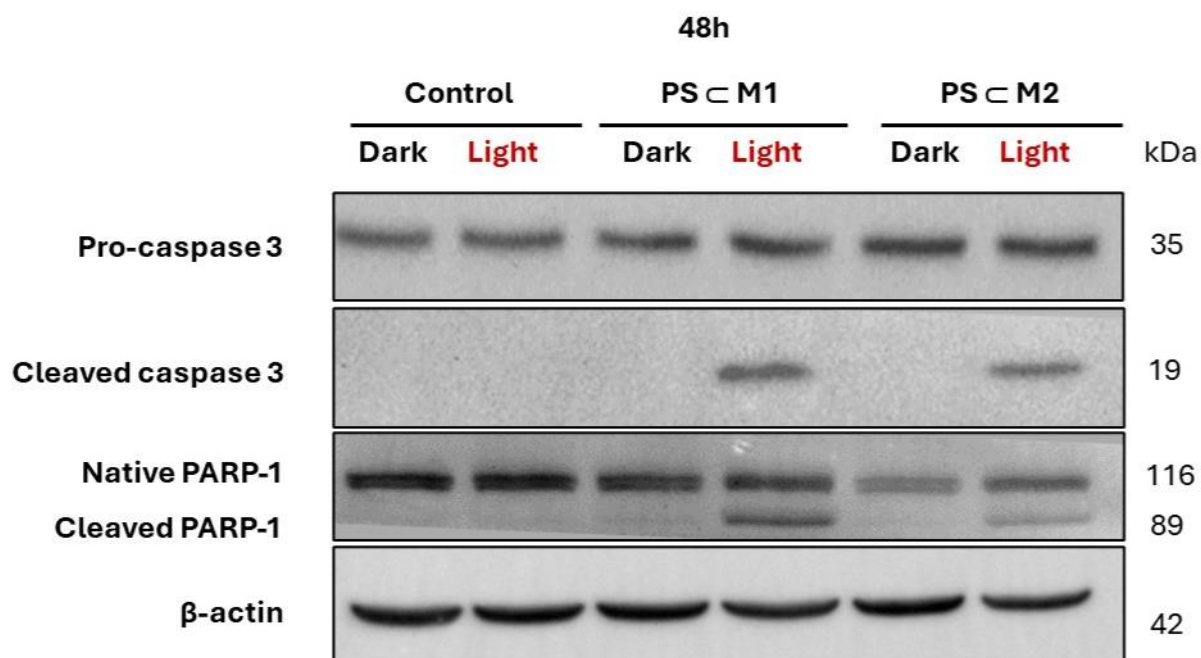
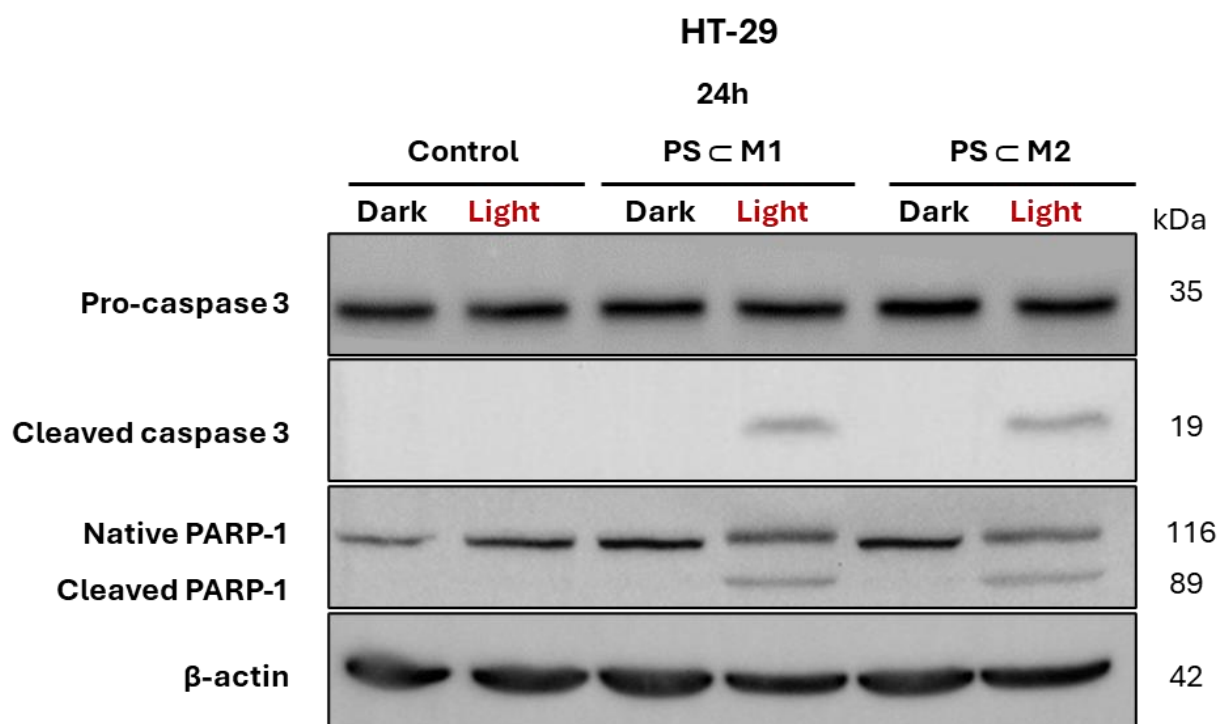


Figure 74: Effects of the assemblies with/without PDT on the protein expression of apoptotic markers in the HCT116 cell line.

Protein expression was evaluated by WB. HCT116 cells were seeded and incubated for 24 h, and then were treated or not at IC_{50} values of **PSCM1** or **PSCM2**. After treatment, cells were either illuminated (630 nm, 75 J/cm²) or not and collected 24 h and 48 h post-illumination. Proteins were extracted and the levels of protein expression in the different conditions were revealed. β -actin was used as a loading control. Representative images are shown.



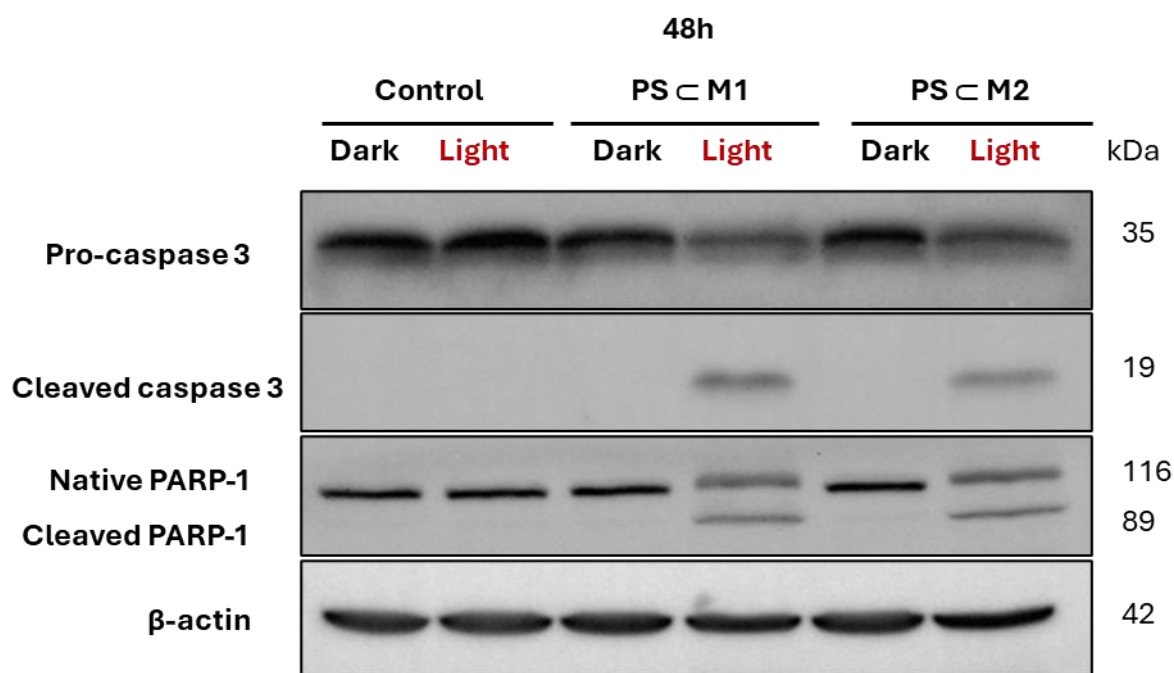


Figure 75: Effects of the assemblies with/without PDT on the protein expression of apoptotic markers in the HT-29 cell line.

Protein expression was evaluated by WB. HT-29 cells were seeded and incubated for 24 h, and then were treated or not at IC_{50} values of **PScM1** or **PScM2**. After treatment, cells were either illuminated (630 nm, 75 J/cm²) or not and collected 24 h and 48 h post-illumination. Proteins were extracted and the levels of protein expression in the different conditions were revealed. β -actin was used as a loading control. Representative images are shown.

To further validate the onset of apoptosis, we also examined the expression of Bax, a pro-apoptotic protein in the different cellular conditions. An increase in Bax protein expression was detected in cells treated with **PScM1** and **PScM2** after both 24 and 48 h of illumination as compared to the treated non-illuminated, and control cells. Bax promotes apoptosis by antagonizing the anti-apoptotic effects of other proteins, thereby inducing programmed cell death. Bax protein was highly expressed in the treated and illuminated cells at both 24 h and 48h post-illumination for both HCT116 and HT-29 cell lines. Conversely, the expression of Bcl-2, an anti-apoptotic protein, was strongly inhibited in the treated and illuminated cells, prominently visible at 24 h post-illumination in the HCT116 cells and at 48 h post-illumination in the HT-29 cells. Here, these results show a time lag in response to **PScM1** and **PScM2** treatment with illumination, depending on the cell line. Our findings emphasize the targeted and effective nature of these assemblies in inducing apoptosis after illumination (**Figures 76 and 77**).

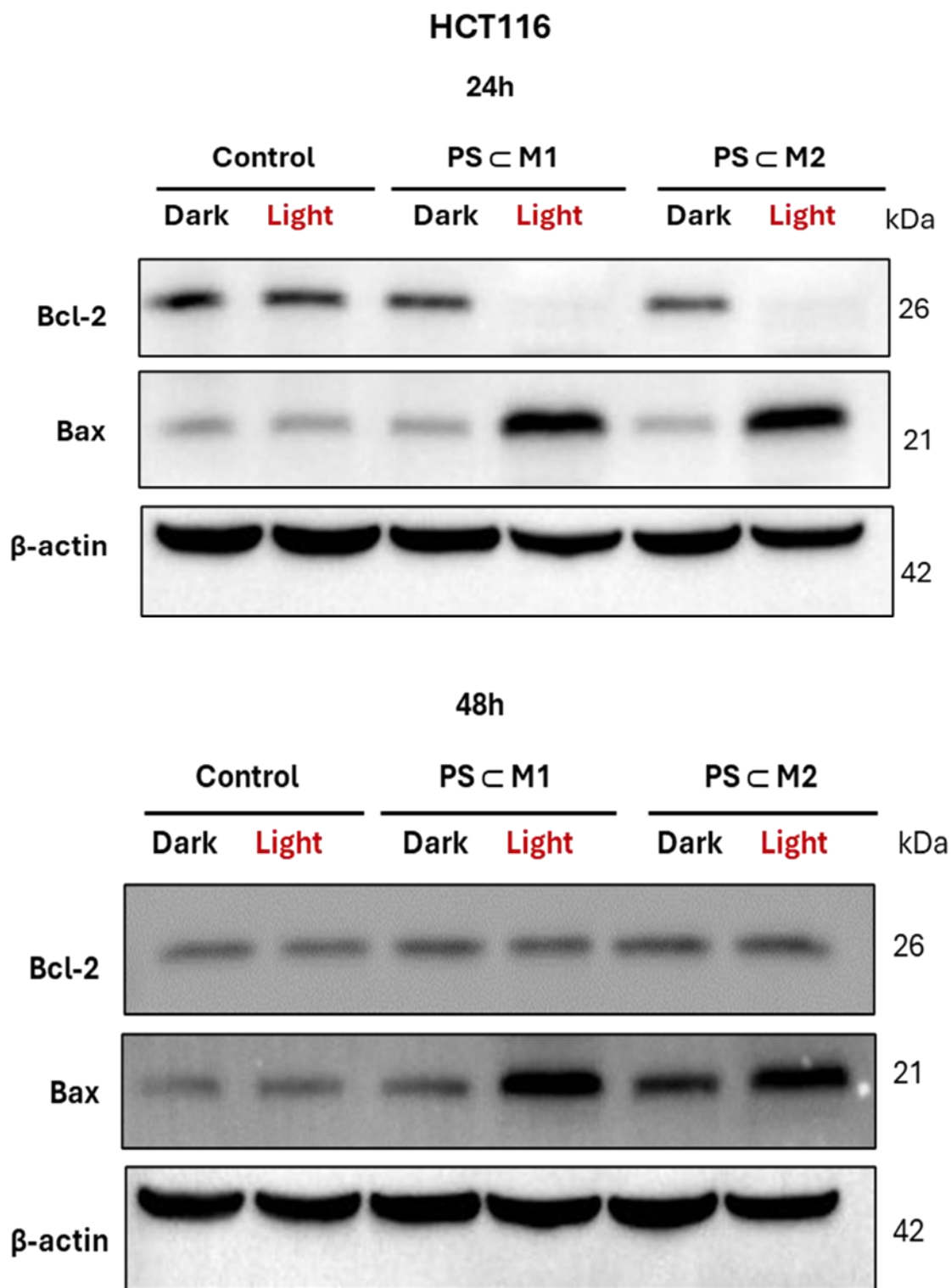


Figure 76: Effects of the assemblies with/without PDT on the expression of pro-apoptotic and anti-apoptotic proteins in the HCT116 cell line.

Protein expression was evaluated by WB. HCT116 cells were seeded and incubated for 24 h, and then were treated or not at IC_{50} values of **PSCM1** or **PSCM2**. After treatment, cells were either illuminated (630 nm, 75 J/cm²) or not and collected 24 h and 48 h post-illumination. Proteins were extracted and the levels of protein expression in the different conditions were revealed. β -actin was used as a loading control. Representative images are shown.

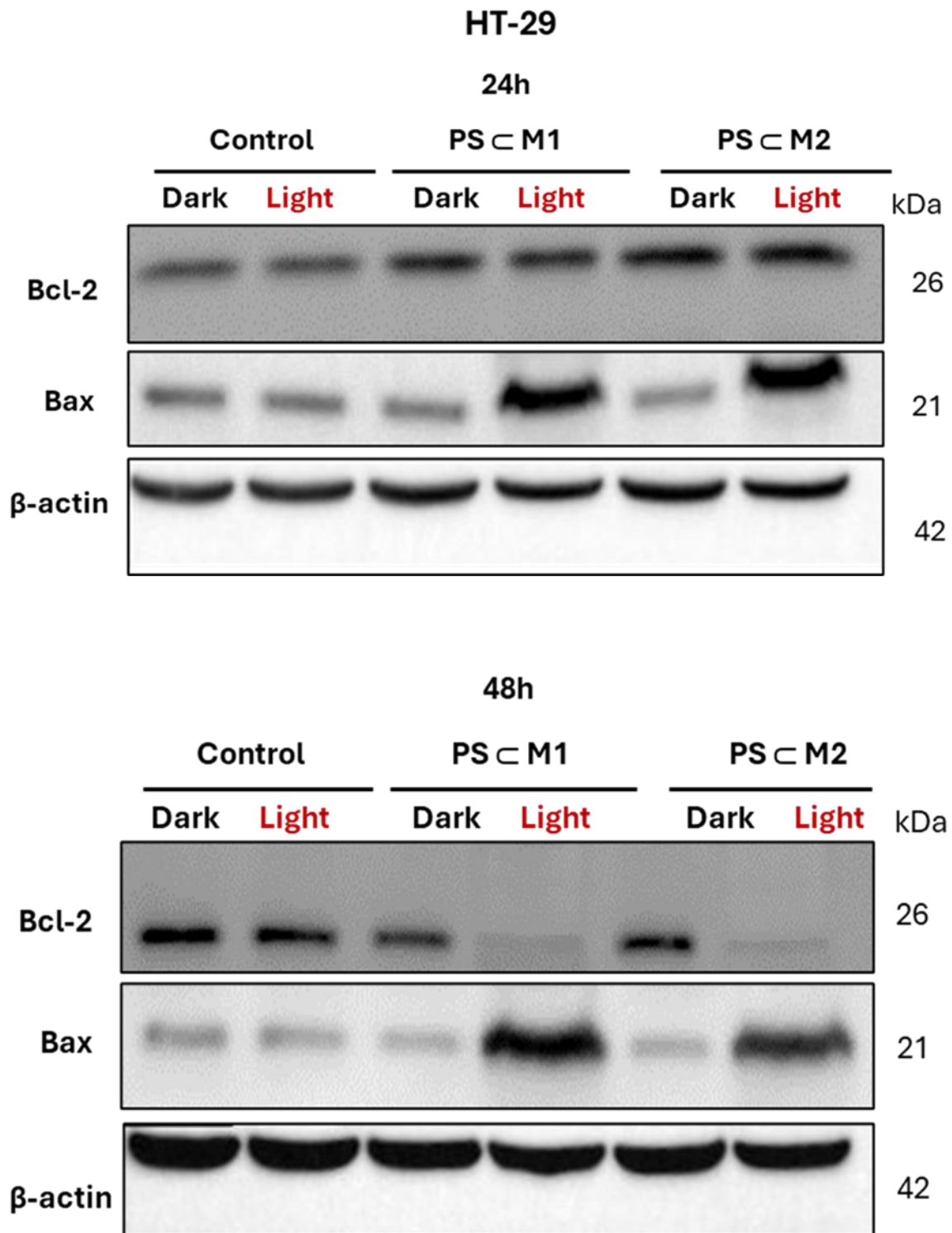


Figure 77: Effects of the assemblies with/without PDT on the expression of pro-apoptotic and anti-apoptotic proteins in the HT-29 cell line.

Protein expression was evaluated by WB. HT-29 cells were seeded and incubated for 24 h, and then were treated or not at IC₅₀ values of **PSCM1** or **PSCM2**. After treatment, cells were either illuminated (630 nm, 75 J/cm²) or not and collected 24 h and 48 h post-illumination. Proteins were extracted and the levels of protein expression in the different conditions were revealed. β-actin was used as a loading control. Representative images are shown.

In summary, these consistent findings concerning the activation of caspase-3, cleavage of PARP-1, and increased expression of Bax, along with reduced expression of Bcl-2 in treated and illuminated cells of both HCT116 and HT-29 cell lines, validate the effectiveness of our assemblies. This demonstrates their potential as effective agents for inducing apoptosis through a light-dependent mechanism.

VII.5.4. DNA fragmentation

To gain deeper insights into the apoptotic mechanisms activated by our treatments, we analyzed nuclear changes by assessing DNA fragmentation using an ELISA assay in both HCT116 and HT-29 cell lines. DNA fragmentation is a hallmark of apoptosis, representing the final stages of cellular destruction where the DNA is cleaved into small fragments by endonucleases. This process is a crucial indicator of the extent of apoptosis occurring within the cells.

In the HCT116 cell line, a significant increase in DNA fragmentation was observed at 24 h post-illumination which indicates the activation of the apoptotic pathway (**Figure 78**). Specifically, 24 h after exposure to red light illumination, the DNA fragmentation levels increased by 4.7-fold for cells treated with **PS_CM1** and by an even more pronounced 6.2-fold for those treated with **PS_CM2** as compared to the control cells. This marked elevation suggests that the apoptotic response peaks around this time point. However, by 48 h post-illumination, the extent of DNA fragmentation slightly decreased, showing a 3.1-fold increase for **PS_CM1** and a 4.4-fold increase for **PS_CM2** relative to controls.

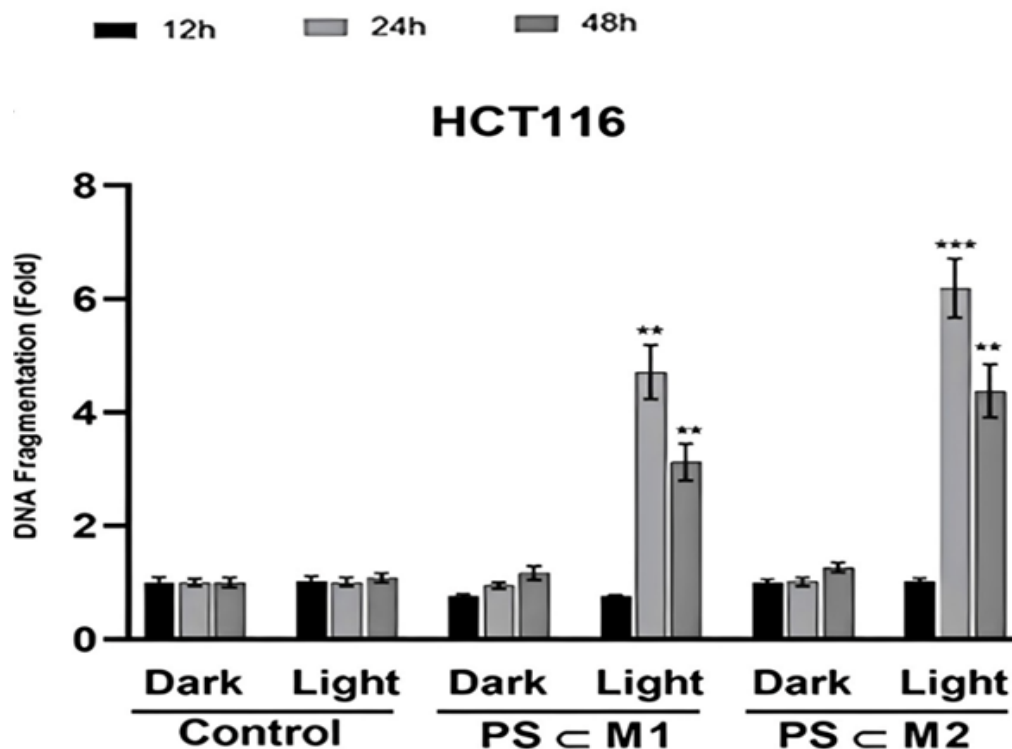


Figure 78: PDT-induced DNA fragmentation in the HCT116 cell line.

DNA fragmentation in the HCT116 cell line was analyzed from cytosol extracts using an ELISA assay. After seeding the cells for 24 h followed by treatment, cells were illuminated (630 nm, 75 J/cm²) or not. After 12 h, 24 h, and 48 h post-illumination, cells were collected, and the level of DNA fragmentation was analyzed. Histograms are represented as a mean ± SEM of at least three independent experiments. **p < 0.01 and ***p < 0.001.

For the HT-29 cell line (**Figure 79**), at 24 h post-illumination, there was a noticeable rise in DNA fragmentation with a 2.5-fold increase for **PS_CM1** and a 2.9-fold increase for **PS_CM2** as compared to the control cells. Unlike HCT116 cells, where DNA fragmentation peaked at 24 h, the HT-29 cells continued to show an increase in DNA fragmentation up to 48 h post-illumination. At this time point, the fold increase in DNA fragmentation reached 4.2 for **PS_CM1** and 5.6 for **PS_CM2** relative to controls.

Importantly, in both cell lines, no significant increase in DNA fragmentation was detected at 12 h post-illumination after treatment with either **PS_CM1** or **PS_CM2**. This lack of early response further highlights the delayed but potent apoptotic activity triggered by these assemblies upon illumination. Moreover, cells treated with **PS_CM1** or **PS_CM2** that were not subjected to illumination did not exhibit any significant changes in DNA fragmentation levels at 12 h, 24 h, or 48 h compared to control cells. This underscores the specificity of the apoptotic response to the light-dependent activation of these PS assemblies, confirming that illumination is crucial for initiating the apoptotic cascade.

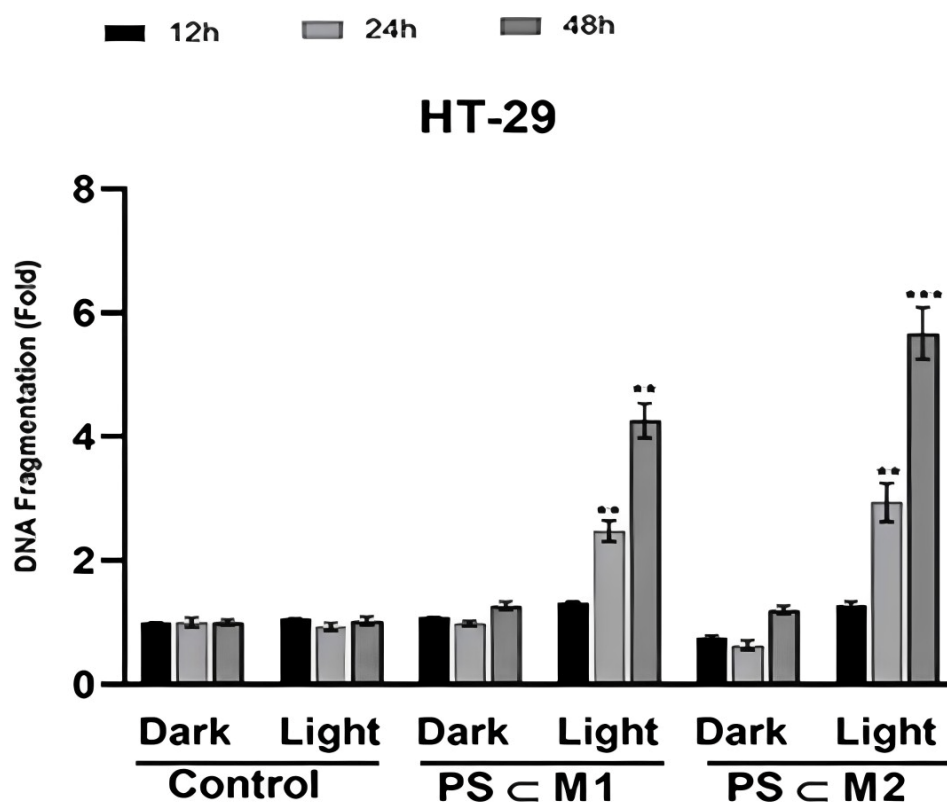


Figure 79: PDT-induced DNA fragmentation in the HT-29 cell line.

DNA fragmentation in the HT-29 cell line was analyzed from cytosol extracts using an ELISA assay. After seeding the cells for 24 h followed by treatment, cells were illuminated (630 nm, 75 J/cm²) or not. After 12 h, 24 h, and 48 h post-illumination, cells were collected, and the level of DNA fragmentation was analyzed. Histograms are represented as a mean ± SEM of at least three independent experiments. **p < 0.01 and ***p < 0.001.

These findings underscore the critical role of **PS_CM1** and **PS_CM2** in inducing DNA fragmentation, a key event in the apoptotic process. The most significant changes in DNA fragmentation were observed at 24 h post-illumination in HCT116 cells, while HT-29 cells

demonstrated a progressively increasing response up to 48 h. The absence of significant DNA fragmentation in non-illuminated cells and at earlier point further emphasizes the specificity and timing of the apoptotic response induced by these PS assemblies.

PDT is known for its extensive historical background, when a lot of light-based therapies were tested on different types of diseases including cancer [71], [72], [73]. Since conventional anticancer therapies are often associated with numerous undesirable side effects, PDT came as a breakthrough in cancer therapy for its effectiveness and selectivity towards the tumor site. As an innovative therapy, PDT is still under current elaboration and advancement, as new PS systems are being developed and modulated to fit a targeted and selective approach in the treatment of cancer. In particular, the involvement of PDT in the treatment of CRC had grabbed the interest of scientists in various research domains because CRC is distinguished by a high frequency of incidence and mortality rates, worldwide [24], [27].

Only a few PSs have been approved for medical applications, with porphyrin-based compounds being the most prominent [258]. However, this class of PSs has a low solubility in biological media which often constrains their use, applications, and implications in different studies. Fortunately, this limitation can be managed through the use of delivery vectors that encapsulate the PS so that a facilitated delivery and effective internalization by cells can be reached. To attain this outcome, the conjugation of porphyrin with metal-based drugs is considered a strategic approach for the treatment of several cancer types including CRC [259].

Ru complexes exhibit distinctive photochemical and photophysical properties conferring their uniqueness among metal-based therapies such as their ability to interact with cellular biomolecules and selectively accumulate in cancer cells [256], [260]. As reported in previous studies, Ru has grabbed the attention of many researchers as a modality of treatment of various cancer types including prostate, colorectal, bladder, and hepatic cancer due to its ability to act as a chemotherapeutic cytotoxic agent with selectivity towards the cancer cells [257], [261], [262], [263], [264]. Furthermore, it is demonstrated that the combination of tetrapyridylporphyrin and Ru(II) arene complexes played a crucial role as PDT-conjugated anticancer agent for the treatment of synovial sarcoma [265]. Several studies have highlighted that porphyrin-Ru complexes have significant anticancer effects. Bogoeva et al., demonstrated a porphyrin-Ru-induced photolesions in bladder cancer cells [263]. Also, a study by Schmitt et al. reported that five Ru(II) arene derivatives 5,10,15,20-tetra(4-pyridyl)porphyrin (TPP), as well as one *p*-cymeneosmium a and two pentamethylcyclopentadi-enyliridium showed significant phototoxicities towards melanoma cells after exposure to 652 nm laser light [266].

More recently, it was reported that arene-Ru cubic or prismatic cages could serve as ideal carriers of PS for the treatment of rheumatoid arthritis [267]. In our study, a similar advanced PDT approach involving two distinct host-guest systems where the porphyrin PS acts as a guest in a hexanuclear arene-Ru metalla-prismatic hosts, is investigated on two CRC cell lines of different stages: HCT116 and HT-29. These prismatic cages are composed of three major components including *p*-cymene-ruthenium vertices, spacers joining these vertices and acting as edges, and two *tp* panels. The particular difference among both tested cages is in the structure of the spacers that act as the cages' edges, in which one cage carries "donq" spacers that are composed of two aromatic rings and the other one holds "dotq" spacers that are composed of four aromatic rings. This variation yielded metal cages with similar-sized cavities but different-sized portals.

The same cages were previously described and studied by Barry et al. who used different guest molecules such as pyrene-R and Pd-(acac)₂. In their study, it was mentioned that once the system enters the cell by endocytosis, the PS guest is usually released from its host cage through the cage's portal without the destruction or rupture of the host. Once released, the PS gets excited by an appropriate light wavelength and exerts its potential to induce oxidative stress and cell damage. The dynamism between the host and the guest can interfere with the

excitation energy normally absorbed by the guest through static quenching and might enable energy transfer from the guest to the host. This energy transfer can reduce the fluorescence emission of the guest through partial quenching as the spectral absorbance of the metal prisms might overlap with the emission spectrum of the guest. Hence, it is preferred that the PS guest is released from its host for proper tracking, excitation and induction of action mechanisms [255]. Besides, as these encapsulation structures are cationic, the electric repulsion between the assemblies will prevent the formation of aggregates, thereby enhancing their solubility [268]. This could positively impact the PDT efficacy and improve the therapeutic index.

- **Photocytotoxic activity and ROS generation**

Primarily, the cellular metabolic activity of HCT116 and HT-29 cell lines was assessed after their treatment with the two assemblies containing porphyrin in their inner cavities, or with the empty cages, and showed different activity profiles after exposure or not to red illumination. In the presence of light, the assemblies containing porphyrin PS, showed a potent photocytotoxic activity in a dose and time-dependent manner. However, in the dark the cell viability was rarely affected demonstrating the ability of these assemblies to exert a selective potential in PDT. Interestingly, the determined IC_{50} values were found in nanomolar ranges on the two cell lines studied after 12, 24 and 48 h post-illumination. Both compounds exerted a relatively similar efficacy on the viability of the cell with a preferable effect associated with the cage having the larger spacer "dotq". Additionally, our findings demonstrated the potency of the Ru metallacages (**M1** and **M2**) to act as delivery systems of porphyrin since they did not exhibit a cytotoxic effect under the studied concentration range either in the presence or in the absence of illumination. Hence, the IC_{50} of the **PS<M** systems determined with light illumination after different time points, ranging between 500 and 900 nM, is mainly due to the porphyrin PS rather than the metallacages. In the study of Gallardo-Villagrán et al., a correlation between the spacer size and the release of porphyrin PS was proved through the IC_{50} determination. In their study, the same metallacages with porphyrin PS inside the cavity were investigated on rheumatoid arthritis synoviocytes, and the IC_{50} of the **PS<M2** (named G1<M3 in their study) was around two-fold lower than that of **PS<M1** (named G1<M2 in their study) at 18 h post-illumination. This was linked to the fact that a bulkier spacer made up of four aromatic rings (**M2**) allows a facilitated release of PS from the internal cavity of the cage as compared to that with two aromatic rings (**M1**). Additionally, the spacer that was made up of only one aromatic ring had a significantly higher IC_{50} value compared to both **PS<M1** and **PS<M2** [244]. However, in a previous study, the latter spacer was also included in the same cage with porphyrin PS inside and investigated on DU 145 and PC-3 prostate cancer cell lines, and the determined IC_{50} values were found in nanomolar ranges between 500 and 650 nM after 24 h of illumination [257]. These values were close to our findings with **PS<M1** and **PS<M2** treatments on HCT116 and HT-29 CRC cell lines. We can still notice that in our study **PS<M2** with the larger spacer has a better overall effect than **PS<M1** validating the study of Gallardo-Villagrán et al., yet the difference is not significant.

Here, we can demonstrate that the cell lines originating from different diseases will ultimately possess different sensitivity to the same treatment, also taking into consideration the impact of the difference in the drug-light time intervals. Even the different cell lines originating from the same disease will rationally not display similar outcomes. This was validated in our study when HCT116 and HT-29 CRC cell lines did not exhibit equal responses to the same treatment. As HCT116 is more sensitive than HT-29, the IC_{50} values obtained in our study with the same treatment at 12 h post-illumination was about two-fold lower than that of HT-29. Additionally, the observed apoptotic effect was reached faster in HCT116 than in the HT-

29 cell line where the maximal effect of the complexes was obtained 24 h post-illumination in the HCT116 whereas a relatively similar effect was obtained 48 h post-illumination on the HT-29 cell line. In our study, the anti-cancer efficacy of the **PS◄M1** and **PS◄M2** complexes could not be compared with the free porphyrin PS, as it exhibits a strong hydrophobicity in physiological media, as previously mentioned, leading to the formation of aggregates which strongly limit their biodistribution and availability [269], [270].

The principle of PDT is based on the generation of ROS following the photoactivation of PS. Indeed, depending on the intensity of the generated oxidative stress, the produced lesions can induce cell death. Even so, this is also related to the ROS concentration, lifespan, and site of production [90]. To confirm the involved photocytotoxicity of our complexes, it is essential to investigate the production of ROS. Our data revealed that these assemblies induce ROS production in the cells directly after their illumination. The ROS levels were significantly high, which strongly validates the use of these compounds in PDT of CRC. However, this was not observed with the cells that were not illuminated. These results are compatible with many previous findings [162], [257], [261].

Taken together, these results confirm that **PS◄M1** and **PS◄M2** meet the key criteria of an ideal PS: stability and constant solubility, low dose for high therapeutic efficacy, no dark toxicity, and potential absorbance in the red-light spectrum. The selectivity to tumor cells contributed to the presence of Ru in the cage's structure enabling its binding to transferrin receptors on tumor cells through its affinity to transferrin binding sites [97], [271].

- **Localization, protein expression, and enzymatic activity**

The determination of the cellular localization of the drugs paves the way to the understanding of the involved cellular mechanisms in response to treatment. In the context of PDT, the induced mode of the apoptotic pathway is dependent on the PS localization within the cell. As porphyrin PS is auto-fluorescent in the visible red-light regions, this allowed its efficient tracking by confocal microscopy [256]. Also, since the absorbance spectrum of our PS is in red, this allows our complexes to be a good fit for an ideal PS involved in the treatment of deeply situated tumor tissues. Generally, when PS is excited, it follows the "Jablonski scheme" where it reaches a higher energy state (excited singlet state). Fluorescence is the consequence of the energetic decay of the excited state of the PS towards a minimal energy state or ground state [269], [270]. As previously stated, the fluorescence is emitted at its best when the PS is released from the cage as the dynamism between the guest and the host could potentially diminish the excitation and emission properties of the PS.

In our study, the fluorescence associated with the PS was primarily observed in the cytoplasm of the cell. Moreover, to further investigate the possible localization of these PS in cellular organelles, staining of ER, mitochondria, and lysosomes was used for their efficient tracking in HCT116 and HT-29 cell lines. The co-localization was only observed with the mitochondria, which is consistent with the mechanism of action of PDT. However, no co-localization of the PS was observed in the ER and lysosomes. This finding reveals that when the metal cages are internalized, by endocytosis, the PS is released via the cage's aperture, leading to its primary localization within the mitochondria of the cells. The absence of lysosomal co-localization aligns with the study of Barry et al., which demonstrated that these cages do not deliver their content to lysosomal targets. The internalization of the metal cages was also confirmed by the inductively coupled plasma mass spectrometry (ICP-MS) technique, which quantified the Ru concentrations within the cell and showed a positive result [255]. Another study involving $[\text{Ru}_4-(\eta_6\text{-C}_6\text{H}_5\text{CH}_3)_4(\text{TPP})\text{Cl}_8]$ and $[\text{Ru}_4-(\eta_5\text{-C}_5\text{Me}_5)_4(\text{TPP})\text{Cl}_8]$ showed that they

accumulated in the cytoplasm of melanoma cells in granular structures different from lysosomes [266]. It was also demonstrated that when ROS are generated in the cytoplasm or mitochondria, they trigger the induction of apoptosis. At this level, ROS facilitates the opening of pores in the mitochondrial membrane, eventually inducing the activation of caspases and promoting the apoptotic cell death mechanism [272].

Moreover, the regulation of the apoptotic process via mitochondria is mediated by members of the Bcl-2 family. Indeed, the ratio between pro- and anti-apoptotic proteins determines the cell's susceptibility to apoptosis. The antagonistic Bcl-2 and Bax proteins bind and neutralize each other. The Bcl-2 protein prevents homodimerization of Bax, Bak and other multi-domain pro-apoptotic proteins of the same family. The Bax homodimer binds to the mitochondrial outer membrane. This leads to perforation of the mitochondrial membrane and release of cytochrome c into the cytosol that can form apoptosome and activate caspases resulting in cell death [181], [186], [187].

Thus, it can be interpreted from our data that when the porphyrin PS is released, it will mainly localize in the mitochondria, and generate ROS, which will alter the mitochondrial membrane potential and compromise the membrane integrity. This will induce the corresponding release of cytochrome c that can form apoptosome and induce the activation of apoptotic markers such as caspase-3 and PARP-1 enzymes. This was confirmed by our results of WB where we observed cleavage of caspase-3 and PARP-1 enzymes only in the samples treated with our **PS-M1** and **PS-M2** assemblies and exposed to red illumination (630 nm and 75 J/ cm²), mainly 24 and 48 h post-illumination. Additionally, the expression of the Bcl-2 anti-apoptotic protein was reduced in these samples; whereas an increased expression of the Bax, pro-apoptotic protein, was observed in these samples as compared to the control and treated non-illuminated conditions.

Being a programmed cell death mechanism, apoptosis is distinguished by the formation of apoptotic bodies budding off the cells which are subsequently phagocytosed. Other morphological features of cells undergoing apoptosis include cell shrinkage, chromatin condensation, and nuclear fragmentation [273]. During the early stages of apoptosis, phosphatidylserines translocate from the inferior side of the plasma membrane to the outer side. The externalization of the phosphatidylserines in early apoptotic cells was evaluated on HCT116 and HT-29 cell lines through annexin V staining and the total loss of membrane integrity in late apoptotic cells was measured through PI staining. Our data showed a significant increase in the percentage of apoptotic cells (early and late) after treatment and exposure to red illumination at different time points post-illumination, mainly 24 and 48 h.

This was also validated by our findings using the IncuCyte[®] S3 system in which the high green fluorescence intensity was only observed with the treated and photo-activated samples which is correlated with the caspase-3/7 activity. Our findings are supported by a study conducted by Peña et al. which demonstrated that Ru(II) polypyridyl compounds with nitrogen ligands induced apoptosis of human lung adenocarcinoma cells after photo-activation through the activation of caspase-3/7 [274]. Also, a study performed by Li et al. on a group of Ru complexes showed an overexpression of Bax and a reduced expression of Bcl-2 in human lung carcinoma A549 cells [275]. Another study by Jiang et al. revealed that their Ru complexes decreased the expression of the anti-apoptotic protein Bcl-xL but increased the expression of the pro-apoptotic proteins Bax, Bad and Bid [276].

In our results, the cleavage of caspase-3 and in turn of PARP-1, which is a DNA repair enzyme and a substrate of the active caspase-3, strongly confirm our first conclusions. Eventually, it is

expected that this will lead to the emergence of high levels of DNA damage and fragmentation in these conditions and will possibly induce cell cycle arrest to pave the way for repairing the formed DNA damage.

- **Cell cycle analysis and DNA fragmentation**

The inhibition of cancer cell proliferation by cytotoxic drugs could result from induction of apoptosis or cell cycle arrest, or from a dual combination of both phenomena [277]. After the evaluation of the progression of the cell cycle, we observed a peak of sub-G1 marking an apoptotic cell death after photoactivation in both cell lines. Li et al. established a successful apoptotic effect on A549 lung carcinoma cells distinguished by a sub-G1 peak after treatment with several Ru complexes [275].

Also, we demonstrated that the cell cycle blockage was not the same on both cell lines, as mentioned earlier, the studied systems caused an arrest of the cell cycle at the G1 phase in the HCT116 cell line and at the G2 phase in the HT-29 cell line. Another study showed that Ru tetrapyrrolylporphyrin assemblies investigated on CRC caused a blockage in the S phase of the cell cycle [261]. Cell cycle regulation recruits a well-demonstration of the cellular integrity and its constituents. Upon DNA damage, the cell cycle is arrested at specific checkpoints to provide time for DNA repair mechanisms to take place. If the damage was successfully repaired the cell continues its cycle; however, in the case of failure of DNA repair, apoptotic signals will be induced, and the cell enters apoptosis [278]. Therefore, these results validate our hypothesis of apoptosis and cell cycle arrest. A study by Rani-Beeram et al. carried on melanoma cells demonstrated a strong interaction of fluorinated porphyrin-Ru with DNA, inducing its cleavage [279]. This can also be correlated with the photophysical and photochemical properties of Ru complexes which allow them to bind to DNA and induce their cleavage after photoactivation [280]. Additionally, these results are in agreement with the study of Lu et al. who reported the anticancer effect of Ru complexes on hepatocellular carcinoma through cell growth inhibition, induction of apoptosis revealed by the sub-G1 peak, and the activation of caspases along with DNA fragmentation [264].

Cumulatively, the observed sub-G1 peak in the cell cycle assay, the externalization of phosphatidylserines, the cleavage of caspase-3 and PARP-1 enzymes and the DNA fragmentation also confirm the apoptotic cell death mechanism exerted by these assemblies on HCT116 and HT-29 CRC cell lines. Proteases of the caspase family are generally activated during apoptosis. The caspase family contains initiator caspases which, once activated, activate effector caspases represented mainly by caspase-3 and caspase-7. This activation occurs during the executor phase of apoptosis leading to the cleavage of numerous cellular substrates including PARP-1 enzyme. Caspase-3 also activates endonucleases during the late apoptotic stages which cleave the DNA into oligonucleosomal fragments [170], [185], [273].

Similarly, a study by Li et al. reported the induction of apoptosis in HepG2 liver cancer cells after the photoactivation of the Ru porphyrin complex Rup-03 [281]. Another study conducted by Pan et al. demonstrated the induction of apoptosis by a Ru polypyridine (Ru3) complex conjugated to a 5-FU derivative acting as a ligand on HeLa cervical cancer cells [282]. Also, Bomfim et al. proved that the complexes of Ru(II) with 6-methyl-2-thiouracil induced a reduction in cell proliferation, externalization of phosphatidylserines, a reduced mitochondrial membrane potential, and activation of caspase-3, -8 and -9 in the HL-60 myeloid leukemia cells [283]

In summary, the inhibition of cell proliferation after the photoactivation with red illumination of **PS<M1** and **PS<M2** assemblies is due to the production of ROS that can trigger the cell cycle

arrest and apoptosis of HCT116 and HT-29 CRC cell lines. This makes these complexes potential candidates of PDT agents to undergo further testing *in vivo* and in clinical phase trials. Also, by understanding the timing and magnitude of apoptotic responses, clinicians can better design treatment schedules that maximize therapeutic efficacy while minimizing potential side effects, laying the groundwork for more personalized and precise cancer treatments.

Currently, one of the major obstacles associated with the conventional cancer therapies is their non-selectivity to tumor cells. This leads to a significantly reduced therapeutic index and numerous side effects in cancer patients. Conversely, PDT, based on using non-cytotoxic PS in the absence of photoactivation, emerged as a promising focal therapy limiting the undesirable side effects. However, some challenges are also associated with PDT including the low solubility of PS in biological media, limited biodistribution, and poor tumor targeting. In this context, this study was conducted to evaluate the combination of PS in arene-Ru carriers, which can enhance the hydrophilicity of PS and improve tumor targeting, thereby overcoming the PDT-associated challenges. Particularly, this study was performed on two CRC cell lines HCT116 and HT-29 of stages I, and II, respectively. The choice of this type of cancer is based on the fact that CRC is among the most common malignant tumors in terms of incidence and death, distinguished by high mortality, rapid metastasis, and recurrence.

Indeed, the conjugation of porphyrins to Ru complexes has proven to be a valuable approach in advancing the design of anticancer agents. This approach aims to combine the cytotoxicity and selectivity of the Ru metal with the phototoxicity of porphyrin chromophore for a synergistic effect. To bypass the challenges of stability and solubility of Ru-based PSs, arene-Ru metal cages were synthesized to encapsulate the PS. This encapsulation system provides an isolated environment to protect the PS from degradation and enhance its solubility.

Our collaborators Gallardo-Villagran et al., synthesized these encapsulation systems where arene-Ru metal cages were used to lodge a porphyrin PS in their inner cavity, and reported their efficacy on primary cultures of fibroblast-like synoviocytes from patients with rheumatoid arthritis [244]. Additionally, these systems showed anticancer photocytotoxicity against prostate cancer cell lines [257]. In this encapsulation form, the prismatic or cubic-shaped cages act as hosts for the PS guests in their inner cavities, transport them as delivery vehicles and release them intracellularly. Also, there is another type of cage that can be either prismatic or cubic, not studied in this project, where the PS is integrated within the initial structure of the cage host, thereby maintaining excellent solubility in biological media and always ensuring the availability of the PS for excitation.

The prismatic arene-Ru metal cages studied in this project, carries 21H, 23H-porphyrin PS in their inner cavities. As mentioned earlier, this structure provides advantageous characteristics, making them one of the best PS delivery systems. In view of the cage's metallic structure and its effect after photoactivation, it was confirmed that these cages are mainly used as delivery vehicles of the photosensitive porphyrin. The aim of this project was to evaluate the anti-cancer efficacy of two different arene-Ru cages encapsulating porphyrin PS in comparison to the empty arene-Ru cages and the involved phototoxic mechanisms *in vitro* on CRC.

The results showed that the two photoactivated arene-Ru-PS assemblies (**PS◊M1** and **PS◊M2**) exerted a potent anticancer efficacy on HCT116 and HT-29 CRC cell lines, especially that the determined IC₅₀ values were low, in the nanomolar range. It is also noticed that due to the bulkier spacer contributing to a larger portal size of the **M2** cage, there was a more facilitated release of PS and an overall better effect of the assemblies as compared to **M1** cage. However, the difference in the effect exerted with both systems is not significant and both systems showed a very promising encapsulation potential. Furthermore, we demonstrated that both complexes did not exert any cytotoxic effect in the absence of illumination in both HCT116 and HT-29 cell lines. We also reported that the good cellular internalization of PS with mitochondrial accumulation of both encapsulation systems is correlated to the anticancer apoptotic potential of our complexes. To gain a deeper understanding, we evaluated the mechanisms induced after the internalization of PS where we found that once they are photoactivated, they induce the production of ROS inducing an

oxidative stress within the cell. The oxidative stress triggers the activation of the pro-apoptotic protein, Bax, and the inhibition of its antagonist, Bcl-2 proteins. This causes a loss of mitochondrial membrane potential which subsequently triggers the activation of caspase-3/7 through cleavage. The active caspase-3/7, in turn, can now activate its downstream proteins such as the PARP (DNA repair enzyme). This will eventually lead to DNA fragmentation and apoptosis of cells. Also, the apoptosis was remarked by the sub-G1 peak during the analysis of the cell cycle progression. Interestingly, we found that these assemblies triggered the cell cycle arrest in the G1 phase of the HCT116 cell line and the G2 phase of the HT-29 cell line. We can mention that both cell lines exhibited differences in their response to the treatment. The HCT116 cell line exhibited a more rapid response which peaked at 24 h post-illumination. Nevertheless, to reach the same apoptotic outcome, the HT-29 cell line required more time, particularly 48 h after illumination. The difference in the response profiles obtained seemed logical as the HCT116 cell line is more sensitive than the HT-29 cell line.

Hence, we can conclude that **PS◀M1** and **PS◀M2** complexes exerted their anti-proliferative by inducing ROS generation and apoptotic mechanisms. Their significant phototoxic effect, reduced required doses for a therapeutic effect, lack of toxicity in the dark, stability, and tumor selectivity, position these metal cages as one of the most promising PS vectorization systems for therapeutic purposes against CRC.

More *in vitro* experiments can be conducted to gain a deeper insight into the mechanisms involved and those that may interfere with the success of these complexes in PDT applications. This includes the evaluation of the kinetics involving the timing and rate of PS uptake and release into the cells to help scientists better decide on the strategy to follow in further studies. Also, the investigation of the affected signaling pathways responsible for cell proliferation such as the MAPK/ERK, PI3K/Akt, JAK/STAT, NF-κB, and TGF-β signaling pathways.

As autophagy of cells plays a significant role in resistance to apoptosis during PDT treatment, autophagy appears to be a target of choice for increasing the anticancer efficacy of PSs. Some studies have demonstrated that the inhibition of autophagy during PDT potentiates its therapeutic index [243] [244]. Therefore, it would be interesting to analyze *in vitro* the effect of our complexes in PDT after inhibition of autophagy process. In addition, it is important to study the presence of necrosis markers in order to determine whether this other form of cell death could also be associated with the effects produced by our PDT complexes. One of the major challenges in the processes of drug discovery and evaluation, *in vitro*, is the development of predictive cell-based assays and biological conditions that mimic the actual physiological environment for optimal PS screening. The integration of three-dimensional (3D) assay models is becoming more common for conducting research that bridges basic science and clinical applications. These cell culture models have the advantage of closely mimicking human physiological tissues and their corresponding microenvironments through offering relevant features such as cellular organization, cell-cell interactions, cell-matrix dynamism, and improved drug penetration. This also enables better analysis of the involved resistance mechanisms and provides the opportunity of creating extended studies of chronic effects and long term-drug responses. Thus, the use of 3D cell assays enhances research by connecting the insights gained from 2D cell cultures to observations from animal models, thereby increasing the relevance of the results for clinical applications. Hence, it would then be of great prominence to assess the anticancer efficacy of red-light photoactivated **PS◀M1** and **PS◀M2** on 3D CRC models.

Importantly, for a treatment to progress to the clinical phase trials, it must be subjected to *in vivo* testing on animal models. To enhance the study of the antiproliferative and apoptotic effect of our assemblies in PDT, it would be crucial to test these two complexes on a subcutaneous

xenograft model of human CRC using genetically modified immunodeficient mice as well as to evaluate their biocompatibility, biodistribution, kinetics, and effect on various body organs.

Briefly, the encapsulation of the porphyrin PS into arene-Ru metal assemblies has demonstrated a promising potential, notably in terms of stability, solubility, phototoxicity and induction of apoptotic pathways on CRC. The arene-Ru cages effectively served as delivery vehicles of PS, facilitating its intracellular transport. Once delivered, the PS predominantly accumulates in cell cytoplasm, particularly in the mitochondria. The activation of apoptotic markers has provided solid evidence for the relevance of PDT treatment following cellular oxidative stress. It is now essential to set up a pre-clinical model to validate the results obtained in vitro, so that this therapeutic approach using arene-Ru complexes can one day make its appearance in the clinic.

- [1] V. Mahadevan, "Anatomy of the caecum, appendix and colon," *Surgery (Oxford)*, vol. 35, no. 3, pp. 115–120, Mar. 2017, doi: 10.1016/j.mpsur.2017.01.014.
- [2] J. Gordon Betts, *Anatomy and Physiology Second Edition*. Houston, Texas: Pearson, 2019. doi: 10.24918/1155528.
- [3] H. H. Li-Chang *et al.*, *Atlas of Intestinal Pathology*. Cham, Switzerland: Springer International Publishing, 2019. doi: 10.1007/978-3-030-12379-6.
- [4] P. Poitras, Ed., *L'appareil digestif*. Montréal, Canada: Les Presses de l'Université de Montréal, 2016. doi: 10.2307/j.ctv69tdtm.
- [5] V. Martin and F. Vicari, "Atlas d'anatomie humaine," *Acta Endoscopica*, vol. 34, no. 4, pp. 630–630, Aug. 2004, doi: 10.1007/BF03006357.
- [6] M. Zahaf, "Les principaux médicaments responsables de diarrhées et de vomissements iatrogènes." [Online]. Available: <https://dumas.ccsd.cnrs.fr/dumas-01804053>
- [7] A. Young, R. Hobbs, and D. Kerr, *ABC of Colorectal Diseases Anatomy and Physiology of the Colon, Rectum, and Anus*. London: BMJ Publishing Group, 2011.
- [8] J. K. and N. W. Yamni Nigam, "190925-Gastrointestinal-tract-5-the-anatomy-and-functions-of-the-large-intestine." [Online]. Available: <https://www.nursingtimes.net/clinical-archive/gastroenterology/gastrointestinal-tract-5-anatomy-functions-large-intestine-23-09-2019/>
- [9] Y. Z. Zhang and Y. Y. Li, "Inflammatory bowel disease: Pathogenesis," *World J Gastroenterol*, vol. 20, no. 1, pp. 91–99, Jan. 2014, doi: 10.3748/wjg.v20.i1.91.
- [10] M. Fakhoury, R. Negrulj, A. Mooranian, and H. Al-Salami, "Inflammatory bowel disease: Clinical aspects and treatments," Jun. 23, 2014, *Dove Medical Press Ltd*. doi: 10.2147/JIR.S65979.
- [11] H. E. Lockhart-Mummery and B. C. Morson, "Crohn's disease of the large intestine," 1964.
- [12] M. F. Neurath, "Targeting immune cell circuits and trafficking in inflammatory bowel disease," *Nat Immunol*, vol. 20, no. 8, pp. 970–979, Aug. 2019, doi: 10.1038/s41590-019-0415-0.
- [13] H. H. Uhlig, "Monogenic diseases associated with intestinal inflammation: implications for the understanding of inflammatory bowel disease," *Gut*, vol. 62, no. 12, pp. 1795–1805, Dec. 2013, doi: 10.1136/gutjnl-2012-303956.
- [14] J. Z. Liu and C. A. Anderson, "Genetic studies of Crohn's disease: Past, present and future," *Best Pract Res Clin Gastroenterol*, vol. 28, no. 3, pp. 373–386, Jun. 2014, doi: 10.1016/j.bpg.2014.04.009.
- [15] J. Torres, S. Mehandru, J.-F. Colombel, and L. Peyrin-Biroulet, "Crohn's disease," *The Lancet*, vol. 389, no. 10080, pp. 1741–1755, Apr. 2017, doi: 10.1016/S0140-6736(16)31711-1.

- [16] B. G. SHAFIROFF, "Applied anatomy of the colon and rectum," *Pediatr Clin North Am*, vol. 3, no. 1, pp. 3–13, Feb. 1956, doi: 10.1016/S0031-3955(16)30321-2.
- [17] J. Z. Liu *et al.*, "Association analyses identify 38 susceptibility loci for inflammatory bowel disease and highlight shared genetic risk across populations," *Nat Genet*, vol. 47, no. 9, pp. 979–986, Sep. 2015, doi: 10.1038/ng.3359.
- [18] N. Dmochowska, H. R. Wardill, and P. A. Hughes, "Advances in Imaging Specific Mediators of Inflammatory Bowel Disease," *Int J Mol Sci*, vol. 19, no. 9, p. 2471, Aug. 2018, doi: 10.3390/ijms19092471.
- [19] A. F. Peery *et al.*, "A high-fiber diet does not protect against asymptomatic diverticulosis," *Gastroenterology*, vol. 142, no. 2, pp. 486–492, 2012, doi: 10.1053/j.gastro.2011.10.035.
- [20] L. L. Strate and A. M. Morris, "Epidemiology, Pathophysiology, and Treatment of Diverticulitis," *Gastroenterology*, vol. 156, no. 5, pp. 1282–1298, Apr. 2019, doi: 10.1053/j.gastro.2018.12.033.
- [21] L. L. Strate, R. Modi, E. Cohen, and B. M. R. Spiegel, "Diverticular Disease as a Chronic Illness: Evolving Epidemiologic and Clinical Insights," *American Journal of Gastroenterology*, vol. 107, no. 10, pp. 1486–1493, Oct. 2012, doi: 10.1038/ajg.2012.194.
- [22] Children's Health, "Diverticulitis," <https://www.childrens.com/specialties-services/conditions/diverticulitis>.
- [23] D. Hanahan and R. A. Weinberg, "Hallmarks of Cancer: The Next Generation," *Cell*, vol. 144, no. 5, pp. 646–674, Mar. 2011, doi: 10.1016/j.cell.2011.02.013.
- [24] H. Sung *et al.*, "Global Cancer Statistics 2020: GLOBOCAN Estimates of Incidence and Mortality Worldwide for 36 Cancers in 185 Countries," *CA Cancer J Clin*, vol. 71, no. 3, pp. 209–249, May 2021, doi: 10.3322/caac.21660.
- [25] Y. Xi and P. Xu, "Global colorectal cancer burden in 2020 and projections to 2040," Oct. 01, 2021, *Neoplasia Press, Inc.* doi: 10.1016/j.tranon.2021.101174.
- [26] J. Ferlay *et al.*, "Global Cancer Observatory," Global Cancer Observatory: Cancer Today. Lyon, France: International Agency for Research on Cancer. [Online]. Available: <https://gco.iarc.who.int/today>
- [27] L. H. Biller and D. Schrag, "Diagnosis and Treatment of Metastatic Colorectal Cancer: A Review," *JAMA*, vol. 325, no. 7, pp. 669–685, Feb. 2021, doi: 10.1001/JAMA.2021.0106.
- [28] K. Katsaounou *et al.*, "Colon Cancer: From Epidemiology to Prevention," *Metabolites*, vol. 12, no. 6, p. 499, Jun. 2022, doi: 10.3390/metabo12060499.
- [29] M. Song and A. T. Chan, "Environmental Factors, Gut Microbiota, and Colorectal Cancer Prevention," *Clinical Gastroenterology and Hepatology*, vol. 17, no. 2, pp. 275–289, Jan. 2019, doi: 10.1016/j.cgh.2018.07.012.

- [30] J. M. Carethers and B. H. Jung, "Genetics and Genetic Biomarkers in Sporadic Colorectal Cancer," *Gastroenterology*, vol. 149, no. 5, pp. 1177–1190, Oct. 2015, doi: 10.1053/j.gastro.2015.06.047.
- [31] G. Mori and M. R. Pasca, "Gut microbial signatures in sporadic and hereditary colorectal cancer," *Int J Mol Sci*, vol. 22, no. 3, pp. 1–23, Feb. 2021, doi: 10.3390/ijms22031312.
- [32] V. Stigliano, L. Sanchez-Mete, A. Martayan, and M. Anti, "Early-onset colorectal cancer: A sporadic or inherited disease?," Sep. 21, 2014, *WJG Press*. doi: 10.3748/wjg.v20.i35.12420.
- [33] A. Malki, R. A. Elruz, I. Gupta, A. Allouch, S. Vranic, and A. E. Al Moustafa, "Molecular mechanisms of colon cancer progression and metastasis: Recent insights and advancements," *Int J Mol Sci*, vol. 22, no. 1, pp. 1–24, Jan. 2021, doi: 10.3390/ijms22010130.
- [34] W. M. Grady and S. D. Markowitz, "Genetic and Epigenetic Alterations in Colon Cancer," *Annu Rev Genomics Hum Genet*, vol. 3, no. 1, pp. 101–128, Sep. 2002, doi: 10.1146/annurev.genom.3.022502.103043.
- [35] E. F. Fearon and B. Vogelstein, "A Genetic Model for Colorectal Tumorigenesis," *Cell*, vol. 61, pp. 759–767, Jun. 1990.
- [36] N. Shussman and S. D. Wexner, "Colorectal polyps and polyposis syndromes," *Gastroenterol Rep (Oxf)*, vol. 2, no. 1, pp. 1–15, Feb. 2014, doi: 10.1093/gastro/got041.
- [37] S. Gupta, "Screening for Colorectal Cancer," Jun. 01, 2022, *W.B. Saunders*. doi: 10.1016/j.hoc.2022.02.001.
- [38] S. Bhattacharya, A. Page, S. Maru, and S. Dawre, *Colorectal Cancer Diagnosis and Therapeutic Updates*. Bentham Science Publishers, 2022. doi: 10.2174/97898150409441220101.
- [39] M. Świdarska *et al.*, "Review The diagnostics of colorectal cancer," *Współczesna Onkologia*, vol. 1, pp. 1–6, Jan. 2014, doi: 10.5114/wo.2013.39995.
- [40] W. Jelski and B. Mroczko, "Biochemical markers of colorectal cancer – present and future," *Cancer Manag Res*, vol. 12, pp. 4789–4797, Jun. 2020, doi: 10.2147/CMAR.S253369.
- [41] Ö. Akgül, E. Çetinkaya, Ş. Ersöz, and M. Tez, "Role of surgery in colorectal cancer liver metastases," *World J Gastroenterol*, vol. 20, no. 20, pp. 6113–6122, May 2014, doi: 10.3748/wjg.v20.i20.6113.
- [42] E. Lezoehe *et al.*, "Laparoscopic vs open hemicolectomy for colon cancer Long-term outcome," *Surg Endosc*, vol. 16, pp. 596–598, Apr. 2002.
- [43] K. De Campos, L. H. B. Bot, A. Petroianu, P. A. Rebelo, A. A. C. De Souza, and I. Panhoca, "The impact of colostomy on the patient's life," *Journal of Coloproctology*, vol. 37, no. 3, pp. 205–210, Jul. 2017, doi: 10.1016/j.jcol.2017.03.004.
- [44] B. M. P. Aleman, H. Bartelink, and L. L. Gunderson, "The Current Role of Radiotherapy in Colorectal Cancer," *Eur J Cancer*, vol. 31, no. 7–8, pp. 1333–1339, Apr. 1995.

- [45] M. F. Häfner and J. Debus, "Radiotherapy for colorectal cancer: Current standards and future perspectives," *Visc Med*, vol. 32, no. 3, pp. 172–177, Jun. 2016, doi: 10.1159/000446486.
- [46] S. Y. Tam and V. W. C. Wu, "A review on the special radiotherapy techniques of colorectal cancer," *Front Oncol*, vol. 9, pp. 1–9, Apr. 2019, doi: 10.3389/fonc.2019.00208.
- [47] B. Gustavsson *et al.*, "A Review of the Evolution of Systemic Chemotherapy in the Management of Colorectal Cancer," *Clin Colorectal Cancer*, vol. 14, no. 1, pp. 1–10, Mar. 2015, doi: 10.1016/j.clcc.2014.11.002.
- [48] L.-C. Fan *et al.*, "Pharmacological Targeting SHP-1-STAT3 Signaling Is a Promising Therapeutic Approach for the Treatment of Colorectal Cancer," *Neoplasia*, vol. 17, no. 9, pp. 687–696, Sep. 2015.
- [49] E. C. LaCasse, D. J. Mahoney, H. H. Cheung, S. Plenchette, S. Baird, and R. G. Korneluk, "IAP-targeted therapies for cancer," *Oncogene*, vol. 27, no. 48, pp. 6252–6275, Oct. 2008, doi: 10.1038/onc.2008.302.
- [50] M. Vanneman and G. Dranoff, "Combining immunotherapy and targeted therapies in cancer treatment," *Nat Rev Cancer*, vol. 12, no. 4, pp. 237–251, Apr. 2012, doi: 10.1038/nrc3237.
- [51] K. Ganesh *et al.*, "Immunotherapy in colorectal cancer: rationale, challenges and potential," Jun. 2019, *Nature Publishing Group*. doi: 10.1038/s41575-019-0126-x.
- [52] A. L. C. de S. L. Oliveira, T. Schomann, L.-F. de Geus-Oei, E. Kapiteijn, L. J. Cruz, and R. F. de Araújo Junior, "Nanocarriers as a Tool for the Treatment of Colorectal Cancer," *Pharmaceutics*, vol. 13, no. 8, p. 1321, Aug. 2021, doi: 10.3390/pharmaceutics13081321.
- [53] S. Gavas, S. Quazi, and T. M. Karpiński, "Nanoparticles for Cancer Therapy: Current Progress and Challenges," *Nanoscale Res Lett*, vol. 16, no. 1, Oct. 2021, doi: 10.1186/s11671-021-03628-6.
- [54] R. W. Wilkinson and A. J. Leishman, "Further Advances in Cancer Immunotherapy: Going Beyond Checkpoint Blockade," *Front Immunol*, vol. 9, Jun. 2018, doi: 10.3389/fimmu.2018.01082.
- [55] N. K. Vishvakarma, G. P. Nagaraju, and D. Shukla, Eds., *Colon Cancer Diagnosis and Therapy*. Cham, Switzerland: Springer International Publishing, 2021. doi: 10.1007/978-3-030-64668-4.
- [56] F. Z. Ilyas, J. D. Beane, and T. M. Pawlik, "The State of Immunotherapy in Hepatobiliary Cancers," *Cells*, vol. 10, no. 8, p. 2096, Aug. 2021, doi: 10.3390/cells10082096.
- [57] E. Vigna and P. M. Comoglio, "Targeting the oncogenic Met receptor by antibodies and gene therapy," *Oncogene*, vol. 34, no. 15, pp. 1883–1889, Apr. 2015, doi: 10.1038/onc.2014.142.

- [58] R. M. Zwacka and M. G. Dunlop, "Gene Therapy For Colon Cancer," *Hematol Oncol Clin North Am*, vol. 12, no. 3, pp. 595–615, Jun. 1998, doi: 10.1016/S0889-8588(05)70010-1.
- [59] Y. Tian, H. Kim, and H. W. Kang, "In vitro anti-tumor effect of high-fluence low-power laser light on apoptosis of human colorectal cancer cells," *Lasers Med Sci*, vol. 36, no. 3, pp. 513–520, Apr. 2021, doi: 10.1007/s10103-020-03050-x.
- [60] A. Bienia, O. Wiecheć-Cudak, A. A. Murzyn, and M. Krzykawska-Serda, "Photodynamic Therapy and Hyperthermia in Combination Treatment—Neglected Forces in the Fight against Cancer," *Pharmaceutics*, vol. 13, no. 8, p. 1147, Jul. 2021, doi: 10.3390/pharmaceutics13081147.
- [61] "Study Details | Immunotherapy Using Tumor Infiltrating Lymphocytes for Patients With Metastatic Cancer | ClinicalTrials.gov." [Online]. Available: <https://clinicaltrials.gov/study/NCT01174121>
- [62] T. K. Nikolouzakis *et al.*, "Current and Future Trends of Colorectal Cancer Treatment: Exploring Advances in Immunotherapy," *Cancers (Basel)*, vol. 16, no. 11, Jun. 2024, doi: 10.3390/cancers16111995.
- [63] A. Kumar, V. Gautam, A. Sandhu, K. Rawat, A. Sharma, and L. Saha, "Current and emerging therapeutic approaches for colorectal cancer: A comprehensive review," *World J Gastrointest Surg*, vol. 15, no. 4, pp. 495–519, Apr. 2023, doi: 10.4240/wjgs.v15.i4.495.
- [64] T. Ohishi, M. K. Kaneko, Y. Yoshida, A. Takashima, Y. Kato, and M. Kawada, "Current Targeted Therapy for Metastatic Colorectal Cancer," *Int J Mol Sci*, vol. 24, no. 2, p. 1702, Jan. 2023, doi: 10.3390/ijms24021702.
- [65] S. T. Williams and R. W. Beart, "Staging of colorectal cancer," *Semin Surg Oncol*, vol. 8, no. 2, pp. 89–93, 1992, doi: 10.1002/ssu.2980080208.
- [66] A. Shaukat *et al.*, "Endoscopic Recognition and Management Strategies for Malignant Colorectal Polyps: Recommendations of the US Multi-Society Task Force on Colorectal Cancer," *Gastroenterology*, vol. 159, no. 5, pp. 1916-1934.e2, Nov. 2020, doi: 10.1053/j.gastro.2020.08.050.
- [67] P. Quirke, G. T. Williams, N. Ectors, A. Ensari, F. Piard, and I. Nagtegaal, "The future of the TNM staging system in colorectal cancer: time for a debate?," *Lancet Oncol*, vol. 8, no. 7, pp. 651–657, Jul. 2007, doi: 10.1016/S1470-2045(07)70205-X.
- [68] N. W. N. Simelane and H. Abrahamse, "Nanoparticle-mediated delivery systems in photodynamic therapy of colorectal cancer," *Int J Mol Sci*, vol. 22, no. 22, p. 12405, Nov. 2021, doi: 10.3390/ijms222212405.
- [69] R. Labianca *et al.*, "Colon cancer," *Crit Rev Oncol Hematol*, vol. 74, no. 2, pp. 106–133, May 2010, doi: 10.1016/j.critrevonc.2010.01.010.
- [70] J. A. Meyerhardt and R. J. Mayer, "Systemic Therapy for Colorectal Cancer," *New England Journal of Medicine*, vol. 352, no. 5, pp. 476–487, Feb. 2005, doi: 10.1056/NEJMra040958.

- [71] T. J. Dougherty *et al.*, “Review Photodynamic Therapy,” *Cancer*, vol. 83, no. 12, pp. 1591–1600, Jun. 1998, doi: 10.1093/jnci/90.12.889.
- [72] M. D. Daniell and J. S. Hill, “A History of Photodynamic Therapy,” *Photomedicine and Laser Surgery*, vol. 61, no. 5, pp. 340–348, 1991, doi: 10.1111/j.1445-2197.1991.tb00230.x.
- [73] G. I. Stables and D. V Ash, “Photodynamic therapy,” *Cancer Treat Rev*, vol. 21, no. 4, pp. 311–323, Oct. 1995, doi: 10.1016/0305-7372(95)90035-7.
- [74] Á. Juarranz, P. Jaén, F. Sanz-Rodríguez, J. Cuevas, and S. González, “Photodynamic therapy of cancer. Basic principles and applications,” *Clinical and Translational Oncology*, vol. 10, no. 3, pp. 148–154, 2008, doi: 10.1007/s12094-008-0172-2.
- [75] L. B. Josefsen and R. W. Boyle, “Photodynamic therapy and the development of metal-based photosensitisers,” *Met Based Drugs*, vol. 2008, no. 1, pp. 1–23, Mar. 2008, doi: 10.1155/2008/276109.
- [76] N. Hodgkinson, C. A. Kruger, and H. Abrahamse, “Targeted photodynamic therapy as potential treatment modality for the eradication of colon cancer and colon cancer stem cells,” *Tumor Biology*, vol. 39, no. 10, p. 101042831773469, Oct. 2017, doi: 10.1177/1010428317734691.
- [77] F. Aydogan, V. Ozben, E. Aytac, H. Yilmaz, A. Cercel, and V. Celik, “Excision of Nonpalpable Breast Cancer with Indocyanine Green Fluorescence-Guided Occult Lesion Localization (IFOLL),” *Breast Care*, vol. 7, no. 1, pp. 48–51, Jan. 2012, doi: 10.1159/000336497.
- [78] J. R. van der Vorst *et al.*, “Intraoperative near-infrared fluorescence imaging of parathyroid adenomas with use of low-dose methylene blue,” *Head Neck*, vol. 36, no. 6, pp. 853–858, Jun. 2014, doi: 10.1002/hed.23384.
- [79] Q. R. J. G. Tummers *et al.*, “Real-time intraoperative detection of breast cancer using near-infrared fluorescence imaging and Methylene Blue,” *European Journal of Surgical Oncology (EJSO)*, vol. 40, no. 7, pp. 850–858, Jul. 2014, doi: 10.1016/j.ejso.2014.02.225.
- [80] T. B. Manny, A. S. Pompeo, and A. K. Hemal, “Robotic Partial Adrenalectomy Using Indocyanine Green Dye With Near-infrared Imaging: The Initial Clinical Experience,” *Urology*, vol. 82, no. 3, pp. 738–742, Sep. 2013, doi: 10.1016/j.urology.2013.03.074.
- [81] F. Acerbi *et al.*, “Is fluorescein-guided technique able to help in resection of high-grade gliomas?,” *Neurosurg Focus*, vol. 36, no. 2, p. E5, Feb. 2014, doi: 10.3171/2013.11.FOCUS13487.
- [82] A. Kawczyk-Krupka, A. M. Bugaj, W. Latos, K. Zaremba, K. Wawrzyniec, and A. Sieroń, “Photodynamic therapy in colorectal cancer treatment: The state of the art in clinical trials,” *Photodiagnosis Photodyn Ther*, vol. 12, no. 3, pp. 545–553, Sep. 2015, doi: 10.1016/J.PDPDT.2015.04.004.
- [83] S. R. De Annunzio, N. C. S. Costa, M. A. S. Graminha, C. R. Fontana, and R. D. Mezzina, “Chlorin, phthalocyanine, and porphyrin types derivatives in phototreatment of

cutaneous manifestations: A review,” *Int J Mol Sci*, vol. 20, no. 16, Aug. 2019, doi: 10.3390/ijms20163861.

- [84] A. Juzeniene and J. Moan, “The history of PDT in Norway. Part II. Recent advances in general PDT and ALA-PDT,” *Photodiagnosis Photodyn Ther*, vol. 4, no. 2, pp. 80–87, Jun. 2007, doi: 10.1016/j.pdpdt.2006.11.001.
- [85] J. H. Correia, J. A. Rodrigues, S. Pimenta, T. Dong, and Z. Yang, “Photodynamic therapy review: Principles, photosensitizers, applications, and future directions,” *Pharmaceutics*, vol. 13, no. 9, Sep. 2021, doi: 10.3390/pharmaceutics13091332.
- [86] E. Dumont and A. Monari, “Understanding DNA under oxidative stress and sensitization: the role of molecular modeling,” *Front Chem*, vol. 3, Jul. 2015, doi: 10.3389/fchem.2015.00043.
- [87] Barry Halliwell and John M. C. Gutteridge, “Free Radicals in Biology and Medicine,” *Acta Crystallogr D Struct Biol*, vol. 73, no. 4, pp. 384–385, Apr. 2017, doi: 10.1107/S2059798317004533.
- [88] I. Dalle-Donne, R. Rossi, D. Giustarini, A. Milzani, and R. Colombo, “Protein carbonyl groups as biomarkers of oxidative stress,” *Clinica Chimica Acta*, vol. 329, no. 1–2, pp. 23–38, Mar. 2003, doi: 10.1016/S0009-8981(03)00003-2.
- [89] C. P. Sabino and M. R. Hamblin, “Molecular Damage,” in *Photodynamic Therapy in Veterinary Medicine: From Basics to Clinical Practice*, Cham: Springer International Publishing, 2016, pp. 45–56. doi: 10.1007/978-3-319-45007-0_4.
- [90] J. Duan and D. L. Kasper, “Oxidative depolymerization of polysaccharides by reactive oxygen/nitrogen species,” *Glycobiology*, vol. 21, no. 4, pp. 401–409, Apr. 2011, doi: 10.1093/glycob/cwq171.
- [91] Q. Chang, P. Wang, Q. Zeng, and X. Wang, “A review on ferroptosis and photodynamic therapy synergism: Enhancing anticancer treatment,” *Heliyon*, vol. 10, no. 7, p. e28942, Apr. 2024, doi: 10.1016/j.heliyon.2024.e28942.
- [92] P. Mroz, A. Yaroslavsky, G. B. Kharkwal, and M. R. Hamblin, “Cell Death Pathways in Photodynamic Therapy of Cancer,” *Cancers (Basel)*, vol. 3, no. 2, pp. 2516–2539, Jun. 2011, doi: 10.3390/cancers3022516.
- [93] H. Singh, J. Bishop, and J. Merritt, “Singlet oxygen and ribosomes: Inactivation and sites of damage,” *Journal of Photochemistry*, vol. 25, no. 2–4, pp. 295–307, Jun. 1984, doi: 10.1016/0047-2670(84)87032-X.
- [94] N. L. Oleinick, R. L. Morris, and I. Belichenko, “The role of apoptosis in response to photodynamic therapy: what, where, why, and how,” *Photochemical & Photobiological Sciences*, vol. 1, no. 1, pp. 1–21, Jan. 2002, doi: 10.1039/b108586g.
- [95] V. Stoka *et al.*, “Lysosomal Protease Pathways to Apoptosis,” *Journal of Biological Chemistry*, vol. 276, no. 5, pp. 3149–3157, Feb. 2001, doi: 10.1074/jbc.M008944200.
- [96] T. Verfaillie, A. D. Garg, and P. Agostinis, “Targeting ER stress induced apoptosis and inflammation in cancer,” *Cancer Lett*, vol. 332, no. 2, pp. 249–264, May 2013, doi: 10.1016/j.canlet.2010.07.016.

- [97] P. Agostinis *et al.*, "Photodynamic therapy of cancer: An update," *CA Cancer J Clin*, vol. 61, no. 4, pp. 250–281, Jul. 2011, doi: 10.3322/CAAC.20114.
- [98] K. Kalka, H. Merk, and H. Mukhtar, "Photodynamic therapy in dermatology," *J Am Acad Dermatol*, vol. 42, no. 3, pp. 389–413, Mar. 2000, doi: 10.1016/S0190-9622(00)90209-3.
- [99] L. Benov, "Photodynamic therapy: Current status and future directions," in *Medical Principles and Practice*, S. Karger AG, Apr. 2015, pp. 14–28. doi: 10.1159/000362416.
- [100] R. Bonnett and G. Martínez, "Photobleaching of sensitizers used in photodynamic therapy," *Tetrahedron*, vol. 57, no. 47, pp. 9513–9547, Nov. 2001, doi: 10.1016/S0040-4020(01)00952-8.
- [101] T. T. Tasso *et al.*, "Photobleaching Efficiency Parallels the Enhancement of Membrane Damage for Porphyrazine Photosensitizers," *J Am Chem Soc*, vol. 141, no. 39, pp. 15547–15556, Oct. 2019, doi: 10.1021/jacs.9b05991.
- [102] A. C. Kübler, "Photodynamic therapy," *Medical Laser Application*, vol. 20, no. 1, pp. 37–45, May 2005, doi: 10.1016/j.mla.2005.02.001.
- [103] N. Choudhary, T. E. Collignon, D. Tewari, and A. Bishayee, "Hypericin and its anticancer effects: From mechanism of action to potential therapeutic application," Oct. 01, 2022, *Elsevier GmbH*. doi: 10.1016/j.phymed.2022.154356.
- [104] P. Agostinis, A. Vantieghem, W. Merlevede, and P. A. M. De Witte, "Hypericin in cancer treatment: more light on the way," *Int J Biochem Cell Biol*, vol. 34, no. 3, pp. 221–241, Mar. 2002, doi: 10.3389/fphar.2022.991554.
- [105] A. Kubin, H. G. Loew, U. Burner, G. Jessner, H. Kolbabek, and F. Wierrani, "How to make hypericin water-soluble," *Pharmazie*, vol. 63, no. 4, pp. 263–269, Apr. 2008, doi: 10.1691/ph.2008.7292.
- [106] G. Kah, R. Chandran, and H. Abrahamse, "Curcumin a Natural Phenol and Its Therapeutic Role in Cancer and Photodynamic Therapy: A Review," *Pharmaceutics*, vol. 15, no. 2, p. 639, Feb. 2023, doi: 10.3390/pharmaceutics15020639.
- [107] L. D. Dias, K. C. Blanco, I. S. Mfouo-Tynga, N. M. Inada, and V. S. Bagnato, "Curcumin as a photosensitizer: From molecular structure to recent advances in antimicrobial photodynamic therapy," *Journal of Photochemistry and Photobiology C: Photochemistry Reviews*, vol. 45, p. 100384, Dec. 2020, doi: 10.1016/j.jphotochemrev.2020.100384.
- [108] E. M. Klosowski *et al.*, "The photodynamic and direct actions of methylene blue on mitochondrial energy metabolism: A balance of the useful and harmful effects of this photosensitizer," *Free Radic Biol Med*, vol. 153, pp. 34–53, Jun. 2020, doi: 10.1016/j.freeradbiomed.2020.04.015.
- [109] S. H. Sharifi Pajaie, S. Archin, and G. Asadpour, "Optimization of Process Parameters by Response Surface Methodology for Methylene Blue Removal Using Cellulose Dusts," *Civil Engineering Journal*, vol. 4, no. 3, p. 620, Apr. 2018, doi: 10.28991/cej-0309121.

- [110] Y. Ye, H. Bruning, D. Yntema, M. Mayer, and H. Rijnaarts, "Homogeneous photosensitized degradation of pharmaceuticals by using red light LED as light source and methylene blue as photosensitizer," *Chemical Engineering Journal*, vol. 316, pp. 872–881, 2017, doi: 10.1016/j.cej.2017.02.053.
- [111] S. D.-M. Islam and O. Ito, "Solvent effects on rates of photochemical reactions of rose bengal triplet state studied by nanosecond laser photolysis," *J Photochem Photobiol A Chem*, vol. 123, no. 1–3, pp. 53–59, May 1999, doi: 10.1016/S1010-6030(99)00042-8.
- [112] P. P. Hankare and V. Jadhav, "Photocatalytic degradation of Rose Bengal in visible light with Cr substituted MnFe₂O₄ ferrosin," *Arch. Phys. Res.*, vol. 3, no. 4, pp. 269–276, Dec. 2012, [Online]. Available: <https://www.researchgate.net/publication/326260635>
- [113] F. H. Niazi, Z. Qamar, M. Noushad, and A. K. Bin Muhareb, "Use of rose bengal, methylene blue and curcumin photosensitizers activated using light emitting diode on post space disinfection bonded to fiber post: An assessment of extrusion bond strength," *Pak J Med Sci*, vol. 38, no. 1, pp. 34–39, Jan. 2022, doi: 10.12669/pjms.38.1.4780.
- [114] V. Balzani, P. Ceroni, A. Credi, and M. Venturi, "Ruthenium tris(bipyridine) complexes: Interchange between photons and electrons in molecular-scale devices and machines," *Coord Chem Rev*, vol. 433, p. 213758, Apr. 2021, doi: 10.1016/j.ccr.2020.213758.
- [115] K. M. Mahmud, M. S. Niloy, M. S. Shakil, and M. A. Islam, "Ruthenium Complexes: An Alternative to Platinum Drugs in Colorectal Cancer Treatment," *Pharmaceutics*, vol. 13, no. 8, p. 1295, Aug. 2021, doi: 10.3390/pharmaceutics13081295.
- [116] A. R. Battersby, "Tetrapyrroles: the pigments of life," *Nat Prod Rep*, vol. 17, no. 6, pp. 507–526, Oct. 2000, doi: 10.1039/b002635m.
- [117] S. Bouramtane, "Vectorisation cellulaire et adressage mitochondrial de photosensibilisateurs par des nanoparticules formées de xylane de bois de feuillus : nouvelle voie de valorisation d'hémicellulose pour une application en PDT," 2019. [Online]. Available: <https://theses.hal.science/tel-02468447>
- [118] M. R. Hamblin and C. P. Sabino, *Photosensitizers*. Cham, Switzerland: Springer International Publishing, 2016. doi: 10.1007/978-3-319-45007-0_3.
- [119] S. Kwiatkowski *et al.*, "Photodynamic therapy – mechanisms, photosensitizers and combinations," *Biomedicine & Pharmacotherapy*, vol. 106, pp. 1098–1107, Oct. 2018, doi: 10.1016/j.biopha.2018.07.049.
- [120] L. B. Josefsen and R. W. Boyle, "Photodynamic therapy and the development of metal-based photosensitisers," 2008. doi: 10.1155/2008/276109.
- [121] H. Abrahamse and M. R. Hamblin, "New photosensitizers for photodynamic therapy," *Biochemical Journal*, vol. 473, no. 4, pp. 347–364, Feb. 2016, doi: 10.1042/BJ20150942.
- [122] D. Kessel, "Photosensitization with Derivatives of Haematoporphyrin," *Int J Radiat Biol Relat Stud Phys Chem Med*, vol. 49, no. 6, pp. 901–907, Jan. 1986, doi: 10.1080/09553008514553131.

- [123] M. O. Senge and J. C. Brandt, "Temoporfin (Foscan®; 5,10,15,20-Tetra(m-hydroxyphenyl)chlorin)—A Second-generation Photosensitizer," *Photochem Photobiol*, vol. 87, no. 6, pp. 1240–1296, Nov. 2011, doi: 10.1111/j.1751-1097.2011.00986.x.
- [124] W. M. Chan, T.-H. Lim, A. Pece, R. Silva, and N. Yoshimura, "Verteporfin PDT for non-standard indications—a review of current literature," *Graefe's Archive for Clinical and Experimental Ophthalmology*, vol. 248, no. 5, pp. 613–626, May 2010, doi: 10.1007/s00417-010-1307-z.
- [125] C. M. Moore *et al.*, "Determination of optimal drug dose and light dose index to achieve minimally invasive focal ablation of localised prostate cancer using WST11-vascular-targeted photodynamic (VTP) therapy," *BJU Int*, vol. 116, no. 6, pp. 888–896, Dec. 2015, doi: 10.1111/bju.12816.
- [126] C. Y. Anderson *et al.*, "A comparative analysis of silicon phthalocyanine photosensitizers for in vivo photodynamic therapy of RIF-1 tumors in C3H mice.," *Photochem Photobiol*, vol. 67, no. 3, pp. 332–6, Jan. 2008, doi: 10.1111/j.1751-1097.1998.tb05206.x.
- [127] L. Bretin, "Thérapie photodynamique (PDT) dans un modèle in vitro et in vivo de cancer colorectal: utilisation d'un photosensibilisateur nanovectorisé," Université de Limoges, 2019. [Online]. Available: <https://theses.hal.science/tel-02443215/>
- [128] C. Fidanzi-Dugas, "Utilisation de nouveaux photosensibilisateurs pour le traitement du cancer de la prostate par photothérapie dynamique," Université de Limoges, 2016. [Online]. Available: <https://theses.hal.science/tel-01435144>
- [129] C. L. N. and M. S. R. F. P. Sellera, *Photodynamic Therapy in Veterinary Medicine: From Basics to Clinical Practice*. Cham, Switzerland: Springer International Publishing, 2016. doi: 10.1007/978-3-319-45007-0.
- [130] J. F. Algorri, M. Ochoa, P. Roldán-Varona, L. Rodríguez-Cobo, and J. Miguel López-Higuera, "Photodynamic Therapy: A Compendium of Latest Reviews," *Cancers (Basel)*, vol. 13, no. 17, p. 4447, 2021, doi: 10.3390/cancers13174447.
- [131] G. Vandongen, G. Visser, and M. Vroenraets, "Photosensitizer-antibody conjugates for detection and therapy of cancer," *Adv Drug Deliv Rev*, vol. 56, no. 1, pp. 31–52, Jan. 2004, doi: 10.1016/j.addr.2003.09.003.
- [132] P. Gierlich, A. I. Mata, C. Donohoe, R. M. M. Brito, M. O. Senge, and L. C. Gomes-da-Silva, "Ligand-Targeted Delivery of Photosensitizers for Cancer Treatment," *Molecules*, vol. 25, no. 22, p. 5317, Nov. 2020, doi: 10.3390/molecules25225317.
- [133] A. Marconi *et al.*, "Dissecting the Interactions between Chlorin e6 and Human Serum Albumin," *Molecules*, vol. 28, no. 5, p. 2348, Mar. 2023, doi: 10.3390/molecules28052348.
- [134] R. Li *et al.*, "Asymmetric, amphiphilic RGD conjugated phthalocyanine for targeted photodynamic therapy of triple negative breast cancer," *Signal Transduct Target Ther*, vol. 7, no. 1, p. 64, Feb. 2022, doi: 10.1038/s41392-022-00906-2.
- [135] S. Ballut *et al.*, "Tumor targeting in photodynamic therapy. From glycoconjugated photosensitizers to glycodendrimeric one. Concept, design and properties," *Org Biomol Chem*, vol. 10, no. 23, p. 4485, Jun. 2012, doi: 10.1039/c2ob25181g.

- [136] N. El-Akra, A. Noiro, J.-C. Faye, and J.-P. Souchard, "Synthesis of estradiol-pheophorbide a conjugates: evidence of nuclear targeting, DNA damage and improved photodynamic activity in human breast cancer and vascular endothelial cells," *Photochemical & Photobiological Sciences*, vol. 5, no. 11, pp. 996–999, Nov. 2006, doi: 10.1039/b606117f.
- [137] A. Stallivieri *et al.*, "Folic acid conjugates with photosensitizers for cancer targeting in photodynamic therapy: Synthesis and photophysical properties," *Bioorg Med Chem*, vol. 25, no. 1, pp. 1–10, Jan. 2017, doi: 10.1016/j.bmc.2016.10.004.
- [138] S. S. Lucky, K. C. Soo, and Y. Zhang, "Nanoparticles in Photodynamic Therapy," *Chem Rev*, vol. 115, no. 4, pp. 1990–2042, Feb. 2015, doi: 10.1021/cr5004198.
- [139] M. Toussaint, M. Barberi-Heyob, S. Pinel, and C. Frochet, "How Nanoparticles Can Solve Resistance and Limitation in PDT Efficiency," 2015, pp. 197–211. doi: 10.1007/978-3-319-12730-9_9.
- [140] M. R. Hamblin and C. P. Sabino, *Photosensitizers*. Cham, Switzerland: Springer International Publishing, 2016. doi: 10.1007/978-3-319-45007-0_3.
- [141] S. Li *et al.*, "Amplified Singlet Oxygen Generation in Semiconductor Polymer Dots for Photodynamic Cancer Therapy," *ACS Appl Mater Interfaces*, vol. 8, no. 6, pp. 3624–3634, Feb. 2016, doi: 10.1021/acsami.5b07995.
- [142] Fiona, "What is Quantum dots? ," Zhengzhou Alfa Chemical. Accessed: Oct. 15, 2024. [Online]. Available: <https://www.alfachemch.com/info/what-is-quantum-dots-44057145.html>
- [143] A. El-Hussein, I. Mfouo-Tynga, M. Abdel-Harith, and H. Abrahamse, "Comparative study between the photodynamic ability of gold and silver nanoparticles in mediating cell death in breast and lung cancer cell lines," *J Photochem Photobiol B*, vol. 153, pp. 67–75, Dec. 2015, doi: 10.1016/j.jphotobiol.2015.08.028.
- [144] F. Vázquez-Hernández *et al.*, "Use of nanostructured materials in drug delivery," in *Nanobiomaterials*, Elsevier, 2018, pp. 503–549. doi: 10.1016/B978-0-08-100716-7.00020-9.
- [145] S. Jin *et al.*, "A new near infrared photosensitizing nanoplatform containing blue-emitting up-conversion nanoparticles and hypocrellin A for photodynamic therapy of cancer cells," *Nanoscale*, vol. 5, no. 23, p. 11910, Jan. 2013, doi: 10.1039/c3nr03515h.
- [146] N. Zhou, J. Ni, and R. He, "Advances of Upconversion Nanoparticles for Molecular Imaging," *Nano Biomed Eng*, vol. 5, no. 3, Oct. 2013, doi: 10.5101/nbe.v5i3.p137-145.
- [147] N. Spyropoulos-Antonakakis *et al.*, "Selective aggregation of PAMAM dendrimer nanocarriers and PAMAM/ZnPc nanodrugs on human atheromatous carotid tissues: a photodynamic therapy for atherosclerosis," *Nanoscale Res Lett*, vol. 10, no. 1, p. 210, Dec. 2015, doi: 10.1186/s11671-015-0904-5.
- [148] "Dendritech," Dendritech, Inc. [Online]. Available: <https://www.dendritech.com/pamam.html>

- [149] J. Tu *et al.*, “Multifunctional ZnPc-loaded mesoporous silica nanoparticles for enhancement of photodynamic therapy efficacy by endolysosomal escape,” *Biomaterials*, vol. 33, no. 31, pp. 7903–7914, Nov. 2012, doi: 10.1016/j.biomaterials.2012.07.025.
- [150] M. O. Senge, “mTHPC – A drug on its way from second to third generation photosensitizer?,” *Photodiagnosis Photodyn Ther*, vol. 9, no. 2, pp. 170–179, Jun. 2012, doi: 10.1016/j.pdpdt.2011.10.001.
- [151] S. Ghosh, K. A. Carter, and J. F. Lovell, “Liposomal formulations of photosensitizers,” *Biomaterials*, vol. 218, p. 119341, Oct. 2019, doi: 10.1016/j.biomaterials.2019.119341.
- [152] A. Escudero, C. Carrillo-Carrión, M. C. Castillejos, E. Romero-Ben, C. Rosales-Barrios, and N. Khiar, “Photodynamic therapy: Photosensitizers and nanostructures,” *Mater Chem Front*, vol. 5, no. 10, pp. 3788–3812, May 2021, doi: 10.1039/d0qm00922a.
- [153] J. Wang *et al.*, “A Porous Au@Rh Bimetallic Core–Shell Nanostructure as an H₂O₂-Driven Oxygenator to Alleviate Tumor Hypoxia for Simultaneous Bimodal Imaging and Enhanced Photodynamic Therapy,” *Advanced Materials*, vol. 32, no. 22, Jun. 2020, doi: 10.1002/adma.202001862.
- [154] M. R. Hamblin and C. P. Sabino, “Systemic Effects,” in *Photodynamic Therapy in Veterinary Medicine: From Basics to Clinical Practice*, Cham: Springer International Publishing, 2016, pp. 73–91. doi: 10.1007/978-3-319-45007-0_6.
- [155] D. A. Bellnier, Y. Ho, R. K. Pandey, J. R. Missert, and T. J. Dougherty, “Distribution and Elimination of Photofrin II in Mice,” *Photochem Photobiol*, vol. 50, no. 2, pp. 221–228, Aug. 1989, doi: 10.1111/j.1751-1097.1989.tb04152.x.
- [156] M. J. Egorin, E. G. Zuhowski, D. L. Sentz, J. M. Dobson, P. S. Callery, and J. L. Eiseman, “Plasma pharmacokinetics and tissue distribution in CD 2 F 1 mice of Pc4 (NSC 676418), a silicone phthalocyanine photodynamic sensitizing agent,” *Cancer Chemother Pharmacol*, vol. 44, no. 4, pp. 283–294, Aug. 1999, doi: 10.1007/s002800050979.
- [157] H. Maeda, “The enhanced permeability and retention (EPR) effect in tumor vasculature: the key role of tumor-selective macromolecular drug targeting,” *Adv Enzyme Regul*, vol. 41, no. 1, pp. 189–207, May 2001, doi: 10.1016/S0065-2571(00)00013-3.
- [158] A. K. Iyer, G. Khaled, J. Fang, and H. Maeda, “Exploiting the enhanced permeability and retention effect for tumor targeting,” *Drug Discov Today*, vol. 11, no. 17–18, pp. 812–818, Sep. 2006, doi: 10.1016/j.drudis.2006.07.005.
- [159] A. G. Niculescu and A. M. Grumezescu, “Photodynamic therapy—an up-to-date review,” *Applied Sciences*, vol. 11, no. 8, Apr. 2021, doi: 10.3390/app11083626.
- [160] J. A. Rodrigues and J. H. Correia, “Photodynamic Therapy for Colorectal Cancer: An Update and a Look to the Future,” *Int J Mol Sci*, vol. 24, no. 15, Aug. 2023, doi: 10.3390/ijms241512204.
- [161] A. I. Gavrina *et al.*, “Photodynamic therapy of mouse tumor model using chlorin e6-polyvinyl alcohol complex,” *J Photochem Photobiol B*, vol. 178, pp. 614–622, Jan. 2018, doi: 10.1016/j.jphotobiol.2017.12.016.

- [162] L. Bretin *et al.*, “Photodynamic Therapy Activity of New Porphyrin-Xylan-Coated Silica Nanoparticles in Human Colorectal Cancer,” *Cancers (Basel)*, vol. 11, no. 10, p. 1474, Sep. 2019, doi: 10.3390/cancers11101474.
- [163] N. W. N. Simelane, C. A. Kruger, and H. Abrahamse, “Targeted nanoparticle photodynamic diagnosis and therapy of colorectal cancer,” *Int J Mol Sci*, vol. 22, no. 18, Sep. 2021, doi: 10.3390/ijms22189779.
- [164] J. Xu *et al.*, “Near-Infrared-Triggered Photodynamic Therapy with Multitasking Upconversion Nanoparticles in Combination with Checkpoint Blockade for Immunotherapy of Colorectal Cancer,” *ACS Nano*, vol. 11, no. 5, pp. 4463–4474, May 2017, doi: 10.1021/acsnano.7b00715.
- [165] C. He *et al.*, “Core-shell nanoscale coordination polymers combine chemotherapy and photodynamic therapy to potentiate checkpoint blockade cancer immunotherapy,” *Nat Commun*, vol. 7, Aug. 2016, doi: 10.1038/ncomms12499.
- [166] S. Pervaiz and M. Olivo, “Art and science of photodynamic therapy,” *Clin Exp Pharmacol Physiol*, vol. 33, no. 5–6, pp. 551–556, May 2006, doi: 10.1111/j.1440-1681.2006.04406.x.
- [167] X. Wang, X. Ouyang, J. Chen, Y. Hu, X. Sun, and Z. Yu, “Nanoparticulate Photosensitizer Decorated With Hyaluronic Acid for photodynamic/photothermal Cancer Targeting Therapy,” *Nanomedicine*, vol. 14, no. 2, pp. 151–167, Jan. 2019, doi: 10.2217/nnm-2018-0204.
- [168] X. Yang *et al.*, “Sub-100 nm, long tumor retention SN-38-loaded photonic micelles for tri-modal cancer therapy,” *Journal of Controlled Release*, vol. 261, pp. 297–306, Sep. 2017, doi: 10.1016/j.jconrel.2017.07.014.
- [169] V. Zuzarte-Luis and J. M. Hurle, “Programmed cell death in the embryonic vertebrate limb,” *Semin Cell Dev Biol*, vol. 16, no. 2, pp. 261–269, Apr. 2005, doi: 10.1016/j.semcd.2004.12.004.
- [170] P. S. Bisen, S. Profile, Z. Khan, and S. Bundela, *Apoptotic Regulations*. New York, USA: Taylor & Francis Group, 2013. [Online]. Available: <https://www.researchgate.net/publication/280005320>
- [171] F. Akhtar and S. R. A. Bokhari, *Apoptosis*. New York, USA: Nova Science Publishers, 2024.
- [172] J. Masse, T. Watrin, A. Laurent, S. Deschamps, D. Guerrier, and I. Pellerin, “The developing female genital tract: from genetics to epigenetics,” *Int J Dev Biol*, vol. 53, no. 2–3, pp. 411–424, May 2009, doi: 10.1387/ijdb.082680jm.
- [173] A. Pérez-Garijo and H. Steller, “Spreading the word: Non-autonomous effects of apoptosis during development, regeneration and disease,” *Development*, vol. 142, no. 19, pp. 3253–3262, Oct. 2015, doi: 10.1242/dev.127878.
- [174] B. A. Carneiro and W. S. El-Deiry, “Targeting apoptosis in cancer therapy,” *Nat Rev Clin Oncol*, vol. 17, no. 7, pp. 395–417, Jul. 2020, doi: 10.1038/s41571-020-0341-y.

- [175] C. P. Dillon and D. R. Green, "Molecular Cell Biology of Apoptosis and Necroptosis in Cancer," 2016, pp. 1–23. doi: 10.1007/978-3-319-39406-0_1.
- [176] A. Ashkenazi and G. Salvesen, "Regulated Cell Death: Signaling and Mechanisms," *Annu Rev Cell Dev Biol*, vol. 30, no. 1, pp. 337–356, Oct. 2014, doi: 10.1146/annurev-cellbio-100913-013226.
- [177] S. H. MacKenzie and A. C. Clark, "Death by Caspase Dimerization," New York, USA: Springer, 2012, pp. 55–73. doi: 10.1007/978-1-4614-3229-6_4.
- [178] D. R. Mcllwain, T. Berger, and T. W. Mak, "Caspase Functions in Cell Death and Disease," *Cold Spring Harb Perspect Biol*, vol. 5, no. 4, pp. a008656–a008656, Apr. 2013, doi: 10.1101/cshperspect.a008656.
- [179] S. Kumar, M. Kinoshita, M. Noda, N. G. Copeland, and N. A. Jenkins, "Induction of apoptosis by the mouse Nedd2 gene, which encodes a protein similar to the product of the *Caenorhabditis elegans* cell death gene *ced-3* and the mammalian IL-1 beta-converting enzyme.," *Genes Dev*, vol. 8, no. 14, pp. 1613–1626, Jul. 1994, doi: 10.1101/gad.8.14.1613.
- [180] A. Bulotta, L. Farilla, H. Hui, and R. Perfetti, "The role of GLP-1 in the regulation of islet cell mass," *Cell Biochem Biophys*, vol. 40, no. S3, pp. 65–77, Oct. 2004, doi: 10.1385/CBB:40:3:65.
- [181] J. Chai and Y. Shi, "Apoptosome and inflammasome: conserved machineries for caspase activation," *Natl Sci Rev*, vol. 1, no. 1, pp. 101–118, Mar. 2014, doi: 10.1093/nsr/nwt025.
- [182] C. Pop and G. S. Salvesen, "Human Caspases: Activation, Specificity, and Regulation," *Journal of Biological Chemistry*, vol. 284, no. 33, pp. 21777–21781, Aug. 2009, doi: 10.1074/jbc.R800084200.
- [183] D. Kaur and R. Deshmukh, "Physiology of cellular demise: Apoptosis, necrosis, and autophagy," in *Clinical Perspectives and Targeted Therapies in Apoptosis*, Amsterdam, Netherlands: Elsevier, 2021, pp. 23–78. doi: 10.1016/B978-0-12-815762-6.00002-0.
- [184] D. R. Green, "Caspases and Their Substrates," *Cold Spring Harb Perspect Biol*, vol. 14, no. 3, Mar. 2022, doi: 10.1101/cshperspect.a041012.
- [185] R. Jan and G. e. S. Chaudhry, "Understanding apoptosis and apoptotic pathways targeted cancer therapeutics," *Adv Pharm Bull*, vol. 9, no. 2, pp. 205–218, Jun. 2019, doi: 10.15171/apb.2019.024.
- [186] S. W. G. Tait and D. R. Green, "Mitochondrial Regulation of Cell Death," *Cold Spring Harb Perspect Biol*, vol. 5, no. 9, pp. a008706–a008706, Sep. 2013, doi: 10.1101/cshperspect.a008706.
- [187] S. Yuan and C. W. Akey, "Apoptosome structure, assembly, and procaspase activation," *Structure*, vol. 21, no. 4, pp. 501–515, Apr. 2013, doi: 10.1016/j.str.2013.02.024.
- [188] O. Raducka-Jaszul, D. M. Bogusławska, N. Jędruchiewicz, and A. F. Sikorski, "Role of extrinsic apoptotic signaling pathway during definitive erythropoiesis in normal patients

and in patients with β -thalassemia,” *Int J Mol Sci*, vol. 21, no. 9, May 2020, doi: 10.3390/ijms21093325.

- [189] S. Roy and D. W. Nicholson, “Commentary Cross-Talk in Cell Death Signaling,” in *J. Exp. Med*, vol. 192, no. 8, Cell Press, 2000, pp. 21–25. [Online]. Available: <http://www.jem.org/cgi/content/full/192/8/F21>
- [190] J. X. Zhou and X. Li, “Apoptosis in Polycystic Kidney Disease: From Pathogenesis to Treatment,” in *Polycystic Kidney Disease*, Singapore: Codon Publications, 2015, pp. 197–230. doi: 10.15586/codon.pkd.2015.ch9.
- [191] C. M. Pfeffer and A. T. K. Singh, “Apoptosis: A target for anticancer therapy,” *Int J Mol Sci*, vol. 19, no. 2, Feb. 2018, doi: 10.3390/ijms19020448.
- [192] E. D. Baron *et al.*, “Silicon phthalocyanine (pc 4) photodynamic therapy is a safe modality for cutaneous neoplasms: Results of a phase 1 clinical trial,” *Lasers Surg Med*, vol. 42, no. 10, pp. 888–895, Oct. 2010, doi: 10.1002/lsm.20984.
- [193] R. Bissonnette, J. F. Tremblay, P. Juzenas, M. Boushira, and H. Lui, “Systemic photodynamic therapy with aminolevulinic acid induces apoptosis in lesional T lymphocytes of psoriatic plaques,” *Journal of Investigative Dermatology*, vol. 119, no. 1, pp. 77–83, 2002, doi: 10.1046/j.1523-1747.2002.01827.x.
- [194] T. Lazarević, A. Rilak, and Ž. D. Bugarčić, “Platinum, palladium, gold and ruthenium complexes as anticancer agents: Current clinical uses, cytotoxicity studies and future perspectives,” *Eur J Med Chem*, vol. 142, pp. 8–31, Dec. 2017, doi: 10.1016/j.ejmech.2017.04.007.
- [195] U. Ndagi, N. Mhlongo, and M. E. Soliman, “Metal complexes in cancer therapy – An update from drug design perspective,” *Drug Des Devel Ther*, vol. 11, pp. 599–616, Mar. 2017, doi: 10.2147/DDDT.S119488.
- [196] M. Rozenzweig, “Cis -diamminedichloroplatinum (II),” *Ann Intern Med*, vol. 86, no. 6, p. 803, Jun. 1977, doi: 10.7326/0003-4819-86-6-803.
- [197] X. Wang, L. Ren, L. Ye, and J. Cao, “Photodynamic therapy augments oxaliplatin-induced immunogenic cell death in colorectal cancer,” *Central European Journal of Immunology*, vol. 48, no. 3, pp. 189–202, 2023, doi: 10.5114/ceji.2023.132053.
- [198] M. Corte-Rodríguez *et al.*, “Quantitative evaluation of cellular uptake, DNA incorporation and adduct formation in cisplatin sensitive and resistant cell lines: Comparison of different Pt-containing drugs,” *Biochem Pharmacol*, vol. 98, no. 1, pp. 69–77, Nov. 2015, doi: 10.1016/j.bcp.2015.08.112.
- [199] D. Tsvetkova and S. Ivanova, “Application of Approved Cisplatin Derivatives in Combination Therapy against Different Cancer Diseases,” *Molecules*, vol. 27, no. 8, Apr. 2022, doi: 10.3390/molecules27082466.
- [200] D. Dospivova *et al.*, “Catalytic electrochemical analysis of platinum in Pt-DNA adducts,” *Int J Electrochem Sci*, vol. 7, no. 4, pp. 3072–3088, Apr. 2012, doi: 10.1016/s1452-3981(23)13936-8.

- [201] C. R. R. Rocha, M. M. Silva, A. Quinet, J. B. Cabral-Neto, and C. F. M. Menck, "DNA repair pathways and cisplatin resistance: An intimate relationship," *Clinics*, vol. 73, Oct. 2018, doi: 10.6061/clinics/2018/e478s.
- [202] Ž. D. Bugarčić, J. Bogojeski, B. Petrović, S. Hochreuther, and R. van Eldik, "Mechanistic studies on the reactions of platinum(ii) complexes with nitrogen- and sulfur-donor biomolecules," *Dalton Transactions*, vol. 41, no. 40, p. 12329, Oct. 2012, doi: 10.1039/c2dt31045g.
- [203] I. Kostova, "Ruthenium Complexes as Anticancer Agents," *Curr Med Chem*, vol. 13, no. 9, pp. 1085–1107, Apr. 2006, doi: 10.2174/092986706776360941.
- [204] S. Medici, M. Peana, V. M. Nurchi, J. I. Lachowicz, G. Crisponi, and M. A. Zoroddu, "Noble metals in medicine: Latest advances," *Coord Chem Rev*, vol. 284, pp. 329–350, Feb. 2015, doi: 10.1016/j.ccr.2014.08.002.
- [205] J. Mosquera, M. I. Sánchez, M. E. Vázquez, and J. L. Mascareñas, "Ruthenium bipyridyl complexes as photocleavable dimerizers: deactivation of DNA-binding peptides using visible light," *Chem. Commun.*, vol. 50, no. 75, pp. 10975–10978, Dec. 2014, doi: 10.1039/C4CC04512B.
- [206] J. Liu, H. Lai, Z. Xiong, B. Chen, and T. Chen, "Functionalization and cancer-targeting design of ruthenium complexes for precise cancer therapy," *Chemical Communications*, vol. 55, no. 67, pp. 9904–9914, Dec. 2019, doi: 10.1039/C9CC04098F.
- [207] W. Su *et al.*, "Synthesis, Characterization, and Anticancer Activity of a Series of Ketone-N 4 -Substituted Thiosemicarbazones and Their Ruthenium(II) Arene Complexes," *Inorg Chem*, vol. 52, no. 21, pp. 12440–12449, Nov. 2013, doi: 10.1021/ic401362s.
- [208] S. Y. Lee, C. Y. Kim, and T. G. Nam, "Ruthenium complexes as anticancer agents: A brief history and perspectives," *Drug Des Devel Ther*, vol. 14, pp. 5375–5392, Dec. 2020, doi: 10.2147/DDDT.S275007.
- [209] S. Silvestri *et al.*, "Evaluation of anticancer role of a novel ruthenium(II)-based compound compared with NAMI-A and cisplatin in impairing mitochondrial functionality and promoting oxidative stress in triple negative breast cancer models," *Mitochondrion*, vol. 56, pp. 25–34, Jan. 2021, doi: 10.1016/j.mito.2020.11.004.
- [210] M. Bouma *et al.*, "Stability and compatibility of the investigational antimetastatic ruthenium complex NAMI-A in infusion systems and its hemolytic potential," *Journal of Oncology Pharmacy Practice*, vol. 10, no. 1, pp. 7–15, 2004, doi: 10.1191/1078155204jp118oa.
- [211] K. Lin, Z. Z. Zhao, H. Ben Bo, X. J. Hao, and J. Q. Wang, "Applications of ruthenium complex in tumor diagnosis and therapy," *Front Pharmacol*, vol. 9, Nov. 2018, doi: 10.3389/fphar.2018.01323.
- [212] M. S. Galanski, V. B. Arion, M. A. Jakupec, and B. K. Keppler, "Recent Developments in the Field of Tumor-Inhibiting Metal Complexes," *Curr Pharm Des*, vol. 9, no. 25, pp. 2078–2089, Oct. 2003, doi: 10.2174/1381612033454180.

- [213] P. K. Shah, N. R. Jena, and P. K. Shukla, "Reactions of Ru(III)-drugs KP1019 and KP418 with guanine, 2'-deoxyguanosine and guanosine: a DFT study," *J Mol Model*, vol. 28, no. 10, p. 291, Oct. 2022, doi: 10.1007/s00894-022-05304-7.
- [214] S. Kapitza *et al.*, "Heterocyclic complexes of ruthenium(III) induce apoptosis in colorectal carcinoma cells," *J Cancer Res Clin Oncol*, vol. 131, no. 2, pp. 101–110, Feb. 2005, doi: 10.1007/s00432-004-0617-0.
- [215] P. Heffeter *et al.*, "Intrinsic and Acquired Forms of Resistance against the Anticancer Ruthenium Compound KP1019 [Indazolium *trans* -[tetrachlorobis(1 *H* -indazole)ruthenate (III)] (FFC14A)," *Journal of Pharmacology and Experimental Therapeutics*, vol. 312, no. 1, pp. 281–289, Jan. 2005, doi: 10.1124/jpet.104.073395.
- [216] C. G. Hartinger *et al.*, "KP1019, A New Redox-Active Anticancer Agent – Preclinical Development and Results of a Clinical Phase I Study in Tumor Patients," *Chem Biodivers*, vol. 5, no. 10, pp. 2140–2155, Oct. 2008, doi: 10.1002/cbdv.200890195.
- [217] R. Trondl, P. Heffeter, C. R. Kowol, M. A. Jakupec, W. Berger, and B. K. Keppler, "NKP-1339, the first ruthenium-based anticancer drug on the edge to clinical application," *Chem Sci*, vol. 5, no. 8, pp. 2925–2932, Jan. 2014, doi: 10.1039/c3sc53243g.
- [218] H. Geisler *et al.*, "Tridentate 3-Substituted Naphthoquinone Ruthenium Arene Complexes: Synthesis, Characterization, Aqueous Behavior, and Theoretical and Biological Studies," *Inorg Chem*, vol. 60, no. 13, pp. 9805–9819, Jul. 2021, doi: 10.1021/acs.inorgchem.1c01083.
- [219] D. A. Smithen *et al.*, "Synthesis and Photobiological Activity of Ru(II) Dyads Derived from Pyrrole-2-carboxylate Thionoesters," *Inorg Chem*, vol. 56, no. 7, pp. 4121–4132, Apr. 2017, doi: 10.1021/acs.inorgchem.7b00072.
- [220] M. Pernet, R. Vanderesse, C. Frochot, F. Guillemin, and M. Barberi-Heyob, "Stability of peptides and therapeutic success in cancer," *Expert Opin Drug Metab Toxicol*, vol. 7, no. 7, pp. 793–802, Jul. 2011, doi: 10.1517/17425255.2011.574126.
- [221] R. Schneider *et al.*, "Design, synthesis, and biological evaluation of folic acid targeted tetraphenylporphyrin as novel photosensitizers for selective photodynamic therapy," *Bioorg Med Chem*, vol. 13, no. 8, pp. 2799–2808, Apr. 2005, doi: 10.1016/j.bmc.2005.02.025.
- [222] B. Di Stasio *et al.*, "The 2-aminoglucosamide motif improves cellular uptake and photodynamic activity of tetraphenylporphyrin," *Eur J Med Chem*, vol. 40, no. 11, pp. 1111–1122, Nov. 2005, doi: 10.1016/j.ejmech.2005.04.007.
- [223] F. Schmitt, P. Govindaswamy, O. Zava, G. Süss-Fink, L. Juillerat-Jeanneret, and B. Therrien, "Combined arene ruthenium porphyrins as chemotherapeutics and photosensitizers for cancer therapy," *JBIC Journal of Biological Inorganic Chemistry*, vol. 14, no. 1, pp. 101–109, Jan. 2009, doi: 10.1007/s00775-008-0427-y.
- [224] T. Gianferrara *et al.*, "Ruthenium–Porphyrin Conjugates with Cytotoxic and Phototoxic Antitumor Activity," *J Med Chem*, vol. 53, no. 12, pp. 4678–4690, Jun. 2010, doi: 10.1021/jm1002588.

- [225] S. Swavey and K. J. Brewer, "Visible Light Induced Photocleavage of DNA by a Mixed-Metal Supramolecular Complex: $\{[(bpy)_2 Ru(dpp)]_2 RhCl_2\}^+_{5+}$," *Inorg Chem*, vol. 41, no. 24, pp. 6196–6198, Dec. 2002, doi: 10.1021/ic0257726.
- [226] M. Juszczak, M. Kluska, D. Wysokiński, and K. Woźniak, "Anti-cancer properties of ruthenium compounds: NAMI-A and KP1019," *Postepy Hig Med Dosw*, vol. 74, pp. 12–19, Feb. 2020, doi: 10.5604/01.3001.0013.8549.
- [227] E. Alessio and L. Messori, "NAMI-A and KP1019/1339, Two Iconic Ruthenium Anticancer Drug Candidates Face-to-Face: A Case Story in Medicinal Inorganic Chemistry," *Molecules*, vol. 24, no. 10, p. 1995, May 2019, doi: 10.3390/molecules24101995.
- [228] G. Jaouen, Ed., *Bioorganometallics*. Weinheim, Germany: Wiley, 2005. doi: 10.1002/3527607692.
- [229] G. Süss-Fink, "Arene ruthenium complexes as anticancer agents," *Dalton Trans.*, vol. 39, no. 7, pp. 1673–1688, May 2010, doi: 10.1039/B916860P.
- [230] C. G. Hartinger and P. J. Dyson, "Bioorganometallic chemistry—from teaching paradigms to medicinal applications," *Chem. Soc. Rev.*, vol. 38, no. 2, pp. 391–401, Feb. 2009, doi: 10.1039/B707077M.
- [231] C. Scolaro *et al.*, "In Vitro and in Vivo Evaluation of Ruthenium(II)–Arene PTA Complexes," *J Med Chem*, vol. 48, no. 12, pp. 4161–4171, Jun. 2005, doi: 10.1021/jm050015d.
- [232] F. Wang, H. Chen, J. A. Parkinson, P. del S. Murdoch, and P. J. Sadler, "Reactions of a ruthenium(II) arene antitumor complex with cysteine and methionine," *Inorg Chem*, vol. 41, no. 17, pp. 4509–4523, Aug. 2002, doi: 10.1021/ic025538f.
- [233] B. S. Murray, M. V. Babak, C. G. Hartinger, and P. J. Dyson, "The development of RAPTA compounds for the treatment of tumors," *Coord Chem Rev*, vol. 306, no. P1, pp. 86–114, Jan. 2016, doi: 10.1016/j.ccr.2015.06.014.
- [234] C. A. Vock, A. K. Renfrew, R. Scopelliti, L. Juillerat-Jeanneret, and P. J. Dyson, "Influence of the Diketonato Ligand on the Cytotoxicities of $[Ru(\eta^6-p\text{-cymene})(R_2\text{acac})(PTA)]^+$ Complexes (PTA = 1,3,5-triaza-7-phosphaadamantane)," *Eur J Inorg Chem*, vol. 2008, no. 10, pp. 1661–1671, Apr. 2008, doi: 10.1002/ejic.200701291.
- [235] A. Alguacil, F. Scalambra, and A. Romerosa, "Insights into the $\kappa\text{-P,N}$ Coordination of 1,3,5-Triaza-7-phosphaadamantane and Derivatives: $\kappa\text{-P,N}$ -Heterometallic Complexes and a ^{15}N Nuclear Magnetic Resonance Survey," *Inorg Chem*, vol. 61, no. 15, pp. 5779–5791, Apr. 2022, doi: 10.1021/acs.inorgchem.1c03831.
- [236] B. Therrien, "Unmasking Arene Ruthenium Building Blocks," *Chemical Record*, vol. 21, no. 3, pp. 460–468, Mar. 2021, doi: 10.1002/tcr.202000128.
- [237] V. Vajpayee *et al.*, "Growth Inhibitory Activity of a Bis-Benzimidazole-Bridged Arene Ruthenium Metalla-Rectangle and -Prism," *Organometallics*, vol. 32, no. 6, pp. 1563–1566, Mar. 2013, doi: 10.1021/om301174s.

- [238] B. Therrien and J. Furrer, "The Biological Side of Water-Soluble Arene Ruthenium Assemblies," *Advances in Chemistry*, vol. 2014, pp. 1–20, Jul. 2014, doi: 10.1155/2014/589686.
- [239] M. Gaschard, F. Nehzat, T. Cheminel, and B. Therrien, "Arene Ruthenium Metalla-Assemblies with Anthracene Moieties for PDT Applications," *Inorganics (Basel)*, vol. 6, no. 3, p. 97, Sep. 2018, doi: 10.3390/inorganics6030097.
- [240] J.-J. Zhang, S. A. Gamboa, B. J. Davis, and A. Lachgar, "Self-Assembly of Cluster-Based Nanoscopic Supramolecules into One-Dimensional Coordination Polymers," *Advances in Materials Science and Engineering*, vol. 2009, no. 1, Jan. 2009, doi: 10.1155/2009/579123.
- [241] C. J. Pedersen, "The Discovery of Crown Ethers (Noble Lecture)," *Angewandte Chemie International Edition in English*, vol. 27, no. 8, pp. 1021–1027, Aug. 1988, doi: 10.1002/ANIE.198810211.
- [242] B. Therrien and J. Furrer, "The Biological Side of Water-Soluble Arene Ruthenium Assemblies," *Advances in Chemistry*, vol. 2014, pp. 1–20, Jul. 2014, doi: 10.1155/2014/589686.
- [243] M. Gallardo-Villagrán *et al.*, "Ruthenium-based assemblies incorporating tetrapyrrolylporphyrin panels: a photosensitizer delivery strategy for the treatment of rheumatoid arthritis by photodynamic therapy," *Dalton Transactions*, vol. 51, no. 25, pp. 9673–9680, Aug. 2022, doi: 10.1039/D2DT00917J.
- [244] M. Gallardo-Villagrán *et al.*, "Evaluation of Ruthenium-Based Assemblies as Carriers of Photosensitizers to Treat Rheumatoid Arthritis by Photodynamic Therapy.," *Pharmaceutics*, vol. 13, no. 12, Dec. 2021, doi: 10.3390/pharmaceutics13122104.
- [245] T. Galliard, D. R. Phillips, and J. A. Matthew, "Enzymic reactions of fatty acid hydroperoxides in extracts of potato tuber II. Conversion of 9- and 13-hydroperoxy-octadecadienoic acids to monohydroxydienoic acid, epoxyhydroxy- and trihydroxymonoenoic acid derivatives," *Biochimica et Biophysica Acta (BBA) - Lipids and Lipid Metabolism*, vol. 409, no. 2, pp. 157–171, Nov. 1975, doi: 10.1016/0005-2760(75)90151-4.
- [246] J. Usuda *et al.*, "Photodynamic Therapy (PDT) for Lung Cancers," *Journal of Thoracic Oncology*, vol. 1, no. 5, pp. 489–493, Jun. 2006, doi: 10.1016/S1556-0864(15)31616-6.
- [247] W. Zhu *et al.*, "Comparison between porphyrin, chlorin and bacteriochlorin derivatives for photodynamic therapy: Synthesis, photophysical properties, and biological activity," *Eur J Med Chem*, vol. 160, pp. 146–156, Dec. 2018, doi: 10.1016/j.ejmech.2018.10.005.
- [248] J. Kou, D. Dou, and L. Yang, "Porphyrin photosensitizers in photodynamic therapy and its applications," *Oncotarget*, vol. 8, no. 46, pp. 81591–81603, Aug. 2017, [Online]. Available: www.impactjournals.com/oncotarget/
- [249] A. Akbar, S. Khan, T. Chatterjee, and M. Ghosh, "Unleashing the power of porphyrin photosensitizers: Illuminating breakthroughs in photodynamic therapy," Nov. 2023, *Elsevier B.V.* doi: 10.1016/j.jphotobiol.2023.112796.

- [250] R. Bonnett, B. D. Djelal, and A. Nguyen, "Physical and chemical studies related to the development of m-THPC (FOSCAN ®) for the photodynamic therapy (PDT) of tumours," *J Porphyr Phthalocyanines*, vol. 05, no. 08, pp. 652–661, Aug. 2001, doi: 10.1002/jpp.377.
- [251] M. Gallardo-Villagrán, D. Y. Leger, B. Liagre, and B. Therrien, "Photosensitizers Used in the Photodynamic Therapy of Rheumatoid Arthritis," *Int J Mol Sci*, vol. 20, no. 13, p. 3339, Jul. 2019, doi: 10.3390/ijms20133339.
- [252] N. P. E. Barry, F. Edafe, and B. Therrien, "Anticancer activity of tetracationic arene ruthenium metalla-cycles," *Dalton Transactions*, vol. 40, no. 27, pp. 7172–7180, Jul. 2011, doi: 10.1039/c1dt10489f.
- [253] A. J. Amoroso, A. M. W. C. Thompson, J. P. Maher, J. A. McCleverty, and M. D. Ward, "and Tetranucleating Pyridyl Ligands Which Facilitate Multicenter Magnetic Exchange between Paramagnetic Molybdenum Centers," *Inorg. Chem*, vol. 34, no. 18, pp. 4828–4835, Aug. 1995, [Online]. Available: <https://pubs.acs.org/sharingguidelines>
- [254] D. K. Dogutan, M. Ptaszek, and J. S. Lindsey, "Direct synthesis of magnesium porphine via 1-formyldipyrromethane," *Journal of Organic Chemistry*, vol. 72, no. 13, pp. 5008–5011, Jun. 2007, doi: 10.1021/jo070532z.
- [255] N. P. E. Barry, O. Zava, P. J. Dyson, and B. Therrien, "Excellent correlation between drug release and portal size in metalla-cage drug-delivery systems," *Chemistry - A European Journal*, vol. 17, no. 35, pp. 9669–9677, Aug. 2011, doi: 10.1002/chem.201003530.
- [256] F. Schmitt, J. Freudenreich, N. P. E. Barry, L. Juillerat-Jeanneret, G. Süss-Fink, and B. Therrien, "Organometallic cages as vehicles for intracellular release of photosensitizers," *J Am Chem Soc*, vol. 134, no. 2, pp. 754–757, Jan. 2012, doi: 10.1021/JA207784T.
- [257] L. Paulus *et al.*, "The Effect of Photosensitizer Metalation Incorporated into Arene–Ruthenium Assemblies on Prostate Cancer," *Int J Mol Sci*, vol. 24, no. 17, Sep. 2023, doi: 10.3390/ijms241713614.
- [258] R. Baskaran, J. Lee, and S. G. Yang, "Clinical development of photodynamic agents and therapeutic applications," *Biomater Res*, vol. 22, no. 25, pp. 1–13, May 2018, doi: 10.1186/s40824-018-0140-z.
- [259] R. W. Y. Sun, M. Zhang, D. Li, M. Li, and A. S. T. Wong, "Enhanced anti-cancer activities of a gold(III) pyrrolidinedithiocarbamate complex incorporated in a biodegradable metal-organic framework," *J Inorg Biochem*, vol. 163, pp. 1–7, Oct. 2016, doi: 10.1016/j.jinorgbio.2016.06.020.
- [260] J. Liu, C. Zhang, T. W. Rees, L. Ke, L. Ji, and H. Chao, "Harnessing ruthenium(II) as photodynamic agents: Encouraging advances in cancer therapy," May 2018, *Elsevier B.V.* doi: 10.1016/j.ccr.2018.03.002.
- [261] J. Massoud *et al.*, "A Combination of Ruthenium Complexes and Photosensitizers to Treat Colorectal Cancer," *Inorganics (Basel)*, vol. 11, no. 12, Dec. 2023, doi: 10.3390/inorganics11120451.

- [262] Z. Janbeih, M. Gallardo-Villagrán, B. Therrien, M. Diab-Assaf, B. Liagre, and L. Benov, "Cellular Uptake and Phototoxicity Optimization of Arene Ruthenium Porphyrin Derivatives," *Inorganics (Basel)*, vol. 12, no. 3, Mar. 2024, doi: 10.3390/inorganics12030086.
- [263] V. Bogoeva *et al.*, "Ruthenium porphyrin-induced photodamage in bladder cancer cells," *Photodiagnosis Photodyn Ther*, vol. 14, no. 1, pp. 9–17, Jan. 2016, doi: 10.1016/j.pdpdt.2016.01.012.
- [264] Y. Lu, T. Shen, H. Yang, and W. Gu, "Ruthenium complexes induce HepG2 human hepatocellular carcinoma cell apoptosis and inhibit cell migration and invasion through regulation of the Nrf2 pathway," *Int J Mol Sci*, vol. 17, no. 5, May 2016, doi: 10.3390/ijms17050775.
- [265] M. Gallardo-Villagrán, L. Paulus, Y. Champavier, D. Y. Leger, B. Therrien, and B. Liagre, "Combination of tetrapyridylporphyrins and arene ruthenium(II) complexes to treat synovial sarcoma by photodynamic therapy," *J Porphyr Phthalocyanines*, vol. 26, no. 08n09, pp. 533–541, Aug. 2022, doi: 10.1142/S1088424622500018.
- [266] F. Schmitt *et al.*, "Ruthenium Porphyrin Compounds for Photodynamic Therapy of Cancer," *J Med Chem*, vol. 51, no. 6, pp. 1811–1816, Mar. 2008, doi: 10.1021/jm701382p.
- [267] M. Gallardo-Villagrán, D. Y. Leger, B. Liagre, and B. Therrien, "Photosensitizers Used in the Photodynamic Therapy of Rheumatoid Arthritis," *Int J Mol Sci*, vol. 20, no. 13, p. 3339, Jul. 2019, doi: 10.3390/ijms20133339.
- [268] Manuel Ángel Gallardo-Villagrán, "New anti-inflammatory and pro-apoptotic photosensitizers against arthritis and synovial sarcoma," University of Limoges, 2022.
- [269] L. Shi *et al.*, "Encapsulation of Hydrophobic Porphyrins into Biocompatible Nanoparticles: An Easy Way to Benefit of Their Two-Photon Phototherapeutic Effect without Hydrophilic Functionalization," *Cancers (Basel)*, vol. 14, no. 10, p. 2358, May 2022, doi: 10.3390/cancers14102358.
- [270] Y. Zhou, X. Liang, and Z. Dai, "Porphyrin-loaded nanoparticles for cancer theranostics," *Nanoscale*, vol. 8, no. 25, pp. 12394–12405, Jun. 2016, doi: 10.1039/C5NR07849K.
- [271] W. Guo *et al.*, "Transferrin serves as a mediator to deliver organometallic ruthenium(II) anticancer complexes into cells.," *Inorg Chem*, vol. 52, no. 9, pp. 5328–38, May 2013, doi: 10.1021/ic4002626.
- [272] X. Li *et al.*, "Synergistic antitumor activity of withaferin A combined with oxaliplatin triggers reactive oxygen species-mediated inactivation of the PI3K/AKT pathway in human pancreatic cancer cells," *Cancer Lett*, vol. 357, no. 1, pp. 219–230, Feb. 2015, doi: 10.1016/j.canlet.2014.11.026.
- [273] S. Elmore, "Apoptosis: A Review of Programmed Cell Death," *Toxicol Pathol*, vol. 35, no. 4, pp. 495–516, Jun. 2007, doi: 10.1080/01926230701320337.
- [274] B. Peña, S. Saha, R. Barhoumi, R. C. Burghardt, and K. R. Dunbar, "Ruthenium(II)-Polypyridyl Compounds with π -Extended Nitrogen Donor Ligands Induce Apoptosis in Human Lung Adenocarcinoma (A549) Cells by Triggering Caspase-3/7 Pathway," *Inorg*

- [275] W. Li *et al.*, “Ruthenium(II) complexes: DNA-binding, cytotoxicity, apoptosis, cellular localization, cell cycle arrest, reactive oxygen species, mitochondrial membrane potential and western blot analysis,” *J Photochem Photobiol B*, vol. 140, pp. 94–104, 2014, doi: 10.1016/j.jphotobiol.2014.07.011.
- [276] G.-B. Jiang, Y.-Y. Xie, G.-J. Lin, H.-L. Huang, Z.-H. Liang, and Y.-J. Liu, “Synthesis, characterization, DNA interaction, antioxidant and anticancer activity studies of ruthenium(II) polypyridyl complexes,” *J Photochem Photobiol B*, vol. 129, pp. 48–56, Dec. 2013, doi: 10.1016/j.jphotobiol.2013.09.009.
- [277] P. Zhao *et al.*, “DNA binding and photocleavage properties of a novel cationic porphyrin-anthraquinone hybrid,” *Biophys Chem*, vol. 134, no. 1–2, pp. 72–83, Apr. 2008, doi: 10.1016/j.bpc.2008.01.009.
- [278] K. J. Barnum and M. J. O’Connell, “Cell Cycle Regulation by Checkpoints,” New York, USA: Springer, 2014, pp. 29–40. doi: 10.1007/978-1-4939-0888-2_2.
- [279] S. Rani-Beeram, K. Meyer, A. McCrate, Y. Hong, M. Nielsen, and S. Swavey, “A fluorinated ruthenium porphyrin as a potential photodynamic therapy agent: Synthesis, characterization, DNA binding, and melanoma cell studies,” *Inorg Chem*, vol. 47, no. 23, pp. 11278–11283, Dec. 2008, doi: 10.1021/ic8015589.
- [280] A. K. Mishra and L. Mishra, Eds., *Ruthenium Chemistry*. Singapore: Jenny Stanford Publishing, 2018. doi: 10.1201/9781315110585.
- [281] W. Li *et al.*, “In vitro evaluation of ruthenium complexes for photodynamic therapy,” *Photodiagnosis Photodyn Ther*, vol. 18, pp. 83–94, Jun. 2017, doi: 10.1016/j.pdpdt.2017.02.001.
- [282] N.-L. Pan *et al.*, “Lysosome-targeted ruthenium(II) complexes induce both apoptosis and autophagy in HeLa cells,” *J Inorg Biochem*, vol. 229, p. 111729, Apr. 2022, doi: 10.1016/j.jinorgbio.2022.111729.
- [283] L. M. Bomfim *et al.*, “Ruthenium(II) complexes with 6-methyl-2-thiouracil selectively reduce cell proliferation, cause DNA double-strand break and trigger caspase-mediated apoptosis through JNK/p38 pathways in human acute promyelocytic leukemia cells,” *Sci Rep*, vol. 9, no. 1, p. 11483, Aug. 2019, doi: 10.1038/s41598-019-47914-x.



Article

Photodynamic Therapy against Colorectal Cancer Using Porphin-Loaded Arene Ruthenium Cages

Suzan Ghaddar^{1,2}, Aline Pinon¹, Manuel Gallardo-Villagran^{1,3}, Jacquie Massoud¹, Catherine Ouk⁴, Claire Carrion⁴, Mona Diab-Assaf², Bruno Therrien^{3,*} and Bertrand Liagre^{1,*}

¹ Faculté de Pharmacie, Univ. Limoges, LABCIS, UR 22722, F-87000 Limoges, France; suzan.ghaddar@etu.unilim.fr (S.G.); aline.pinon@unilim.fr (A.P.); villagran@outlook.com (M.G.-V.); jacquie.massoud@hotmail.com (J.M.)

² Doctoral School of Sciences and Technology, Lebanese University, Beirut 21219, Lebanon; mdiabassaf@u.edu.lb

³ Institut de Chimie, Université de Neuchâtel, Avenue de Bellevaux 51, CH-2000 Neuchâtel, Switzerland

⁴ Univ. Limoges, CNRS, Inserm, CHU Limoges, BISCEm, UAR 2015, US 42, F-87000 Limoges, France; catherine.ouk@unilim.fr (C.O.); claire.carrion@unilim.fr (C.C.)

* Correspondence: bruno.therrien@unine.ch (B.T.); bertrand.liagre@unilim.fr (B.L.)

Abstract: Colorectal cancer (CRC) is the third most common cancer in the world, with an ongoing rising incidence. Despite secure advancements in CRC treatments, challenges such as side effects and therapy resistance remain to be addressed. Photodynamic therapy (PDT) emerges as a promising modality, clinically used in treating different diseases, including cancer. Among the main challenges with current photosensitizers (PS), hydrophobicity and low selective uptake by the tumor remain prominent. Thus, developing an optimal design for PS to improve their solubility and enhance their selective accumulation in cancer cells is crucial for enhancing the efficacy of PDT. Targeted photoactivation triggers the production of reactive oxygen species (ROS), which promote oxidative stress within cancer cells and ultimately lead to their death. Ruthenium (Ru)-based compounds, known for their selective toxicity towards cancer cells, hold potential as anticancer agents. In this study, we investigated the effect of two distinct arene-Ru assemblies, which lodge porphin PS in their inner cavity, and tested them as PDT agents on the HCT116 and HT-29 human CRC cell lines. The cellular internalization of the porphin-loaded assemblies was confirmed by fluorescence microscopy. Additionally, significant photocytotoxicity was observed in both cell lines after photoactivation of the porphin in the cage systems, inducing apoptosis through caspase activation and cell cycle progression disruptions. These findings suggest that arene-Ru assemblies lodging porphin PS are potent candidates for PDT of CRC.

Keywords: colorectal cancer; photodynamic therapy; photosensitizers; arene-ruthenium assemblies; apoptosis



Citation: Ghaddar, S.; Pinon, A.; Gallardo-Villagran, M.; Massoud, J.; Ouk, C.; Carrion, C.; Diab-Assaf, M.; Therrien, B.; Liagre, B. Photodynamic Therapy against Colorectal Cancer Using Porphin-Loaded Arene Ruthenium Cages. *Int. J. Mol. Sci.* **2024**, *25*, 10847. <https://doi.org/10.3390/ijms251910847>

Academic Editor: Christos K. Kontos

Received: 18 September 2024

Revised: 30 September 2024

Accepted: 6 October 2024

Published: 9 October 2024



Copyright © 2024 by the authors. Licensee MDPI, Basel, Switzerland. This article is an open access article distributed under the terms and conditions of the Creative Commons Attribution (CC BY) license (<https://creativecommons.org/licenses/by/4.0/>).

1. Introduction

Colorectal cancer (CRC) is the third most common cancer and the second leading cause of cancer-related deaths worldwide. Annually, it accounts for about 1.85 million diagnoses and 850,000 deaths [1]. The primary treatments include standard systemic chemotherapy, immunotherapy, and alternative therapies that target the mechanisms responsible for promoting cancer spread and progression [2]. In recent decades, substantial advancements in treating CRC have been made through the introduction of innovative medications and treatment strategies. However, an augmentation in the resistance of tumor cells combatting these therapies is a widespread phenomenon, and most of these therapies do not show selective targeting of cancer cells, which harms healthy tissues and generates a variety of adverse effects [3–6]. Therefore, the development of innovative drugs with high efficiency and selectivity has become a must.

Photodynamic therapy (PDT) has undergone significant historical development, beginning with observing photodynamic effects in the early 20th century. The pivotal discovery of hematoporphyrin derivatives in the 1960s laid the groundwork for PDT's therapeutic applications. Subsequent clinical trials culminated in the approval of PDT by the U.S. Food and Drug Administration (FDA) in 1993 for treating cancers, making it a viable cancer treatment modality [7–9]. The mechanism of PDT revolves around the interaction of photosensitizers (PS), light, and molecular oxygen to induce cytotoxic effects in target tissues. Upon light absorption at specific wavelengths [10], PS undergoes excitation and transfers energy to molecular oxygen, generating reactive oxygen species (ROS). These ROS, particularly singlet oxygen, initiate a cascade of biochemical reactions leading to cellular damage and eventually cell death. The key principle of PDT lies in its ability to selectively target tumor cells while sparing adjacent healthy tissues [11].

CRC, as a prevalent malignancy, presents an area of interest for investigating the efficacy of PDT through the evaluation of novel PS on human CRC cell lines [12]. In this context, the PDT action mechanism should be well understood. This process starts when the PS is activated through the absorption of photons from light allowing its transformation from a singlet ground state to a short-lived electronically excited singlet state. At this stage, the PS is very unstable and can decay back to its ground state by losing excess energy through light emission and/or heat production. On the other hand, this excited singlet state can also undergo intersystem crossing to develop into a more stable long-lived electronically excited triplet state, which can directly transfer energy into molecular oxygen (O_2) through type I and/or type II photochemical reactions. In the type I process, the excited PS reacts with biological substrates such as cell membranes to give free radicals and radical ions through hydrogen atom abstraction or electron transfer. These species can undergo a reaction with O_2 and stimulate the production of superoxide anion, hydroxyl radical, or hydrogen peroxide. The kinetics of both reactions are highly dependent on the availability of oxygen, the nature of the PS, and the substrate concentration, as well as occurring simultaneously, leading to the reversion of the excited state into its ground state. Indeed, ROS are highly cytotoxic and can oxidize diverse biomolecules through the induction of redox reactions, causing oxidative stress and subsequent cell death [13–15].

Among PS used in PDT, tetrapyrrole derivatives including porphyrins, chlorins, bacteriochlorins, and phthalocyanines are known to have low solubility in water and biological media, forcing their aggregation and generating improper photophysical properties, thus limiting their selectivity, and overall, their attractiveness in healthcare modalities [16]. Therefore, to enhance the PS absorption rate and bioavailability, drug delivery systems are often used [17]. This includes vectorization through nanoparticles that can selectively transport the PS into the tumor sites by passive diffusion due to the enhanced permeability and retention (EPR) effect. The EPR effect is an outcome of increased vessel permeability, poor lymphatic drainage, and leaky vasculature. Vectorization can also augment the hydrophilicity of PS, allowing their proper characterization in water and increasing their availability in blood [18–20]. Lodging of PS within carriers was elaborated through the development of the third-generation PS to overcome the limitations associated with the first- and second-generation PS [21]. Such a strategy has been previously used by us, showing that arene-Ru metalla-assemblies can act as drug delivery vectors [22–24].

In parallel, metal-based chemotherapeutic agents including cisplatin, carboplatin, and oxaliplatin are frequently used to treat cancer. In this context, Ru-based complexes are also used and showed better overall efficiency as compared to the other metal-based agents, because they can facilitate more selective targeting to tumor sites. Essentially, Ru ions can bind to transferrin proteins, which accordingly bind to transferrin receptors that are highly expressed on cancer cells [25–27]. This highlights the advantage of Ru derivatives in chemotherapy since the ruthenium toxicity, antiangiogenic, antimetastatic, and overall effects on cellular processes are well documented [28,29]. Therefore, using coordination-driven self-assembled arene-Ru cages to carry the PS to cancer cells is quite efficient, as demonstrated in previous studies [22–24].

Herein, the biological effect of two prismatic arene-Ru water-soluble organometallic cages (**M1** and **M2**) encapsulating 21*H*, 23*H*-porphyrin (**PS**) within their cavity was evaluated (Figure 1). This encapsulation yielded **PS**⊂**M1** and **PS**⊂**M2** host–guest systems (Figure 2), which can be internalized into cancer cells after the Ru-transferrin-mediated binding to transferrin receptors. Once internalized, the **PS** gets excited at specific wavelengths of light illumination to induce cellular oxidative stress, cycle arrest, and apoptosis.

The lodging of porphyrin inside their cavities was designed to enhance the solubility of porphyrin in biological media, with porphyrin being the simplest porphyrin-based **PS**. However, porphyrin alone is not soluble in water, like most porphyrinic compounds [30], and therefore, the use of organometallic cages was essential for this study. The organometallic cages, $[(p\text{-cymene})_6\text{Ru}_6(\text{donq})_3(\text{tpt})_2][\text{CF}_3\text{SO}_3]^{6+}$ (**M1**) and $[(p\text{-cymene})_6\text{Ru}_6(\text{dotq})_3(\text{tpt})_2][\text{CF}_3\text{SO}_3]^{6+}$ (**M2**), were built from three main components, including the arene-Ru vertices, the panels (tpt = 2,4,6-tris(pyridin-4-yl)-1,3,5-triazine), and the spacers (donq = 5,8-dioxido-1,4-naphthoquinonato; dotq = 6,11-dioxido-5,12-naphthacenedionato) that act as edges. The anti-inflammatory activity of these assemblies after PDT was previously evaluated for the first time in vitro on a primary, non-cancerous rheumatoid arthritis fibroblast-like synoviocytes (RA-FLS) cell line, which mainly focused on the influence of PDT on key mediators of the inflammatory process, without delving into the PDT-induced cell death mechanism [31]. In contrast, our study shifts the focus entirely to the anticancer potential of these assemblies by evaluating their ability to induce photocytotoxicity and cell death, specifically in a CRC model, which represents a distinctly different disease type. To establish their therapeutic efficacy, we assessed the effect of these assemblies on two human CRC cell lines of different stages, HCT116 and HT-29, and thoroughly investigated their ability to generate ROS, induce apoptotic cell death, and alter the cell cycle progression through various biological assays. HCT116 cells are known to be less resistant than HT-29 cells due to their less differentiated state, which allows this study to encompass the investigations on more than one stage of CRC development [32].

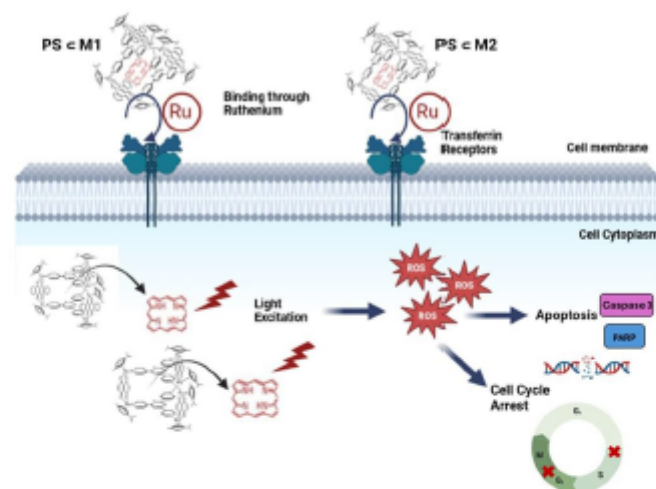


Figure 1. Schematic description of the cellular mechanisms induced by **PS**⊂**M1** and **PS**⊂**M2**, evaluated in this study. (Created with BioRender.com (accessed on 29 June 2024)).

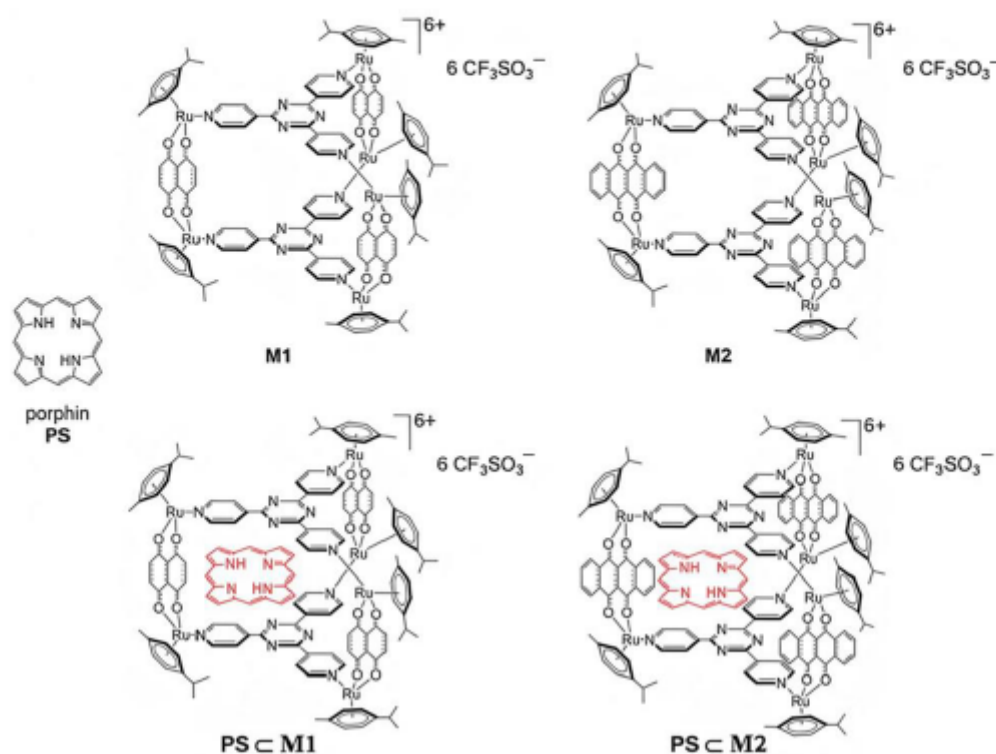


Figure 2. Chemical structure of porphyrin (PS) and the arene-ruthenium assemblies M1 and M2, together with the host-guest systems PS⊂M.

2. Results

2.1. Cell Viability and Phototoxic Effect Evaluation

To investigate the effects of our arene-Ru assemblies *in vitro*, we conducted a series of experiments on HCT116 and HT-29 human CRC cell lines. The cell lines were treated with the compounds PS⊂M1 and PS⊂M2, as well as the empty assemblies M1 and M2, which lack the PS component in their inner cavity. Following treatment, the cells were either exposed to red light illumination (630 nm and 75 J/cm²) or kept in the dark. The impact on cell viability was assessed at 12 h, 24 h, and 48 h post-illumination using the MTT assay, a standard method for measuring cellular metabolic activity as an indicator of cell viability and proliferation. The results of the MTT assay revealed that in the absence of light, there was not any significant cytotoxic effect exhibited on the HCT116 and HT-29 cell lines after treatment with PS⊂M1, PS⊂M2, M1, or M2 (> 1000 nM). This indicates that these compounds are non-toxic to cells under dark conditions, ensuring that any observed cytotoxicity can be attributed to photoactivation rather than intrinsic toxicity. However, upon exposure to red light, a marked decrease in cell viability was observed for both PS⊂M1 and PS⊂M2 systems (Figure 3). This phototoxic effect was both dose- and time-dependent, with significant reductions in cell viability noted at 12 h, 24 h, and 48 h post-illumination for both HCT116 and HT-29 cell lines (Figure 3A,B). Specifically, the IC₅₀ values, representing the concentration at which 50% of the cells are inhibited, were found to be in the nanomolar range for both the PS⊂M1 and PS⊂M2 host-guest systems, indicating the high potency of these compounds under light activation. For the HCT116 cell line, the IC₅₀ determined for PS⊂M1 at 12 h, 24 h, and 48 h post-illumination were 666 nM,

602 nM, and 588 nM, respectively. Moreover, the IC_{50} values determined for **PS_CM2** at 12, 24, and 48 h post-illumination were 647 nM, 541 nM, and 518 nM, respectively. For the HT-29 cell line, the IC_{50} values of **PS_CM1** were 892 nM, 672 nM, and 536 nM, and for **PS_CM2**, were 884 nM, 593 nM, and 539 nM at 12 h, 24 h, and 48 h post-illumination, respectively (Figure 3C). We notice that the determined IC_{50} values of **PS_CM1** at each time post-illumination were slightly greater than those of **PS_CM2** in both the HCT116 and HT-29 cell lines. In illuminated conditions, the phototoxicity was significantly high, whereas in the dark, the IC_{50} values could not be determined, underscoring the lack of cytotoxicity without light activation. Interestingly, the individual components **M1** and **M2**, when not carrying porphrin, did not exhibit significant changes in cell viability under illuminated or non-illuminated conditions (Figure 3A,B). This indicates that the full assemblies **PS_CM1** and **PS_CM2** are crucial for the observed photodynamic activity facilitating the targeted delivery and effective photoactivation of the PS. In summary, these results demonstrate that the **PS_CM1** and **PS_CM2** assemblies possess significant phototoxic activity, leading to substantial reductions in cell viability upon light exposure. For subsequent experiments, the IC_{50} values determined after illumination are used to further explore the therapeutic potential and mechanistic aspects of the compounds.

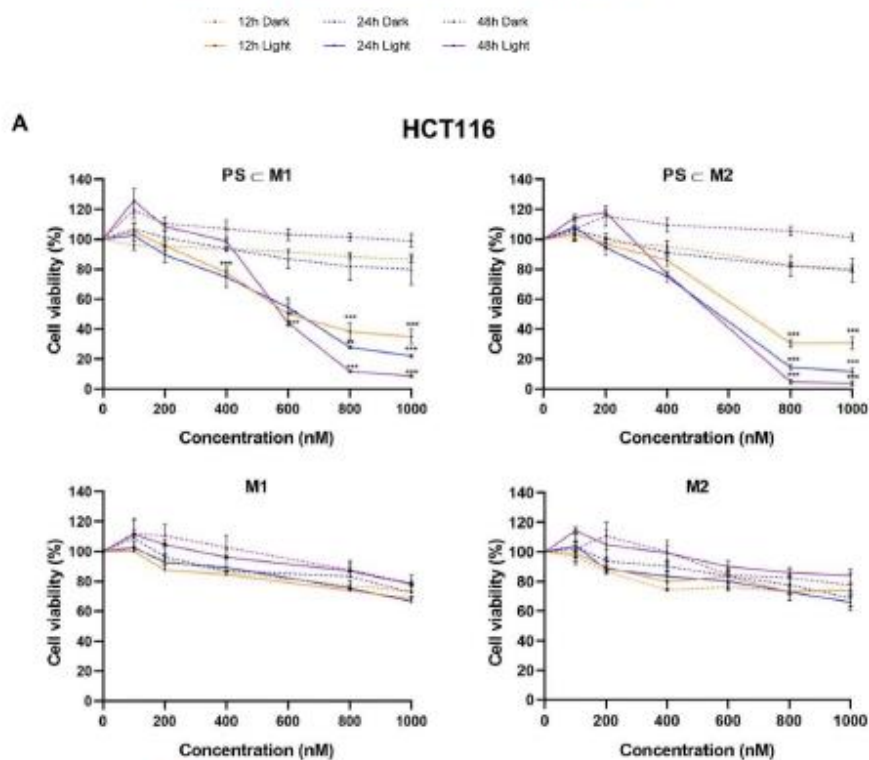


Figure 3. Cont.

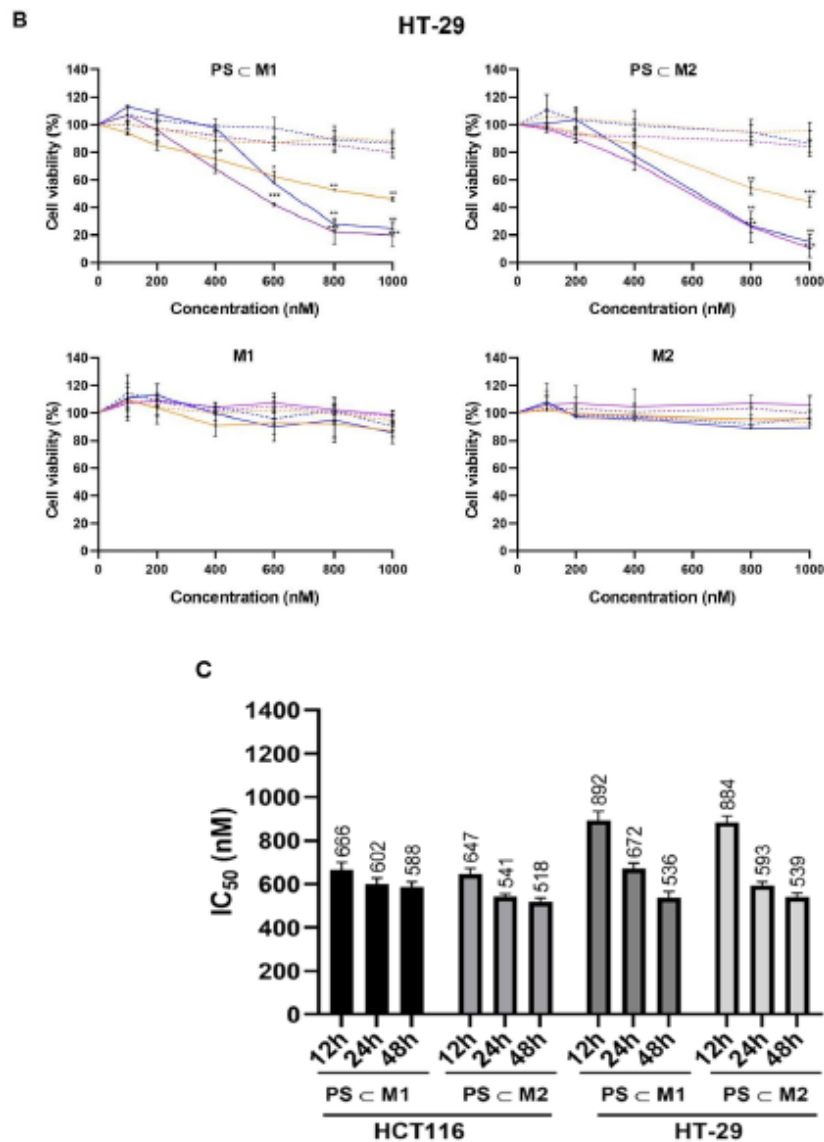


Figure 3. Phototoxicity of arene-Ru porphyrin PS assemblies on human CRC cell lines. (A) HCT116 and (B) HT-29 cell lines were cultured in RPMI medium for 24 h. After 24 h, cells were treated or not with PS⊂M1, PS⊂M2, M1, or M2. Illumination (630 nm, 75 J/cm²) of the cells occurred 24 h after treatment, and the cell viability for all the conditions was determined 12 h, 24 h, and 48 h post-illumination. Data are represented as a mean ± SEM of three independent experiments. * *p* < 0.05; ** *p* < 0.01; and *** *p* < 0.001. (C) Graphical representation of the IC₅₀ values (nM) of PS⊂M1 and PS⊂M2 determined by MTT assay on HCT116 and HT-29 cell lines. Data are represented as a mean ± SEM of three independent experiments.

2.2. ROS Production

The efficacy of PDT is directly linked to the production of ROS, a crucial aspect. To assess ROS levels, the cells were stained with the dichlorodihydrofluorescein (DCFDA) substrate and analyzed using flow cytometry immediately after illumination, with hydrogen peroxide (H_2O_2) being used as a positive control. The results revealed a substantial increase in ROS production following illumination in the treated cells compared to the treated non-illuminated and control cells. Specifically, in the HCT116 cell line, treatment with the **PSCM1** assembly under light exposure resulted in a remarkably high level of ROS production of 88.46%, significantly exceeding the 12.79% observed in the absence of light (Figure 4A). Similarly, the **PSCM2** assembly induced a notable ROS level of 89.20% under light exposure, compared to 16.79% in the dark. Parallel findings were observed in the HT-29 cell lines, with the ROS levels reaching 83.02% and 87.68% for **PSCM1** and **PSCM2**, respectively, under light exposure. These values were significantly higher than the 6.03% and 7.40% observed in the absence of light for **PSCM1** and **PSCM2**, respectively (Figure 4B). These results underscore the photoactivation of the **PSCM1** and **PSCM2** assemblies through ROS production, affirming their role in exerting the PDT effect. The substantial increase in ROS levels following illumination provides compelling evidence of the effectiveness of these assemblies in generating cytotoxic ROS species, validating their potential as promising candidates for PDT applications.

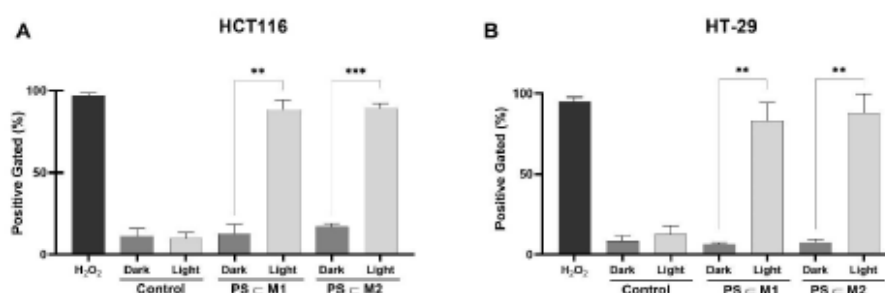


Figure 4. Intracellular ROS production was evaluated in (A) HCT116 and (B) HT-29 human CRC cell lines immediately after illumination (630 nm, 75 J/cm²) using DCFDA staining. Cells were analyzed using flow cytometry. Quantification of the intensity of fluorescence emitted due to DCF formation is correlated to the level of ROS generation. Data are represented as a mean \pm SEM of three independent experiments. ** $p < 0.01$ and *** $p < 0.001$.

2.3. Cellular Internalization

The molecular uptake and internalization of the **PSCM** assemblies within cells were determined by confocal microscopy. After the internalization of the metallacages into the cells by endocytosis, the guest molecule was released from the host, allowing it to be excited by light and to undergo photoactivation [33]. Porphin, which is inherently auto-fluorescent in the red or infrared regions, can be efficiently tracked after its internalization into the cells [34]. After treatment with **PSCM1** and **PSCM2** assemblies, the fluorescence was predominantly observed in the cytoplasm of the HCT116 and HT-29 cell lines. This cytoplasmic accumulation confirms the cellular uptake of these assemblies, which potentially permits their interaction with cytosolic targets (Figure 5A,B). Indeed, this cytoplasmic localization is crucial for understanding the intracellular distribution and potential mechanisms of action of these assemblies.

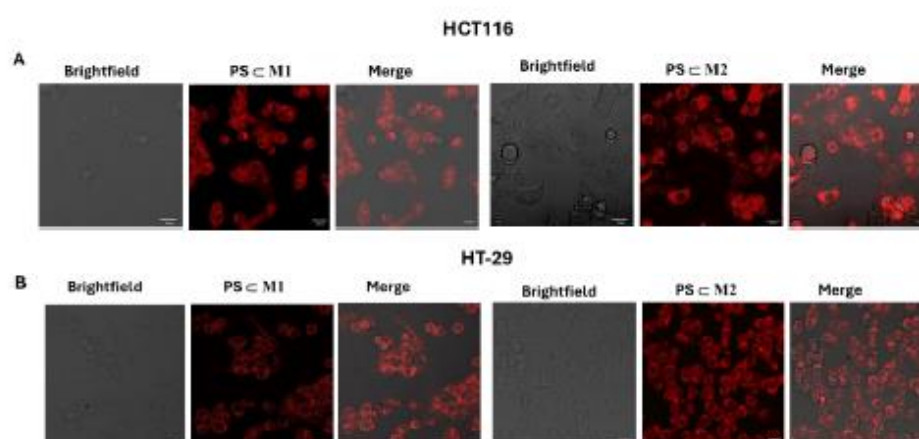


Figure 5. Detection of the cellular internalization of PSCM1 and PSCM2 in HCT116 (A) and HT-29 (B) cell lines by confocal microscopy. The cells were seeded into incubation chambers and cultured for 24 h. The cells were then treated with the compounds, and the fluorescence was measured by confocal microscopy (laser Zeiss LSM 510 Meta— $\times 1000$). The internalization was processed using the ImageJ image-processing software (version 1.54f). White scale bar = 20 μ m.

2.4. Cell Cycle Analysis

As cancer cells possess a rapid proliferation rate, it is important to investigate the effects of the PSCM assemblies on the cell cycle progression. The number of cells present at each phase of the cell cycle was monitored through DNA labeling with propidium iodide (PI). The effect of the PSCM1 and PSCM2 assemblies on cell cycle progression was examined in the HCT116 and HT-29 cell lines. The distribution of cells across different phases of the cell cycle was analyzed by flow cytometry (Figure 6A,B). In the HCT116 cell line, the sub-G1 phase, indicative of apoptotic cells, was 8.43% after 12 h of illumination with PSCM1 and 8.23% with PSCM2, which were higher than that of the control cells (1.48%). At 24 h post-illumination, there was a significant increase in the sub-G1 phase for the treated and illuminated cells, rising to 21.42% for PSCM1 and 34.34% for PSCM2 as compared to the control cells (0.60%). Similar trends were observed at 48 h post-illumination, with sub-G1 phase cells reaching 24.14% for PSCM1 and 36.67% for PSCM2 as compared to the control cells (3.66%) (Figure 6C). The data indicate that the sub-G1 phase culminates at 24 h post-illumination, with no significant change observed at 48 h compared to 24 h. Furthermore, there was a noticeable accumulation of cells in the G1 phase with a decrease in the number of cells passing into the S-phase in the illuminated cells compared to the control cells, which was more prominent at 12 h and 24 h post-illumination. These findings suggest that the maximum phototoxic effect of the PSCM1 and PSCM2 assemblies in the HCT116 cell line is reached at 24 h post-illumination, with a pronounced increase in apoptosis and G1 phase arrest contributing to this effect. In the HT-29 cell line, at 12 h post-illumination, the sub-G1 phase was not observed; nevertheless, at 24 h post-illumination, the emergence of the sub-G1 phase was evident, with 3.96% of cells observed with PSCM1 and 2.49% with PSCM2 as compared to 0.03% in the control cells. The proportion of cells in the sub-G1 phase increased significantly at 48 h post-illumination, reaching 11.02% for PSCM1 and 12.28% for PSCM2 (Figure 6D). This delayed onset of the sub-G1 phase highlights a time-dependent apoptotic response to the treatment contributing to a progressive accumulation of apoptotic cells over time. Additionally, a persistent accumulation of cells in the G2 phase was observed at 12 h, 24 h, and 48 h post-illumination accompanied by a significant decrease in the number of cells entering the G1 phase. This indicates that these assemblies induce a cell cycle arrest in the G2 phase of the HT-29 cell line, blocking the ability of the

cells to proceed to mitosis. In both cell lines, the assemblies do not influence the overall cell cycle progression in the dark. However, after illumination, we can conclude that the difference indicates that HT-29 cells have a slower apoptotic response compared to HCT116 cells, potentially due to variations in their cellular machinery or sensitivity to treatments.

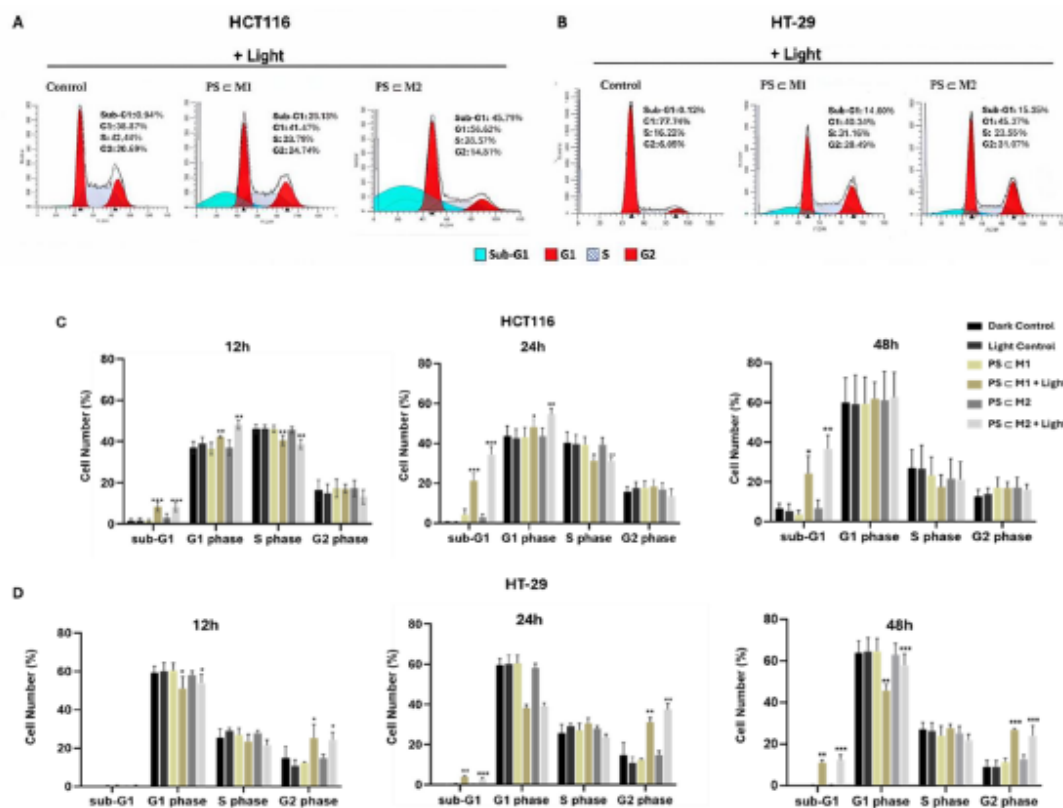


Figure 6. Cell cycle distribution analysis on HCT116 and HT-29 cell lines after the photoactivation of PSCM1 and PSCM2. Cells were seeded for 24 h in a culture medium before the treatment or not with the assemblies at their determined IC₅₀ concentrations. After 24 h of treatment, cells were illuminated or not with red light at 630 nm and 75 J/cm². Cells were collected at 12 h, 24 h, and 48 h post-illumination for analysis by flow cytometry using PI staining. Images of the cell cycle distribution on (A) HCT116 cells at 24 h post-illumination and (B) HT-29 cell line at 48 h post-illumination are represented. Histograms representing the percentage cell numbers at each phase of the cell cycle on (C) HCT116 and (D) HT-29 cell lines are displayed as a mean ± SEM of three independent experiments. * $p < 0.05$; ** $p < 0.01$ and *** $p < 0.001$.

2.5. Annexin V-PI

To investigate the apoptotic mechanisms as suggested by the sub-G1 phase of the cell cycle, we conducted an Annexin V-FITC/PI dual staining assay, analyzed via flow cytometry. This assay distinguishes early apoptotic cells, marked by Annexin V after membrane flip flop and phosphatidylserine exposure, as well as late apoptotic and necrotic cells, identified by PI uptake due to membrane integrity loss. In the HCT116 and HT-29 cell lines, the number of cells that were positively stained with Annexin V and PI increased significantly following the treatment with PSCM1 and PSCM2 assemblies

after illumination, as compared to the control (Figure 7A,B). In the HCT116 cell line, at 12 h post-illumination, the percentage of apoptotic cells (early + late apoptosis) was 17.64% for **PS_CM1** and 19.81% for **PS_CM2**, indicating an early onset of apoptosis. This increased dramatically at 24 h post-illumination to 34.38% for **PS_CM1** and 49.05% for **PS_CM2**, nearly tripling the apoptotic response observed in non-illuminated treated cells (11.96% and 14.50%, respectively). By 48 h, apoptosis rates were 23.90% for **PS_CM1** and 36.37% for **PS_CM2**, still elevated compared to the non-illuminated cells of 9.07% and 10.98%, respectively, but lower than the 24 h peak, indicating a maximal apoptotic activity around 24 h post-illumination (Figure 7C). In the HT-29 cell line, the apoptotic response was also evident but exhibited a distinct pattern. At 12 h post-illumination, the percentage of apoptotic cells was 19.04% for **PS_CM1** and 21.59% for **PS_CM2**. At 24 h post-illumination, apoptosis increased to 31.68% for **PS_CM1** and 34.13% for **PS_CM2** while remaining relatively constant in the non-illuminated cells, 7.81% and 11.86%, respectively. At 48 h post-illumination, the percentage of apoptotic cells further increased to 40.12% for **PS_CM1** and 41.56% for **PS_CM2**, whereas the non-illuminated groups showed minimal apoptosis, 6.11% and 6.95%, respectively (Figure 7D). These results demonstrate that these PS assemblies induce significant apoptotic cell death in the HCT116 and HT-29 cell lines following illumination. The apoptotic response in the HCT116 cells peaks at 24 h post-illumination, while the HT-29 cells exhibit a more gradual increase in apoptosis, reaching a significant level at 48 h. The observed apoptotic responses confirm the photocytotoxic effects of these porphyrin-based PS assemblies, supporting their potential use in PDT.

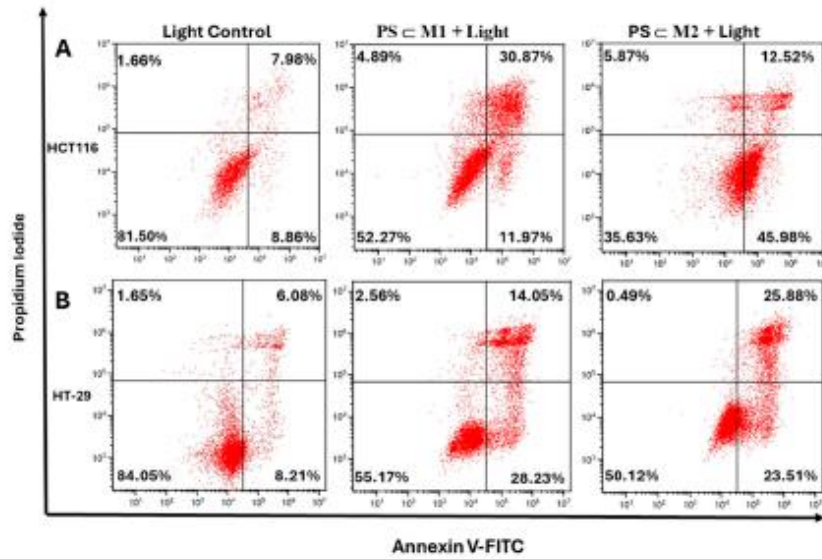


Figure 7. Cont.

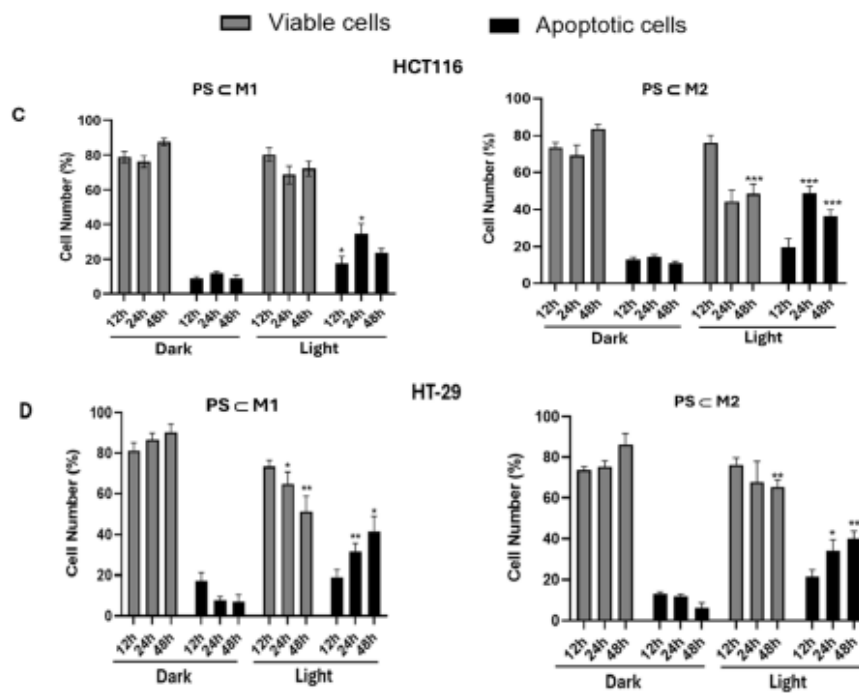


Figure 7. Apoptosis due to photoactivation was assessed on HCT116 and HT-29 cell lines. Cells were seeded and incubated for 24 h then treated or not with $PS_{C M1}$ and $PS_{C M2}$ assemblies at IC_{50} concentrations. Cells were either illuminated (630 nm , $75\text{ J}/\text{cm}^2$) or not after 24 h of treatment, and then, they were collected at 12 h, 24 h, and 48 h post-illumination. The collected cells were stained with Annexin V- FITC and PI, and their state was revealed by flow cytometry. Representative data from flow cytometry for the HCT116 cell line at 24 h post-illumination (A) and HT-29 at 48 h post-illumination (B) are displayed. Histograms represent the viable and apoptotic cell percentages of the treated HCT116 (C), and HT-29 (D) cells subjected to prior illumination. Data are represented as a mean \pm SEM of three independent experiments. * $p < 0.05$; ** $p < 0.01$; and *** $p < 0.001$.

2.6. Western Blot

To evaluate the onset of apoptosis, the expression of different proteins was analyzed by Western blot. During apoptosis, a complex cascade of events is initiated within cells, culminating in the activation of various apoptotic proteins, including caspase 3. Caspase 3 is initially synthesized in its inactive form, pro-caspase 3, which can become activated after a proteolytic cleavage. Once activated, caspase 3 will target and cleave poly (ADP-ribose) polymerase-1 (PARP-1). The cleavage of PARP-1 by active caspase 3 impairs the enzyme's ability to repair DNA, effectively signaling the cell to proceed with apoptosis. Hence, the level of expression of caspase 3 and PARP-1 in the HCT116 and HT-29 cell lines was evaluated after photoactivation or not of the $PS_{C M}$ assemblies (Figure 8A,B). Our analysis revealed that in both cell lines, the activation of caspase 3, indicated by the presence of its cleaved form, was detected exclusively in cells that were subjected to illumination after treatment with $PS_{C M1}$ and $PS_{C M2}$. In contrast, the cells that were kept in the dark and the control cells exhibited no sign of caspase 3 cleavage. This activation pattern was consistent at both 24 h and 48 h post-illumination, designating the induction of apoptosis in response to our treatment. Similarly, we observed that the cleavage of PARP-1, which serves as a hallmark of apoptosis, occurred only in the treated and illuminated cells. This

4.2-fold for **PS_CM1** and 5.6-fold for **PS_CM2**, indicating a sustained and progressively increasing apoptotic response (Figure 9B). For both cell lines, no significant increase in DNA fragmentation was observed at 12 h post-illumination after treatment with either **PS_CM1** or **PS_CM2**. Additionally, non-illuminated cells treated with **PS_CM1** or **PS_CM2** did not exhibit any significant changes in DNA fragmentation levels at 12 h, 24 h, and 48 h compared to the control cells. These findings underscore the role of **PS_CM1** and **PS_CM2** in inducing DNA fragmentation as part of the apoptotic process, with the most significant changes observed at 24 h post-illumination for HCT116 cells and a progressive increase up to 48 h for HT-29 cells. The lack of significant DNA fragmentation in non-illuminated cells and at earlier time points highlights the specificity and timing of the apoptotic response triggered by these PS assemblies upon illumination.

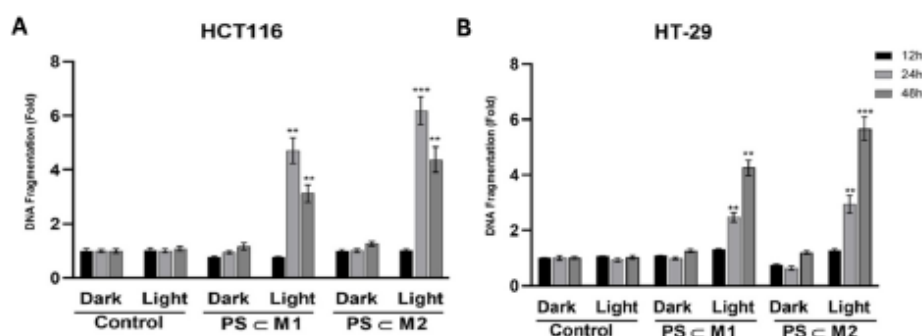


Figure 9. DNA fragmentation in HCT116 (A) and HT-29 (B) cells analyzed from cytosol extracts using ELISA assay. After seeding the cells for 24 h, followed by treatment, the cells were illuminated (630 nm , $75 \text{ J}/\text{cm}^2$) or not. After 12 h, 24 h, and 48 h post-illumination, the cells were collected, and the level of DNA fragmentation was analyzed. Histograms are represented as a mean \pm SEM of at least three independent experiments. ** $p < 0.01$ and *** $p < 0.001$.

3. Discussion

As conventional anticancer therapies are often associated with numerous undesirable side effects, PDT came as a breakthrough in cancer therapy for its effectiveness and selectivity towards the tumor site. Only a few PS have been approved for medical applications, with porphyrin-based compounds being the most prominent [35]. However, this class of PS has a low solubility in biological media, which often constrains their use, applications, and implications in different studies. Fortunately, this limitation can be managed through the use of delivery vectors that encapsulate the PS so that a facilitated delivery and effective internalization by cells can be reached. To attain this outcome, the conjugation of porphyrin with metal-based drugs is considered a strategic approach for the treatment of several cancer types including CRC [36]. Ru complexes exhibit distinctive photochemical and photophysical properties conferring their uniqueness among metal-based therapies such as their ability to interact with cellular biomolecules and selectively accumulate in cancer cells [34,37]. As reported in previous studies, Ru has grabbed the attention of many researchers as a modality of treatment of various cancer types including prostate, colorectal, bladder, and hepatic cancer due to its ability to act as a chemotherapeutic cytotoxic agent with selectivity to the cancer cells [22–24,38,39].

In this research, we examined the anticancer efficacy of arene-Ru assemblies lodging porphyrin PS within their cavity on HCT116 and HT-29 CRC cell lines. Our findings demonstrated the potency of the Ru metallacages (**M1** and **M2**) to act as delivery systems of the porphyrin since they did not exhibit a cytotoxic effect under the studied concentration range either in the presence or in the absence of illumination. Hence, the IC_{50} of the **PS_CM** systems determined with light illumination after different times, ranging between 500 and

900 nM, is mainly due to the porphyrin PS rather than the metallacage. In this study, the main difference between our **PSCM** systems was in the spacer acting as the edges of the cage and joining the Ru ions. In the study of Gallardo-Villagrán et al., a correlation between the spacer size and the release of porphyrin PS was proved through IC_{50} determination. In their study, the same metallacages with porphyrin PS inside the cavity were investigated on rheumatoid arthritis (RA) synoviocytes, and the IC_{50} of the **PSCM2** (named **G1C3** in their study) was around two-fold lower than that of **PSCM1** (named **G1C2** in their study) at 18 h post-illumination. This was linked to the fact that a bulkier spacer made up of four aromatic rings (**M2**) allows for the facilitated release of PS from the internal cavity of the cage as compared to that with two aromatic rings (**M1**). Additionally, the spacer that was made up of only one aromatic ring had a significantly higher IC_{50} value compared to both **PSCM1** and **PSCM2** [31]. However, in a previous study, the latter spacer was also included in the same cage with porphyrin PS inside and investigated on DU 145 and PC-3 prostate cancer cell lines, and the determined IC_{50} values were found to be in nanomolar ranges between 500 and 650 nM after 24 h of illumination [23]. These values were close to our findings with **PSCM1** and **PSCM2** treatments on HCT116 and HT-29 CRC cell lines. We also notice that in our study, **PSCM2** with the larger spacer has a slightly better overall effect than **PSCM1**, validating the study of Gallardo-Villagrán et al. [31], yet the difference is not significant. Here, we can demonstrate that the cell lines originating from different diseases will ultimately possess different sensitivities to the same treatment, also taking into consideration the impact of the difference in the drug-light time intervals. Even the different cell lines originating from the same disease will rationally not display similar outcomes. This was confirmed in our study when the HCT116 and HT-29 CRC cell lines showed a different overall outcome to the same treatment. As HCT116 is more sensitive than HT-29, the IC_{50} values obtained in our study with the same treatment at 12 h post-illumination were about two-fold lower than that of HT-29. Additionally, the observed apoptotic effect was reached faster in the HCT116 than in the HT-29 cell line where the maximal effect of the complexes was obtained 24 h post-illumination in the HCT116 cell line, whereas a relatively similar effect was obtained 48 h post-illumination on the HT-29 cell line. This was confirmed by the apoptotic phenomenon observed through Annexin V-PI staining and DNA fragmentation levels relative to time. DNA fragmentation can be enhanced when the PS is chemically modified or conjugated to facilitate its binding and interaction with DNA, as evidenced by the study of Zhao et al. [40]. Similarly, a study conducted by Rani-Beeram et al. demonstrated that fluorinated porphyrin-Ru showed a significant interaction with DNA, causing their cleavage in melanoma cells [41]. Additionally, the apoptotic induction of HepG2 liver cancer cells after photoactivation of the Ru porphyrin complex Rup-03 has been previously established [42]. Apoptotic cell death was further confirmed by Western blot through the cleavage of pro-caspase 3 and PARP-1 proteins. In the dark, there was a total absence of cytotoxicity in the treatment, which is also consistent with many previous studies [20,22–24,31]. Furthermore, we assessed the progression of the cell cycle and observed a peak for sub-G1, marking the cell death after photoactivation in both cell lines. Another study by Li et al. established a successful apoptotic effect on A549 lung carcinoma cells, distinguished by a sub-G1 peak after treatment with several Ru complexes [43]. Also, it was demonstrated that the cell cycle blockage was not the same on both cell lines; as mentioned earlier, the studied systems caused an arrest of the cell cycle at the G1 phase in the HCT116 cell line and the G2 phase in HT-29. Another study showed that Ru tetrapyrrolylporphyrin assemblies investigated on CRC caused a blockage in the S phase of the cell cycle [22]. As our systems are intrinsically auto-fluorescent, their intracellular accumulation was tracked by confocal microscopy, and image acquisitions showed that they are localized in the cytoplasm of the cells. Previous studies mentioned that the PS can be released from the cage either through a partial/ total rupture of the cage or through an aperture, which is the case in our study. It was also demonstrated that these cages enter the cell to deliver their contents through the assessment of the Ru ions inside the cells by inductively coupled plasma mass spectrometry (ICP-MS) [33,34].

After internalization into the cells, the released PS gets excited in the cytoplasm at specific wavelength (630 nm) and thereby contributes to detrimental effects on cells through the production of ROS. The cytoplasmic localization of Ru assemblies including PS, as well as ROS production triggering apoptosis, was also recognized in earlier investigations [22,23]. Overall, our results agree with the study of Lu et al., which demonstrated the anticancer potential of Ru complexes on hepatocellular carcinoma through growth inhibition of the HCC cells, induction of apoptosis marked by the sub-G1 peak, activation of caspases, and DNA fragmentation [39].

Further studies to elaborate on the involved mechanisms that these systems follow to release PS after internalization as well as the involved kinetics would be remarkable. Also, performing pre-clinical research on these systems through advanced culturing and in vivo models would be a principal objective for their further use as treatment options in clinics as they hold promising potential as candidates for PDT agents.

4. Materials and Methods

4.1. Materials

RPMI 1640 medium, RPMI 1640 red-phenol-free medium, fetal bovine serum (FBS), L-glutamine, and penicillin-streptomycin were purchased from Gibco BRL (Cergy-Pontoise, France). 3-(4,5-dimethylthiazol-2-yl)-2,5-diphenyltetrazolium bromide (MTT), cell death detection enzyme-linked immunosorbent assay (ELISA)^{PLUS}, 2',7'-dichlorofluorescein diacetate (DCFDA), and human anti- β -actin antibody were obtained from Sigma-Aldrich (Saint-Quentin-Fallavier, France). Pro-caspase 3, cleaved caspase 3, poly-ADP-ribose polymerase-1 (PARP-1) antibodies, and goat anti-rabbit IgG secondary antibody conjugated to horseradish peroxidase (HRP) were acquired from Cell Signaling Technology-Ozyme (Saint-Quentin-en-Yvelines, France). Rabbit anti-mouse IgG-IgM H&L HRP secondary antibody, Annexin V-FITC, and PI were obtained from Invitrogen-Thermo Fisher Scientific (Villebon-Sur-Yvette, France). Immobilon Western Chemiluminescent HRP Substrate was acquired from Merck (Lyon, France).

4.2. Synthesis of the Arene-Ruthenium Assemblies Lodging a Photosensitizer

The assemblies were synthesized according to the literature [31]. The PS, 21H, 23H-porphin (PS), was synthesized as reported in the literature [44], and the corresponding lodging into arene Ru assemblies was attained by host-guest interactions. Stock solutions were prepared at 1 mM concentration in DMSO and stored at -20°C .

4.3. Cell Culture and Treatment

The human CRC cell lines HCT116 and HT-29 were purchased from the American Type Culture Collection (ATCC-LGC Standards, Molsheim, France). The cells were grown in RPMI 1640 medium for culturing and were supplemented with 10% FBS, 1% L-glutamine, 100 U/mL penicillin, and 100 $\mu\text{g}/\text{mL}$ streptomycin. The cultures were maintained in a humidified atmosphere containing 5% CO_2 at 37°C . For all experiments, the cells were seeded at 1.2×10^4 and 2.1×10^4 cells/ cm^2 for the HCT116 and HT-29 cells, respectively. The stock solution **PS-CM1** and **PS-CM2** assemblies were diluted in a culture medium to obtain the final concentration required, and the medium was replaced by a red phenol-free culture medium before PDT. The maximal concentration of DMSO in the culture medium was less than 0.1% in all cases, which is non-toxic.

4.4. Light Source

Illumination of the cells was achieved using a Lumidox[®] II device (Analytical Sales and Services, Flanders, NJ, USA) under red visible light at 630 nm, at 75 J/ cm^2 , and 70 mW/LED for 6 min.

4.5. Cell Viability Assay

The cell viability was assessed using an MTT reagent (Sigma-Aldrich) as an indicator of the metabolic activity of the cells. The cells were seeded in 96-well culture plates and incubated for 24 h before treatment with the **PS_CM1** and **PS_CM2** assemblies, which were diluted in RPMI 1640 medium to obtain an appropriate range of concentration. After 24 h, the cells were illuminated or not using a Lumidox lamp 70 mW/LED. MTT assays were performed at 12 h, 24 h, and 48 h post-illumination, and cell viability was expressed as a percentage of cell viability for each treatment condition normalized to the untreated cells.

4.6. Intracellular ROS Generation

Cellular ROS generated after the illumination of the cells was quantified using a DCFDA substrate (Sigma-Aldrich). The cells were seeded in 75 cm² culture flasks for 24 h; then, they were treated or not with **PS_CM1** and **PS_CM2** assemblies at their determined IC₅₀ values. After 24 h, the cells with different treatment conditions were collected and incubated with DCFDA for 30 min before illumination. The quantification of cellular ROS production was determined directly after illumination through CytoFLEX LX (Beckman Coulter, Brea, CA, USA). H₂O₂ was used as a positive control at 800 μM concentration.

4.7. Cellular Internalization

The internalization of the compounds within the HCT116 and HT-29 cells was determined by confocal microscopy. The cells were seeded into incubation chambers (ibidi μ-Slide 8 wells; Clinisciences, Martinsreid, Germany) with a density of 2.5×10^4 and 3.5×10^4 cells/well for the HCT116 and HT-29 cell lines, respectively. The wells were coated with a gel prepared by mixing collagen type I (3 mg/mL) and acetic acid (20 mM) and incubated for 24 h before their treatment or not with **PS_CM1** and **PS_CM2** at their IC₅₀ values. After treatment, image acquisitions were taken by a Carl Zeiss LSM 510 Meta—×1000 confocal laser microscope. The natural fluorescence of the assemblies permitted their observation within the cells with emission (excitation: 405/561 nm; emission: 650/673 nm).

4.8. Cell Cycle Analysis

The distinct phases of the cell cycle progression were assessed for both the HCT116 and HT-29 cell lines by flow cytometry using PI staining. The cells were seeded into 75 cm² flasks and incubated for 24 h. The treatment or not with **PS_CM1** and **PS_CM2** assemblies at their determined IC₅₀ values was performed after 24 h of incubation. Illumination of the cells was carried out after 24 h, and then, pellets of 1×10^6 cells were collected at 12 h, 24 h, and 48 h post-illumination. The cells were washed with PBS and fixed by the addition of 1 mL of chilled 70% ethanol in PBS and stored at −20 °C. Before flow cytometry analysis, the cell pellets were washed with cold PBS and centrifuged, and then, they were resuspended with 500 μL of cold PBS along with 30 μL of RNase A (10 mg/mL) and incubated for 30 min at room temperature. After incubation, the cells were stained with 25 μL of PI (1 mg/mL), allowing the determination of the percentage of cells present in each phase of the cell cycle using the FACs system (BD Biosciences, San Jose, CA, USA).

4.9. Apoptotic Assays

4.9.1. Annexin V-FITC/PI Dual Staining Assay

The cells were seeded into 75 cm² flasks and were treated or not based on the determined IC₅₀ values of the **PS_CM1** and **PS_CM2** assemblies after 24 h of incubation. After 24 h, the cells were illuminated or not and were harvested by trypsin at 12 h, 24 h, and 48 h post-illumination. Cell pellets of 2.5×10^5 for each condition were prepared, washed in PBS, centrifuged, and resuspended in 300 μL of Annexin V lysis buffer (1X). The cells were labelled with 5 μL Annexin V-FITC and 1 μL of PI (0.1 mg/mL) and then were kept in the dark and at room temperature for 15 min. The percentage of cells undergoing apoptosis was then determined by CytoFLEX LX (Beckman Coulter).

4.9.2. Protein Extraction and Western Blot Analysis

Cells of different conditions were gathered to extract and identify specific proteins of interest. After cell seeding for 24 h, the cells were treated or not with **PS_CM1** and **PS_CM2** assemblies at the determined IC_{50} values and collected 12 h, 24 h, and 48 h post-illumination. For total protein extraction, the cells were lysed with RIPA lysis buffer containing protease inhibitors according to the manufacturer's instructions, as described [20]. The protein levels were quantified using the Bradford method; then, were separated on 12.5% SDS-PAGE gels; and then, transferred to PVDF membranes (Amersham Pharmacia Biotech, Saclay, France). Apoptosis-related human proteins were studied by membrane probing with primary anti-PARP-1 (1:1000), primary anti-cleaved caspase 3 (1:1000), and primary anti-pro-caspase 3 (1:1000). For the loading control, primary human anti- β -actin (1:5000) was used. After incubation with the primary antibodies overnight at 4 °C, appropriate secondary antibodies were used to incubate the membranes for at least 1 h. The blots were revealed using an Immobilon Western Chemiluminescent HRP substrate in a G: BOX system (Syngene, Cambridge, UK).

4.9.3. DNA Fragmentation

A Cell Death ELISA^{PLUS} kit was used to assess the level of DNA fragmentation in the different cell conditions. After the cells were seeded in 75 cm² flasks for 24 h, the cells were treated or not using the IC_{50} values of the **PS_CM1** and **PS_CM2** assemblies. After 24 h, the cells were illuminated or not and cell pellets of 2×10^5 cells were collected for each condition. The DNA fragmentation levels were assessed according to the manufacturer's protocol [22] and expressed as a fold change compared to the control cells.

4.10. Statistical Analysis

All data are expressed as the mean \pm standard error of the mean (SEM) of three independent experiments. The statistical significance of the results was evaluated by a two-tailed unpaired Student's *t*-test and expressed as * $p < 0.05$, ** $p < 0.01$, and *** $p < 0.001$.

5. Conclusions

In this *in vitro* study, we investigated the effects of arene-Ru assemblies with porphyrin sitting in their cavity (**PS_CM**) on the HCT116 and HT-29 human CRC cell lines. The two host-guest systems showed relatively similar effects on both cell lines, with **PS_CM2** exhibiting a slightly greater efficacy, possibly due to its bulkier structure facilitating the release of the PS. After being internalized into the cell cytoplasm, the assemblies demonstrated significant phototoxicity, primarily through the production of ROS, leading to oxidative stress, cell cycle arrest, and apoptosis. These findings suggest the potential use of these assemblies in anticancer PDT.

Author Contributions: Conceptualization, S.G., B.T. and B.L.; methodology, S.G., J.M., and A.P.; software, S.G., J.M., A.P., M.G.-V., C.C. and C.O.; validation, B.T., B.L., and M.D.-A.; formal analysis, S.G.; investigation, S.G., M.G.-V. and A.P.; data curation, B.T., and B.L.; writing—original draft preparation, S.G.; writing—review and editing, B.T., and B.L.; project administration, B.L. and M.D.-A.; funding acquisition, B.L. All authors have read and agreed to the published version of the manuscript.

Funding: This study was funded by the Ligue contre le Cancer Haute-Vienne (R2307834 and R2307836), 23 Av. des Bénédictins, 87000 Limoges, and the Université de Limoges, 33 Rue François Mitterrand, 87000 Limoges.

Institutional Review Board Statement: Not applicable.

Informed Consent Statement: Not applicable.

Data Availability Statement: The data are contained within the article.

Conflicts of Interest: The authors declare no conflicts of interest.

Abbreviations

ATCC: American Type Culture Collection; CRC: colorectal cancer; cym: cymene; DCFDA: 2',7'-dichlorofluorescein diacetate; DMSO: dimethyl sulfoxide; DNA: deoxyribonucleic acid; donq: 5,8-dioxydo-1,4-naphthoquinonato; dotq: 6,11-dioxydo-5,12-naphthacenedionato; ELISA: enzyme-linked immunosorbent assay; FBS: fetal bovine serum; H₂O₂: hydrogen peroxide; HRP: horseradish peroxidase; IC₅₀: half-maximal inhibitory concentration; kDa: kilodalton; M: metallacage MTE: 3-(4,5-dimethylthiazol-2-yl)-2,5-diphenyltetrazolium bromide; PARP-1: poly-ADP-ribose polymerase-1; PBS: phosphate-buffered saline; PDT: photodynamic therapy; PI: propidium iodide; PI: phototoxic index; P_S: photosensitizer; PVDF membrane: polyvinylidene fluoride membrane; RA: rheumatoid arthritis; RIPA: radio immuno precipitation assay; Ru: ruthenium; ROS: reactive oxygen species; RPMI: Roswell Park Memorial Institute medium; SDS-PAGE: electrophoresis in polyacrylamide gel containing sodium dodecyl sulfate; SEM: standard error of the mean; tpt: 2,4,6-tri(pyridin-4-yl)-1,3,5-triazine.

References

1. Biller, L.H.; Schrag, D. Diagnosis and Treatment of Metastatic Colorectal Cancer: A Review. *JAMA* **2021**, *325*, 669–685. [CrossRef] [PubMed]
2. Papavassiliou, A.G.; Delle Cave, D. Novel Therapeutic Approaches for Colorectal Cancer Treatment. *Int. J. Mol. Sci.* **2024**, *25*, 2228. [CrossRef]
3. Negarandeh, R.; Salehifar, E.; Saghafi, F.; Jalali, H.; Janbabaei, G.; Abdhaghghi, M.J.; Nosrati, A. Evaluation of Adverse Effects of Chemotherapy Regimens of 5-Fluoropyrimidines Derivatives and Their Association with DPYD Polymorphisms in Colorectal Cancer Patients. *BMC Cancer* **2020**, *20*, 560. [CrossRef] [PubMed]
4. Shan, J.; Han, D.; Shen, C.; Lei, Q.; Zhang, Y. Mechanism and Strategies of Immunotherapy Resistance in Colorectal Cancer. *Front. Immunol.* **2022**, *13*, 1016646. [CrossRef]
5. Zhou, J.; Ji, Q.; Li, Q. Resistance to Anti-EGFR Therapies in Metastatic Colorectal Cancer: Underlying Mechanisms and Reversal Strategies. *J. Exp. Clin. Cancer Res.* **2021**, *40*, 328. [CrossRef]
6. Kozovska, Z.; Gabrisova, V.; Kucerova, I. Colon Cancer: Cancer Stem Cells Markers, Drug Resistance and Treatment. *Biomed. Pharmacother.* **2014**, *68*, 911–916. [CrossRef]
7. Federica, A.; Aebischer, D.; Bartusik-Aebischer, D. Photodynamic Therapy. In *The Biochemical Guide to Enzymes*; Nova Science Publishers, Inc.: Hauppauge, NY, USA, 2023.
8. Agostinis, P.; Berg, K.; Cengel, K.A.; Foster, T.H.; Girotti, A.W.; Gollnick, S.O.; Hahn, S.M.; Hamblin, M.R.; Juzeniene, A.; Kessel, D.; et al. Photodynamic Therapy of Cancer: An Update. *CA Cancer J. Clin.* **2011**, *61*, 250–281. [CrossRef]
9. Kwiatkowski, S.; Knap, B.; Przystupski, D.; Sazoko, J.; Kedzierska, E.; Knap-Czop, K.; Kotlińska, J.; Michel, O.; Kotowski, K.; Kulbacka, J. Photodynamic Therapy—Mechanisms, Photosensitizers and Combinations. *Biomed. Pharmacother.* **2018**, *106*, 1098–1107. [CrossRef]
10. Zhu, W.; Gao, Y.H.; Liao, P.Y.; Chen, D.Y.; Sun, N.N.; Nguyen Thi, P.A.; Yan, Y.J.; Wu, X.F.; Chen, Z.L. Comparison between Porphin, Chlorin and Bacteriochlorin Derivatives for Photodynamic Therapy: Synthesis, Photophysical Properties, and Biological Activity. *Eur. J. Med. Chem.* **2018**, *160*, 146–156. [CrossRef]
11. Sharifkazemi, H.; Amini, S.M.; Koohi Ortakand, R.; Narouie, B. A Review of Photodynamic Therapy in Different Types of Tumors. *Transl. Res. Urol.* **2022**, *4*, 61–70.
12. Kawczyk-Krupka, A.; Bugaj, A.M.; Latos, W.; Zaremba, K.; Wawrzyniec, K.; Sieroń, A. Photodynamic Therapy in Colorectal Cancer Treatment: The State of the Art in Clinical Trials. *Photodiagnosis Photodyn. Ther.* **2015**, *12*, 545–553. [CrossRef] [PubMed]
13. De Annunzio, S.R.; Costa, N.C.S.; Graminha, M.A.S.; Fontana, C.R.; Mezzina, R.D. Chlorin, Phthalocyanine, and Porphyrin Types Derivatives in Phototreatment of Cutaneous Manifestations: A Review. *Int. J. Mol. Sci.* **2019**, *20*, 3861. [CrossRef] [PubMed]
14. Juzeniene, A.; Moan, J. The History of PDT in Norway. Part II. Recent Advances in General PDT and ALA-PDT. *Photodiagnosis Photodyn. Ther.* **2007**, *4*, 80–87. [CrossRef] [PubMed]
15. Luksiene, Z. Photodynamic Therapy: Mechanism of Action and Ways to Improve the Efficiency of Treatment. *Medicina* **2003**, *39*, 1137–1150.
16. Plekhova, N.; Shevchenko, O.; Korshunova, O.; Stepanyugina, A.; Tananaev, I.; Apanasevich, V. Development of Novel Tetrapyrrole Structure Photosensitizers for Cancer Photodynamic Therapy. *Bioengineering* **2022**, *9*, 82. [CrossRef]
17. Park, J.; Jiang, Q.; Feng, D.; Mao, L.; Zhou, H.-C. Size-Controlled Synthesis of Porphyrinic Metal-Organic Framework and Functionalization for Targeted Photodynamic Therapy. *J. Am. Chem. Soc.* **2016**, *138*, 3518–3525. [CrossRef]
18. Nakamura, Y.; Mochida, A.; Choyke, P.L.; Kobayashi, H. Nanodrug Delivery: Is the Enhanced Permeability and Retention Effect Sufficient for Curing Cancer? *Bioconjug. Chem.* **2016**, *27*, 2225–2238. [CrossRef]
19. Ejjajah, V.; Owoseni, O.; Bataille-Backer, P.; Ogundipe, O.D.; Fisusi, F.A.; Adesina, S.K. Approaches to Improve Macromolecule and Nanoparticle Accumulation in the Tumor Microenvironment by the Enhanced Permeability and Retention Effect. *Polymers* **2022**, *14*, 2601. [CrossRef]

20. Bétrin, L.; Pinon, A.; Bouramtane, S.; Ouk, C.; Richard, L.; Perrin, M.L.; Chaunavel, A.; Carrion, C.; Bregier, F.; Sol, V.; et al. Photodynamic Therapy Activity of New Porphyrin-Xylan-Coated Silica Nanoparticles in Human Colorectal Cancer. *Cancers* **2019**, *11*, 1474. [CrossRef]
21. Mfouo-Tynga, L.S.; Dias, L.D.; Inada, N.M.; Kurachi, C. Features of Third Generation Photosensitizers Used in Anticancer Photodynamic Therapy: Review. *Photodiagnosis Photodyn. Ther.* **2021**, *34*, 102091. [CrossRef]
22. Massoud, J.; Pinon, A.; Gallardo-Villagrán, M.; Paulus, L.; Ouk, C.; Carrion, C.; Antoun, S.; Diab-Assaf, M.; Therrien, B.; Liagre, B. A Combination of Ruthenium Complexes and Photosensitizers to Treat Colorectal Cancer. *Inorganics* **2023**, *11*, 451. [CrossRef]
23. Paulus, L.; Gallardo-Villagrán, M.; Carrion, C.; Ouk, C.; Martin, F.; Therrien, B.; Léger, D.Y.; Liagre, B. The Effect of Photosensitizer Metalation Incorporated into Arene-Ruthenium Assemblies on Prostate Cancer. *Int. J. Mol. Sci.* **2023**, *24*, 13614. [CrossRef]
24. Janbeih, Z.; Gallardo-Villagrán, M.; Therrien, B.; Diab-Assaf, M.; Liagre, B.; Benov, L. Cellular Uptake and Phototoxicity Optimization of Arene Ruthenium Porphyrin Derivatives. *Inorganics* **2024**, *12*, 86. [CrossRef]
25. Candelaria, P.V.; Leoh, L.S.; Penichet, M.L.; Daniels-Wells, T.R. Antibodies Targeting the Transferrin Receptor 1 (TfR1) as Direct Anti-Cancer Agents. *Front. Immunol.* **2021**, *12*, 607692. [CrossRef] [PubMed]
26. Wang, M.; Wang, H.; Xu, X.; Lai, T.P.; Zhou, Y.; Hao, Q.; Li, H.; Sun, H. Binding of Ruthenium and Osmium at Non-iron Sites of Transferrin Accounts for Their Iron-Independent Cellular Uptake. *J. Inorg. Biochem.* **2022**, *234*, 111885. [CrossRef]
27. Guo, W.; Zheng, W.; Luo, Q.; Li, X.; Zhao, Y.; Xiong, S.; Wang, F. Transferrin Serves as a Mediator to Deliver Organometallic Ruthenium(II) Anticancer Complexes into Cells. *Inorg. Chem.* **2013**, *52*, 5328–5338. [CrossRef]
28. Biancalana, L.; Pampaloni, G.; Marchetti, F. Arene Ruthenium(II) Complexes with Phosphorous Ligands as Possible Anticancer Agents. *Chimia* **2017**, *71*, 573–579. [CrossRef]
29. Gandioso, A.; Purkait, K.; Gasser, G. Recent Approaches towards the Development of Ru(II) Polypyridyl Complexes for Anticancer Photodynamic Therapy. *Chimia* **2021**, *75*, 845–855. [CrossRef]
30. Abraham, M.H.; Acree, W.E. Solvation Descriptors for Porphyrins (Porphines). *New J. Chem.* **2016**, *40*, 9945–9950. [CrossRef]
31. Gallardo-Villagrán, M.; Paulus, L.; Charissoux, J.-L.; Sutour, S.; Vergne-Salle, P.; Léger, D.Y.; Liagre, B.; Therrien, B. Evaluation of Ruthenium-Based Assemblies as Carriers of Photosensitizers to Treat Rheumatoid Arthritis by Photodynamic Therapy. *Pharmaceutics* **2021**, *13*, 2104. [CrossRef]
32. Zhang, L.; Deng, M.; Liu, J.; Zhang, J.; Wang, F.; Yu, W. The Pathogenicity of Vancomycin-Resistant *Enterococcus faecalis* to Colon Cancer Cells. *BMC Infect. Dis.* **2024**, *24*, 230. [CrossRef] [PubMed]
33. Barry, N.P.E.; Zava, O.; Dyson, P.J.; Therrien, B. Excellent Correlation between Drug Release and Pore Size in Metalla-Cage Drug-Delivery Systems. *Chem. Eur. J.* **2011**, *17*, 9669–9677. [CrossRef] [PubMed]
34. Schmitt, F.; Freudenberg, J.; Barry, N.P.E.; Juillerat-Jeanneret, L.; Süß-Fink, G.; Therrien, B. Organometallic Cages as Vehicles for Intracellular Release of Photosensitizers. *J. Am. Chem. Soc.* **2012**, *134*, 754–757. [CrossRef] [PubMed]
35. Baskaran, R.; Lee, J.; Yang, S.G. Clinical Development of Photodynamic Agents and Therapeutic Applications. *Biomater. Res.* **2018**, *22*, 25. [CrossRef]
36. Sun, R.W.Y.; Zhang, M.; Li, D.; Li, M.; Wong, A.S.T. Enhanced Anti-Cancer Activities of a Gold(III) Pyrrolidinedithiocarbamate Complex Incorporated in a Biodegradable Metal-Organic Framework. *J. Inorg. Biochem.* **2016**, *163*, 1–7. [CrossRef]
37. Liu, J.; Zhang, C.; Rees, T.W.; Ke, L.; Ji, L.; Chao, H. Harnessing Ruthenium(II) as Photodynamic Agents: Encouraging Advances in Cancer Therapy. *Coord. Chem. Rev.* **2018**, *363*, 17–28. [CrossRef]
38. Bogoeva, V.; Siksjø, M.; Sæterbø, K.G.; Melo, T.B.; Bjørkøy, A.; Lindgren, M.; Gederaas, O.A. Ruthenium Porphyrin-Induced Photodamage in Bladder Cancer Cells. *Photodiagnosis Photodyn. Ther.* **2016**, *14*, 9–17. [CrossRef]
39. Lu, Y.; Shen, T.; Yang, H.; Gu, W. Ruthenium Complexes Induce HepG2 Human Hepatocellular Carcinoma Cell Apoptosis and Inhibit Cell Migration and Invasion through Regulation of the Nrf2 Pathway. *Int. J. Mol. Sci.* **2016**, *17*, 775. [CrossRef]
40. Zhao, P.; Xu, L.C.; Huang, J.W.; Zheng, K.C.; Liu, J.; Yu, H.C.; Ji, L.N. DNA Binding and Photocleavage Properties of a Novel Cationic Porphyrin-Anthraquinone Hybrid. *Biophys. Chem.* **2008**, *134*, 72–83. [CrossRef]
41. Rani-Beeram, S.; Meyer, K.; McCrate, A.; Hong, Y.; Nielsen, M.; Swavey, S. A Fluorinated Ruthenium Porphyrin as a Potential Photodynamic Therapy Agent: Synthesis, Characterization, DNA Binding, and Melanoma Cell Studies. *Inorg. Chem.* **2008**, *47*, 11278–11283. [CrossRef]
42. Li, W.; Xie, Q.; Lai, L.; Mo, Z.; Peng, X.; Leng, E.; Zhang, D.; Sun, H.; Li, Y.; Mei, W.; et al. In Vitro Evaluation of Ruthenium Complexes for Photodynamic Therapy. *Photodiagnosis Photodyn. Ther.* **2017**, *18*, 83–94. [CrossRef] [PubMed]
43. Li, W.; Jiang, G.B.; Yao, J.H.; Wang, X.Z.; Wang, J.; Han, B.J.; Xie, Y.Y.; Lin, G.J.; Huang, H.L.; Liu, Y.J. Ruthenium(II) Complexes: DNA-Binding, Cytotoxicity, Apoptosis, Cellular Localization, Cell Cycle Arrest, Reactive Oxygen Species, Mitochondrial Membrane Potential and Western Blot Analysis. *J. Photochem. Photobiol. B* **2014**, *140*, 94–104. [CrossRef] [PubMed]
44. Dogutan, D.K.; Ptaszek, M.; Lindsey, J.S. Direct Synthesis of Magnesium Porphine via 1-Formyldipyromethane. *J. Org. Chem.* **2007**, *72*, 5008–5011. [CrossRef] [PubMed]

Disclaimer/Publisher's Note: The statements, opinions and data contained in all publications are solely those of the individual author(s) and contributor(s) and not of MDPI and/or the editor(s). MDPI and/or the editor(s) disclaim responsibility for any injury to people or property resulting from any ideas, methods, instructions or products referred to in the content.

Nouveaux Photosensibilisateurs Encapsulés dans des Complexes d'Arène-Ruthénium Actifs en Thérapie Photodynamique : Signalisation Intracellulaire et Évaluation dans le Cancer Colorectal

Le cancer colorectal (CCR) est le troisième cancer le plus fréquent dans le monde et son incidence ne cesse d'augmenter. Malgré des avancées dans les traitements du CCR, des défis tels que les effets secondaires et la résistance aux thérapies restent à relever. La thérapie photodynamique (PDT) apparaît comme une modalité prometteuse, utilisée cliniquement dans le traitement de différentes maladies, dont le cancer. Elle repose sur l'utilisation de molécules photosensibles appelées photosensibilisateurs (PSs), suivie d'une photoactivation par illumination des tissus malades. Les PSs peuvent être conçus pour s'accumuler spécifiquement dans les cellules cancéreuses, ce qui permet lors de leur photoactivation ciblée de déclencher la production d'espèces réactives de l'oxygène. Cela provoquera un stress oxydatif conduisant à la mort cellulaire. Les composés à base de ruthénium (Ru), connus pour leur toxicité sélective à l'égard des cellules cancéreuses, ont un potentiel en tant qu'agents anticancéreux. Dans cette étude, nous avons évalué l'effet de deux assemblages arène-Ru distincts, hébergeant des porphines dans leur cavité interne, comme agents de PDT sur les lignées cellulaires humaines HCT116 et HT-29 de CCR. L'internalisation et la localisation cellulaire des assemblages chargés de porphine ont été confirmées par microscopie à fluorescence. De plus, une photocytotoxicité significative a été observée dans les deux lignées cellulaires après la photoactivation de la porphine dans les systèmes de cages, perturbant la progression du cycle cellulaire et induisant l'apoptose par l'induction de la voie apoptotique mitochondriale avec activation de la caspase-3. Ces résultats suggèrent que les assemblages arène-Ru hébergeant un PS sont des candidats potentiels pour le traitement du CCR.

Mots-clés : cancer colorectal ; thérapie photodynamique ; photosensibilisateurs ; assemblages arène-ruthénium ; apoptose

New Photosensitizers Encapsulated within Arene-Ruthenium Complexes Active in Photodynamic Therapy: Intracellular Signaling and Evaluation in Colorectal Cancer

Colorectal cancer (CRC) is the third most common cancer in the world with an ongoing rising incidence. Despite advances in CRC treatments, challenges such as side effects and therapy resistance remain to be addressed. Photodynamic therapy (PDT) emerges as a promising modality, clinically used in treating different diseases, including cancer. It is based on the use of photosensitive molecules called photosensitizers (PSs), followed by photoactivation through illumination of the diseased tissues. The PSs can be designed to specifically accumulate in cancer cells, enabling their targeted photoactivation to trigger the production of reactive oxygen species. This will cause oxidative stress leading to cell death. Ruthenium (Ru)-based compounds, known for their selective toxicity towards cancer cells, hold potential as anti-cancer agents. In this study, we investigated the effect of two distinct arene-Ru assemblies lodging porphin in their inner cavity, as PDT agents on HCT116 and HT-29 human CRC cell lines. The cellular internalization and localization of the porphin-loaded assemblies were confirmed by fluorescence microscopy. Additionally, significant photocytotoxicity was observed in both cell lines after photoactivation of the porphin in the cage systems, disrupting the cell cycle progression and inducing apoptosis through induction of the mitochondrial apoptotic pathway with caspase-3 activation. These findings suggest that arene-Ru assemblies lodging a PS are potent candidates for CRC treatment.

Keywords: colorectal cancer; photodynamic therapy; photosensitizers; arene-ruthenium assemblies; apoptosis